11-4-2015 12:00 AM

The Development and Validation of a Molecular Imaging Probe Targeted to Cathepsin D for the In-vivo Detection of Alzheimer Disease

Jonatan Snir
The University of Western Ontario

Supervisor
Drs. Robert Bartha
The University of Western Ontario Joint Supervisor
Stephen Pasternak
The University of Western Ontario

Graduate Program in Medical Biophysics
A thesis submitted in partial fulfillment of the requirements for the degree in Doctor of Philosophy

The Development and Validation of a Molecular Imaging Probe Targeted to Cathepsin D for the In-vivo Detection of Alzheimer Disease

(Thesis format: Integrated Article)

by

Jonatan Snir

Graduate Program in the Medical Biophysics (CAMPEP)
In Collaboration with Molecular Imaging

A thesis submitted in partial fulfillment
of the requirements for the degree of
Doctor of Philosophy in Medical Biophysics

The School of Graduate and Postdoctoral Studies
The University of Western Ontario
London, Ontario, Canada

Abstract

Background: Currently there is no widely accepted test to diagnose AD. The involvement of the lysosomal system in Alzheimer's disease (AD) progression provides an opportunity to develop associated biomarkers. The lysosomal enzyme Cathepsin D (CatD) has been shown to be over-expressed in the AD brain before clinical onset. We have developed a dual modality contrast agent (CA) to detect CatD activity which consists of an HIV-1 Tat Cell Penetrating Peptide (CPP) conjugated to a CatD cleavage sequence and two imaging moieties consisting of a fluorescently- tagged probe and a DOTA cage for chelating Gallium-68. The purpose of this work was to validate CatD as an AD biomarker across multiple AD disease models and to test our novel CA in-vivo by means of optical near infra-red (NIR) fluorescence imaging and positron emission tomography (PET). Methods: Three transgenic (Tg) mouse AD model strains were tested for CatD expression by Western blot and immunohistochemistry analysis. The chosen mouse line (5XFAD) and controls were imaged at 5 and 12 months of age using an eXplore Optix scanner (GE Healthcare, Milwaukee, WI, USA). Next, mice at 2, 6 and 9 months of age were tested using an Inveon microPET system (Siemens Medical Solutions, Knoxville TN, USA) using a ^{68}Ga-labeled CatD targeted CA. Results: All 3 AD mice demonstrated an elevation of CatD expression in parallel with AD pathology. The 5XFAD had the highest levels of CatD, making it the best mouse model to study CatD upregulation. The rate of the NIR CatD Targeted CA washout was significantly slower in the 5XFAD mice ($p<0.05$) at 5 and 12 months of age compared to controls. The control CAs showed no differences in washout. MicroPET imaging of the 5XFAD Tg mice showed significantly higher uptake rate of the CatD targeting CA in the forebrain relative to hindbrain at 2, 6 and 9 months of age compared to controls. Conclusion: Both the optical and the microPET data demonstrated increased retention of our agent in the brain of 5XFAD mice compared to age-matched controls. These studies show that this agent may be useful for AD early detection.

Keywords: Alzheimer's disease, Early detection, Cathepsin D, Optical Imaging, positron emission tomography, contrast agent, Magnetic Resonance Imaging.

Co-Authorship Statement

All three chapters excluding the introduction have been submitted as manuscripts for publication in peer review journals or are in preparation for submission. The following description provides information regarding the contribution of each co-author:

Chapter 2: Cathepsin D Expression in the Brain across Alzheimer Disease Mice Models

Jonatan Snir – Formulation of experimental design; Selection of mice strains, antibodies, and time points; Performed euthanasia, collected and prepared tissue for processing at the Pathology lab; Performed Western blots; Analysed all Western blots and histological slices; Main author of introduction, methods, results and discussion.
Dr. Stephen Pasternak – Scientist, clinician, primary investigator. Experimental and contrast agent design. Supervisory role with contribution to data interpretation.
Dr. Robert Bartha – Scientist, primary investigator. Experimental and contrast agent design, supervisory role with contribution to data interpretation.

Chapter 3: Prolonged in-vivo retention of a Cathepsin D targeted optical contrast agent in a mouse model of Alzheimer's disease

Jonatan Snir – Formulation of experimental design; Selection of the Near-Infrared dye, the optical imaging system and the mouse model; Majority of intravenous catheterization and subject pre-imaging preparations; Collection and analysis of all imaging data; Performed euthanasia, collected and prepared tissue for processing at the Pathology lab; Analysed of all Western blots and histological slices; Main author of introduction, methods, results and discussion.
Dr. Mojmir Suchey – Chemist. Synthesis and chemical characterization of yield for all in-house developed contrasts agents.
Dr. Keith St. Lawrance – Scientist. Experimental design, training and supervision of optical scanner use.
Dr. Robert Hudson – Chemist. Contrast agent development and experimental design.
Dr. Stephen Pasternak – Scientist, clinician, primary investigator. Experimental and contrast agent design. Supervisory role with contribution to data interpretation.
Dr. Robert Bartha – Scientist, primary investigator. Experimental and contrast agent design, supervisory role with contribution to data interpretation.

Chapter 4: A Novel Positron Emission Tomography Contrast Agent Targeting Cathepsin-D: In-vivo retention in an Alzheimer's disease mouse model

Jonatan Snir – Formulation of experimental design; Selection of radio-isotope and the mouse model; Majority of intravenous catheterization and subject pre-imaging preparations; Collection and analysis of all imaging data; Performed euthanasia, collected and prepared tissue for processing at the Pathology lab; Analysed all histological slices; Performed all biodistribution data collection and analysis; Main author of introduction, methods, results and discussion.

Dr. Mojmir Suchey – Chemist. Synthesis and chemical characterization of yield for all in-house developed contrasts agents.
Dr. Geron A. Bindseil – Physicist. Provided expertise on microPET system. Consultation
Dr. Blaine A. Chronik – Scientist. Experimental design, expertise and supervision of microPET scanner use.
Dr. Robert Hudson – Chemist. Contrast agent development and experimental design.
Dr. Stephen Pasternak – Scientist, clinician, primary investigator. Experimental and contrast agent design. Supervisory role with contribution to data analysis.
Dr. Robert Bartha – Scientist, primary investigator. Experimental and contrast agent design, supervisory role with contribution to data analysis.

Acknowledgments

This thesis converges together several multidisciplinary fields to form a unified hypothesis for the realization of an early diagnosis tool of Alzheimer's disease. It would not have been possible without the foresight, mentorship, of my supervisors, the advice and help of many scientists, assistance staff, colleagues, friends and family. The following is a small gesture of gratitude and acknowledgement for the much appreciative support over the course of the past four years.

Firstly, I would like to express my sincere gratitude to my supervisors Drs. Robert Bartha and Stephen Pasternak for the continuous support of my Ph.D study and related research. Their guidance for this work is second to none. Rob's patience, immense knowledge, kind demeanor, enthusiasm and curiosity continually provided me with the motivation and drive throughout my studies. Steve's insightful comments and encouragement, generosity and innovative outlook really help guide my work. His dark sense of humour always brings a smile to my face. With Steve's and Rob's respective background, specialization and expertise I could not have imagined having a better pair of advisors and mentors for my Ph.D study.

Besides my mentors, I would like to thank the rest of my thesis committee: Drs. Keith St. Lawrence and Giles Santyr. Their perspective, encouragement and input helped shape my methods and analysis. Additionally, Keith's research laboratory provided us with the preclinical optical scanner that was necessary for the first sustainable in-vivo imaging trials of our contrast agent. His expertise was necessary for our successful Near Infrared study. Giles' questions and comments helped produce a careful and meaningful analysis of the data even after his unfortunate departure from Robarts and move to Toronto's scientific community.

My sincere thanks also go to Dr. Mojmir Suchy, Dr. Robert Hudson, who provided the opportunity for this project to become a reality. The collaborative effort required their expertise and their contribution. Mojmir dedication to the project and his hard work to synthesize our contrast agent on a timely basis is forever appreciated.

In addition, recognition and thanks goes to Drs. Blaine Chronik and Geron Bindseil for the training and access to the preclinical microPET scanner for which our second, more clinically translatable in-vivo study heavily relied on. Without their support it would not be possible to conduct the microPET studies.

Special thanks go to the support staff at both Robarts Research Institute and St. Joseph hospital. The help of Jennifer Hadway and Lise Desjardins was paramount to the success of my studies at St. Joseph, and that of Ashley Kirley and Miranda Bellyou at Robarts. I am so very thankful for their help and humour in lightening up the spirit during the various experiments. I am in debt to Wendy Hough, a fantastic, caring person whom I owe for all the reminders, checks and updates required for the successful pursue of this degree. Anne Leaist – you are delightful as you are helpful – thank you.

Next, I would like to thank Drs. Flavio Beraldo for all his help with tissue collection and Amanda Hamilton with CryoViz ™ data collection as well as Claudia Seah for laboratory help - their advice, support, and assistance is much appreciated. Also, I am grateful for the hard work by the pathology lab crew at Robarts: Drs. Caroline O'Neil and Nong Zengxuan. I must acknowledge all the work done by Rob Ta, whose research preceded mine and was a building block on which my research stood. I would also like thank my fellow labmates and other graduate students at Robarts for the stimulating discussions and fun de-stressing times. My friends Patrick, Dan, Kathryn, Kristin, Matt, Damien, Nikhil, Adam, Sandy, Kyle, Ilma and of course Clover-Thunder to name a few – have been a great source of distraction from the stress of graduate school.

I have to acknowledge Dr. Paula Foster, my M.Sc supervisor for her mentorship that has carried with me since I graduated in 2008, and instilled in me the flame for research. She has been a friend, a listening ear - providing input and advice at times of need. Her lab and students always welcomed me with open arms.

Acknowledgement and thanks go to Drs. Jerry Battista and Robert Stodilka for their input, discussions and responsibility with the CAMPEP accreditation of the Medical Biophysics department at UWO. Their efforts on providing one-on-one support for the CAMPEP students group is much appreciated. In addition, my appreciation to Dr. Savita

Dhanbantari for establishing the molecular imaging program within the department. Her on-going enthusiasm, engagement and involvement in the research community are of great value for all of the students enrolled. I have learned much from her.

Warm gratitude goes to Ann Langeman for checking over the thesis grammar and raising a wonderful person, her daughter - I'm soon to call my wife.

Almost last but far from least; I would like to thank my family. My parents who have sacrificed so much to bring my twin and I into this world, and years later immigrate into Canada. Both my parents are a source of inspiration for their accomplishments and achievements. From my father immense knowledge, strength and wisdom to my mom's intellect and compassion - your support and love has been un-parallel and unconditional for which I am eternally grateful for. I'm thankful for both my sisters for all their help raising me despite being an annoyingly inquisitive child. Ati, you have defeated many obstacles and have become a wonderful women, and Eldar – you are a great addition to the family and it's my pleasure to have you as my brother-in-law. David, my twin, whom I love and care for, always brings a fresh and even often cynical yet enlightening perspective to any subject. His help with expediting the production of some of the figures for my work is greatly appreciative. David is one of the most creative, capable and innovative people I know - I am very proud of him and lucky to have him as my brother. Finally, Julie, my fiancée, has been a monumental support and a source of inspiration for pursuing her dreams of becoming a Veterinarian. Your unconditional love, kindness and patience with the long sleepless nights of work have been the corner stone for enjoying the process of completing this work. I love and cherish you and looking forward to our life together.

Table of Contents

List of Tables

List of Figures

List of Equations

List of Appendices

List of Abbreviations

ACD	Annihilation Coincidence Detection
AD	Alzheimer's Disease
ANOVA	Analysis Of Variance
APH-1	Anterior Pharynx-Defective 1
ApoE	Apolipoprotein E
APP	Amyloid Precursor Protein
ARRIVE	Animal Research: Reporting Of In Vivo Experiments
AUC	Area Under The Curve
Aβ	Amyloid Beta
BACE	Beta-Site Amyloid Precursor Protein Cleaving Enzyme 1
BBB	Blood Brain Barrier
Bl	Bladder
Bq	Becquerel
Br	Brain
CA	Contrast Agent
CB	Cerebellum
CCD	Charged-Coupled Device
CEST	Chemical Exchange Saturation Transfer
Cor	Cortex
CPP	Cell Penetrating Peptide
CSF	Cerebral Spinal Fluid
CT	Computed Tomography
CW	Continuous Wave
DIPEA	N,N-Diisopropylethylamine
DMF	Dimethylformamide
DNA	Deoxyribonucleic Acid
DOI	Depth Of Interaction Effect
DOTA	1,4,7,10-Tetraazacyclododecane-1,4,7,10-Tetraacetic Acid
DOTAM	1,4,7,10-Tetrakis(Carbamoylmethyl)-1,4,7,10-Tetraazacyclododecane.
ECL	Enhanced Chemiluminescence Reagents
EM	Expectation Maximization
EPR	Enhanced Permeability And Retention Effect
FAD	Familial Alzheimer's Disease
FBP	Analytical Filtered Back Projection
FD	Frequency Domain
FDG	Fluorodeoxyglucose

FLASH	Fast Low Angle Shot
FUS	Focused Ultrasound
FWHM	Pulse Width
H&E	Haematoxylin And Eosin Stain
HBTU	(2-(1h-Benzotriazol-1-Yl)-1,1,3,3-Tetramethyluronium Hexafluorophosphate)
Hip	Hippocampus,
HPLC	High-Performance Liquid Chromatography
Hrt	Heart
ID	Injected Dose
IHC	Immunohistochemistry
Liv	Liver
LOR	Line Of Response
LSCM	Laser Scanning Confocal Microscope Incorporates
LTP	Long Term Potentiation
Lun	Lungs
MAP	Maximum A Priori
MCI	Mild Cognitive Impairment
Mid	Midbrain
MRI	Magnetic Resonance Imaging
MRS	Magnetic Resonance Spectroscopy
NBF	Neutral Buffered Formalin
NFT	Neurofibrillary Tangle
NIR	Near Infrared
NMDA	N-Methyl-D-Aspartate
non-Tg	Non-Transgenic
NSAIDs	Anti-Inflammatory Drugs
Olf	Olfactory
OPARACHEE	On-Resonance Paramagnetic Chemical Exchange Effect
OP-MAP	Poisson Maximum A Posteriori
OSEM	Iterative Ordered Subset Expectation Maximization
OSEM3D	3D Iterative Ordered Subset Expectation Maximization
PARACEST	Paramagnetic Species
PC3M	Prostate Cancer Cell Line
PEN-2	Presenilin Enhancer 2
PET	Positron Emission Tomography
PHF	Paired Helical Filaments
PK/PD	Pharmacokinetics/ Pharmacodynamics

PMT	Photomultiplier Tube
PrP	Prion Protein
PS1	Presenilin-1
PSEN-1	Ps1 Gene
ROC	Receiver Operating Characteristic
ROI	Region Of Interest
ROS	Reactive Oxygen Species
SEM	Standard Error Of The Mean
SNR	Signal-To-Noise Ratio
SPECT	Single Photon Emission Computed Tomography
SPPS	Standard Solid Phase Peptide Synthesis
Str	Striatum
SUV	Standard Uptake Value
SUVR	Relative Standard Uptake Value
T	Temperature
TAC	Time Activity Curves
Tat	Peptide Derived From Transactivator Of Transcription
TCSPC	Time-Correlated Single Photon Counting
TD	Time Domain
TE	Echo Time
Tg	Transgenic
Thal	Thalamus
TPSF	Temporal Point Spread Functions
TR	Repetition Time
UPLC	Ultra Performance Liquid Chromatography
UVB	Ultraviolet (290-320 Nm)
VOI	Volume Of Interest
WALTZ	Low Power Radiofrequency Pulse Train
WB	Western Blot
WT	Wild Type

Preface

Alzheimer's disease (AD) is a terrible, incurable, insidious neurodegenerative disorder. It is the most common form of dementia and is responsible for a crippling economic burden on the health care system and grave emotional, physical, and mental burden on family care-givers and patients. The disease slowly disintegrates an individual's identity, their memories, capacity to perform daily tasks and eventually leads to death. Currently, there are no definitive tests to detect AD. A probable AD diagnosis is made by a clinician based on clinical presentation: memory impairment, cognitive decline, and family and individual medical history. Ironically, the budget allocated by western-world countries to develop a cure and improve diagnostic approaches is approximated to be well below 1% of the budget assigned for the care of those affected by the disease. Sadly, the most popular and sought after diagnostic tactics still rely either on a century old, albeit momentous, observation of β Amyloid (Aβ) plaques and neurofibrillary tangles (NFT) in post-mortem brains from people with the disease, or other downstream pathogenic changes *in-vivo*. The latter includes cerebral spinal fluid biomarker tests and structural or functional changes in the brain as measured by magnetic resonance imaging (MRI) /fMRI, ^{18}F Fluorodeoxyglucose (FDG), and contrast agents (CA) targeting Aβ/ NFT for use with either MRI or positron emission tomography (PET). To complicate things further, many tests lack the ability to differentiate AD from other pathologies, or normal aging unless used in tandem with a large number of complimentary tests. While early results are promising based on on-going observations, targeting the two hallmark pathologies (Aβ and NFT) may be inherently flawed due to the very high prevalence of these pathologies in cognitively normal older adults (80% of adults over the age of 80). Although not commonly acknowledged, the lysosomal system has been proven to play an important, yet not fully elucidated, role in the development of the disease. It is the main objective of this work to provide an alternative early diagnostic paradigm for AD. The hypothesized approach was successfully demonstrated in this thesis using AD model mice that are shown to recapitulate increased levels of Cathepsin D (CatD) and are differentiated from age-matched controls using both optical and the more clinically-relevant positron emission tomography imaging systems.

The thesis core chapters are organized as follows: First an introduction provides background information about the disease. Second, the search for an appropriate animal model is reported. Third, the first in-vivo attempt at using a targeted, as well as two control (a non-targeting, and a non-penetrating) CAs to differentiate diseased animals from controls is described. Forth, a more clinically translatable imaging modality evaluation is reported using only the targeted CA. Finally, a conclusion and integration of all the data collected is reported together with a description of future directions. By carefully reviewing the introduction, the reader is expected to learn first about AD pathology, prevalence, the involvement of the lysosomal system, and the common diagnostic / treatments models. The reader will learn about the power of molecular imaging, the utilization of targeted CAs and the benefit of using a cell penetrating peptide to cross the blood-brain-barrier (BBB). In addition, the reader will learn the basics of the modalities and assays used in this study such as microscopy, fluorescence optical imaging, positron imaging, magnetic resonance imaging and finally, histology and Western blot protein quantification. Following the introduction, the reader will be presented with findings that summarize the planning, execution, analysis, and successful implementation of a molecular imaging approach for the detection of increased CatD levels in an AD model mouse. First the evaluation of CatD levels as well as Aβ (as a measure of disease progression) is performed in three different strains of AD mouse models. These data lead to the selection of the 5XFAD model, which was found to be very aggressive, yet provides several advantageous characteristics for the testing of our novel CatD targeting probe in-vivo. Next the 5XFAD model is examined in-vivo using optical imaging techniques and specially designed control CA (lacking the cell penetrating peptide, or lacking the targeting moiety). The CA is modified to have a Near Infrared dye that allows the detection of minute concentrations (10^{-12}) at depths up to 1 cm. The results are conclusive and indicate that the preferential uptake and retention of our CA require both penetration across the BBB and the targeting of CatD. The sensitivity of this approached allowed the differentiation of transgenic (Tg) mice from wild-type controls at not only 12 months of age but also at 5 months of age. Finally, a more clinically translatable approach examined a slightly modified CA structure to accommodate imaging the mice longitudinally using microPET. This was accomplished

by incorporating ^{68}Ga, a positron emitting radioisotope with a short half-life that can be made readily available at any clinic without the use of a cyclotron. This tomographic approach allowed the measurement of activity over time directly in the brain of the mice as well as other body regions. It was shown that Tg mice could be differentiated from age-matched non-Tg littermates as early as 2 months of age by measuring the rate of change of activity in the forebrain relative to the hindbrain. Similarly, significant differences were noted at 6 and 9 months of age.

This study showcases several important findings and achievements. First, significantly increased levels of CatD (compared with controls) correlate with Aβ pathology, and are detected in multiple mouse models that already recapitulate other AD-like pathologies. Second, the HIV-1 tat peptide provides an adequate penetration of a large (>3kDa) CA across the BBB into the brain for successful molecular targeted optical, MRI, or PET imaging. Finally, CatD targeting allows the differentiation of AD mice from controls using multiple modalities, and at multiple ages, as early as 2 months.

Chapter 1 : Introduction

1 Introduction

The work accomplished and documented here is motivated by the lack of clinical standards for a conclusive, ante mortem, early diagnosis of Alzheimer's disease (AD). This initial chapter is meant to provide a concise review of relevant background information with respect to AD and the different tools developed to better understand its pathogenesis including animal models, contrast agent (CA) development, and imaging modalities.

1.1 Mild Cognitive Impairment

Mild Cognitive Impairment (MCI) is a state at which an individual experiences mild but noticeable changes in some aspects of cognitive function (e.g. thinking abilities). These changes do not immediately pose a threat to the individual's capability to perform daily activities, but may represent a transitional stage from normal aging to early dementia [1]. Amnestic MCI, the most common subtype of MCI, requires a memory complaint, preferably with objective corroboration but no significant change in daily functioning [2]. MCI prevalence is estimated to be approximately 16% in non-demented geriatric individuals [3] with an annual conversion rate to dementia ranging up to 15%, or 50% over 5 years [2]. All subtypes of MCI are associated with increased risk for dementias; however, individuals with this diagnosis may remain stable or even revert to normal, suggesting the course of MCI is quite heterogeneous [4]. Regardless, it has been shown that people with amnestic MCI are more likely to develop AD [5].

1.2 Dementia and Alzheimer's Disease

By definition, dementia is a neurocognitive disorder severe enough to interfere with performing social or occupational daily basic tasks [5]. There are many types of

dementia, with increasing evidence indicating that many people with dementia have mixed dementia – that is, the combination of more than one single pathology [6]. AD is an insidious disease, and the most common cause of dementia [5]. It was first described over 100 years ago by Dr. Alois Alzheimer who presented his early findings to the medical community in Tübingen, Germany [7]. Since then large research efforts have focused on understanding the cause of AD, developing tools to diagnose it in the clinic, and attempting to treat or even cure the disease [5]. Research advances have underscored the complex pathology of the disorder requiring additional studies to elucidate the intricate processes involved in its development.

AD symptoms can present differently in different people [6]. However, the most common early symptom is the gradual loss of short term memory. This symptom is thought to be caused initially by loss of synapses in areas of the brain responsible for forming new memories [5]. As AD progresses, patients present with impairment with other spheres of cognition, including impairments in language and an increasing inability to plan or solve problems. They have difficulty completing familiar tasks and they have difficulty understanding visual images, spatial relationships and motor movements. In the mid stage of the disease, patients lose their independence and have difficulty with basic daily activities such as bathing, dressing and eating. This eventually evolves into an "akinetic mute" end stage. A concise simplified summary of some other common forms of dementia and their respective clinical presentation is shown in Table 1. It is worth noting that Parkinson and Dementia of Lewy Body share the pathology of α-synuclein aggregates, Frontotemporal lobe dementia and AD share the pathology of tau tangles, but only AD (from the list above) exhibits β-amyloid plaques.

Table 1-1. Common types of dementias.

Type of dementia	Clinical presentation	Pathology
Alzheimer's disease	Early symptoms: Impaired short term memory, e.g. difficulty remembering recent conversations, names, or events; apathy and depression. Late symptoms: Impaired communication, disorientation, confusion, poor judgment, behavior changes and ultimately difficulty speaking swallowing and walking.	Protein fragment β-amyloid (plaques) outside neurons in the brain and twisted strands of the protein Tau (tangles) inside neurons.
Vascular dementia	Impaired judgment or ability to make decisions, plan or organize. Typically also have signs of stroke	Blood vessel blockage or damage leading to infarcts (strokes) and/or bleeding in the brain.
Dementia of Lewy Body	Sleep disturbances, well-formed visual hallucinations, slowness, gait imbalance and visuospatial impairment. Motor features of Parkinson's disease	Brain neurons accumulate Lewy bodies and lewy neurites, abnormal aggregations of the protein α-synuclein. (Especially in the Cortex).
Frontotemporal lobe dementia	Changes in personality and behavior and difficulty with producing or comprehending language.	Frontal and temporal lobes become atrophied; upper layers of the cortex develop protein inclusions (e.g Tau protein).
Parkinson's disease	Slowness, rigidity, intention tremor and changes in gait.	α-synuclein aggregates in substantia nigra believed to cause degeneration of nerve cells that produce dopamine.

Table has been adapted from the 2014 Alzheimer's disease facts and Figures [5].

1.2.1 Alzheimer's Disease Epidemiology and Risk Factors

AD is the most common form of dementia accounting for 50-60% of all dementia cases. The prevalence of AD is less than 1% in people over 60 and under 65 years of age. However there is an exponential increase in AD with age, to 1 out of 3.5 people affected in the age group of 85 years and over and living in the western world [8]. It is expected that by 2050 there will be 115 million people living with AD in the world including more than one million Canadians [9, 10]. This surge is due to the anticipated increase in life expectancy [8] with the greatest risk factor for AD being aging. Despite the prevalence, AD is not a normal part of aging. The main risk factors for developing AD are age and education. Other risk factors include, but are not limited to, stroke/vascular risk factors, family history, environmental and lifestyle factors, genetic mutations, and MCI.

Over 20 years ago, two separate research groups made an association between the apolipoprotein E (ApoE) ε4 allele and sporadic AD [11, 12]. Since then, many other genes have been associated with sporadic AD, although these genes account for only a small amount of relative risk [13]. However, the ApoE ε4 allele has been corroborated now by many groups in a very large cohort of AD patients and is the largest known contributor of genetic risk for the development of sporadic AD [14]. In fact, a meta-analysis showed that the ApoE ε4 allele increases the risk of developing AD by three times in heterozygotes and by 15 times in homozygotes [15]. Regardless of ApoE involvement, it is estimated that 60-80% of AD risk may be heritable [16]. Therefore, when AD runs in a family, heredity and shared environmental and lifestyle factors play a role as is evident by the significantly higher risk (nearly double) in those with a first degree relative such as parent or sibling that have the disease [17].

AD can be either *sporadic* or *familial*. Only 1% of cases are familial, with the majority due to mutations in genes encoding the proteins amyloid precursor protein (APP on chromosome 21), presenilin 1 (PSEN1 on chromosome 14) and presenilin 2 (PSEN2 on chromosome 1) and are referred to as *familial AD* (FAD). In FAD, an individual inheriting the associated gene mutations usually develops the disease much earlier than in the sporadic form of the disease, often in their 40's. For FAD cases, the PSEN1 mutation

accounts for the largest number of known mutations (177) implicated with the development of the disease, followed by APP (32), and lastly PSEN2 (14). Three main categories of FAD APP mutations exist: one that increases the rate of production of all isoforms of amyloid species [18] (e.g. Swedish), another increases the relative amount of the more toxic $A\beta_{42}$ produced [19] (e.g. London), and finally one that decreases α-cleavage by increasing the stability of Aβ or increases its propensity to aggregate [20] (e.g. Arctic mutations).

Other risk factors have been suggested and include low cognitive reserve (e.g. low education and occupation attainment, social and cognitive engagement), high cholesterol, high blood pressure, atherosclerosis, coronary heart disease, smoking, obesity and diabetes [21].

1.2.2 Alzheimer's Disease Pathology

Brain changes leading to AD may begin 20 years or more before symptoms appear [22]. A healthy adult brain has billions of neurons, each with long branching extensions connecting neurons with other neurons. These connections, called synapses, create the cellular basis for memories, sensations, emotions and movements. Earlier in life, before clinical presentation, AD disrupts proper functioning of neurons and synapses. In AD, information transfer at synapses begins to fail, with the number of synapses declining, in a potentially reversible phase of AD. Eventually neurons also begin dying, leading to tissue atrophy and irreversible cognitive decline. The hallmark pathologies used for a conclusive post-mortem diagnosis involves the accumulation of the protein β-amyloid (Aβ) in plaques [5] and an abnormal form of the protein Tau in brain cells [5]. Additionally and allegedly because of the former pathologies, neurotransmitter systems impairment and neuroinflammation have been implicated in AD.

1.2.2.1 Amyloid plaques

At the microscopic level, there are characteristic lesions, known as senile plaques in the brains of AD patients (Figure 1-1). It was only in the 1980's that Aβ protein was

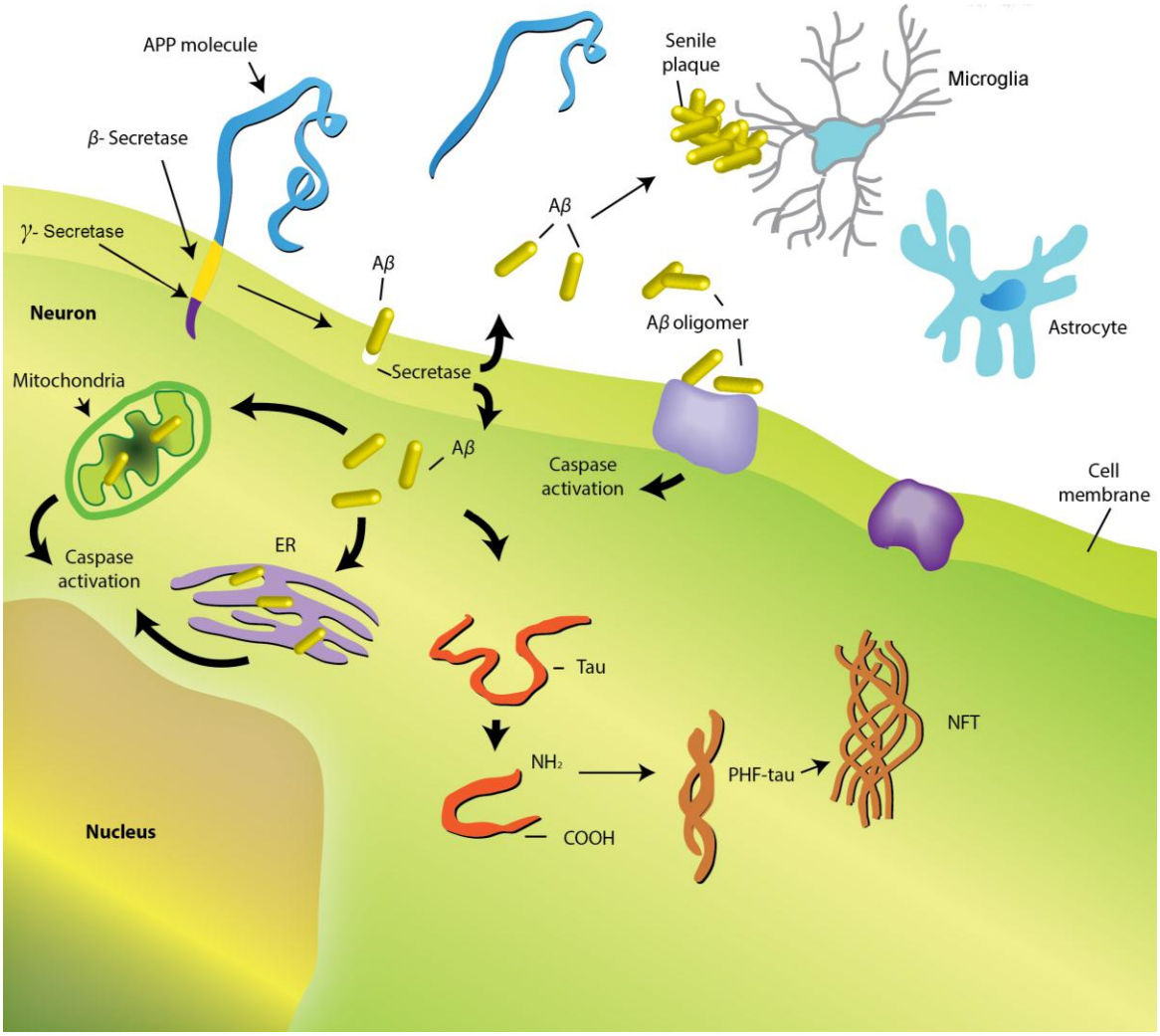

Figure 1-1. Cellular processing and environment of AD pathology. The APP (top-left) is cleaved to produce the A_β segment which can then aggregate into small oligomers or longer peptides that cause the Endoplasmic Reticulum (ER) or mitochondria to activate caspase leading to cell death. Alternatively these oligomers may affect a variety of receptors that may also lead to cell death. Extracellularly, A_β are also found in senile plaques, nearby interacting microglia, and astrocytes, presumably perpetrating inflammation and oxidative stress. Downstream from A_β production, potentially due to the effect of A_β on Tau synthesis, there is destabilization of microtubules as well as the eventual formation of neurofibrillary tangles (NFT).

identified as the major constituent of these plaques [23]. This discovery in turn led to the amyloid cascade hypothesis, which is the leading model of the pathophysiology of Alzheimer's disease [24]. Aβ is produced by the cleavage of the large transmembrane APP (Figure 1-1) at the β site by an aspartyl proteinase [25] called beta-site APP-cleaving enzyme (BACE). Alternatively, APP may be cleaved by a family of enzymes referred to as α–secretases that prevent the production of Aβ [26]. This latter pathway is less common in neurons [27]. The leftover fragment from BACE cleavage is then cleaved at an additional γ cleavage site, which is variably located along the APP segment (Figure 1-1 Adapted from [28]) by the intramembranous protease complex referred to as the γ-secretase. The γ-secretase consists of four components: PSEN-1 , nicastrin, PEN-2 and APH-1 with PSEN-1 occupying the active site [29]. The central dogma states that an imbalance between the production and clearance of Aβ in the brain is the initiating event, ultimately leading to synaptic loss, neuronal degeneration, and dementia [30].

While senile plaques have remained the key feature of AD, it is the oligomers that should be considered the culprit of AD-related synapse loss and probably eventual neuronal cell death [31]. Despite the indisputable connection between Aβ and AD, which has yet to be completely understood – amyloid plaque load does not correlate well with cognitive function or disease progression in humans [32]. This lack of correlation has highlighted the potential drawbacks of the original amyloid hypothesis. Consequently, some researchers believe that the abnormal Tau protein formations, described next, could be the critical causative agent in AD since the latter correlates better with cognitive impairment [32].

1.2.2.2 Tau

Almost in parallel with the identification of Aβ in plaques, intracellular neurofibrillary tangles were also described. These tangles are composed of abnormally hyperphosphorylated Tau protein [33] processed as described below and shown in Figure 1-1. Normal Tau is an axonal protein that binds to microtubules promoting assembly and stability of microtubules, which are structural elements and enable the transport of organelles and other essential molecules within all cells in the brain (and elsewhere).

Abnormal Tau is believed to contribute to cell death by disrupting the normal function of microtubules by forming paired helical filaments (PHF) that aggregate to form neurofibrillary tangles or NFT [5]. Tau phosphorylation is regulated by the balance between multiple kinases and phosphatases [34]. Hyperphosphorylation in AD leads to sequestration of normal Tau and other microtubule-associated proteins. These microtubules are destabilized and the abnormal Tau aggregates into insoluble fibrils, then larger tangles, ultimately compromising neuronal function and leading to cell death [34].

While NFTs correlate well with AD onset and progression [35], to date no Tau mutations have been found in FAD cases [24] implying that Tau plays a secondary role to Aβ in AD progression. In fact, Tau mutations have been found in association with other distinct diseases such as frontotemporal dementia (which lacks Aβ pathology) [36, 37]. The secondary role of Tau is further supported by the order of appearance of Aβ plaques prior to NFTs in Down syndrome [38]. Moreover, experimental changes (reductions, or increases) in Aβ oligomers in mice resulted in directly proportional changes in Tau [39, 40]. Therefore, it is likely that Tau effects are downstream from Aβ and yet still have an important role in AD progression and severity [24].

1.2.2.3 Lysosomal System and Cathepsin D

The lysosomal/endosomal system comprises a series of intracellular compartments responsible for many different functions in cells [24]. Their main function is the processing (e.g. digestion, post-processing) of extracellular materials and cellular proteins, lipids and carbohydrates which is accomplished by having a highly acidic (pH of 4.5) environment and containing many different catabolic (digestive) enzymes [41]. There are more than 40 lysosomal storage diseases, which are usually caused by the absence of a critical enzyme, many of which can lead to dementia and eventually death [24]. Specifically, the endosomal/lysosomal system has been shown to play a role in Aβ production and clearance and this system has been shown to be up-regulated (increase in the size and number of lysosomal bodies and the expression of lysosomal enzymes) in AD [42-45]. Lysosomes are highly enriched in APP and γ-secretase proteins (e.g presenilin) with the capacity for γ-secretase activity [46]. Several experiments where

APP on the cell surface was labeled with a fluorescent tag have shown the APP gets internalized within lysosomes, cleaved into Aβ and then secreted or retained intracellularly by the endosomal/lysosomal system [24, 47]. Three pathways have been previously described. APP originating from the cell surface can either migrate into endosomes through endocytosis [48], directly from the cell surface to the lysosomes [49], or through autophagosome processing [50]. Furthermore, in a recent elegant set of experiments, a fourth newly recognized pathway of APP trafficking was identified that involved the direct passage of APP from the Golgi apparatus to the lysosome [51]. All four pathways are illustrated in Figure 1-2 (adapted from Tam et al. [51]).

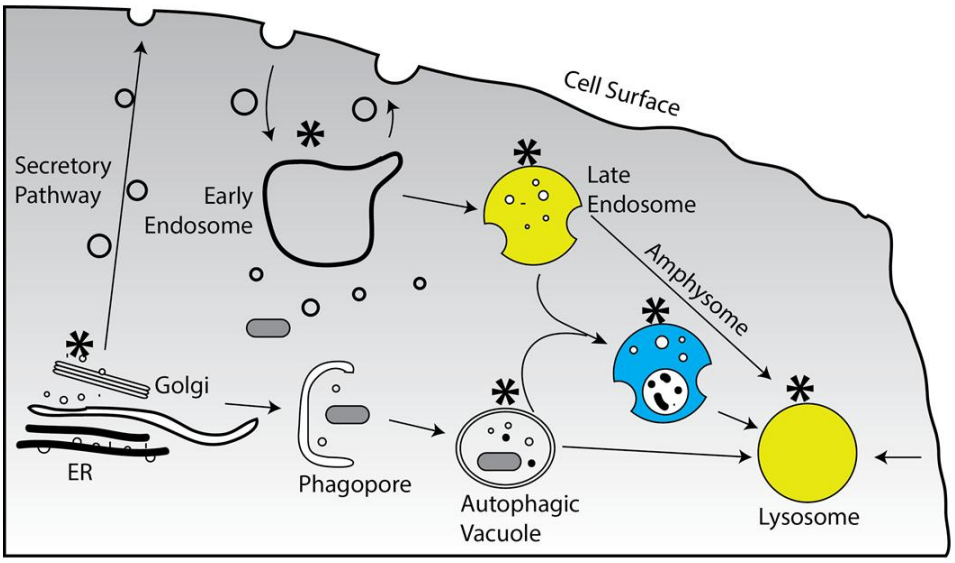

Figure 1-2. Overview of the endosomal/lysosomal and autophagy systems. APP is synthesized in the ER and transits to the Golgi, where it is glycosylated and exported to the cell surface or alternatively to internal structures and eventually the lysosome. From the cell surface the APP may be cleaved and/or endocytosed into early endosomes, then late endosome and finally to the lysosome. APP can also be transported directly from the cell surface to the lysosome. Compartments implicated in Aβ productions are marked with an asterisk (*), while those implicated in Aβ accumulation are coloured yellow.

It has been suggested that PSEN1 may be a unifying gene factor in AD as it may be the connection between the lysosomal system and APP. PSEN1 mutations are responsible for producing toxic Aβ species from APP and blocking autophagy (a form of a regulated cellular components destruction), impairing the cell's ability to clear toxic Aβ species or aggregates and other toxic features (e.g. abnormal Tau). Additionally, PSEN1

is necessary for the clearance of proteins from the endosomes [52] and trafficking through the endosomal/lysosomal system [53]. Therefore, PSEN1 mutations reveal impaired lysosomal function [54], which implies FAD (and maybe AD in general) could be considered a lysosomal storage disease [24].

One of the many (>80) lysosomal enzymes, an aspartyl protease (protein cleaning enzyme) called Cathepsin D (CatD) is known to be involved in tissue homeostasis including tissue renewal, remodeling, regulation of aging and programmed cell death under normal physiological conditions and base-line expression [55]. CatD has also been associated with the processing of the amyloid precursor protein [56], Tau protein [57] and apolipoprotein E [58] – all of which are considered important factors of AD pathology [59]. Other studies indicated an alternatively positive role for CatD in the degradation of toxic $A\beta_{42}$ and Tau aggregations [60]. Moreover, increased expression and activity of CatD within the brain is shown to precede known histopathological features of AD including neurodegeneration [41-43]. Additional connections between CatD activity and AD pathogenesis have been made. Specifically, it has been shown that the CatD gene and its genetic polymorphism are associated with a higher risk for developing sporadic AD [61, 62]. Cerebral Spinal Fluid (CSF) collected from AD patients indicates that increased levels of CatD are released into the extracellular space, which is an active ongoing process in the AD brain. Furthermore, a recent study demonstrated that neural-derived plasma exosomal (membrane vesicles originating from endosomes) levels of CatD were significantly higher [63]. Considering the progressive state of AD involves cell death, it is no surprise that CatD has also been implicated, speculatively, in neurodegenerative apoptotic pathways [64] potentially by increasing the activity of caspases, increasing Reactive Oxygen Species (ROS), and decreasing mitochondrial function [65-68], but may be a failed attempt of lysosomes to deal with increased levels of amyloid accumulation in vulnerable neurons [42].

The involvement of CatD in AD makes it a potentially useful biological marker of disease progression [44]. In fact, the targeting of CatD for AD imaging is unique, because it is a marker of biochemical function rather than just protein or peptide accumulation. It is hoped that targeting CatD may provide a means to diagnose AD earlier than current

clinical tools [69]. However, to first test the CatD targeting concept and the use of CatD to differentiate between AD and normal controls, experiments in non-human subjects must be used for initial validation. The goals of such studies include determining the best route of administration, and optimal concentration of the agent used to target CatD. These optimization studies are commonly performed in mice that mimic human pathologies most often by the use of genetic modification.

1.2.3 Pre-Clinical Models of Alzheimer's disease

Some species such as monkeys, dogs and cats [70-72] develop age related cognitive impairment and Aβ plaques. However animals (almost all including mice) do not naturally develop AD; in order to develop AD animal models, human genes for Familial AD (human APP and PS1 bearing FAD mutations, further discussed later) must be introduced. The easiest and most commonly used animal models for studying AD pathology are genetically engineered transgenic (Tg) mouse models, the more recently available Tg rat models [73], the sparingly used non-human primates [74] and some invertebrate models [75, 76]. Animal models have been created and studied extensively to help researchers understand the etiology and pathophysiology of human neurodegenerative diseases and to develop and test new diagnostic techniques. Animal models are an essential component in the generation of therapeutic assessments [77]. While invertebrate models such as Drosophila melanogaster [75] and Caenorhabditis elegans [76] might offer the advantage of cost, sample size and short life spans over mouse models, they are evolutionarily more distant from humans than rodent models and caution must be taken when drawing conclusions from these models. Mice are the most commonly used model for AD studies. This over-representation of animal studies in mice is largely due to the ease of genomic manipulation capability, benefits of cost (e.g. less expensive than rats), ease of handling and relatively short life-span allowing a thorough pathogenesis investigation over the life-time of the animal. However, due to very small brain size, mouse models pose additional technical challenges (e.g. resolution, signal-to-noise ratio, scan durations, partial volume effect) for any research using, testing or developing new imaging techniques.

1.2.3.1 Murine Models

Transgenic mouse AD models advanced from the contentious discovery of FAD mutations, allowing these models to be developed based on the amyloid hypothesis. AD mouse models have contributed widely to the understanding of the pathophysiology of the disease as well as the development and testing of new imaging modalities/ techniques [77]. The discovery of the FAD mutations in APP as was described above, provided the opportunity to investigate AD pathogenesis more rigorously via the generation of AD mouse models carrying these mutations. One of the first AD mouse models overexpressed the Indiana mutation and was shown to exhibit an 18-fold increase in APP levels leading to age-dependent increase in senile plaque deposition [78]. Since then, the Tg2576 mouse, which expresses the Swedish mutation, has become one of the most widely studied models and has shown plaque pathology development at 9-12 months of age [79]. Other FAD mutations (e.g PSEN1) have been generated in mice to drive early AD pathology with increased $A\beta_{42}$ levels [80] but also require a human APP transgene, usually with an FAD mutation to develop overt plaque deposition [81]. Previously, many of the available AD mouse models were hampered by the lack of NFTs and neuron loss. NFTs were recently achieved by either the incorporation of Frontotemporal lobe dementia Tau mutation into APP Tg mice, as in the 3XTg strain [82], or by the incorporation of wild-type human Tau gene into APP Tg mice [83]. The latter discovery further supported the hypothesis that Tau pathology develops downstream from Aβ. Neuronal cell death has been recently detected in more progressive Tg mouse models such as the 5XFAD where multiple mutations are expressed [84].

Currently there is no consensus on any particular gene(s) that can be used for creating an animal model representing the sporadic (most common) form of AD. An alternative has been suggested utilizing transduction of rat pup-brains with human genes that code for proteins that are downstream from another lysosomal enzyme activity, asparaginyl endopeptidase, leading to neurodegeneration as well as Tau and Aβ pathology. However, while animal models of sporadic AD do exist, they usually require extended periods of time to develop and pathological features of both sporadic and familial human AD are similar [85]. Thus, any Tg mouse model of AD is a compromise

and should be chosen to answer the specific question addressed by the study. In general, all AD Tg mouse models face some criticism due to the overexpression of one or more FAD mutations unlike humans and yet have provided invaluable insight into AD pathogenesis and therapeutic strategies. Although AD mice recapitulate few characteristics of the pathology (e.g. depending on the transgene incorporated, these mice may develop amyloid plaques or NFT), caveats must be considered when interpreting the data [84] especially considering only the 5XFAD mice present neuronal loss [86]. The following three AD mouse model strains were selected from Jackson Laboratories (Bar Harbor, ME, USA) for this work. Figure 1-3 summarizes the life-span reported pathological features of AD in these specific strains, which will be described in the next sections, based on several studies [40, 84, 87-94].

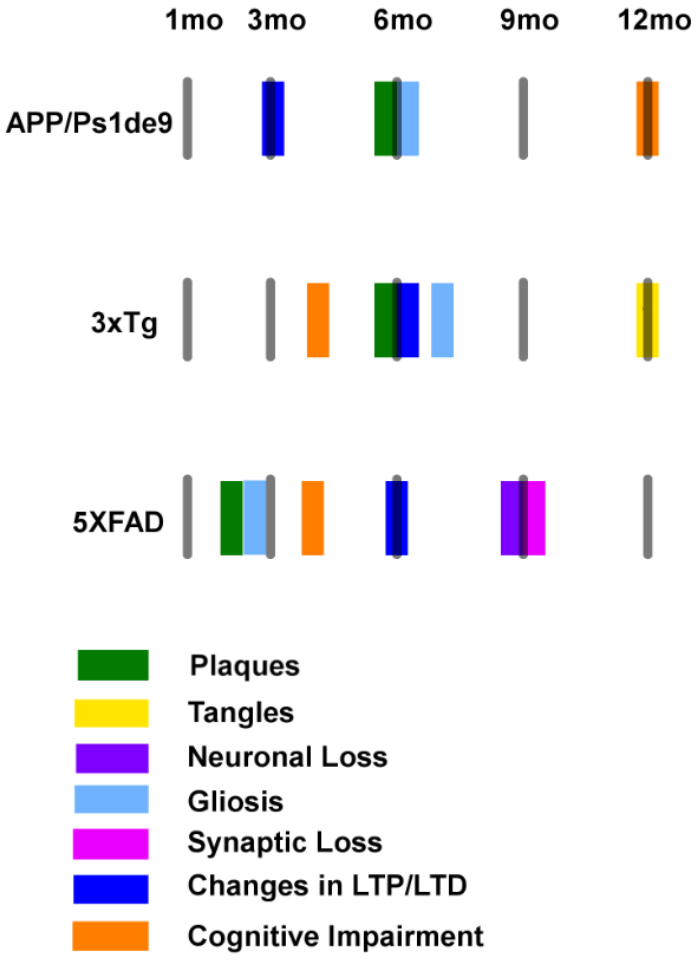

Figure 1-3. AD pathology progression with time in three Tg mice models. Colour markers are used to indicate the time of discovery and are not suggestive of quantitative measurement and pathological burden. Adapted from [86, 104, 105].

1.2.3.1.1 APP/Ps1dE9

The APPswe/PS1dE9 or B6C3-Tg(APPswe,PSEN1dE9) is a hemizygote double transgenic mouse strain (2X) on the parent background lines of B6C3F1/J and C57BL/6J strains. This model expresses a chimeric mouse/human amyloid precursor protein (Mo/HuAPP695swe) and a mutant human presenilin 1 (PS1-delta-exon 9) protein both controlled by independent mouse prion protein (PrP) promoter elements directed to neurons [95]. The overexpression of the transgene APP with the Swedish (K595N/M596L; also called K670N/M671L) mutation of APP, together with PS1 deleted in exon 9 leads to the overproduction of APP and PS1 splice variants. There is a concomitant increase in Aβ load with double the amount of toxic $A\beta_{42}$ deposited compared to the less toxic $A\beta_{40}$ [90]. Consequently, plaques are abundant in the hippocampus and cortex by 9 months of age with occasional deposits found in mice as young as 6 months of age [90, 93]. In addition, in the hippocampus, activated microglia and astrocytes, signs of inflammation/gliosis, surround the deposits [93]. Furthermore, at 13 months of age and above, Tg mice weigh less than controls, exhibit a reduced ability to maintain balance on a rotarod and commit more errors in the water maze than controls. At 7 months of age, both groups test similarly [93]. Even though these mice do not exhibit neuronal loss, they do display a variety of other clinically relevant AD-like symptoms; for example, mild neuritic abnormalities [96], transient long-term potentiation (LTP/LTD)[93] and increased mortality [97]. These mice present with cognitive decline that correlates with soluble Aβ, accumulation of senile plaques, and neuroinflammation (gliosis), offering a valuable tool in AD studies [98].

1.2.3.1.2 3xTg

The 3xTg or B6;129-Psen1^{tm1Mpm} Tg(APPSwe,tauP301L) is a triple transgenic homozygous mouse strain (3X) on the parental background lines of 129S1/Sv, 129X1/SvJ, and C57BL/6. This model was created in a unique way [99] where single-cell embryos from mice bearing the presenilin PS1M146V knock-in mutation on a mixed C7BL/6;129X1/SvJ;129S1/Sv genetic background (B6;129-Psen1tm1Mpm) were co-injected with two independent mutant human transgenes: human amyloid beta precursor

protein (Swedish mutation KM670/671NL) and microtubule-associated protein Tau (tauP30IL). Both transgenes are integrated at the same locus and are under the control of the mouse Thy1.2 regulatory element [95]. Consequently, Aβ oligomers extracellularly and intraneuronally, begin to accumulate before 6 months of age, and continue with age-dependent increases observed between 12 and 20 months [100]. In addition, Tau pathology including NFT is detected by 6 months of age with advanced NFT burden by 20 months [100]. At age 6.5 months 3xTg mice display learning and memory deficits in the Barnes maze; however, compared to the 2xTg, 3xTg perform better on the Rotarod and water maze tests [101, 102]. Similar to the 2xTg, even though these mice do not exhibit neuronal loss, they do display a variety of other clinically relevant AD-like symptoms such as $A\beta_{42}$ plaque and abnormal Tau accumulation. These mice have progressive accumulation of senile plaques, tangle pathology, and are associated with synaptic dysfunction leading to cognitive decline offering another valuable tool in AD studies.

1.2.3.1.3 5XFAD Tg6799

The 5XFAD or B6SJL-Tg(APPSwFlLon, PSEN1*M146L*L286V) 6799Vas/Mmjax is a double transgenic hemizygote mouse strain model of AD with five FAD mutations (5X) maintained on a c57Bl/6 x SJL parental background. This strain overexpresses mutant human APP(695) containing the Swedish (K670N, M671L), Florida (I716V) and London (V717I) Familial Alzheimer's Disease (FAD) mutations along with human PS1 gene harboring two FAD mutations M146L and L286V. Both transgenes are regulated by the mouse Thy1 promoter to drive overexpression in the brain. The model was generated by introducing APP (Swedish, Florida and London mutations), and PS1 (M146L and L286V mutations) into APP (695) and PS1 cDNA sequences followed by insertion into exon 2 of the mouse Thy-1 promoter gene which was finally injected into pronuclei of the single-cell embryos. The presence of the Swedish mutation results in higher levels of total Aβ, whereas Florida, London, M146L and L286V mutations increase the production of $A\beta_{42}$ specifically [84]. Consequentially, this abundance of FAD mutations is reflected by an early onset of plaque deposition, astrocytosis and microgliosis, age-dependent synaptic degeneration, working memory

impairments in Y-maze (~5 months) and neuronal loss at ~9 months [84]. In addition, certain presynaptic terminals and fine axonal processes undergo a process of swelling followed by dystrophy and are associated with the emergence and deposition of extracellular Aβ [103]. Similar to the 2xTg and the 3xTg, these mice preferentially produce toxic $A\beta_{42}$ and form plaques aggressively. Unlike the 3xTg (but similarly to the 2xTg) the 5XFAD model does not demonstrate Tau pathology. However, the 5XFAD mice do demonstrate neuronal cell death, which is unlike the 2xTg and 3xTg and many other AD mouse models. The 5XFAD mice therefore recapitulate many major features of Alzheimer's disease amyloid pathology and may be a useful model of intraneuronal Abeta-42 induced neurodegeneration, amyloid plaque formation, synaptic disruption and loss, and resultant cognitive impairments. This mouse model was selected despite having very aggressive genetically-driven brain changes that are accelerated compared to the typical human presentation. However, it is among the very few models that display neuronal loss with increased Cathepsin D activity, and can be rapidly examined for AD-like pathology.

1.2.4 Evaluation and Diagnosis of Alzheimer's disease

Alzheimer's disease is a clinical diagnosis. However, conclusive diagnosis of AD can only be achieved by the gold standard examination of postmortem tissue for the hallmark pathologies described above: amyloid plaques and NFTs [106]. However, as much as 20-40% of non-demented individuals have enough plaques and tangles to warrant a neuropathological AD diagnosis [107]. A non-invasive diagnosis of probable AD is possible by taking into consideration different individual/familial history and cognitive tests accompanied by limited imaging (see next section). Less than ~30% of patients with probable AD diagnosed have pure (not mixed) AD pathology [108]. However the aforementioned studies concentrated on patients with advanced age and disease and the findings of mix dementia could be incidental.

With the advent of biomarkers, a modification to the criteria and guidelines for standardized diagnosis of AD has recently been proposed. The modified guidelines bared two notable changes: 1. There should be a distinction between three stages of AD:

preclinical AD, MCI due to AD, and dementia due to AD. 2. There should be an incorporated biomarker test agreed upon that provides measurements of certain biological factors that can be used to indicate the presence of disease [5]. However, the most effective test or combination of tests may differ depending on the stage of the disease and the type of dementia [109].

1.2.4.1 Clinic

Currently, a diagnosis of AD in the clinic is made by an individual's primary care physician who obtains a medical, family and psychiatric history as well as a history of cognitive and behavioral changes [5]. While the patient's medical history obtained directly from the patient and corroborated by a seperate informant is a basic practice in the diagnosis, the neurological and physical examinations serve as important parts of the differential diagnosis of dementia detecting memory impairments in early stages of the disease [110]. One such test is the Mini Mental State Exam, or MMSE [111]. Blood tests are necessary to identify secondary causes of dementia and coexisting disorders [112] that are common in elderly people (e.g. thyroid-function and serum vitamin B12). Unfortunately, the diagnostic accuracy is still relatively low, with a sensitivity and specificity of around 80% and 70% respectively [112]. To improve the diagnostic accuracy, the physician may request the patient to undergo Magnetic Resonance Imaging (MRI) to test for any obvious brain changes (e.g. tumour or stroke) [5]. More recently, the application of other imaging tools targeting AD pathology have been FDA approved and are slowly becoming more common in the clinic to assist in the discrimination of different types of dementia [5]. These consist of different diagnostic techniques that are in use, including but not limited to Magnetic Resonance Imaging (MRI), positron emission tomography (PET) and Cerebral Spinal Fluid (CSF) biomarkers.

MRI has mainly been used to exclude alternative causes of dementia such as stroke, brain tumors, normal pressure hydrocephalus, and subdural hematoma [110]. However, additional research in the field holds promise to place MRI as a diagnostic tool for MCI/AD by measuring atrophy or other volumetric changes in the temporal lobe, entorhinal cortex, ventricles and hippocampus [113]. Blood flow and metabolism using

arterial spin-labeling perfusion magnetic resonance imaging [114] and functional magnetic resonance imaging [115] have also provided valuable information.

PET offers the highest sensitivity for the detection of targeted molecular imaging contrast agents (further details provide in Chapter 1.3). In addition to glucose utilization, PET studies have focused on the hallmark pathologies namely Aβ plaques and NFT as well as others such as the neurotransmitter systems and inflammatory cells involvement [116, 117]. FDG is a glucose analogue [117]. FDG PET detects the amount of ^{18}F FDG-6P accumulated in the brain cells where the amount of radioactivity is used to provide an estimate of the brain's glucose-consumption rate which indicates the level of synaptic activity [118]. Specific brain regions displaying reduced signal, interpreted as hypometabolism (reduced metabolism), identified by FDG in PET could be used to differentiate AD patients from cognitively normal elderly people with high sensitivity and with a good specificity to other dementias [119]. Aβ Plaques imaging was first made possible by the use of the ^{11}C-labelled Pittsburgh compound B (PiB) and three new Aβ plaque-targeting CA have recently been FDA approved with the purpose of confirming Aβ pathology. Caution must be taken using brain amyloid (and associated imaging thereof) as a biomarker of AD because of the large number of clinically normal healthy older adults presenting Aβ positive imaging test results. This argument applies equally to CAs that targets the NFT (discussed next) as NFT are predominantly believed to be downstream from amyloid pathology, and in fact, CAs can have reduced specificity to AD due to non-AD tauopathies such as frontotemporal lobe dementia.

Only very recently, there have been several tauopathy-targeting CAs developed. Some promising results have already been reported [120]. However, some challenges to tauopathy imaging include the much lower levels of Tau aggregates in the brain, relative to β-amyloid and the multiple structural conformations and differential distribution within neuronal subpopulations [120]. Because increasing Tau deposition with age is a normal part of aging, this increase must be addressed and standardized to provide a reliable threshold value of the normal deposition in order to avoid false positive detection [120]. Finally, while Tau pathology burden correlates very well with synaptic disruption

and cognitive decline, it may still not be an early diagnostic tool as Tau is downstream from Aβ synthesis.

1.2.4.1.1.1 Other Imaging Targets

Other important targeting features of AD include the main neurotransmitter systems and neuroinflammation. Both fields have gained smaller popularity, in part, because of limited findings. The cholinergic, dopaminergic and serotonergic systems are all impaired in AD [117]. PET imaging showed in-vivo clinical imaging of the neurotransmitter system altered function can be detected in AD by targeting features of the cholinergic system [121, 122], dopaminergic system [123, 124] and serotonergic system [125]. In addition, inflammatory features of AD have been argued to be both part cause and part an effect of AD pathology [116]. Thus, targeting activated inflammatory cells may help shed light on the disease progression (e.g. response to therapy). While preliminary work was able to detect differences between severe AD and normal controls by detecting different levels of inflammatory cells [126], other research has found no significant differences in mild AD and MCI or normal controls [127].

1.2.4.1.2 Cerebral Spinal Fluid Biomarkers

Cerebral spinal fluid (CSF) biomarkers such as reduced $A\beta_{42}$, increased total Tau (T-Tau) and phosphorylated tau (P-Tau) have been investigated as diagnostic biomarkers for AD [128]. Generally, CSF T-Tau has been shown to increase to approximately 300% and CSF-$A\beta_{42}$ reduced to 50% of the control concentration in AD. These changes lead to an increase in specificity to above 80% for differentiating AD from other dementias [112].

1.2.4.2 Pre-clinical Studies of AD

There are countless studies published on AD as a result of the many AD animal models (mostly mice) [129]. There are many benefits to the use of pre-clinical AD models. Broadly, the animals provide a uniform system that develops disease rapidly and reliably in a well characterized time frame. In addition, mice present a model that allows

the use of more invasive or dangerous procedures. Additionally, AD animal models can help in the discovery of new biomarkers that can be translated to human patients in the clinic. Crucial information can be gathered, in parallel, using longitudinal in vivo neuroimaging of hypothetical and established biomarkers to better understand the disease progression allowing multiple tests elucidating the connection between imaging, pathophysiology, cognitive capacity and behavior. Finally, the preclinical biomarkers can be used to test the safety, performance, pharmacokinetics and pharmacodynamics of new drugs as well as studying the disease progression following drug administration.

1.2.5 Treatment of Alzheimer's disease

Treatment regiments can be divided into pharmacologic and nonpharmacologic. The former are treatments in which the drugs are designed to slow or stop the disease or alleviate its symptoms. None of the treatments available today for AD slow or stop the malfunction and death of neurons in the brain that cause AD symptoms [5]. There have been at least five FDA approved drugs that temporarily improve symptoms of AD by increasing the amount of chemicals called neurotransmitters in the brain. Studies consistently indicate that active management of AD can improve the quality of life [130]. The management includes the application of drugs, coordination of care, participation in activities and/or adults day care programs, being in support groups and utilizing support services. Nonpharmacologic therapies include physical therapy, cognitive training and/or stimulation as well as training in daily activities. These may alter the rate of disease progression. The most successful nonpharmacologic interventions were found to be multicomponent; tailored to the needs of each patient [131]. There are many drugs in clinical trials, and a plethora in pre-clinical development, all of which are aimed at treating the symptoms, the underlying disease, or both. None of the drugs developed to date have been successful at curing or stopping the disease progression, reverse clinical signs, or consistently improve quality of life long-term.

1.2.6 Importance of Early Detection of Alzheimer's Disease

Clinical trials of treatments have been disappointing with cholinergic function targeting drugs being the most consistent at alleviating symptoms temporarily, however, showing only modest clinical effect in late-phase trials [132]. It is possible that the lack of success is due to the progressive state of the disease by the time diagnosis is made, and therefore, the time delay from onset of disease to attempted therapy trials. In a study of anti-inflammatory drugs (NSAIDs) it was noted that drugs might be protective only if given during mid-life but will not reverse the degenerative process in patients with established pathology and therefore an on-going clinical trial of NSAIDs has been started to test whether they can be protective in patients with MCI [133]. Furthermore, in a failed study of Aβ immunotherapy it was estimated that antibodies targeting Aβ in the brain may provide the greatest efficacy when given before the development of clinical AD symptoms, i.e. during a period before substantial cognitive loss [134]. It is therefore imperative that an earlier method of detecting the disease in patients is found. Such a method would allow researchers to have access to a whole new cohort of patients that could be better suited to evaluate new and previously tested potential treatments. Drugs that had no beneficial effect in AD patients at late-stage could be re-tested in those with early-stage disease, only if there was a reliable diagnostic test to detect patients at the early stages of the disease.

1.3 Molecular Imaging

The in-vivo characterization and measurement of biologic processes at the cellular and molecular levels has been defined as the quintessential molecular imaging purpose [135]. Despite being a relatively new multidisciplinary field, being utilized more increasingly in the past 15-20 years, it aims to provide unequivocal pertinent disease-related information [136] that can be used for the diagnosis or to direct the treatment of underlying pathologies. To do this successfully four key features are required [135, 136]: 1. Identifying a disease-specific molecular target. 2. Identifying an affinity ligand (e.g a peptide, antibody) for the molecular target. 3. Choosing an appropriate imaging modality that provides adequate spatial resolution, sensitivity, and depth penetration. 4.

Successfully synthesizing a non-toxic, stable CA that can detect the molecular target using the chosen modality.

Molecular imaging utilizes an arsenal of innovative methods that span the fields of engineering, physics, chemistry, biochemistry, molecular biology and others. These methods have allowed non-invasive pre-clinical and clinical investigations of a variety of pathologies [135-137]. A general approach (adapted from James ML et al. [138]) for a successful molecular imaging investigation targeting any pathology is described next. The first step (Step **1**) requires the identification of the pathology of interest and the associated biochemical processes involved. Next, a potential molecular target implicated in the latter is chosen and a targeting moiety could either be investigated or decided upon from literature (**2**). An imaging modality is then carefully selected (**3**). More than one modality can be utilized with the benefit of having multiple methods of visualization and localization of the targeting agent without the need of modification. Thus, an agent could be designed to have both optical, and MRI properties. Now, the synthesis of the probe may begin (**4**). Next, a series of in-vitro tests should be utilized to check for the probe specificity to its target, stability and safety when cultured with cells (**5**). At this point, any optimization necessary could be performed going back a step and repeating the process until successful preliminary data are obtained. Often, in-vitro results are not sufficient as these may not recapitulate in-vivo conditions and molecular outcomes (e.g. [139]). Sometimes, ex-vivo studies (**6**) will follow for assays that are too invasive (e.g. histology) or not practical for in-vivo studies (e.g. extremely long scans providing high imaging resolution [140]) but are necessary as a proof of principle prior to in-vivo attempts (e.g. due to associated costs). If the results are promising, addressing the in-vivo performance of the agent becomes of prime concern, and it is generally tested in small animals (e.g. mice) to test again for safety, and specificity to the target (**7**). Important information regarding the probe elimination and metabolism could be sought during these pre-clinical studies to better predict the pharmacokinetics and pharmacodynamics of the probes in humans. Finally, after successful pre-clinical performance the probe could be considered to move forward for clinical trials (**8**).

There are several imaging modalities that are commonly used for molecular imaging. Each has strengths and weaknesses (illustrated in Figure 1-4; strength in black, weakness in white) with respect to their utilization for imaging anatomical, physiological, or molecular processes details [137]. CT, US and MRI are commonly utilized for anatomic imaging purposes, even though all have the capacity to be used to varying degrees, for physiologic assessments. MRI has a stronger capability for molecular imaging assessments compared to CT and US. Where PET and optical imaging provide relatively less anatomic information, they can provide very sensitive molecular and, to a lesser degree, physiologic imaging information.

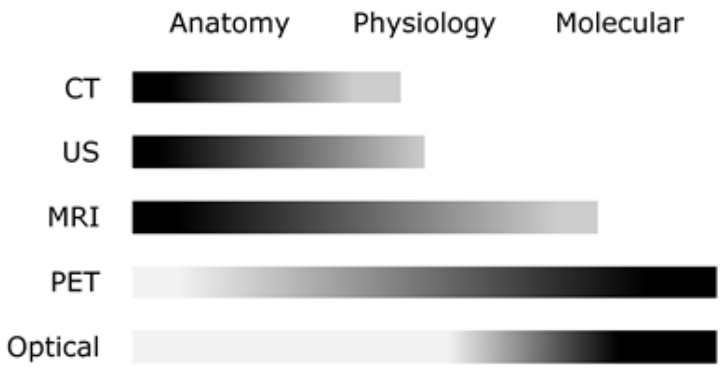

Figure 1-4. Different imaging modalities comparison. Adapted from Hoffman et al. [137]. Strength of a modality is congruent with darker loci.

1.3.1 Blood Brain Barrier Delivery

The brain is a very delicate organ and therefore its estimated surface area of 12 m^2 of capillaries is safely guarded from many toxic substances by the blood brain barrier (BBB). The impermeability of the BBB is due to the tight junctions connecting adjacent endothelial cells composing the vasculature system and highly regulated transport systems which only permit transport of select molecules [141]. The BBB is practically inaccessible for lipid-insoluble compounds such as polar molecules and small ions. However, small hydrophilic molecules essential for the survival of brain cells, such as amino acids, glucose, and other molecules employ specialized transporters to allow their

transport across the BBB. Larger essential molecules such as hormones, transferrin for iron, insulin, and lipoproteins utilize specific receptors to transport across the BBB. In contrast, small lipophilic molecules can diffuse passively across the BBB into the brain, but they are exposed to efflux pumps.

Different strategies to deliver therapeutics and imaging agents have been described previously [142]. Drug delivery approaches to the brain must be safe as well as effective and many are being intensively explored for either diagnostic or therapeutic purposes [141]. For example, in a novel approach using the ligand angiopep-2, it was demonstrated high BBB crossing capability and parenchymal accumulation may be mediated by the low-density lipoprotein receptor-related protein-1 [143]. On the other hand, lipid nanoparticles (NPs), having potentially lower cytotoxicity and higher drug loading capacity [144], and have been employed for targeting brain tumors [145]. In another example, recent advances in bispecific-antibody design (two different antibodies for two different targets conjugated together) show promising results. For example, targeting transferrin first to cross the BBB was used to deliver a β-secretase antibody into the brain to shift processing of APP in a Tg AD mouse model away from toxic Aβ [146].

Delivering diagnostic, therapeutic, or theranostic compounds across the BBB remains the rate-limiting step in brain-targeted diagnostic/therapeutic compound development. Several tools have been developed to permeate the BBB where the two most common approaches are described next. Mannitol (a type of sugar) is responsible for producing a transient hyperosmotic disruption of the BBB to facilitate its increased permeability. However, mannitol may preferentially permeate healthy BBB, thereby potentially increasing neurotoxicity and introducing bias in drug or diagnostic CA delivery [147]. Focused ultrasound (an oscillating sound pressure wave) for the transport of drugs across the BBB, is achieved by disruption of cell membranes. This procedure is considered safe for human use though some evidence does also suggest that damage may occur but is limited to minor hemorrhage [148] as well as notable but limited neuronal apoptosis [149]. In contrast, another approach supports a process that conjugates the cargo of interest (drug or diagnostic property) to a chaperon/ligand in order to deliver the

cargo across the BBB to its target. The following sections describe a special family of BBB penetrating molecules to allow drug/CA delivery across the BBB.

1.3.1.1 Cell Penetrating Peptides

Cell Penetrating Peptides (CPP) may be able to successfully deliver a large cargo (drug or imaging probe) across the intact BBB and into cells [150-152]. CPPs are classified into three classes: protein derived CPPs (e.g. Penetratin, Tat), model peptides (e.g. MAP) and designed CPPs (e.g. Transportan). Very generally, CPPs are short peptides of less than 30 amino acids that are able to translocate different cargos across the BBB by mechanisms that require no energy and may or may not be receptor mediated [153]. The mechanisms of internalization of CPPs have not yet been resolved. The only two features in common for all CPPs are positive charge at physiological pH, and amphipathicity (having both polar and non-polar portions; with polyarginines as exceptions to this rule) [153]. While the role of endocytosis isn't negligible for some CPP and may in fact be their exclusive form of internalization [154], efficient translocation was observed at low temperatures (0-4°C) with many different inhibitors of endocytosis [155].

The rate of internalization of CPP is a relatively fast process (at 37°C). The maximal concentration of internalized peptide is achieved after less than 1 hour of incubation with cells. Small cargos do not affect the rate of internalization, while larger hydrophilic cargoes such as proteins get internalized more slowly [153]. Following internalization into cells, some CPP may undergo degradation. This was demonstrated, for example, for Transportan in vitro [156] where it is likely the disulphide bridge that is used to couple the CPP to cargo which dissociates quickly in the cell [153]. With respect to toxicity, most CPP are not considered very toxic [153]. However, MAP has been associated with adopting an α-helical structure causing pore formation in the cell membrane [157] exerting toxic effects at concentrations over 1 μM in vitro [158]. In contrast, Transportan showed less toxicity starting at 5 μM, Penetratin showed even lower toxicity and Tat appeared to cause practically no harm to the cell membranes [153].

The Tat peptide (YGRKKRRQRRR) of the HIV-1 virus, which allows transport both into and out of the brain [150], is of particular interest. It is believed that hydrophilic arginine-rich CPPs such as HIV-1 Tat may be transported across membranes by direct penetration at high concentrations and by endocytosis at lower concentrations, with heparin sulfate as the binding site candidate [159-162]. In addition, Tat shows no toxicity at concentrations as high as 20 μM (highest tested) and produces no cell membrane leakage [163]. Furthermore, Tat displays a relatively long half-live in human serum (8.8 hours compared to 1.2 for Penetratin) considering the number of available enzymes in serum able to digest the peptides [164].

In vivo utilization of some of the CPPs mentioned has shown promise for transporting molecules to their targets within the CNS across the BBB, particularly Tat and Penetratin peptides. For example, Penetratin was successfully detected in rat brain and spinal cord cells after intravenous administration [165]; D-JNKI1 peptide (conjugated to HIV transporter sequence) was shown to be a potent neuroprotectant against both transient and permanent ischemia [166]; PSD-95-TAT-NR2B9c (conjugated to Tat) attenuated brain injury in epilepsy as well as chronic pain inflammation [167]; TAT-NBD (conjugated to Tat) peptide prevented p53 upregulation and as a result reduced (>80%) brain damage in a model of neonatal cerebral hypoxia-ischemia [168]; and finally, TAT-Bcl-xL (conjugated to Tat) peptide protected neurons from death in a Parkinson's disease model [169]. All together, these provide some evidence that CPPs could be used in models of neurodegenerative diseases for diagnostics and therapeutics.

1.4 Fluorescence and Bright Field Imaging

One of the most informative and oldest medical diagnostic and basic research tools utilizes light. The term light usually refers to a "packet" of photons of a specific energy range. It's a portion of the electromagnetic wave spectrum that consists of wave lengths ranging from ~300 (ultraviolet) to about 800 (far red) nm with corresponding range of frequencies described by the following relationship:

$$\boldsymbol{c = \nu\lambda} \qquad \textbf{(1-1)}$$

Where c is the speed of light in vacuum, ν is the frequency of the wave (1/seconds) and λ (meters) is the wavelength. The energy (E) of each photon is given by (in Joules):

$$\boldsymbol{E = h\nu} \qquad \textbf{(1-2)}$$

Where h is known as Planck's constant (Joule seconds) and ν is the frequency (1/seconds). Considering the wave-particle duality, the relationship between the wavelength of a wave and its energy is often written as:

$$\boldsymbol{E\lambda = hc} \qquad \textbf{(1-3)}$$

Photons traveling into, within and out of tissue experience absorption (the process by which energy of light is transferred to a medium), attenuation (the progressive loss of intensity through a particular medium), scatter (the diversion of particles from their original trajectory) and transmission (the process by which particles pass through a medium without being scattered or absorbed).

Since the construction of the first microscope in 1674 by Anton van Leeuwenhoek the field of microscopy has expanded to include bright field, confocal, dark field and differential interference contrast [170]. Furthermore, the introduction of fluorescence microscopy has revolutionized the field of cellular biology by facilitating the visualization of cellular and molecular processes in living cells in real time [170, 171]. The process of fluorescence can be described as a three-stage process that occurs in certain molecules (generally polyaromatic hydrocarbons or heterocycles). The process is demonstrated in Figure 1-5 illustrating the simple electronic-state Jablonski diagram. First, (1; Fig. 1-5), a photon of energy $h\nu_{Ex}$ originating from an external source (e.g. laser, incandescent lamp) becomes absorbed by a molecule, altering the state of an electron which was originally in state (S_0) and now enters an excited electronic singlet state (S_1')[172, 173]. Next, (2; Fig. 1-5), while the excited electron state is short lived (1-10 nanoseconds), several interactions (e.g. low frequency vibrational relaxation or solvent reorganization) between the molecule and its environment can occur, leading to some energy loss which puts the electron in a lower energy singlet excited state (S_1).

Finally, (3; Fig. 1-5) a photon of energy $h\nu_{Em}$ is emitted when the excited electron returns to its ground state S_0. Due to the energy loss during the excited-state lifetime, the energy of the emitted photon is lower and therefore has a longer wavelength than the excitation photon. The energy (and wavelength) difference between the excited versus emitted photon is referred to as the stoke shift [173].

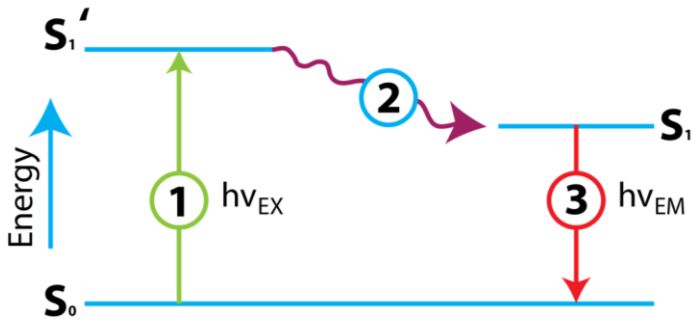

Figure 1-5. Jablonski diagram. Illustrating the processes involved in the creation of an excited electronic singlet state by optical absorption and subsequent emission of fluorescence. Adapted from [172]

For polyatomic molecules in solution, the discrete electronic transitions are replaced by broad energy spectra called the fluorescence excitation spectrum and fluorescence emission spectrum. For each fluorophore (a molecule producing fluorescence), the excitation spectrum is achieved by measuring the emission intensity at one wavelength while changing the excitation wavelength, while the emission spectrum is achieved by measuring the emission intensity at different wavelengths for a single excitation wavelength. The fluorescence emission spectrum is independent of the excitation wavelength due to the partial dissipation of excitation energy during the excited-state lifetime (Fig. 1-5 above) and the emission intensity is proportional to the amplitude of the fluorescence excitation spectrum at the excitation wavelength [173]. For example, if at excitation wavelength 'A', within the excitation spectrum, the intensity was double of that at another excitation wavelength 'B', the emission intensity following an excitation with wavelength 'A' would be double that of the resulting emission intensity following an excitation with wavelength 'B'.

A loss of fluorescence can occur due to the short-range interactions between the fluorophore and a specific local molecular environment. This loss of energy could also be the result of other fluorophores (self-quenching) [174] or the use of specific quenching molecules [175]. While the possibility of self-quenching or un-predicted environmental reduction in fluorescence presents some challenges to the design of CAs in general; it can be utilized beneficially for the functionalization of a CA for the purpose of making them "activatable" following separation of the quencher and fluorophore by a cellular process (e.g. enzymatic activity) of interest [176]. Furthermore, absorption of light by hemoglobin and other molecules (such as water) may reduce fluorescent signals by a factor of ~10 per centimeter of tissue [138]. This absorption of light by hemoglobin is in part why organs such as the liver and spleen with high vascular content and more importantly blood pooling capacity have the lowest transmission. Skin and muscle on the other hand, have a higher transmission of light.

Background fluorescence may originate from endogenous sample constituents (referred to as autofluorescence) or from unbound or nonspecifically bound probes. When utilizing fluorophores *in vivo*, replacing animals' food temporarily with an alfalfa-free diet reduces the amount of tissue autofluorescence substantially especially, from the gastro-intestinal region [177]. By selecting probes that absorb and emit photons at longer wavelengths (>500 nm), specifically in the near infrared (NIR), not only is there less light scattering by dense media such as tissue but the absorbance by hemoglobin and water is lowest [177]. Altogether choosing to image in the NIR results in greater penetration of the excitation light and better signal detection [178].

A number of macroscopic optical imaging modalities have emerged, enabling noninvasive, repetitive, whole body imaging of living small animals. Two examples of such macroscopic optical techniques are fluorescence optical imaging and bioluminescence imaging [138]. The former is discussed next in further detail.

1.4.1 In-vivo Fluorescence Optical Imaging

In order to detect the location of fluorophores (attached to cargo or targeted against molecules of interest), there are a few essential elements that are required and

should be optimized separately and in combination: an excitation light source; a fluorophore; wavelength filters to isolate emission photons from excitation photons; and, finally a detector (e.g. a charge-coupled device camera) that registers emission photons and produces a recordable output. This infrastructure for optical fluorescence is relatively inexpensive and easy to setup resulting in imaging sensitivities as low as picomolar to femtomolar concentrations. Because optical imaging involves the detection of low-energy photons, unlike higher-energy radiation (e.g. PET), it is considered very safe. However, lower energy also means that the depth of penetration is limited to only a few centimeters of tissue with NIR [178] which cannot be overcome by using higher intensity as this energy deposition would result in overheating the tissue/sample [179]. Considering the size of small animals used for research (e.g. rats, mice) optical imaging employing fluorophores in the NIR range enables visualization of internal organs making the modality very practical and more affordable compared to other imaging such as MRI, CT, PET. Generally, for in-vivo optical imaging, the following steps are required and parallel the list described previously for molecular imaging (See section 1.3) [138]. First, the selection of a fluorescent entity with suitable optical and chemical properties is required (e.g. emission and excitation spectra, toxicity). Next the conjugation of the chosen fluorescence entity to a targeting moiety (peptide/aptamer/antibody/nanoparticle) is performed. The targeting moiety is a priori chosen or designed to specifically target the protein or molecular pathway of interest. Finally, the selection of an appropriate animal model is required to test the CA, using an appropriate optical imaging device.

In conventional optical imaging the whole animal is illuminated with a broad beam of light tuned to the excitation wavelength of the fluorophore. Emitted fluorescent light is detected by a highly sensitive and low noise charged-coupled device (CCD) using an appropriate emission filter. Despite its popularity, this approach has inherent limitations with respect to the fluorescent probe localization, quantification and depth of detection. One main limitation is the inability to decouple the separate effects that fluorophore depth and concentration have on the detected signal [180]. The newer generations of optical imaging devices have multiple designs. Detailed description of their differences and relative performance is described elsewhere [180-183]. Three main classes of tomographic-capable optical imaging devices can be either continuous wave

(CW), time domain (TD) or frequency domain (FD) but are not discussed further, as they are not utilized for the purpose of the remaining integral chapters [184].

1.4.1.1 GE/ART eXplore Optix Pre-clinical Scanner

The following information was made available from the supplier [185]. However, the GE/ART eXplore Optix made by Advanced Research Technologies Inc. and distributed by GE is no longer available. The eXplore Optix device was designed to measure, quantify and visualize fluorescence intensity and lifetime for multiple molecular imaging applications in small laboratory animals. Research using this system is varied, from imaging brain amyloid accumulation in mice [186], liver repopulation following hepatocyte transplantation [187] and pharmacokinetics in a human monoclonal single chain fragment antibody for cancer targeting [188]. To scan animals, the illumination source and detector point(s) of the acquisition system of the eXplore Optix device are scanned over the region of interest using galvanometer mirrors (see Figure. 1-6). The pulsed laser source wavelength can be customized to the desired fluorescence excitation wavelength, while the detector is sensitive to the spectral band of 450 - 900 nm. In addition to top and side digital cameras (to capture visible images of the animal) a profilometer camera is incorporated into the system to obtain the shape of the animal. Figure 1-6 is a schematic of the acquisition system. The eXplore Optix system comes with an illumination system consisting of an 80 MHZ pulsed laser diode and pulse width (FWHM) under 100 ps. The excitation wavelength ranges from 900 to 1600 nm with an illumination diameter of 1 mm on imaging plane. The detection system comes with a time correlated single photon counting system that includes a detector photomultiplier tube (PMT) providing a temporal resolution of 250 ps, a depth sensitivity of over 10 mm at 700 nm and detection wavelengths ranging from 450 to 900 nm. The detection spot is 1 mm in diameter anywhere within the scanning area of 20 x 8.5 cm. The spatial resolution ranges from 0.5 to 3 mm and is defined by the user. The animal plate is removable, adjustable (height) and can be heated to any temperature in the range of 26 to 42°C. Raster scanning with longitudinal linear translation of the animal plate is used to obtain spatial information.

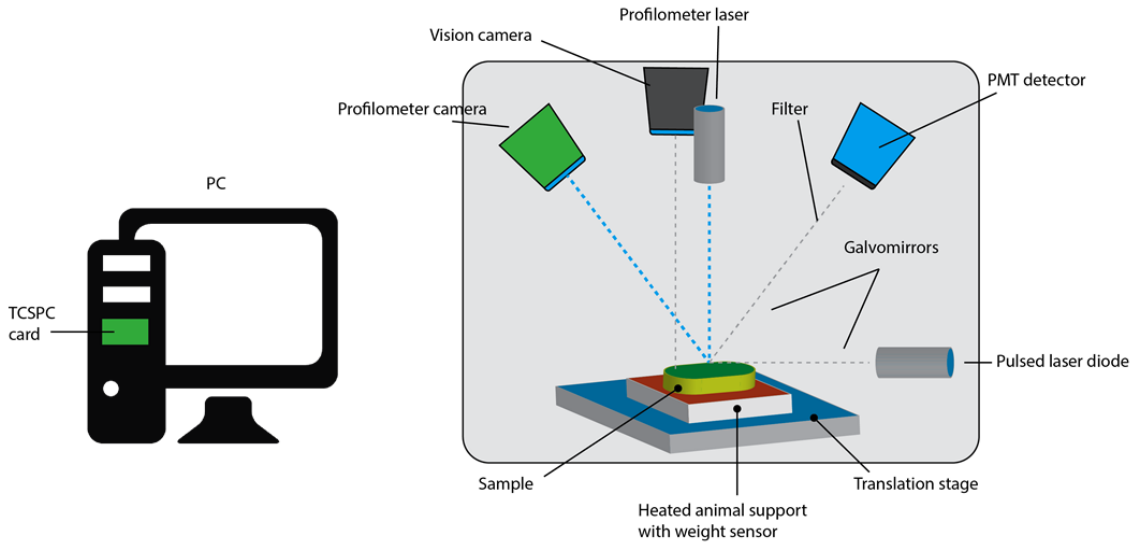

Figure 1-6. eXplore Optix system schematic. The animal is positioned on the animal table and a region of interest is selected using a top and side live camera. The animal is then translated into the imaging section of the system where the optics are housed. The entire system is light tight. TCSPC = time correlated single photon counting; PMT = photon multiplier tube

1.4.2 TissueScope

A fully-integrated high throughput system for brightfield, fluorescence and confocal imaging has been developed to allow large fields of view imaging at high resolution without the requirement for "tiling" of individual smaller field of view images. This system is called the TISSUEscope (*Huron Technologies Inc*. previously *Biomedical Photometrics*, Waterloo, ON) [189, 190]. Using the panoramic, patented, and widefield MACROscope technology, the TISSUEscope can produce high-resolution images of an entire tissue specimen in a single scan. This system will allow images of slide-based tissue specimens common to pathology, cytology, hematology and related laboratory medicine fields to be scanned in a timely manner. Specifications of the scanner are up to 40x magnification for the brightfield and confocal fluorescence imaging. Scanning can accomodate multiple slides or several sizes (maximum 6"x8") and provide an optical resolution of 0.60NA (0.25 μm/pixels at 40x).

1.5 Positron Emission Tomography

Tomography (Greek - *tomós* a slice, a section; *graphos* drawn) is a type of imaging that can acquire multiple two dimensional slices (images) of a three dimensional object. One of the main tomographic radionuclide-based molecular imaging techniques (see also 1.2) that enable evaluation of biochemical changes and levels of molecular targets within a living subject is positron emission tomography (PET). PET scanners detect γ rays (high energy packet of electromagnetic photons) indirectly resulting from the decay of specific radioisotopes. It is has a limitless depth of penetration which enables whole body imaging of molecular targets/processes with very high sensitivity [136]. This chapter briefly describes several aspects of PET image acquisition as may be required to understand the contents of this thesis. The explanations include aspects of physics, detection system, signal corrections as well as the algorithms used to reconstruct PET data.

1.5.1 Physics

Three main physical aspects are involved in PET imaging and will be explained in this section in more detail. One is the generation of short-lived radioisotopes used for PET imaging [191]. Second, the β^+ decay of the radioisotopes which indirectly results in the production of δ rays. Lastly, different interactions are possible by the emitted δ rays with matter that are then detected for the formation of a PET image. The reader is referred to a thorough and easy to follow review by Cherry et al. [192].

1.5.1.1 Radioisotopes for PET

The most common PET radioisotope tracers are produced in a cyclotron which necessitates clinics and research centers interested in using a PET scanner to be in close proximity to facilities able to transport the radioisotopes within a short period of time. The close proximity of a cyclotron to a clinic or research center allows synthesis and preparation to take place while retaining adequate activity for detection following administration to the patient/subject. In short, proton or deuteron beams irradiate targets filled with the raw material for radionuclide production (e.g. ^{18}O enriched water for the

production of ^{18}F) [193]. In cyclotrons, charged particles follow a spiral trajectory due to a constant perpendicular (to their movement) magnetic field as they are accelerated using an electric field (perpendicular to both their movement and magnetic field). Once the accelerated charged particles reach a selective exit "hole" they hit the designated target with a known energy and can produce a variety of predicted and desired unstable radioisotopes. In contrast, there are other radioisotopes like ^{82}Rb and ^{68}Ga which are obtained from long-life mother radioisotopes generators. These produce the desired isotopes as a result of their own slow decay process and in turn are separated from the mother nuclei by a chemical process.

Choosing the appropriate radionuclide depends on the experimental requirements (e.g. duration of scan), the isotope availability (e.g. cyclotron nearby) and its physical and chemical characteristics (e.g. radioactive half-life and metal/non-metal designation) [194]. Table 1.2 lists some frequently used positron emitting radioisotopes and their characteristics. It should be noted that an increase in positron energy, results in an increase in the positron range in water, and therefore a decrease in the optimum PET image resolution possible.

Table 1-2. Radioisotopes for PET imaging and characteristics.
Adapted from Cherry et al and Bailey et al. [192, 195]:

Radioisotopes	Half-life (min)	Source	Max. Range in water (mm)*	Max. Emission energy (MeV)
^{15}O	2.04	Cyclotron	7.3	1.738
^{11}C	20.4	Cyclotron	4.1	0.959
^{68}Ga	68.3	Generator	8.9	1.899
^{18}F	109.8	Cyclotron	2.4	0.633

* In reality, the range traveled by positrons is much shorter (explained below)

1.5.1.2 Beta decay

Nuclei that undergo either β^+ or β^- decay (weak interaction mediated) have an excess of protons or neutrons respectively making them unstable. This instability is

rectified by transforming a proton into a neutron (n), a positron (e^+; antimatter counterpart of electrons) also referred to as a beta particle – hence the name, and a neutrino (ν_e; electrically neutral, weakly interacting elementary subatomic particle) [196]:

$$\boldsymbol{P^+ \rightarrow n + e^+ + \nu_e} \qquad \textbf{(1-4)}$$

This process only occurs with protons in nuclei (not free) when it is energetically possible, resulting in a daughter nucleus having an atomic number decreased by one unit [196] (e.g ${}^{18}_{9}F$ transforms to ${}^{18}_{8}O$ with the latter being a stable isotope of oxygen). Other processes (e.g. β^- decay and electron capture) are mediated by the weak interaction force as well, but do not contribute to the PET signal, and therefore, no further explanation is provided.

The short-lived positron is ejected from the nucleus being repelled by the positive nuclei with varying degree of energy (having a continuous energy spectrum because the available energy in the decay is shared in a variable fashion between the β particle and the neutrino) [196]. Due to the inelastic interactions with electrons in surrounding tissue, the positron follow a tortuous path in tissue, rapidly losing kinetic energy causing it to slow down and collide with an electron; an event known as annihilation [192]. This process annihilates both the positron and electron (hence the name) but releases two photons. Each photon has an energy of 511 keV (due to the conservation laws of energy and momentum, the combined mass of the positron and electron is converted into two photons with equal energy) traveling at roughly opposite directions (~180° apart) to one another. Any residual kinetic energy prior to annihilation is converted to angular momentum, and therefore, the exact photons direction is not exactly 180°; a deviation from *colinearity*, which impacts resolution [197].

The distance from the emission point to the annihilation point is one of the main limiting factors to the spatial resolution of PET [192] and is known as the positron range (See figure 1-7).

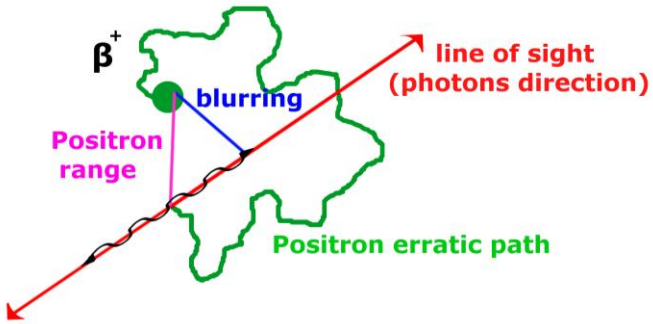

Figure 1-7. Positron annihilation schematic. From emission, the positron (β^+) travels an erratic path (green line) until it combines with an electron to form two high energy photons traveling in opposite directions (red lines). The blurring effect (blue line) is smaller than the positron range (pink line), which in turn is smaller than the complete positron path (green line) completed prior to annihilation.

The latter follows a non-Gaussian distribution as previously described [192, 198] because positrons are emitted with a range of energy and follow an indirect path. A higher energy positron will be more likely to exhibit a longer traveled distance to annihilation, and an environment having a higher electron density will result in a shorter range. The perpendicular distance between the site of positron emission and line of response (LOR) of annihilation products (photons directions) is the positron range blurring (directly affecting image resolution).

1.5.1.3 Gamma (γ) radiation interaction with matter

When the gamma rays (photons), produced in positron-electron annihilation, pass through matter (e.g. tissue, bone) with intensity I_0, some photons will be attenuated (removed out of the incident beam) by absorption after traveling distance x. The type of interaction between photons and matter depends on the atomic number Z and the energy E. However, only two types of interactions are relevant for PET imaging due to the energy produced (511 keV). Namely, the photoelectric absorption, and the Compton effects [192]. Collectively, the total absorption coefficient results from these two absorption coefficients, as well as pair production. However, the latter is not considered here due to negligible contribution to PET and the total absorption coefficient is calculated as:

$$\mu = \tau + \sigma \qquad \textbf{(1-5)}$$

Where the photoelectric absorption (τ), and the Compton effects (σ) are added linearly to give the total absorption coefficient (μ). And therefore the attenuated remaining intensity can be described by:

$$I = I_0 e^{-\mu x} \qquad \textbf{(1-6)}$$

Where the attenuated intensity of the beam (I) is calculated by an exponential decay process dependent on the incident intensity (I_0), the thickness (x) of medium propagated through. In short, during photoelectric absorption, the incident gamma ray is absorbed by an atom resulting in an ejection of an electron from the electron shell of this atom. The resulting hole in the electron shell is then filled by other remaining electrons or any free electrons from the surrounding medium. When a gamma ray interacts with a shell electron by the Compton scattering effect, it is deflected from its incident direction, loses energy according to the conservation of momentum, and may result in the release of a recoiling electron [196].

1.5.2 Localization of Positron Annihilation Event

PET detectors traditionally take the form of a closed circular ring or rings of detectors around a bore large enough for the subject (humans or animals) to be imaged comfortably as well as accommodate the depth of interaction effect (DOI). DOI is the term used to describe the degradation of resolution due to the thickness of detectors and radioactive sources off-center. DOI becomes smaller with a larger detector ring diameter. Each ring is designed to detect the gamma rays from annihilation events (using multiple scintillator detectors coupled to photomultiplier tubes). Using coincidence logic, the resulting electrical signals are converted into sinograms that can be used to reconstruct tomographic images [195]. The individual components and processes are explained in details by Cherry et al. [192].

1.5.2.1 Annihilation coincidence detection and event classification

Near-simultaneous detection of two annihilation photons by two separate detectors within a given time constraint allows PET to localize the origin of beta decay along an annihilation coincidence (ACD) detection line. The ability to define spatial location without the use of absorptive collimators has gained PET an indisputable advantage over single photon emission computed tomography (SPECT) by having much higher sensitivity. Coincidence logic is used to analyze the signal attained by the detectors and is accomplished by time stamping each event (gamma ray detection) registered by any detector. A coincidence event is assumed to have occurred when a pair of events is recorded within a specific coincidence timing window (normally 6-12 nsec in a clinical scanner) by two separate detectors. The use of the timing window permits other types of events (e.g. scattered, random and multiple coincidences) to be interpreted as taking place "in coincidence" - which negatively affects resolution and SNR. Three that are not discarded by the system are summarized in figure 1-8 [192].

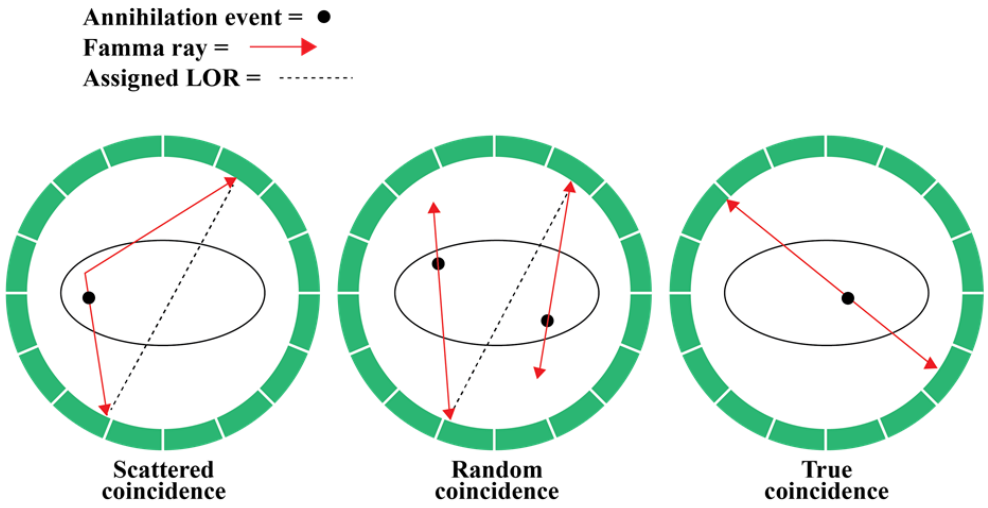

Figure 1-8. Types of coincidences in PET signal detection. True coincidence is when two gamma rays originating from the same e+e− annihilation site are detected as coincidence. Scatter events are registered like a true event, only one or both gamma rays scatter within matter. Random event happens when two separate unrelated events occur close enough in time that they are detected as one single event. Only True coincidence will contribute positively to the SNR.

1.5.3 Corrections

For the PET system to provide users with quantitative and artifact-free images, a few corrections to the acquired data must be incorporated. These include, but are not limited to the time activity curves (TAC) exponential decay, attenuation of photons passing through matter [199], variations in detector-specific efficiency and performance with respect to other detectors in the scanner, the loss of detection of more than one event within the detection coincidence window (dead-time and pile-up effects).

1.6 Magnetic Resonance Imaging

This sophisticated imaging technique has evolved considerably since 1974 when it was published to the public and has become an invaluable clinical and research tool [200]. Unlike other anatomical tomographic imaging devices such as Computer Tomography (CT), positron emission tomography (PET) and Single-Photon Emission Computed Tomography (SPECT), the non-invasive MRI does not utilize ionizing radiation.

1.6.1 CEST, paraCEST and OPARACHEE Imaging

Chemical exchange saturation transfer (CEST) MRI is a relatively new imaging approach that allows the indirect measurement of exogenous or endogenous molecules that go through exchange of target protons with bulk water. As a result of this, the method has been used to provide special insight using MRI including pH, temperature, metabolite detection, imaging of mobile proteins/ peptides and more[201]. Briefly, exchangeable protons become saturated (M_z is destroyed) using radio frequency (RF) energy tuned to the frequency of the exchanging spins when bound to the solute (the minor component in a solution, e.g. urea in water). Next, due to the exchange of protons water (pool *a*) with solute protons (pool *b*), the water magnetization (and therefore the signal) becomes slightly diminished and protons that leave this pool of protons with specific magnetization exchange with solute protons with no magnetization while spin-lattice relaxation is at work returning z-magnetization of pool *a* to equilibrium according to the longitudinal relaxation time. This effect is amplified if the exchange rate is

sufficiently fast (to quickly allow the exchange of more saturated solute protons with those of bulk water) and the saturation time is sufficiently long (to adequately destroy M_z). However the exchange rate should also be sufficiently slow as to allow the two exchanging pools to obey the slow exchange condition. As a result, low concentration solutes can be visualized indirectly by the reduced water signal. This detection amplification means that CEST may be a suitable candidate for molecular and cellular imaging. It is possible to increase the chemical shift by incorporating paramagnetic species (PARACEST) into exogenous CEST agents allowing much higher exchange rates to be used while still adhering to the slow-intermediate MR exchange regime. Clinical application requires careful considerations for the possible toxicity of the agents, scan time limits, the need to scan whole organs and specific absorption rate (SAR). Using higher field strength increases spectral resolution and separation between bulk and solute water resonance frequencies, but the higher frequency RF excitation is also associated with higher power deposition [201]. An alternative approach to detect the effects of a PARACEST agent is based on RF manipulation of the free water peak [202]. This is referred to as On-Resonance Paramagnetic Chemical Exchange Effect (OPARACHEE) and its use in mice *in vivo* was first described by Vinogradov et al. [203] showing that the method is sensitive to as little as micromolar concentrations of the paraCEST agent. Most CEST/ParaCEST studies have employed either continuous or pulsed selective off-resonance saturation of the solute protons exchanging with water-protons [201]. For OPARACHEE contrast, the water signal is excited directly (hence the name "on resonance" [202]) by applying 360° rotations using a low power RF WALTZ [203] pulse train to compensated for B_1- inhomogeneity. Using this approach, protons that exchange between water and the paraCEST agent do not experience the full 360° refocusing pulse and therefore after several series of such pulses, water signal is reduced due to magnetization exchanging from bulk water to the CA [202]. OPARACHEE was shown to be able to provide an indirect measure of the exchanging protons having high sensitivity for the detection of paraCEST CA requiring relatively low RF power deposition. The exact chemical shift position of the exchanging proton does not need to be known a priori [204]. However, one clear disadvantage of OPARACHEE is that it cannot distinguish between different agents or chemically different protons, but it may be the most suitable

and sensitive approach for detecting single agents. Finally due to the lower SAR requirements of this technique clinical translation may be more likely. Preliminary work using a paraCEST CatD targeting CA was pursued to a limited extent. Exciting data was acquired, and received positive response in international conferences (e.g. ISMRI 2013; awarded the Magna Cum Laude Merit award). However more work outside the scope of my studies was required to validate the in-vivo utilization. The limited results are shown in Appendix 1.

1.7 Molecular Biology Assays

1.7.1 Western Blots

Western blotting (WB) is a well-accepted assay that identifies (using specific antibodies) proteins that have been separated from one another according to their size by gel electrophoresis. Briefly, the process begins with preparation of tissue lysates, making all proteins available for separation and detection. The preparation is accomplished by first the introduction of tissue to lysis buffer and protease inhibitors which allows all intracellular proteins to become available. The tissue is homogenized (crushed and mixed thoroughly), agitated (mixed for two hours at 4°C) and sonicated (further breaks up tissue and cellular membranes) prior to being spun down for 20 min at 12000 rpm at 4°C in a microcentrifuge and finally kept at -80°C until ready to use. Antibodies typically recognize a small portion (epitope) of the protein which may reside within the 3D conformation of the protein. In order to unfold the 3D conformation and enable access of the antibodies to these epitopes, it is necessary to denature (unfold) the proteins. Therefore, the second step which can be done briefly before running the assay, is denaturing of the proteins which is accomplished by 60°C heat bath for 20 minutes with a dye and β-mercaptoethanol (to reduce disulphide bridges in proteins). The separation process takes place within a gel by sodium dodecyl sulfate polyacrylamide gel electrophoresis (SDS-PAGE). When SDS is used with proteins, all of the proteins become negatively charged by their attachment to the SDS anions and sos SDS denatures proteins by “wrapping around” the polypeptide backbone as well as provide them all with a negative charge. An application of an electrical current induces the proteins in the gel to

move through it and become separated by their weight. So in effect, the gel acts as a filter, a molecular sieve of sort, and it holds the separated proteins in place once the current has stopped. The blot (hence the name) is a membrane, almost always of nitrocellulose or polyvinylidene fluoride (PVDF) to which the proteins have been transferred to from the original gel used for protein separation. The membrane is a replica of the gel's protein pattern and is subsequently (after being blocked with 5% milk to avoid non-specific antibody binding) stained with primary antibodies targeting different proteins of interest at a time. After washing off unbound primary antibodies with tris-glycine buffered tween-20 (TBST) secondary antibodies are incubated to target the primary set. The secondary antibodies are bound to a reagent that reacts with a chemical solution to provide a chemiluminescent signal that can be detected using a designated sensitive camera. The ability to extract and study individual proteins provides valuable information. For the purpose of this work, the primary use of WB was to explore the CatD expression with reference to that of α-tubulin (α-T) within the same sample. This relative expression (CatD to α-T ratio) is indicative of the amount of target protein available within the sample explored.

1.7.2 Histology and Immunohistochemistry

Histology is the study of tissue structure at the microscopic level, including the cellular and molecular components. It extends from the level of sub-cellular compartments to individual cells to collection of tissue systems, organs and organ systems. Immunohistochemistry (IHC) is the application of antibodies to target specific features (e.g. enzymes, receptors etc). These antibodies in turn are detected using secondary antibodies that can interact with chemical processing creating a stain. Alternatively some secondary antibodies may be "tagged" with fluorescent dye that can allow beautiful multiple channel (colours) producing complex microscopic views of a several features at the same time. The principle behind immunohistochemistry is very similar to that of the WB in the sense one is targeting a specific feature (e.g. pathogenic protein) by the use of an antibody (hence 'immuno') that has high specificity and affinity to this target of interest. Rather than using chemiluminescence like WB, IHC commonly utilizes a colorimetric detection using nickel 3,3'-diaminobenzidine (DAB). As well as

Hematoxylin and Eosin counter staining. This provides 3 main visible colours on a slide: 1. Brown stain for localization of the secondary, and therefore primary antibodies, which indicates the target. 2. Blue stain localizing the nuclei due to hematoxylin, and 3. Pink stain binds to many different intracellular and extracellular proteins due to Eosin. In order to separate the three colours for quantification of the amount of DAB staining (relating to the amount of target proteins) we used ImageJ (v. 1.46r, http://rsbweb.nih.gov/ij/). Color deconvolution plugin written by Dr. Gabriel Landini was used (available via the aforementioned website) and quantified using the ImageJ built-in threshold tool (triangle thresholding with seldom minor manual adjustments if deemed necessary by the primary observer JAS).

1.8 Thesis Overview

The following provides a brief description of each chapter to follow. Combined, the individual studies that are described next provide the proof of concept of an intelligent design of a functionalized molecular imaging contrast agent with multi-modality capabilities for the diagnosis Alzheimer's disease (AD).

Chapter 2 presents the work inspired by the findings nearly 25 years ago of the lysosomal system involvement in AD. Because our lab has developed a novel contrast agent (CA) that targets Cathepsin D (CatD), a lysosomal aspartyl protease, it was necessary to find an appropriate animal AD model that not only presents AD-like pathology but also displays over-expression or increased levels of our target CatD enzyme. Therefore Chapter 2 presents the in-depth longitudinal examination of three different transgenic (Tg) mice strains compared with wild type (WT) controls. We examined the well accepted AD-like pathology of amyloid plaques ($A\beta_{42}$) as well as CatD by means of Western blots (WB) and immunohistochemistry (IHC) analysis. In this study, we found that 5XFAD mice were the best AD model mouse strain for the purpose of testing out our CA. This work is in preparation for submission.

Next, in Chapter 3, we present the preliminary, first in-vivo application of our CA, following a modification to include a Near Infra-red (NIR) dye. The study reports the

preliminary testing of our CA using the eXplore Optix system (GE Healthcare, Milwaukee, Wisconsin) in the 5XFAD mice at 5 and 12 months of age showing remarkable difference between these mice and age-matched WT controls. Furthermore, we synthesized two separate control CAs; one that lacked the CPP, and another that lacked the CatD targeting moiety. There were no significant differences in washout dynamic between the Tg and WT mice when using the control agents, only when using the complete CatD targeted CA. This work was accepted for publication in the Journal of Alzheimer's Disease (JAD) in May 2015.

In Chapter 4 we present a more translatable preclinical examination of our CA performance by using a radioactive ^{68}Ga chelated version of the CatD targeted CA. The Inveon microPET scanner (Siemens Medical Solutions, Knoxville TN, USA) was used. We imaged the 5XFAD mice as well as non-Tg controls at 2, 6 and 9 months of age with the administration of the ^{68}Ga CatD targeted CA intravenously (dynamic list-mode scan). The relative standard uptake values (SUVr) were calculated by analyzing the signal from the forebrain (including the cortex), dividing it by the signal from the hindbrain (including the cerebellum). Remarkably, significant differences were found for the rate of change of SUVr in mice aged 2, 6 and 9 months. Additionally, averaging the signal over the course of the last 30 minutes of the scans provided significantly higher SUVr values in the 5XFAD mice compared with the age-matched non-transgenic littermates. This work is in preparation for submission.

In conclusion, together, the three chapters provide evidence that our novel CatD targeted CA has the capacity to differentiate between the 5XFAD mouse model and age-matched normal controls using both optical NIR imaging techniques and microPET imaging. Future directions will focus on moving this CA closer to clinical trials and are described in more detail in Chapter 5 of the thesis.

1.9 References

[1] J. Neugroschl and S. Wang, Alzheimer's disease: diagnosis and treatment across the spectrum of disease severity, *Mt Sinai J Med*, **78** (2011), 596-612.

[2] R.C. Petersen, R. Doody, A. Kurz, R.C. Mohs, J.C. Morris, P.V. Rabins, K. Ritchie, M. Rossor, L. Thal and B. Winblad, Current concepts in mild cognitive impairment, *Arch Neurol*, **58** (2001), 1985-1992.

[3] R.C. Petersen, R.O. Roberts, D.S. Knopman, Y.E. Geda, R.H. Cha, V.S. Pankratz, B.F. Boeve, E.G. Tangalos, R.J. Ivnik and W.A. Rocca, Prevalence of mild cognitive impairment is higher in men. The Mayo Clinic Study of Aging, *Neurology*, **75** (2010), 889-897.

[4] M. Ganguli, H.H. Dodge, C. Shen and S.T. DeKosky, Mild cognitive impairment, amnestic type: an epidemiologic study, *Neurology*, **63** (2004), 115-121.

[5] 2014 Alzheimer's disease facts and figures, *Alzheimers Dement*, **10** (2014), e47-92.

[6] J.A. Schneider, Z. Arvanitakis, W. Bang and D.A. Bennett, Mixed brain pathologies account for most dementia cases in community-dwelling older persons, *Neurology*, **69** (2007), 2197-2204.

[7] H. Hippius and G. Neundorfer, The discovery of Alzheimer's disease, *Dialogues Clin Neurosci*, **5** (2003), 101-108.

[8] C.P. Ferri, M. Prince, C. Brayne, H. Brodaty, L. Fratiglioni, M. Ganguli, K. Hall, K. Hasegawa, H. Hendrie, Y. Huang, A. Jorm, C. Mathers, P.R. Menezes, E. Rimmer and M. Scazufca, Global prevalence of dementia: a Delphi consensus study, *Lancet*, **366** (2005), 2112-2117.

[9] A.s.D. International, World Alzheimer Report 2012, 2012.

[10] World Alzheimer Report - ExecutiveSummary.

[11] J. Poirier, J. Davignon, D. Bouthillier, S. Kogan, P. Bertrand and S. Gauthier, Apolipoprotein E polymorphism and Alzheimer's disease, *Lancet*, **342** (1993), 697-699.

[12] E.H. Corder, A.M. Saunders, W.J. Strittmatter, D.E. Schmechel, P.C. Gaskell, G.W. Small, A.D. Roses, J.L. Haines and M.A. Pericak-Vance, Gene dose of apolipoprotein E type 4 allele and the risk of Alzheimer's disease in late onset families, *Science*, **261** (1993), 921-923.

[13] M.E. Blomqvist, C. Reynolds, H. Katzov, L. Feuk, N. Andreasen, N. Bogdanovic, K. Blennow, A.J. Brookes and J.A. Prince, Towards compendia of negative genetic association studies: an example for Alzheimer disease, *Hum Genet*, **119** (2006), 29-37.

[14] J. Raber, Y. Huang and J.W. Ashford, ApoE genotype accounts for the vast majority of AD risk and AD pathology, *Neurobiol Aging*, **25** (2004), 641-650.

[15] L.A. Farrer, L.A. Cupples, J.L. Haines, B. Hyman, W.A. Kukull, R. Mayeux, R.H. Myers, M.A. Pericak-Vance, N. Risch and C.M. van Duijn, Effects of age, sex, and ethnicity on the association between apolipoprotein E genotype and Alzheimer disease. A meta-analysis. APOE and Alzheimer Disease Meta Analysis Consortium, *JAMA*, **278** (1997), 1349-1356.

[16] M. Gatz, C.A. Reynolds, L. Fratiglioni, B. Johansson, J.A. Mortimer, S. Berg, A. Fiske and N.L. Pedersen, Role of genes and environments for explaining Alzheimer disease, *Arch Gen Psychiatry*, **63** (2006), 168-174.

[17] N.T. Lautenschlager, L.A. Cupples, V.S. Rao, S.A. Auerbach, R. Becker, J. Burke, H. Chui, R. Duara, E.J. Foley, S.L. Glatt, R.C. Green, R. Jones, H. Karlinsky, W.A. Kukull, A. Kurz, E.B. Larson, K. Martelli, A.D. Sadovnick, L. Volicer, S.C. Waring, J.H. Growdon and L.A. Farrer, Risk of dementia among relatives of Alzheimer's disease patients in the MIRAGE study: What is in store for the oldest old?, *Neurology*, **46** (1996), 641-650.

[18] M. Mullan, F. Crawford, K. Axelman, H. Houlden, L. Lilius, B. Winblad and L. Lannfelt, A pathogenic mutation for probable Alzheimer's disease in the APP gene at the N-terminus of beta-amyloid, *Nat Genet*, **1** (1992), 345-347.

[19] A. Goate, M.C. Chartier-Harlin, M. Mullan, J. Brown, F. Crawford, L. Fidani, L. Giuffra, A. Haynes, N. Irving, L. James and et al., Segregation of a missense mutation in the amyloid precursor protein gene with familial Alzheimer's disease, *Nature*, **349** (1991), 704-706.

[20] I.H. Cheng, J.J. Palop, L.A. Esposito, N. Bien-Ly, F. Yan and L. Mucke, Aggressive amyloidosis in mice expressing human amyloid peptides with the Arctic mutation, *Nat Med*, **10** (2004), 1190-1192.

[21] R. Mayeux, Epidemiology of neurodegeneration, *Annu Rev Neurosci*, **26** (2003), 81-104.

[22] C.R. Jack, Jr., V.J. Lowe, S.D. Weigand, H.J. Wiste, M.L. Senjem, D.S. Knopman, M.M. Shiung, J.L. Gunter, B.F. Boeve, B.J. Kemp, M. Weiner and R.C. Petersen, Serial PIB and MRI in normal, mild cognitive impairment and Alzheimer's disease: implications for sequence of pathological events in Alzheimer's disease, *Brain*, **132** (2009), 1355-1365.

[23] C.L. Masters, G. Simms, N.A. Weinman, G. Multhaup, B.L. McDonald and K. Beyreuther, Amyloid plaque core protein in Alzheimer disease and Down syndrome, *Proc Natl Acad Sci U S A*, **82** (1985), 4245-4249.

[24] J.H. Tam and S.H. Pasternak, Amyloid and Alzheimer's disease: inside and out, *Can J Neurol Sci*, **39** (2012), 286-298.

[25] I. Hussain, D. Powell, D.R. Howlett, D.G. Tew, T.D. Meek, C. Chapman, I.S. Gloger, K.E. Murphy, C.D. Southan, D.M. Ryan, T.S. Smith, D.L. Simmons, F.S. Walsh, C. Dingwall and G. Christie, Identification of a novel aspartic protease (Asp 2) as beta-secretase, *Mol Cell Neurosci*, **14** (1999), 419-427.

[26] T.M. Allinson, E.T. Parkin, A.J. Turner and N.M. Hooper, ADAMs family members as amyloid precursor protein alpha-secretases, *J Neurosci Res*, **74** (2003), 342-352.

[27] S. Sinha and I. Lieberburg, Cellular mechanisms of beta-amyloid production and secretion, *Proc Natl Acad Sci U S A*, **96** (1999), 11049-11053.

[28] T.T. Rohn, The triggering receptor expressed on myeloid cells 2: "TREM-ming" the inflammatory component associated with Alzheimer's disease, *Oxid Med Cell Longev*, **2013** (2013), 860959.

[29] S. Gandy, The role of cerebral amyloid beta accumulation in common forms of Alzheimer disease, *J Clin Invest*, **115** (2005), 1121-1129.

[30] J. Hardy and D.J. Selkoe, The amyloid hypothesis of Alzheimer's disease: progress and problems on the road to therapeutics, *Science*, **297** (2002), 353-356.

[31] L.F. Lue, Y.M. Kuo, A.E. Roher, L. Brachova, Y. Shen, L. Sue, T. Beach, J.H. Kurth, R.E. Rydel and J. Rogers, Soluble amyloid beta peptide concentration as a predictor of synaptic change in Alzheimer's disease, *Am J Pathol*, **155** (1999), 853-862.

[32] T. Gomez-Isla, R. Hollister, H. West, S. Mui, J.H. Growdon, R.C. Petersen, J.E. Parisi and B.T. Hyman, Neuronal loss correlates with but exceeds neurofibrillary tangles in Alzheimer's disease, *Ann Neurol*, **41** (1997), 17-24.

[33] I. Grundke-Iqbal, K. Iqbal, Y.C. Tung, M. Quinlan, H.M. Wisniewski and L.I. Binder, Abnormal phosphorylation of the microtubule-associated protein tau (tau) in Alzheimer cytoskeletal pathology, *Proc Natl Acad Sci U S A*, **83** (1986), 4913-4917.

[34] K. Iqbal, C. Alonso Adel, S. Chen, M.O. Chohan, E. El-Akkad, C.X. Gong, S. Khatoon, B. Li, F. Liu, A. Rahman, H. Tanimukai and I. Grundke-Iqbal, Tau pathology in Alzheimer disease and other tauopathies, *Biochim Biophys Acta*, **1739** (2005), 198-210.

[35] H. Braak and E. Braak, Neuropathological stageing of Alzheimer-related changes, *Acta Neuropathol*, **82** (1991), 239-259.

[36] C. Ballatore, V.M. Lee and J.Q. Trojanowski, Tau-mediated neurodegeneration in Alzheimer's disease and related disorders, *Nat Rev Neurosci*, **8** (2007), 663-672.

[37] J. van Swieten and M.G. Spillantini, Hereditary frontotemporal dementia caused by Tau gene mutations, *Brain Pathol*, **17** (2007), 63-73.

[38] C.A. Lemere, J.K. Blusztajn, H. Yamaguchi, T. Wisniewski, T.C. Saido and D.J. Selkoe, Sequence of deposition of heterogeneous amyloid beta-peptides and APO E in Down syndrome: implications for initial events in amyloid plaque formation, *Neurobiol Dis*, **3** (1996), 16-32.

[39] J. Lewis, D.W. Dickson, W.L. Lin, L. Chisholm, A. Corral, G. Jones, S.H. Yen, N. Sahara, L. Skipper, D. Yager, C. Eckman, J. Hardy, M. Hutton and E. McGowan, Enhanced neurofibrillary degeneration in transgenic mice expressing mutant tau and APP, *Science*, **293** (2001), 1487-1491.

[40] S. Oddo, L. Billings, J.P. Kesslak, D.H. Cribbs and F.M. LaFerla, Abeta immunotherapy leads to clearance of early, but not late, hyperphosphorylated tau aggregates via the proteasome, *Neuron*, **43** (2004), 321-332.

[41] R.A. Nixon, A.M. Cataldo and P.M. Mathews, The endosomal-lysosomal system of neurons in Alzheimer's disease pathogenesis: a review, *Neurochem Res*, **25** (2000), 1161-1172.

[42] A.M. Cataldo, P.A. Paskevich, E. Kominami and R.A. Nixon, Lysosomal hydrolases of different classes are abnormally distributed in brains of patients with Alzheimer disease, *Proc Natl Acad Sci U S A*, **88** (1991), 10998-11002.

[43] A.M. Cataldo, J.L. Barnett, S.A. Berman, J. Li, S. Quarless, S. Bursztajn, C. Lippa and R.A. Nixon, Gene expression and cellular content of cathepsin D in Alzheimer's disease brain: evidence for early up-regulation of the endosomal-lysosomal system, *Neuron*, **14** (1995), 671-680.

[44] A.L. Schwagerl, P.S. Mohan, A.M. Cataldo, J.P. Vonsattel, N.W. Kowall and R.A. Nixon, Elevated levels of the endosomal-lysosomal proteinase cathepsin D in cerebrospinal fluid in Alzheimer disease, *J Neurochem*, **64** (1995), 443-446.

[45] A. Amritraj, C. Hawkes, A.L. Phinney, H.T. Mount, C.D. Scott, D. Westaway and S. Kar, Altered levels and distribution of IGF-II/M6P receptor and lysosomal enzymes in mutant APP and APP + PS1 transgenic mouse brains, *Neurobiol Aging*, **30** (2009), 54-70.

[46] S.H. Pasternak, R.D. Bagshaw, M. Guiral, S. Zhang, C.A. Ackerley, B.J. Pak, J.W. Callahan and D.J. Mahuran, Presenilin-1, nicastrin, amyloid precursor protein, and gamma-secretase activity are co-localized in the lysosomal membrane, *J Biol Chem*, **278** (2003), 26687-26694.

[47] C. Haass, E.H. Koo, A. Mellon, A.Y. Hung and D.J. Selkoe, Targeting of cell-surface beta-amyloid precursor protein to lysosomes: alternative processing into amyloid-bearing fragments, *Nature*, **357** (1992), 500-503.

[48] T. Yamazaki, E.H. Koo and D.J. Selkoe, Trafficking of cell-surface amyloid beta-protein precursor. II. Endocytosis, recycling and lysosomal targeting detected by immunolocalization, *J Cell Sci*, **109 (Pt 5)** (1996), 999-1008.

[49] A. Lorenzen, J. Samosh, K. Vandewark, P.H. Anborgh, C. Seah, A.C. Magalhaes, S.P. Cregan, S.S. Ferguson and S.H. Pasternak, Rapid and direct transport of cell surface APP to the lysosome defines a novel selective pathway, *Mol Brain*, **3** (2010), 11.

[50] W.H. Yu, A.M. Cuervo, A. Kumar, C.M. Peterhoff, S.D. Schmidt, J.H. Lee, P.S. Mohan, M. Mercken, M.R. Farmery, L.O. Tjernberg, Y. Jiang, K. Duff, Y. Uchiyama, J. Naslund, P.M. Mathews, A.M. Cataldo and R.A. Nixon, Macroautophagy--a novel Beta-amyloid peptide-generating pathway activated in Alzheimer's disease, *J Cell Biol*, **171** (2005), 87-98.

[51] J.H. Tam, C. Seah and S.H. Pasternak, The Amyloid Precursor Protein is rapidly transported from the Golgi apparatus to the lysosome and where it is processed into beta-amyloid, *Mol Brain*, **7** (2014), 54.

[52] M. Zhang, A. Haapasalo, D.Y. Kim, L.A. Ingano, W.H. Pettingell and D.M. Kovacs, Presenilin/gamma-secretase activity regulates protein clearance from the endocytic recycling compartment, *FASEB J*, **20** (2006), 1176-1178.

[53] T. Hryciw, J.I. MacDonald, R. Phillips, C. Seah, S. Pasternak and S.O. Meakin, The fibroblast growth factor receptor substrate 3 adapter is a developmentally regulated microtubule-associated protein expressed in migrating and differentiated neurons, *J Neurochem*, **112** (2010), 924-939.

[54] J.H. Lee, W.H. Yu, A. Kumar, S. Lee, P.S. Mohan, C.M. Peterhoff, D.M. Wolfe, M. Martinez-Vicente, A.C. Massey, G. Sovak, Y. Uchiyama, D. Westaway, A.M. Cuervo and R.A. Nixon, Lysosomal proteolysis and autophagy require presenilin 1 and are disrupted by Alzheimer-related PS1 mutations, *Cell*, **141** (2010), 1146-1158.

[55] P. Benes, V. Vetvicka and M. Fusek, Cathepsin D--many functions of one aspartic protease, *Crit Rev Oncol Hematol*, **68** (2008), 12-28.

[56] U.S. Ladror, S.W. Snyder, G.T. Wang, T.F. Holzman and G.A. Krafft, Cleavage at the amino and carboxyl termini of Alzheimer's amyloid-beta by cathepsin D, *J Biol Chem*, **269** (1994), 18422-18428.

[57] A. Kenessey, P. Nacharaju, L.W. Ko and S.H. Yen, Degradation of tau by lysosomal enzyme cathepsin D: implication for Alzheimer neurofibrillary degeneration, *J Neurochem*, **69** (1997), 2026-2038.

[58] W. Zhou, S.A. Scott, S.B. Shelton and K.A. Crutcher, Cathepsin D-mediated proteolysis of apolipoprotein E: possible role in Alzheimer's disease, *Neuroscience*, **143** (2006), 689-701.

[59] D.J. Selkoe, Alzheimer's disease: genes, proteins, and therapy, *Physiol Rev*, **81** (2001), 741-766.

[60] M.A. Leissring, L. Reinstatler, T. Sahara, D. Sevlever, R. Roman, Z. Ji, L. Li, Q. Lu, P. Säftig, Y. Levites, T.E. Golde, J. Burgess, N. Ertekin-Taner and E.A. Eckman,

Cathepsin D knockout mice harbor large and highly selective increases in cerebral Aß42 and tau: Implications for Alzheimer's disease pathogenesis, *Alzheimer's & Dementia: The Journal of the Alzheimer's Association*, **5** (2009), 3.

[61] A. Papassotiropoulos, M. Bagli, O. Feder, F. Jessen, W. Maier, M.L. Rao, M. Ludwig, S.G. Schwab and R. Heun, Genetic polymorphism of cathepsin D is strongly associated with the risk for developing sporadic Alzheimer's disease, *Neurosci Lett*, **262** (1999), 171-174.

[62] M. Schuur, M.A. Ikram, J.C. van Swieten, A. Isaacs, J.M. Vergeer-Drop, A. Hofman, B.A. Oostra, M.M. Breteler and C.M. van Duijn, Cathepsin D gene and the risk of Alzheimer's disease: a population-based study and meta-analysis, *Neurobiol Aging*, **32** (2011), 1607-1614.

[63] E.J. Goetzl, A. Boxer, J.B. Schwartz, E.L. Abner, R.C. Petersen, B.L. Miller and D. Kapogiannis, Altered lysosomal proteins in neural-derived plasma exosomes in preclinical Alzheimer disease, *Neurology*, **85** (2015), 40-47.

[64] M.E. Guicciardi, M. Leist and G.J. Gores, Lysosomes in cell death, *Oncogene*, **23** (2004), 2881-2890.

[65] K. Vancompernolle, F. Van Herreweghe, G. Pynaert, M. Van de Craen, K. De Vos, N. Totty, A. Sterling, W. Fiers, P. Vandenabeele and J. Grooten, Atractyloside-induced release of cathepsin B, a protease with caspase-processing activity, *FEBS Lett*, **438** (1998), 150-158.

[66] M. Zhao, F. Antunes, J.W. Eaton and U.T. Brunk, Lysosomal enzymes promote mitochondrial oxidant production, cytochrome c release and apoptosis, *Eur J Biochem*, **270** (2003), 3778-3786.

[67] N. Bidere, H.K. Lorenzo, S. Carmona, M. Laforge, F. Harper, C. Dumont and A. Senik, Cathepsin D triggers Bax activation, resulting in selective apoptosis-inducing factor (AIF) relocation in T lymphocytes entering the early commitment phase to apoptosis, *J Biol Chem*, **278** (2003), 31401-31411.

[68] S. Conus, R. Perozzo, T. Reinheckel, C. Peters, L. Scapozza, S. Yousefi and H.U. Simon, Caspase-8 is activated by cathepsin D initiating neutrophil apoptosis during the resolution of inflammation, *J Exp Med*, **205** (2008), 685-698.

[69] V.J. De-Paula, M. Radanovic, B.S. Diniz and O.V. Forlenza, Alzheimer's disease, *Subcell Biochem*, **65** (2012), 329-352.

[70] B.J. Cummings, J.H. Su, C.W. Cotman, R. White and M.J. Russell, Beta-amyloid accumulation in aged canine brain: a model of early plaque formation in Alzheimer's disease, *Neurobiol Aging*, **14** (1993), 547-560.

[71] B.J. Cummings, T. Satou, E. Head, N.W. Milgram, G.M. Cole, M.J. Savage, M.B. Podlisny, D.J. Selkoe, R. Siman, B.D. Greenberg and C.W. Cotman, Diffuse plaques

contain C-terminal A beta 42 and not A beta 40: evidence from cats and dogs, *Neurobiol Aging*, **17** (1996), 653-659.

[72] D.L. Price, L.J. Martin, S.S. Sisodia, M.V. Wagster, E.H. Koo, L.C. Walker, V.E. Koliatsos and L.C. Cork, Aged non-human primates: an animal model of age-associated neurodegenerative disease, *Brain Pathol*, **1** (1991), 287-296.

[73] S. Do Carmo and A.C. Cuello, Modeling Alzheimer's disease in transgenic rats, *Mol Neurodegener*, **8** (2013), 37.

[74] K. Meguro, X. Blaizot, Y. Kondoh, C. Le Mestric, J.C. Baron and C. Chavoix, Neocortical and hippocampal glucose hypometabolism following neurotoxic lesions of the entorhinal and perirhinal cortices in the non-human primate as shown by PET. Implications for Alzheimer's disease, *Brain*, **122 (Pt 8)** (1999), 1519-1531.

[75] R. Costa, E. Speretta, D.C. Crowther and I. Cardoso, Testing the therapeutic potential of doxycycline in a Drosophila melanogaster model of Alzheimer disease, *J Biol Chem*, **286** (2011), 41647-41655.

[76] Y. Wu and Y. Luo, Transgenic C. elegans as a model in Alzheimer's research, *Curr Alzheimer Res*, **2** (2005), 37-45.

[77] E.M. Strome and D.J. Doudet, Animal models of neurodegenerative disease: insights from in vivo imaging studies, *Mol Imaging Biol*, **9** (2007), 186-195.

[78] D. Games, D. Adams, R. Alessandrini, R. Barbour, P. Berthelette, C. Blackwell, T. Carr, J. Clemens, T. Donaldson, F. Gillespie and et al., Alzheimer-type neuropathology in transgenic mice overexpressing V717F beta-amyloid precursor protein, *Nature*, **373** (1995), 523-527.

[79] K. Hsiao, P. Chapman, S. Nilsen, C. Eckman, Y. Harigaya, S. Younkin, F. Yang and G. Cole, Correlative memory deficits, Abeta elevation, and amyloid plaques in transgenic mice, *Science*, **274** (1996), 99-102.

[80] K. Duff, C. Eckman, C. Zehr, X. Yu, C.M. Prada, J. Perez-tur, M. Hutton, L. Buee, Y. Harigaya, D. Yager, D. Morgan, M.N. Gordon, L. Holcomb, L. Refolo, B. Zenk, J. Hardy and S. Younkin, Increased amyloid-beta42(43) in brains of mice expressing mutant presenilin 1, *Nature*, **383** (1996), 710-713.

[81] L. Holcomb, M.N. Gordon, E. McGowan, X. Yu, S. Benkovic, P. Jantzen, K. Wright, I. Saad, R. Mueller, D. Morgan, S. Sanders, C. Zehr, K. O'Campo, J. Hardy, C.M. Prada, C. Eckman, S. Younkin, K. Hsiao and K. Duff, Accelerated Alzheimer-type phenotype in transgenic mice carrying both mutant amyloid precursor protein and presenilin 1 transgenes, *Nat Med*, **4** (1998), 97-100.

[82] S. Oddo, A. Caccamo, M. Kitazawa, B.P. Tseng and F.M. LaFerla, Amyloid deposition precedes tangle formation in a triple transgenic model of Alzheimer's disease, *Neurobiol Aging*, **24** (2003), 1063-1070.

[83] T. Umeda, S. Maekawa, T. Kimura, A. Takashima, T. Tomiyama and H. Mori, Neurofibrillary tangle formation by introducing wild-type human tau into APP transgenic mice, *Acta Neuropathol*, **127** (2014), 685-698.

[84] H. Oakley, S.L. Cole, S. Logan, E. Maus, P. Shao, J. Craft, A. Guillozet-Bongaarts, M. Ohno, J. Disterhoft, L. Van Eldik, R. Berry and R. Vassar, Intraneuronal beta-amyloid aggregates, neurodegeneration, and neuron loss in transgenic mice with five familial Alzheimer's disease mutations: potential factors in amyloid plaque formation, *J Neurosci*, **26** (2006), 10129-10140.

[85] R.S. Turner, Alzheimer's disease, *Semin Neurol*, **26** (2006), 499-506.

[86] ALZFORUM 5XFAD, Vol. 2015.

[87] L.M. Billings, S. Oddo, K.N. Green, J.L. McGaugh and F.M. LaFerla, Intraneuronal Abeta causes the onset of early Alzheimer's disease-related cognitive deficits in transgenic mice, *Neuron*, **45** (2005), 675-688.

[88] D. Caruso, A.M. Barron, M.A. Brown, F. Abbiati, P. Carrero, C.J. Pike, L.M. Garcia-Segura and R.C. Melcangi, Age-related changes in neuroactive steroid levels in 3xTg-AD mice, *Neurobiol Aging*, **34** (2013), 1080-1089.

[89] R. Kimura and M. Ohno, Impairments in remote memory stabilization precede hippocampal synaptic and cognitive failures in 5XFAD Alzheimer mouse model, *Neurobiol Dis*, **33** (2009), 229-235.

[90] J.L. Jankowsky, D.J. Fadale, J. Anderson, G.M. Xu, V. Gonzales, N.A. Jenkins, N.G. Copeland, M.K. Lee, L.H. Younkin, S.L. Wagner, S.G. Younkin and D.R. Borchelt, Mutant presenilins specifically elevate the levels of the 42 residue beta-amyloid peptide in vivo: evidence for augmentation of a 42-specific gamma secretase, *Hum Mol Genet*, **13** (2004), 159-170.

[91] M. Garcia-Alloza, E.M. Robbins, S.X. Zhang-Nunes, S.M. Purcell, R.A. Betensky, S. Raju, C. Prada, S.M. Greenberg, B.J. Bacskai and M.P. Frosch, Characterization of amyloid deposition in the APPswe/PS1dE9 mouse model of Alzheimer disease, *Neurobiol Dis*, **24** (2006), 516-524.

[92] W. Kamphuis, C. Mamber, M. Moeton, L. Kooijman, J.A. Sluijs, A.H. Jansen, M. Verveer, L.R. de Groot, V.D. Smith, S. Rangarajan, J.J. Rodriguez, M. Orre and E.M. Hol, GFAP isoforms in adult mouse brain with a focus on neurogenic astrocytes and reactive astrogliosis in mouse models of Alzheimer disease, *PLoS One*, **7** (2012), e42823.

[93] A. Volianskis, R. Kostner, M. Molgaard, S. Hass and M.S. Jensen, Episodic memory deficits are not related to altered glutamatergic synaptic transmission and plasticity in the CA1 hippocampus of the APPswe/PS1deltaE9-deleted transgenic mice model of ss-amyloidosis, *Neurobiol Aging*, **31** (2010), 1173-1187.

[94] R. Lalonde, H.D. Kim, J.A. Maxwell and K. Fukuchi, Exploratory activity and spatial learning in 12-month-old APP(695)SWE/co+PS1/DeltaE9 mice with amyloid plaques, *Neurosci Lett*, **390** (2005), 87-92.

[95] B.H. Jackson Laboratories, ME, USA, Alzheimer's Disease Mouse Model Strains, Vol. 2015.

[96] M. Garcia-Alloza, L.A. Borrelli, B.T. Hyman and B.J. Bacskai, Antioxidants have a rapid and long-lasting effect on neuritic abnormalities in APP:PS1 mice, *Neurobiol Aging*, **31** (2010), 2058-2068.

[97] R. Minkeviciene, S. Rheims, M.B. Dobszay, M. Zilberter, J. Hartikainen, L. Fulop, B. Penke, Y. Zilberter, T. Harkany, A. Pitkanen and H. Tanila, Amyloid beta-induced neuronal hyperexcitability triggers progressive epilepsy, *J Neurosci*, **29** (2009), 3453-3462.

[98] W. Zhang, J. Hao, R. Liu, Z. Zhang, G. Lei, C. Su, J. Miao and Z. Li, Soluble Abeta levels correlate with cognitive deficits in the 12-month-old APPswe/PS1dE9 mouse model of Alzheimer's disease, *Behav Brain Res*, **222** (2011), 342-350.

[99] S. Oddo, A. Caccamo, J.D. Shepherd, M.P. Murphy, T.E. Golde, R. Kayed, R. Metherate, M.P. Mattson, Y. Akbari and F.M. LaFerla, Triple-transgenic model of Alzheimer's disease with plaques and tangles: intracellular Abeta and synaptic dysfunction, *Neuron*, **39** (2003), 409-421.

[100] S. Oddo, A. Caccamo, L. Tran, M.P. Lambert, C.G. Glabe, W.L. Klein and F.M. LaFerla, Temporal profile of amyloid-beta (Abeta) oligomerization in an in vivo model of Alzheimer disease. A link between Abeta and tau pathology, *J Biol Chem*, **281** (2006), 1599-1604.

[101] K.R. Stover, M.A. Campbell, C.M. Van Winssen and R.E. Brown, Early detection of cognitive deficits in the 3xTg-AD mouse model of Alzheimer's disease, *Behav Brain Res*, **289** (2015), 29-38.

[102] K.R. Stover, M.A. Campbell, C.M. Van Winssen and R.E. Brown, Analysis of motor function in 6-month-old male and female 3xTg-AD mice, *Behav Brain Res*, **281** (2015), 16-23.

[103] X.M. Zhang, Y. Cai, K. Xiong, H. Cai, X.G. Luo, J.C. Feng, R.W. Clough, R.G. Struble, P.R. Patrylo and X.X. Yan, Beta-secretase-1 elevation in transgenic mouse models of Alzheimer's disease is associated with synaptic/axonal pathology and amyloidogenesis: implications for neuritic plaque development, *Eur J Neurosci*, **30** (2009), 2271-2283.

[104] ALZFORUM 2xTg, Vol. 2015.

[105] ALZFORUM 3xTg, Vol. 2015.

[106] G. McKhann, D. Drachman, M. Folstein, R. Katzman, D. Price and E.M. Stadlan, Clinical diagnosis of Alzheimer's disease: report of the NINCDS-ADRDA Work Group under the auspices of Department of Health and Human Services Task Force on Alzheimer's Disease, *Neurology*, **34** (1984), 939-944.

[107] Pathological correlates of late-onset dementia in a multicentre, community-based population in England and Wales. Neuropathology Group of the Medical Research Council Cognitive Function and Ageing Study (MRC CFAS), *Lancet*, **357** (2001), 169-175.

[108] A. Lim, D. Tsuang, W. Kukull, D. Nochlin, J. Leverenz, W. McCormick, J. Bowen, L. Teri, J. Thompson, E.R. Peskind, M. Raskind and E.B. Larson, Clinico-neuropathological correlation of Alzheimer's disease in a community-based case series, *J Am Geriatr Soc*, **47** (1999), 564-569.

[109] L.M. Bloudek, D.E. Spackman, M. Blankenburg and S.D. Sullivan, Review and meta-analysis of biomarkers and diagnostic imaging in Alzheimer's disease, *J Alzheimers Dis*, **26** (2011), 627-645.

[110] G. Waldemar, B. Dubois, M. Emre, J. Georges, I.G. McKeith, M. Rossor, P. Scheltens, P. Tariska and B. Winblad, Recommendations for the diagnosis and management of Alzheimer's disease and other disorders associated with dementia: EFNS guideline, *Eur J Neurol*, **14** (2007), e1-26.

[111] M.F. Folstein, S.E. Folstein and P.R. McHugh, "Mini-mental state". A practical method for grading the cognitive state of patients for the clinician, *J Psychiatr Res*, **12** (1975), 189-198.

[112] K. Blennow, M.J. de Leon and H. Zetterberg, Alzheimer's disease, *Lancet*, **368** (2006), 387-403.

[113] R.J. Killiany, M.B. Moss, M.S. Albert, T. Sandor, J. Tieman and F. Jolesz, Temporal lobe regions on magnetic resonance imaging identify patients with early Alzheimer's disease, *Arch Neurol*, **50** (1993), 949-954.

[114] N.A. Johnson, G.H. Jahng, M.W. Weiner, B.L. Miller, H.C. Chui, W.J. Jagust, M.L. Gorno-Tempini and N. Schuff, Pattern of cerebral hypoperfusion in Alzheimer disease and mild cognitive impairment measured with arterial spin-labeling MR imaging: initial experience, *Radiology*, **234** (2005), 851-859.

[115] B.C. Dickerson and R.A. Sperling, Functional abnormalities of the medial temporal lobe memory system in mild cognitive impairment and Alzheimer's disease: insights from functional MRI studies, *Neuropsychologia*, **46** (2008), 1624-1635.

[116] T. Wyss-Coray and J. Rogers, Inflammation in Alzheimer disease-a brief review of the basic science and clinical literature, *Cold Spring Harb Perspect Med*, **2** (2012), a006346.

[117] A. Nordberg, J.O. Rinne, A. Kadir and B. Langstrom, The use of PET in Alzheimer disease, *Nat Rev Neurol*, **6** (2010), 78-87.

[118] S. Minoshima, K.A. Frey, R.A. Koeppe, N.L. Foster and D.E. Kuhl, A diagnostic approach in Alzheimer's disease using three-dimensional stereotactic surface projections of fluorine-18-FDG PET, *J Nucl Med*, **36** (1995), 1238-1248.

[119] R.K. Brown, N.I. Bohnen, K.K. Wong, S. Minoshima and K.A. Frey, Brain PET in suspected dementia: patterns of altered FDG metabolism, *Radiographics*, **34** (2014), 684-701.

[120] E.R. Zimmer, A. Leuzy, S. Gauthier and P. Rosa-Neto, Developments in Tau PET Imaging, *Can J Neurol Sci*, **41** (2014), 547-553.

[121] A. Kadir, O. Almkvist, A. Wall, B. Langstrom and A. Nordberg, PET imaging of cortical 11C-nicotine binding correlates with the cognitive function of attention in Alzheimer's disease, *Psychopharmacology (Berl)*, **188** (2006), 509-520.

[122] J.O. Rinne, V. Kaasinen, T. Jarvenpaa, K. Nagren, A. Roivainen, M. Yu, V. Oikonen and T. Kurki, Brain acetylcholinesterase activity in mild cognitive impairment and early Alzheimer's disease, *J Neurol Neurosurg Psychiatry*, **74** (2003), 113-115.

[123] Z. Walker, D.C. Costa, R.W. Walker, K. Shaw, S. Gacinovic, T. Stevens, G. Livingston, P. Ince, I.G. McKeith and C.L. Katona, Differentiation of dementia with Lewy bodies from Alzheimer's disease using a dopaminergic presynaptic ligand, *J Neurol Neurosurg Psychiatry*, **73** (2002), 134-140.

[124] Y. Tanaka, K. Meguro, S. Yamaguchi, H. Ishii, S. Watanuki, Y. Funaki, K. Yamaguchi, A. Yamadori, R. Iwata and M. Itoh, Decreased striatal D2 receptor density associated with severe behavioral abnormality in Alzheimer's disease, *Ann Nucl Med*, **17** (2003), 567-573.

[125] V. Kepe, J.R. Barrio, S.C. Huang, L. Ercoli, P. Siddarth, K. Shoghi-Jadid, G.M. Cole, N. Satyamurthy, J.L. Cummings, G.W. Small and M.E. Phelps, Serotonin 1A receptors in the living brain of Alzheimer's disease patients, *Proc Natl Acad Sci U S A*, **103** (2006), 702-707.

[126] A. Cagnin, D.J. Brooks, A.M. Kennedy, R.N. Gunn, R. Myers, F.E. Turkheimer, T. Jones and R.B. Banati, In-vivo measurement of activated microglia in dementia, *Lancet*, **358** (2001), 461-467.

[127] C.A. Wiley, B.J. Lopresti, S. Venneti, J. Price, W.E. Klunk, S.T. DeKosky and C.A. Mathis, Carbon 11-labeled Pittsburgh Compound B and carbon 11-labeled (R)-PK11195 positron emission tomographic imaging in Alzheimer disease, *Arch Neurol*, **66** (2009), 60-67.

[128] N. Mattsson, K. Blennow and H. Zetterberg, CSF biomarkers: pinpointing Alzheimer pathogenesis, *Ann N Y Acad Sci*, **1180** (2009), 28-35.

[129] B. Delatour, S. Epelbaum, A. Petiet and M. Dhenain, In vivo imaging biomarkers in mouse models of Alzheimer's disease: are we lost in translation or breaking through?, *Int J Alzheimers Dis*, **2010** (2010).

[130] B.G. Vickrey, B.S. Mittman, K.I. Connor, M.L. Pearson, R.D. Della Penna, T.G. Ganiats, R.W. Demonte, Jr., J. Chodosh, X. Cui, S. Vassar, N. Duan and M. Lee, The effect of a disease management intervention on quality and outcomes of dementia care: a randomized, controlled trial, *Ann Intern Med*, **145** (2006), 713-726.

[131] M.G. Figueiro, B.A. Plitnick, A. Lok, G.E. Jones, P. Higgins, T.R. Hornick and M.S. Rea, Tailored lighting intervention improves measures of sleep, depression, and agitation in persons with Alzheimer's disease and related dementia living in long-term care facilities, *Clin Interv Aging*, **9** (2014), 1527-1537.

[132] L.S. Schneider, F. Mangialasche, N. Andreasen, H. Feldman, E. Giacobini, R. Jones, V. Mantua, P. Mecocci, L. Pani, B. Winblad and M. Kivipelto, Clinical trials and late-stage drug development for Alzheimer's disease: an appraisal from 1984 to 2014, *J Intern Med*, **275** (2014), 251-283.

[133] P.S. Aisen, The potential of anti-inflammatory drugs for the treatment of Alzheimer's disease, *Lancet Neurol*, **1** (2002), 279-284.

[134] J. Cedernaes, H.B. Schioth and C. Benedict, Efficacy of antibody-based therapies to treat Alzheimer's disease: just a matter of timing?, *Exp Gerontol*, **57** (2014), 104-106.

[135] R. Weissleder and U. Mahmood, Molecular imaging, *Radiology*, **219** (2001), 316-333.

[136] F.A. Jaffer and R. Weissleder, Molecular imaging in the clinical arena, *JAMA*, **293** (2005), 855-862.

[137] J.M. Hoffman and S.S. Gambhir, Molecular imaging: the vision and opportunity for radiology in the future, *Radiology*, **244** (2007), 39-47.

[138] M.L. James and S.S. Gambhir, A molecular imaging primer: modalities, imaging agents, and applications, *Physiol Rev*, **92** (2012), 897-965.

[139] S.S. Tunev, C.J. Hastey, E. Hodzic, S. Feng, S.W. Barthold and N. Baumgarth, Lymphoadenopathy during lyme borreliosis is caused by spirochete migration-induced specific B cell activation, *PLoS Pathog*, **7** (2011), e1002066.

[140] A. MacKenzie-Graham, In vivo vs. ex vivo Magnetic Resonance Imaging In Mice, *Front Neuroinform*, **6** (2012).

[141] A. Jain and S.K. Jain, Ligand-Appended BBB-Targeted Nanocarriers (LABTNs), *Crit Rev Ther Drug Carrier Syst*, **32** (2015), 149-180.

[142] I.G. Tucker, Drug delivery to the brain via the blood-brain barrier: a review of the literature and some recent patent disclosures, *Ther Deliv*, **2** (2011), 311-327.

[143] M. Demeule, J.C. Currie, Y. Bertrand, C. Che, T. Nguyen, A. Regina, R. Gabathuler, J.P. Castaigne and R. Beliveau, Involvement of the low-density lipoprotein receptor-related protein in the transcytosis of the brain delivery vector angiopep-2, *J Neurochem*, **106** (2008), 1534-1544.

[144] A.A. Date, M.D. Joshi and V.B. Patravale, Parasitic diseases: Liposomes and polymeric nanoparticles versus lipid nanoparticles, *Adv Drug Deliv Rev*, **59** (2007), 505-521.

[145] P. Blasi, S. Giovagnoli, A. Schoubben, M. Ricci and C. Rossi, Solid lipid nanoparticles for targeted brain drug delivery, *Adv Drug Deliv Rev*, **59** (2007), 454-477.

[146] Y.J. Yu, J.K. Atwal, Y. Zhang, R.K. Tong, K.R. Wildsmith, C. Tan, N. Bien-Ly, M. Hersom, J.A. Maloney, W.J. Meilandt, D. Bumbaca, K. Gadkar, K. Hoyte, W. Luk, Y. Lu, J.A. Ernst, K. Scearce-Levie, J.A. Couch, M.S. Dennis and R.J. Watts, Therapeutic bispecific antibodies cross the blood-brain barrier in nonhuman primates, *Sci Transl Med*, **6** (2014), 261ra154.

[147] B.K. Hendricks, A.A. Cohen-Gadol and J.C. Miller, Novel delivery methods bypassing the blood-brain and blood-tumor barriers, *Neurosurg Focus*, **38** (2015), E10.

[148] E.E. Konofagou, Optimization of the ultrasound-induced blood-brain barrier opening, *Theranostics*, **2** (2012), 1223-1237.

[149] A. Alonso, E. Reinz, M. Fatar, J. Jenne, M.G. Hennerici and S. Meairs, Neurons but not glial cells overexpress ubiquitin in the rat brain following focused ultrasound-induced opening of the blood-brain barrier, *Neuroscience*, **169** (2010), 116-124.

[150] W.A. Banks, S.M. Robinson and A. Nath, Permeability of the blood-brain barrier to HIV-1 Tat, *Exp Neurol*, **193** (2005), 218-227.

[151] W.A. Banks, Characteristics of compounds that cross the blood-brain barrier, *BMC Neurol*, **9 Suppl 1** (2009), S3.

[152] J. Temsamani and P. Vidal, The use of cell-penetrating peptides for drug delivery, *Drug Discov Today*, **9** (2004), 1012-1019.

[153] M. Zorko and U. Langel, Cell-penetrating peptides: mechanism and kinetics of cargo delivery, *Adv Drug Deliv Rev*, **57** (2005), 529-545.

[154] G. Drin, S. Cottin, E. Blanc, A.R. Rees and J. Temsamani, Studies on the internalization mechanism of cationic cell-penetrating peptides, *J Biol Chem*, **278** (2003), 31192-31201.

[155] P.E. Thoren, D. Persson, P. Isakson, M. Goksor, A. Onfelt and B. Norden, Uptake of analogs of penetratin, Tat(48-60) and oligoarginine in live cells, *Biochem Biophys Res Commun*, **307** (2003), 100-107.

[156] M. Pooga, M. Hallbrink, M. Zorko and U. Langel, Cell penetration by transportan, *FASEB J*, **12** (1998), 67-77.

[157] A. Zemel, D.R. Fattal and A. Ben-Shaul, Energetics and self-assembly of amphipathic peptide pores in lipid membranes, *Biophys J*, **84** (2003), 2242-2255.

[158] E. Walum, A. Peterson and L.J. Erkell, Photometric recording of cell viability using trypan blue in perfused cell cultures, *Xenobiotica*, **15** (1985), 701-704.

[159] R. Mishra, W. Su, R. Pohmann, J. Pfeuffer, M.G. Sauer, K. Ugurbil and J. Engelmann, Cell-penetrating peptides and peptide nucleic acid-coupled MRI contrast agents: evaluation of cellular delivery and target binding, *Bioconjug Chem*, **20** (2009), 1860-1868.

[160] F. Madani, S. Lindberg, U. Langel, S. Futaki and A. Graslund, Mechanisms of cellular uptake of cell-penetrating peptides, *J Biophys*, **2011** (2011), 414729.

[161] J.P. Richard, K. Melikov, E. Vives, C. Ramos, B. Verbeure, M.J. Gait, L.V. Chernomordik and B. Lebleu, Cell-penetrating peptides. A reevaluation of the mechanism of cellular uptake, *J Biol Chem*, **278** (2003), 585-590.

[162] A. Ziegler and J. Seelig, Interaction of the protein transduction domain of HIV-1 TAT with heparan sulfate: binding mechanism and thermodynamic parameters, *Biophys J*, **86** (2004), 254-263.

[163] M. Hallbrink, A. Floren, A. Elmquist, M. Pooga, T. Bartfai and U. Langel, Cargo delivery kinetics of cell-penetrating peptides, *Biochim Biophys Acta*, **1515** (2001), 101-109.

[164] D. Sarko, B. Beijer, R. Garcia Boy, E.M. Nothelfer, K. Leotta, M. Eisenhut, A. Altmann, U. Haberkorn and W. Mier, The pharmacokinetics of cell-penetrating peptides, *Mol Pharm*, **7** (2010), 2224-2231.

[165] S.J. Bolton, D.N. Jones, J.G. Darker, D.S. Eggleston, A.J. Hunter and F.S. Walsh, Cellular uptake and spread of the cell-permeable peptide penetratin in adult rat brain, *Eur J Neurosci*, **12** (2000), 2847-2855.

[166] E. Esneault, V. Castagne, P. Moser, C. Bonny and M. Bernaudin, D-JNKi, a peptide inhibitor of c-Jun N-terminal kinase, promotes functional recovery after transient focal cerebral ischemia in rats, *Neuroscience*, **152** (2008), 308-320.

[167] C.M. Dykstra, M. Ratnam and J.W. Gurd, Neuroprotection after status epilepticus by targeting protein interactions with postsynaptic density protein 95, *J Neuropathol Exp Neurol*, **68** (2009), 823-831.

[168] C.H. Nijboer, C.J. Heijnen, F. Groenendaal, M.J. May, F. van Bel and A. Kavelaars, Strong neuroprotection by inhibition of NF-kappaB after neonatal hypoxia-ischemia involves apoptotic mechanisms but is independent of cytokines, *Stroke*, **39** (2008), 2129-2137.

[169] G.P. Dietz, K.V. Stockhausen, B. Dietz, B.H. Falkenburger, P. Valbuena, F. Opazo, P. Lingor, K. Meuer, J.H. Weishaupt, J.B. Schulz and M. Bahr, Membrane-permeable Bcl-xL prevents MPTP-induced dopaminergic neuronal loss in the substantia nigra, *J Neurochem*, **104** (2008), 757-765.

[170] D.B. Schmolze, C. Standley, K.E. Fogarty and A.H. Fischer, Advances in microscopy techniques, *Arch Pathol Lab Med*, **135** (2011), 255-263.

[171] D.J. Stephens and V.J. Allan, Light microscopy techniques for live cell imaging, *Science*, **300** (2003), 82-86.

[172] *Optical Imaging of Neocortical Dynamics*, Springer New York Heidelberg Dordrecht London, 2014.

[173] F. Scheffold, Principles and Fundamentals of Optical Imaging, in: *Optical Imaging of Neocortical Dynamics*, Springer New York Heidelberg Dordrecht London, 2014.

[174] R. Weissleder, C.H. Tung, U. Mahmood and A. Bogdanov, Jr., In vivo imaging of tumors with protease-activated near-infrared fluorescent probes, *Nat Biotechnol*, **17** (1999), 375-378.

[175] M. Ogawa, N. Kosaka, M.R. Longmire, Y. Urano, P.L. Choyke and H. Kobayashi, Fluorophore-quencher based activatable targeted optical probes for detecting in vivo cancer metastases, *Mol Pharm*, **6** (2009), 386-395.

[176] D. Maxwell, Q. Chang, X. Zhang, E.M. Barnett and D. Piwnica-Worms, An improved cell-penetrating, caspase-activatable, near-infrared fluorescent peptide for apoptosis imaging, *Bioconjug Chem*, **20** (2009), 702-709.

[177] Y. Inoue, K. Izawa, S. Kiryu, A. Tojo and K. Ohtomo, Diet and abdominal autofluorescence detected by in vivo fluorescence imaging of living mice, *Mol Imaging*, **7** (2008), 21-27.

[178] C. Cullander, Imaging in the far-red with electronic light microscopy: requirements and limitations, *J Microsc*, **176** (1994), 281-286.

[179] P. Debbage and W. Jaschke, Molecular imaging with nanoparticles: giant roles for dwarf actors, *Histochem Cell Biol*, **130** (2008), 845-875.

[180] S.K. Cool, K. Breyne, E. Meyer, S.C. De Smedt and N.N. Sanders, Comparison of in vivo optical systems for bioluminescence and fluorescence imaging, *J Fluoresc*, **23** (2013), 909-920.

[181] A.H. Hielscher, Optical tomographic imaging of small animals, *Curr Opin Biotechnol*, **16** (2005), 79-88.

[182] A.P. Gibson, J.C. Hebden and S.R. Arridge, Recent advances in diffuse optical imaging, *Phys Med Biol*, **50** (2005), R1-43.

[183] V. Ntziachristos, J. Ripoll, L.V. Wang and R. Weissleder, Looking and listening to light: the evolution of whole-body photonic imaging, *Nat Biotechnol*, **23** (2005), 313-320.

[184] S. Keren, O. Gheysens, C.S. Levin and S.S. Gambhir, A comparison between a time domain and continuous wave small animal optical imaging system, *IEEE Trans Med Imaging*, **27** (2008), 58-63.

[185] A.A.R.T. Inc, GE/ART eXplore Optix Preclinical Optical Scanner, Vol. 2015.

[186] W. Zhang, H. Xiong, D. Callaghan, H. Liu, A. Jones, K. Pei, D. Fatehi, E. Brunette and D. Stanimirovic, Blood-brain barrier transport of amyloid beta peptides in efflux pump knock-out animals evaluated by in vivo optical imaging, *Fluids Barriers CNS*, **10** (2013), 13.

[187] S. Koenig, P. Krause, A.S. Hosseini, C. Dullin, M. Rave-Fraenk, S. Kimmina, A.L. Entwistle, R.M. Hermann, C.F. Hess, H. Becker and H. Christiansen, Noninvasive imaging of liver repopulation following hepatocyte transplantation, *Cell Transplant*, **18** (2009), 69-78.

[188] B. Ramjiawan, R.E. Ariano, H.H. Mantsch, P. Maiti and M. Jackson, Immunofluorescence imaging as a tool for studying the pharmacokinetics of a human monoclonal single chain fragment antibody, *IEEE Trans Med Imaging*, **21** (2002), 1317-1323.

[189] G.M. Clarke, C. Peressotti, G.E. Mawdsley and M.J. Yaffe, Design and characterization of a digital image acquisition system for whole-specimen breast histopathology, *Phys Med Biol*, **51** (2006), 5089-5103.

[190] MICROSCOPY, Vol. 49, Advantage Business Media, 2007, pp. 28-28.

[191] C. Halldin, B. Gulyas, O. Langer and L. Farde, Brain radioligands--state of the art and new trends, *Q J Nucl Med*, **45** (2001), 139-152.

[192] S.R. Cherry, J.A. Sorenson and M.E. Phelps, *Physics in nuclear medicine*, Saunders, Philadelphia, Pa., 2003, xiii, 523 p. pp.

[193] G. Stöcklin and V.W. Pike, *Radiopharmaceuticals for Positron Emission Tomography - Methodological Aspects* Springer Science & Business Media, 1993

[194] M.E. Raichle, Positron emission tomography, *Annu Rev Neurosci*, **6** (1983), 249-267.

[195] D.L. Bailey, D.W. Townsend, P.E. Valk and M.N. Maisey, *Positron emission tomography: basic sciences*, Springer, 2005.

[196] K.S. Krane, Introductory Nuclear Physics, New York, Wiley, 1987.

[197] S. DeBenedetti, C.E. Cowan, W.R. Konneker and H. Primakoff, On the Angular Distribution of Two-Photon Annihilation Radiation.

[198] S.E. Derenzo, *Precision measurement of annihilation point spread distributions for medically important positron emitters*, 1979, Medium: ED; Size: Pages: 9 pp.

[199] S.C. Huang, E.J. Hoffman, M.E. Phelps and D.E. Kuhl, Quantitation in positron emission computed tomography: 2. Effects of inaccurate attenuation correction, *J Comput Assist Tomogr*, **3** (1979), 804-814.

[200] T. Geva, Magnetic resonance imaging: historical perspective, *J Cardiovasc Magn Reson*, **8** (2006), 573-580.

[201] P.C. van Zijl and N.N. Yadav, Chemical exchange saturation transfer (CEST): what is in a name and what isn't?, *Magn Reson Med*, **65** (2011), 927-948.

[202] E. Vinogradov, S. Zhang, A. Lubag, J.A. Balschi, A.D. Sherry and R.E. Lenkinski, On-resonance low B1 pulses for imaging of the effects of PARACEST agents, *J Magn Reson*, **176** (2005), 54-63.

[203] E. Vinogradov, H. He, A. Lubag, J.A. Balschi, A.D. Sherry and R.E. Lenkinski, MRI detection of paramagnetic chemical exchange effects in mice kidneys in vivo, *Magn Reson Med*, **58** (2007), 650-655.

[204] I. Hancu, W.T. Dixon, M. Woods, E. Vinogradov, A.D. Sherry and R.E. Lenkinski, CEST and PARACEST MR contrast agents, *Acta Radiol*, **51** (2010), 910-923.

Chapter 2

2 Cathepsin D Expression in the Brain across Alzheimer Disease Mice Models

Jonatan A. Snir[a,b], Robert Bartha[a,b] and Stephen H. Pasternak [c,d]

[a]Department of Medical Biophysics, University of Western Ontario, London, Ontario, Canada,

[b]Centre for Functional and Metabolic Mapping, Robarts Research Institute, University of Western Ontario, London, Ontario, Canada

[c]J. Allyn Taylor Centre for Cell Biology, Molecular Brain Research Group, Robarts Research Institute, University of Western Ontario, London, Ontario, Canada,

[d]Department of Clinical Neurological Sciences, Schulich School of Medicine, University of Western Ontario, London, Ontario, Canada

2.1 Introduction

Alzheimer's disease (AD) is an insidiously debilitating and lethal condition affecting tens of millions of people over the world [1]. Currently the diagnosis of AD is primarily on clinical grounds. Because AD has a prodromal period estimated to be decades, by the time a patient develops cognitive complaints, permanent neurological damage is already underway. To develop an effective treatment, we must diagnose AD in the early or presymptomatic stage.

An important aspect of AD research focuses on recognizing and the evaluating biomarkers for prodromal AD diagnosis. The hallmark pathologies involved in AD include amyloid beta plaques (Aβ) and neurofibrillary tangles (NFT). The expression levels of Cathepsin D (CatD), a lysosomal aspartyl protease, has also been correlated with AD pathology and was suggested to be a biomarker for AD [2-5]. In AD patients there is a several fold increase in CatD in the Cerebral Spinal Fluid (CSF) compared to age-matched controls [3]. Furthermore, a recent study demonstrated that neural-derived plasma exosomal levels of CatD were significantly higher in AD patients reflecting AD pathology up to 10 years before clinical onset [69]. The exact role CatD plays has yet to be elucidated, however, since its activity has been shown to increase early in AD brains [2] it is a potential biomarker for early AD diagnosis.

Characterizing early signs of the disease development in humans is inherently difficult because post-mortem confirmation of the associated pathology is required for an accurate diagnosis. Genetically engineered transgenic (Tg) rodent models (mostly mice) recapitulate at least the initial phases of AD pathology within a relatively short period of time, offering a window into the development of AD [6]. Because mice do not develop AD naturally, mouse models require the introduction of the human gene for APP; for robust amyloid plaque formation, mice typically rely on the introduction of human APP and Presenilin genes bearing mutations that cause familial Alzheimer's disease. In addition, Tau gene (MAPT) mutations in frontotemporal and related tauopathies cause NFT's to develop in mouse models [6]. The presence of multiple different models of AD makes possible the correlation of biomarkers across disease severity, but also opens the question of how to choose the model best suited for the study at hand [7].

One of the first successful AD mouse models overexpressed a human APP bearing a Familial Alzheimer's disease causing mutation and was shown to exhibit an age-dependent increase in senile plaque deposition [8]. Since then, many mouse models have been developed incorporating human genes with Familial Alzheimer's disease (FAD) mutations (e.g in the PSEN1 gene) to increase $A\beta_{42}$ levels [9] and deposition [10]. For example, double mutation (*2X*) of both APP and PSEN1 is used in the Tg(APPswe,PSEN1dE9) mouse. This model expresses a chimeric mouse/human amyloid precursor protein with a Swedish mutation and a mutant human presenilin 1 with exon 9 deleted (PSEN1-dE9;) both controlled by independent mouse prion protein (PrP) promoter elements [12]. Consequently, plaques are abundant in the hippocampus and cortex by 9 months of age with occasional deposits found in mice as young as 6 months of age [13, 14]. This mouse model leads to the accumulation of senile plaques and cognitive decline offering a valuable tool in AD studies [15].

Previously, many of the available AD mouse models were hampered by the lack of neurofibrillary tangles and neuron loss. NFT were recently achieved by the incorporation of a human Tau gene containing mutations associated with Frontotemporal lobe dementia into AD Tg mice, as is the case of the triple transgenic (*3X*) mouse strain [16]. The 3xTg or B6;129-Psen1^{tm1Mpm} Tg(APPSwe,tauP301L) is a triple transgenic homozygous mouse strain combining the presenilin PS1M146V mutation (increases the ratio of Aβ42/Aβ40) as well as the amyloid beta precursor protein (Swedish mutation KM670/671NL) and microtubule-associated protein Tau mutation (tauP30IL). Both transgenes integrate at the same locus and are under the control of the mouse Thy1.2 regulatory element [12]. In this model, Aβ plaques begin to accumulate before 6 months of age, and continue with age-dependent increases observed between 12 and 20 months [17]. In addition, Tau pathology including NFTs is detected by 6 months of age with advanced NFT burden by 20 months [17].

Despite AD model mice displaying cognitive decline, synaptic loss, and increased mortality - most models seldom present neuronal cell death. However, the latter has been recently detected in more aggressive Tg mouse models such as the 5XFAD where multiple mutations are expressed [18]. The 5XFAD strain, overexpresses a human APP

gene bearing 3 mutations (the Swedish (K670N, M671L), Florida (I716V) and London (V717I) mutations) along with human PSEN1 with two human FAD-causing mutations (M146L and L286V). Consequentially, the 5XFAD presents early (<2 months) onset of plaque deposition, age-dependent synaptic degeneration, working memory impairments and neuronal loss [18].

We have previously developed a contrast agent (CA) to detect CatD activity *in-vivo*, consisting of a magnetic resonance imaging/fluorescent moiety linked to a cell penetrating peptide (CPP) by means of a CatD cleavage site. The objective of this study was to verify that CatD is over expressed in multiple AD mouse models, to characterize the onset of these changes compared to AD pathology, and to select an appropriate model to provide proof of concept for a novel working CatD-targeting CA. To do this, we mapped the levels of CatD as well as Aβ and Tau accumulation across several brain regions and over the age of the mice useing immunohistochemistry (IHC) and Western blot (WB) analysis. We found that CatD expression increased over time in normal mice, and was greatly increased in proportion to Aβ pathology. These findings validate the idea of CatD as a biomarker for Alzheimer's disease.

2.2 Materials and Methods

2.2.1 Animals

All animal studies were conducted in accordance with the guidelines of the Subcommittee on Animal Care at the University of Western Ontario, and conformed to the Canadian Council on Animal Care guide for the care and use of laboratory animals. The required documentation is attached in Appendix 5. All mice were received from Jackson Laboratories (Bar Harbor, ME, USA). Three Tg mouse models of AD were selected. In the current study, a total of three female mice per time point (age) per strain were used (N=63) in total; eighteen controls, fifteen *5X* (5XFAD), fifteen *2X* (APPswe/PS1dE9) and fifteen *3X* (3xTg) mice. All animals, which were used up to twelve months of age, were housed with a 12-h light/12-h dark photoperiod and received food and water *ad libitum*.

2.2.2 Preliminary tissue processing

At each time point (age group), mice were placed into a surgical plane by induction chamber CO_2 inhalation followed by severing the diaphragm, left ventricle heparin injection (2 ml/kg), right atrium cut and ice-cold phosphate buffered saline (PBS) perfusion (at least 10 ml) via the left ventricle catheter and lastly decapitation. Brains were rapidly removed and dissected while kept on ice. One hemisphere was removed and immersed in 10% neutral buffered formalin NBF immersion for at least another 48 hours prior to additional processing. The other hemisphere (contralateral) was dissected further to separate the hippocampus, cortex, and striatum and then stored at -80°C. Tissue collection was performed at 5, 16, 32, 44 and 60 weeks of age for the 2X and 3X mice, 5, 8, 16, 28 and 60 weeks of age for the 5X mice; and finally 5, 8, 16, 32, 44, 60 weeks of age for the WT mice.

2.2.3 Western Blotting

Frozen tissue samples were combined in ice cold lysis buffer [20mM Tris–HCl (pH 8), 150 mM NaCl, 0.1% SDS, 1mM EDTA, 1% Igepal CA-630, 50mM] with protease cocktail inhibitors with pepstatin A (Roche, Mississauga, Ontario, Canada) and homogenized using a Pestle Grinder System (Thermo Fisher Scientific, Massachusetts, USA) and frozen at -80°C. Lanes were run with 20 µg of protein on a 12% SDS–polyacrylamide gel and the resolved proteins were transferred to a nitrocellulose membrane (all from Bio-Rad, Mississauga, Ontario, Canada) using a Trans-Blot Semi-Dry Electrophoretic Transfer Cell (Bio-Rad, Mississauga, Ontario, Canada). The membrane was blocked with 5% nonfat milk (w/v) dissolved in Tris buffered saline with 0.05% Tween-20 (TBST). Blots were probed using Anti-Cat-D antibody at 1:300 dilution factor (chosen to ensure a linear response across a several fold increase in the concentration of target protein) overnight (C-20- sc6486; Santa Cruz Biotechnology, Santa Cruz, CA, USA), and detected using rabbit-anti-goat antibody coupled to horseradish peroxidase using enhanced chemiluminescence reagents (ECL;). Blots were

imaged digitally using the Gel Doc XR+ System (BIORAD; California, USA). Blots were then washed 3 times in TBST and re-probed with anti-α-tubulin at 1:50k dilution factor overnight (Sigma Aldrich, St Louis, MO, USA) as a loading control and imaged the following day. Since immature Cat-D is also the active form and performs the same enzymatic functions as the mature form, both forms were grouped into a total CatD expression {Benes, 2008, Cathepsin D--many functions of one aspartic protease}. Images were analyzed using ImageJ (http://rsbweb.nih.gov/ij/). CatD chemiluminescent bands were evaluated relative to the loading control measurement of α-tubulin as follows using Equation (2-1):

$$\psi_i = \frac{SI_{CatD}}{SI_{\alpha-tubulin}} \quad \textbf{(2-1)}$$

Where ψ is the ratio of CatD compared to α-tubulin. The SI_{CatD} or $SI_{\alpha\_tubulin}$ are the densitometric "signals" measured from the blot for either CatD or α-tubulin respectively, i = 1..3 are the number of animals used. Next, in order to normalize all data across all strains, brain regions and ages - all ψ (of any strain, age, or mouse) were normalized to the ψ of a single five week old WT mouse cortex based on the relative CatD expression previously measured using a separate WB analysis for all 5 week old WT tissues (9 samples: 3 mice, 3 brain regions). This process was completed for each mouse, at each time point, for each brain region (striatum, hippocampus and cortex).

2.2.4 Immunohistochemistry Processing and Analysis of Transgenic and Wild Type Mice

All brains were allowed to fix over time in 10% NBF before switching to 70% ethanol and embedded in paraffin. Five (5) µm thick sections were cut in a coronal orientation to expose the hippocampus, striatum, cortex, as well as the thalamus. All sections were stained (for each primary antibody) at the same time for standardization purposes. In addition, any potential variability in staining between the sections, animals and time points was minimized by using an automatic threshold as described in more

detail below. Endogenous peroxidase activity was inhibited by using hydrogen peroxide (3%) followed by antigen retrieval using formic acid (70%, 2 minutes) and sections were immunolabeled with either an antibody against CatD (1:200 dilution factor; C-20 sc-6486 from Santa Cruz Biotechnology; Santa Cruz, CA, USA) or against $A\beta_{42}$ (1:200 dilution factor; custom made). The dilution factors were chosen after performing serial dilutions of different concentration. A dilution was chosen that did not produce excessive staining of CatD in the younger mice (as well as a linear response in Western blots). In addition, dilution factor was chosen for the $A\beta_{42}$ antibody to produce no staining of note in the older WT mice (non-zero values measured in WT mice set base-line for thresholding/ colour deconvolution). This antibody was detected using an anti-rabbit secondary antibody conjugated to horseradish peroxidase, prior to colorimetric detection using nickel 3,3'-diaminobenzidine (DAB; 0.15 mg/ml in 0.03% H_2O_2; Sigma-Aldrich, Oakville,ON, Canada) with the Vectastain ABC kit (Dako, Burlington, ON, Canada) and counterstaining with Hematoxylin and Eosin (H&E; Leica Microsystems Inc. Concord, Ontario, Canada). Negative control (no primary antibody) did not produce any notable staining. Sections were imaged and digitized using a TISSUEscope CF slide scanner (Huron Technologies, Waterloo, ON) at a 0.5 µm resolution using bright field imaging (at 40X). Slides were measured for positively stained areas in four brain regions (each covering >200,000 μm^2) per mouse, in each of three mice per age group using ImageJ (v. 1.46r, http://rsbweb.nih.gov/ij/). Staining was identified using the color deconvolution plugin written by Dr. Gabriel Landini (available via the aforementioned website) and quantified using the ImageJ built-in threshold tool (triangle thresholding with seldom minor manual adjustments if deemed necessary by the primary observer JAS). To assess intra-observer variability, a subset of the data ($A\beta_{42}$) was analyzed by a second blinded observer (blinded to strain, age, and tissue type).

2.2.5 Statistical analysis

Two-tailed, unequal variance Student's t-test was used to test for significant differences correcting for multiple comparisons using the Sidak-Bonferroni method using Prism5 (GraphPad software, Inc. La Jolla, CA, USA) comparing the amount of DAB staining detected in the different brain regions via both Western blots and

histopathological examination. Additionally, a two-way ANOVA with Tukey's correction for multiple comparisons was used to examine the influence and statistical differences as a result of having AD mutations (strain factor) and aging (age factor). For ANOVA, when comparing WT mice with 2X or 3X, the missing 32-week old WT mice data assumed the values of the available 28-week old data. Finally, a Pearson correlation test as well as Student's t-test was used to check for intra-observer variability and correlation of the measurements performed for CatD and $A\beta_{42}$ staining.

2.3 Results

2.3.1 Immunohistochemistry

As expected, all cells expressed CatD in a punctate pattern consistent with lysosomal/organellar expression. We examined CatD and Aβ42 staining across the lifespan in WT, 2X 3X and 5X experimental animals. CatD (Fig. 2-1) as well as $A\beta_{42}$ (Fig. 2-2) staining was most pronounced in 12 months old Tg mouse brains both intracellularly (Figures open arrow) as well as extracellularly in senile plaque-like morphology (close arrow). WT mice also demonstrated increasing CatD staining with age, but did not show any Aβ deposition.The staining was least in the WT mice, and increased progressively in the age-matched 3X, 2X, and 5X strains. The staining was observed most notibly in the cortex (left pane is zoomed into layers II-III and IV-V) and hippocampus. Within the hippocampal formation of the 2X and 5X mice, the dentate gyrus polymorph layer as well as the CA1, CA3 and dorsal part of the subiculum pyramidal cell layers presented heavy staining in the Tg mice. The thalamus and striatum presented far less positive staining for CatD in the 2X and 3X mice compared to the 5X line, whereas the 3X presented the least amount of the plaque-like extracellular staining.

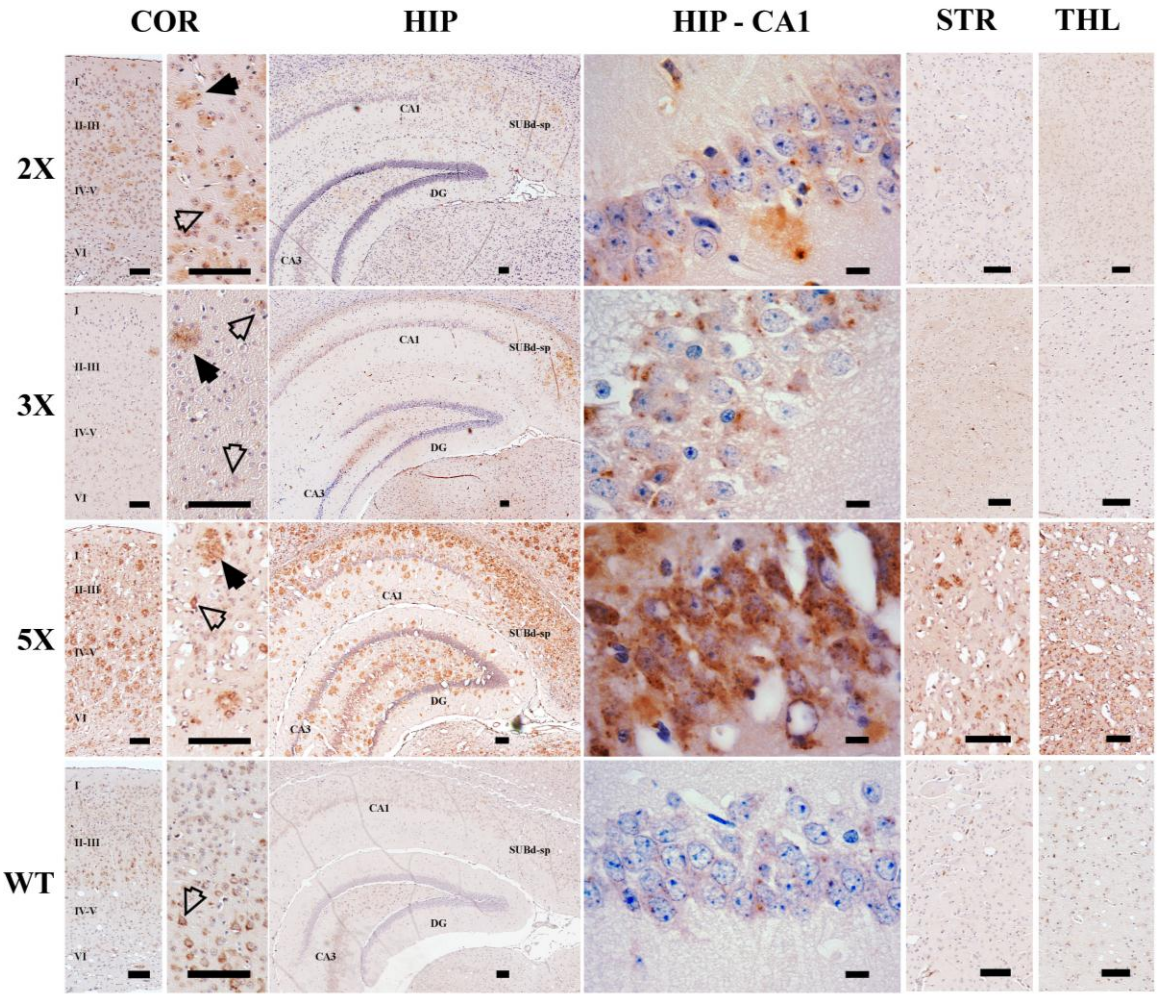

Figure 2-1. CatD staining in older Tg and control WT mice (60 weeks). Progressive CatD positive staining appears throughout the Tg mouse brains in the cortex (COR), hippocampus (HIP), the hippocampal CA1 region (HIP-CA1), striatum (STR) and thalamus (THL) as noted above for the 2X, 3X, 5X and WT as noted on the left, both intracellularly (open arrow) as well as extracellularly in senile plaque-like morphology (close arrow). Different regions of the brain are indicated above for the different AD mouse models indicated on the left (2X, 3X and 5X versus WT controls). Scale bar is 100 µm (for the HIP-CA1 the scale bar is 10µm).

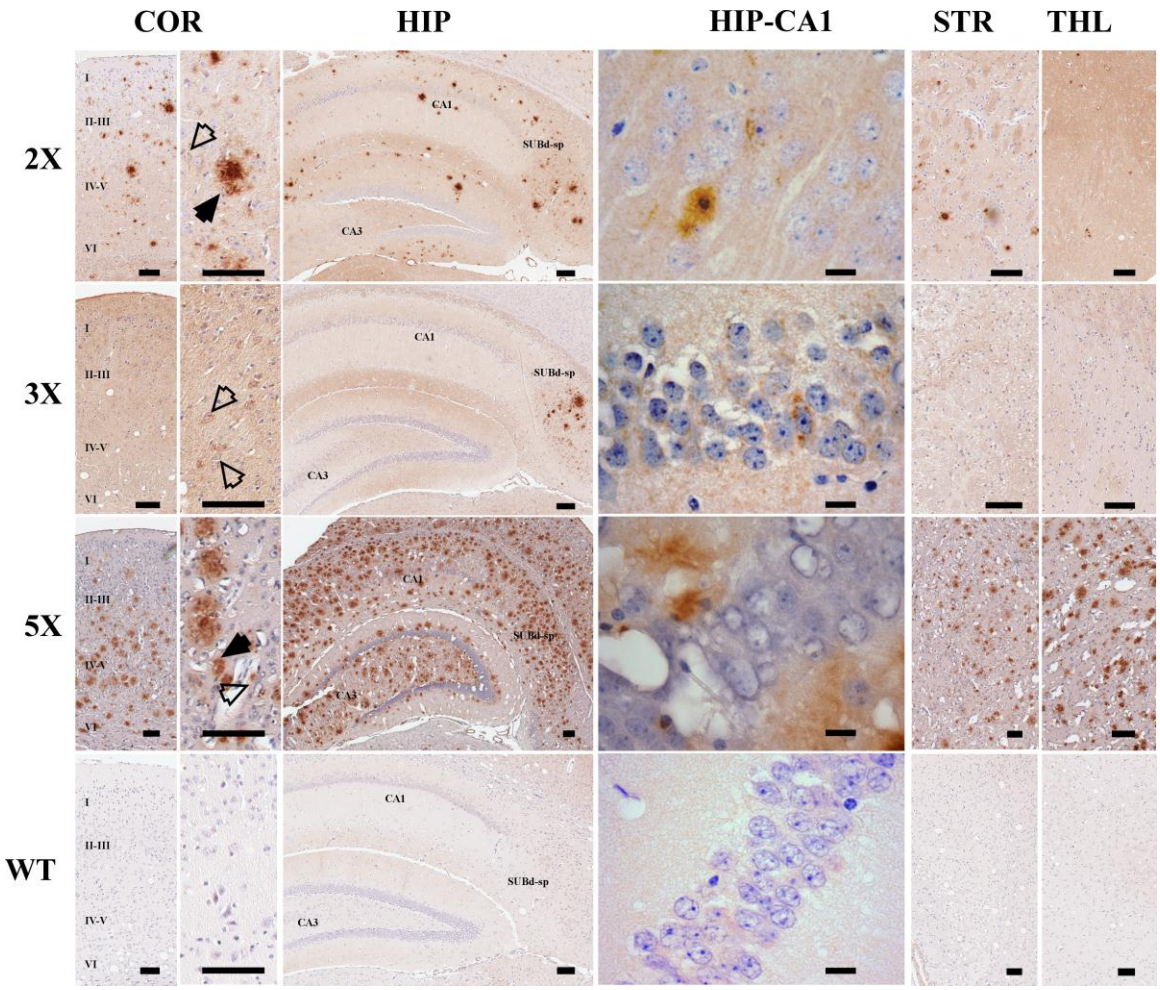

Figure 2-2 $A\beta_{42}$ staining in older Tg and control WT mice (60 weeks). Progressive $A\beta_{42}$ positive staining appears throughout the Tg mouse brains in the cortex (COR), hippocampus (HIP), the hippocampal CA1 region (HIP-CA1), striatum (STR) and thalamus (THL) as noted above for the 2X, 3X, 5X and WT as noted on the left, both intracellularly (open arrow) as well as extracellularly in senile plaque-like morphology (close arrow). Different regions of the brain are indicated above for the different AD mouse models indicated on the left (2X, 3X and 5X versus WT controls). Scale bar is 100 µm (for the HIP-CA1 the scale bar is 10µm).

We used ImageJ to calculate the percent area occupied by DAB stain with respect to a region of interest within the Cortex (Cor) Striatum (Str), Hippocampus (Hip) and Thalamus (Thl). These results are shown in Figure 2-3 plotted over time for all mouse ages and strains.

2.3.1.1 $A\beta_{42}$ Staining Quantification

All measured $A\beta_{42}$ DAB staining is reported in Table 2-1 and plotted in Fig. 2-3.

2.3.1.1.1 2X vs. WT

The amount of 2X cortex $A\beta_{42}$ staining was significantly ($p < 0.05$) higher at 44 (4.48 ± 0.94 vs 1.34 ± 0.16%) and 60 (7.21 ± 1.67 vs 0.85 ± 0.25 %) weeks of age compared to age-matched controls. Both age [F (4, 19) = 6.539, p = .0017, η^2 = 0.232] and strain [F (1, 19) = 32.09, $p < .0001$, η^2 = 0.284] factors contributed to the significant differences. In the hippocampus, there was significantly ($p < 0.05$) more positive staining for $A\beta_{42}$ at 44 (4.20 ± 0.69 vs 1.19 ± 0.17 %) and 60 (5.82 ± 0 .63 vs 1.12 ± 0.38 %) week of age in 2X mice where both strain [F (1, 18) = 42.67, $p < .0001$, η^2 = 0.403] and age [F (4, 18) = 5.274, p = .0054, η^2 = 0.199] contributed to the significant differences. However, in the striatum, only the 60-week old 2X mice had significantly higher staining for $A\beta_{42}$ (3.00 ± 0.88 vs 0.43 ± 0.04 %; $p < 0.05$). Finally, the thalamus presented only strain dependent differences in staining [F (1, 16) = 5.587, p = .0311, η^2 = 0.199].

2.3.1.1.2 3X vs. WT

The 3X mice presented with little pathology in the cortex, with most plaques observed in the hippocampus (primarily in the SUBd region) and thalamus regions near the lateral ventricles. There were no significant differences in staining in the cortex and striatum, but the hippocampus presented significantly higher staining dependent on age [F (1, 18) = 14.6, p = .0013, η2 = 0.362] and strain [F (1, 18) = 7.386, p = .0141, η2 = 0.244].

Table 2-1. $A\beta_{42}$ DAB staining measurements over time (weeks) for all strains.

	$A\beta_{42}$			
Cortex	**WT**	**2X**	**3X**	**5X**
5	1.19 ± 0.36	1.53 ± 0.25	0.96 ± 0.37	2.73 ± 0.87
8	1.53 ± 0.11	NA		**5.18 ± 0.1$^{\alpha}$**
16	1.45 ± 0.77	**2.41 ± 0.74$^{\delta}$**	**1.6 ± 0.44$^{\delta}$**	**8.36 ± 1.14$^{\alpha\beta\gamma}$**
28/32	1.17 ± 0.08	**1.68 ± 0.19$^{\delta}$**	**2.68 ± 1.72$^{\delta}$**	**10.69 ± 0.76$^{\alpha\beta\gamma}$**
44	1.34 ± 0.16	**4.48 ± 0.94$^{\alpha}$**	2.23 ± 0.5	NA
60	0.85 ± 0.25	**7.21 ± 1.67$^{\alpha\delta}$**	**3.10 ± 0.89$^{\delta}$**	**19.44 ± 1.62$^{\alpha\beta\gamma}$**
Hippocampus				
5	0.97 ± 0.34	1.79±0.73	1.63 ± 0.19	**3.54 ± 1.35$^{\alpha}$**
8	1.41 ± 0.03	NA		5.81 ± 3.32
16	1.14 ± 0.32	**2.40 ± 0.60$^{\delta}$**	**2.33 ± 0.75$^{\delta}$**	**6.54 ± 3.37$^{\beta\gamma}$**
28/32	1.29 ± 0.02	**2.37 ± 0.46$^{\delta}$**	**2.86 ± 1.20$^{\delta}$**	**10.15 ± 3.17$^{\alpha\ \beta\gamma}$**
44	1.19 ± 0.17	**4.20 ± 0.69$^{\alpha}$**	3.65 ± 0.72	NA
60	1.12 ± 0.38	**5.82 ± 0 .63$^{\alpha\delta}$**	**3.88 ± 1.15$^{\delta}$**	**13.35 ± 1.44$^{\alpha\beta\gamma}$**
Striatum				
5	1.07 ± 0	0.81 ± 0.07	0.88 ± 0.28	1.32 ± 0.14
8	0.63 ± 0.1	NA		1.72 ± 0.14
16	0.92 ± 0.4	1.01 ± 0.69	**0.89 ± 0.37 $^{\delta}$**	**2.07 ± 0.43$^{\gamma}$**
28/32	0.74 ± 0.04	**0.48 ± 0.21$^{\delta}$**	**0.32 ± 0.05 $^{\delta}$**	**3.71 ± 1.41$^{\beta\ \gamma}$**
44	0.28 ± 0.05	1.63 ± 0.19	0.70 ± 0.16	NA
60	0.43 ± 0.04	**3.00 ± 0.88$^{\alpha\delta}$**	**1.46 ± 1.22$^{\delta}$**	**10.26 ± 0.76 $^{\alpha\beta\gamma}$**
Thalamus				
5	1.3 ± 0.22	2.21 ± 0.26	1.87 ± 0.15	**2.5 ± 0.47$^{\alpha}$**
8	1.12 ± 0.09	NA		**5.79 ± 0.80$^{\alpha}$**
16	1.34 ± 0.17	1.49 ± 0.13	1.87 ± 0.15	**6.23 ± 1.30$^{\alpha}$**
28/32	1.80 ± 0.18	**2.34 ± 0.76$^{\delta}$**	**1.88 ± 0.21$^{\delta}$**	**8.03 ± 1.44 $^{\alpha\beta\gamma}$**
44	1.4 ± 0.15	2.61 ± 0.99	2.62 ± 0.22	NA
60	1.39 ± 0.18	**1.63 ± 0.19$^{\delta}$**	**2.13 ± 0.93$^{\delta}$**	**16.60 ± 0.88 $^{\alpha\beta\gamma}$**

Significance ($p < 0.05$) of data points are bolded and designated according to what they are compared to: Vs. WT – **α**; Vs. 2X – **β**; Vs. 3X – **γ**; Vs. 5X – **δ**. Data is mean ± standard error (N=3).

2.3.1.1.3 5X vs. WT

The 5X mice presented the most progressive amount of pathology. There was a significant ($p < 0.01$) amount of positive area staining for $A\beta_{42}$ in the cortex compared to WT as early as at 8 (5.18 ± 0.1 vs. 1.53 ± 0.11%) followed by 16 (8.36 ± 1.14 vs 1.45 ± 0.77 %), 28 (10.69 ± 0.76 vs 1.17 ± 0.08 %) and 60 (19.44 ± 1.62 vs 0.85 ± 0.25 %) weeks of age. Overall both strain [F (1, 20) = 347.2, $p < .0001$, $\eta^2 = 0.481$] and age [F (4, 20) = 42.06, $p < .0001$, $\eta^2 = 0.233$] factors contributed significantly to the differences. The 5X hippocampal $A\beta_{42}$ staining was significantly higher at 5 (3.54 ± 1.35 vs 0.97 ± 0.34 %), 16 (6.54 ± 3.37 vs 1.14 ± 0.32), 28 (10.15 ± 3.17 vs 1.29 ± 0.02 %) and 60 (13.35 ± 1.44 vs 1.12 ± 0.38 %) week time points ($p < 0.01$). Strain [F (1, 20) = 46.98, $p < .0001$, $\eta^2 = 0.518$] but less so age [F (4, 20) = 2.974, $p = 0.0444$ $\eta^2 = 0.13.11$] both contributed to the significant amount of staining ($\eta_{strain}^2 > \eta_{age}^2$). 5X striatum $A\beta_{42}$ staining was significant ($p < .01$), but only at 60 weeks of age (10.26 ± 0.76 vs 0.43 ± 0.04 %) but both strain [F (1, 17) = 53.47, $p < .0001$, $\eta^2 = 0.224$] and age [F (4, 18) = 16.98, $p < .0001$, $\eta^2 = 0.285$] contributed to the overall significant $A\beta_{42}$ staining noted across the data. Finally, there was a significant ($p < 0.01$) amount of positive staining for $A\beta_{42}$ in the thalamus compared to WT as early as 5 (2.5 ± 0.47vs 1.3 ± 0.22 %), and 8 (5.79 ± 0.80 vs 1.12 ± 0.09) weeks of age, followed by 16 (6.23 ± 1.30 vs 1.34 ± 0.17 %), 28 (8.03 ± 1.44 vs 1.80 ± 0.18 %) and 60 (16.60 ± 0.88 vs 1.39 ± 0.18 %) weeks of age. Both strain [F (1, 17) = 238.5, $p < .0001$, $\eta^2 = 0.428$] and age [F (4, 17) = 35.44, $p < .0001$, $\eta^2 = 0.254$] contributed to the variation in the thalamus DAB stain data.

2.3.1.1.4 Tg vs. other Tg differences

There were no significant differences between the $A\beta_{42}$ staining in all Tg mice at 5 weeks, but at 16 weeks the 5X cortex and hippocampus stained area was larger than 2X and the 3X. At 28/32 weeks, The 5X cortex, striatum, hippocampus and thalamus stained areas were larger than those measured for 2X and 3X. At 60 weeks, the 5X's cortex, hippocampus, striatum and thalamus stained areas were all larger compared to 2X and 3X. At no point was the 2X significantly different than the 3X.

2.3.1.1.5 Inter-observer variability

To test observer variability, a blinded (unaware of the age, the strain, or brain region segmented for calculation of % DAB) observer was tasked with quantifying the $A\beta_{42}$ staining. Measurements were compared to those made by the primary observer (JAS). There were no significant differences (paired two-tailed Student's t-test) and the measurements were highly correlated (Pearson coefficient r >0.8) for the 2X mice (paired Student's t-test $p = 0.065$), 3X mice (paired Student's t-test $p = 0.0638$) and the 5X mice (paired Student's t-test $p = 0.2619$).

2.3.1.1.6 Aβ42 levels at different ages

The levels of DAB staining are shown in Fig. 2-3 over time. In Fig. 2-4, pseudo colour maps are used to show the lease-square linear fitting associated slopes indicating the "rate of change" in positive DAB staining in different brain regions over the age of the mouse (% DAB stain/ week of aging). Of note, are the stark differences between the WT mice and all Tg mice. The linear fit slopes for the 2X cortex, hippocampus and striatum $A\beta_{42}$ data were all significantly different than those of the WT mice (excluding the thalamus) as can be seen in Figure 2-4. The 3X hippocampus and cortex presented significantly higher slopes ($p < 0.05$) than WT mice and only the cortex of the 3X was significantly different ($p < 0.05$) than that of the 2X. The 5X cortex, hippocampus, thalamus and striatum had significantly higher ($p < 0.01$) slopes than those of the 2X (excluding the 2X hippocampus which was not significantly different), 3X and WT corresponding brain regions. It is important to note that none of the WT brain regions showed significant differences with each other ($p = 0.06$) and none of the WT $A\beta_{42}$ slopes significantly deviated from zero.

2.3.1.2 Cathepsin D Staining Quantification

The amount of CatD staining was most notable in the 5X, followed by the 2X, then 3X and finally WT mice. All measured CatD DAB staining is reported in Table 2-2 and shown in Fig. 2-3.

Table 2-2. CatD DAB staining measurements over time (weeks) for all strains.

	CatD			
Cortex	**WT**	**2X**	**3X**	**5X**
5	2.01 ± 0.74	2.28 ± 1.44	1.92 ± 0.19	3.01 ± 0.55
8	2.04 ± 0.31	NA		**5.26 ± 1.01$^{\alpha}$**
16	3.18 ± 0.63	3.39 ± 0.71	**2.54 ± 0.49$^{\delta}$**	**7.07 ± 1.23$^{\alpha\beta\gamma}$**
28/32	3.44 ± 0.11	**4.25 ± 0.43$^{\delta}$**	**2.8 ± 0.61$^{\delta}$**	**10.13 ± 1.34 $^{\alpha\beta\gamma}$**
44	2.96 ± 0.66	**5.62 ± 0.43$^{\alpha\gamma}$**	**2.60 ± 0.52$^{\beta}$**	NA
60	3.58 ± 0.98	**8.64 ± 0.71$^{\alpha\gamma\delta}$**	**2.67 ± 0.58$^{\beta\delta}$**	**15.77 ± 1.96 $^{\alpha\beta\gamma}$**
Hippocampus				
5	2.58 ± 0.61	2.44 ± 0.94	1.88 ± 0.52	3.13 ± 0.98
8	3.5 ± 0.71	NA		4.64 ± 0.52
16	3.89 ± 0.22	4.74 ± 0.61	**1.74 ± 0.72$^{\delta}$**	**7.32 ± 2.07$^{\beta\gamma}$**
28/32	3.29 ± 0.68	5.81 ± 0.98	**3.11 ± 0.10$^{\delta}$**	**12.30 ± 1.09$^{\alpha\beta\gamma}$**
44	3.80 ± 0.81	**8.15 ± 1.15$^{\alpha}$**	3.79 ± 0.15	NA
60	3.66 ± 0.46	**9.80 ± 1.52$^{\alpha}$**	**4.79 ± 0.14$^{\delta}$**	**17.62 ± 1.90$^{\alpha\beta\gamma}$**
Striatum				
5	0.8 ± 0.20	0.66 ± 0	1.16 ± 0.21	0.87 ± 0.22
8	1.01 0.50	NA		0.75 ± 0.16
16	1.50 ± 0.33	**0.76 ± 0.14$^{\delta}$**	**0.67 ± 0.25$^{\delta}$**	**1.95 ± 0.32$^{\beta\gamma}$**
28/32	1.48 ± 0.32	**0.87 ± 0.30$^{\delta}$**	**0.78 ± 0.40$^{\delta}$**	**3.72 ± 0.75$^{\beta\gamma}$**
44	1.40 ± 0.07	1.57 ± 0.27	1.52 ± 0.42	NA
60	1.54 ± 0.90	**1.59 ± 0.04$^{\delta}$**	**1.04 ± 0.50$^{\delta}$**	**15.63 ± 1.26$^{\alpha\beta\gamma}$**
Thalamus				
5	1.79 ± 0.34	1.46 ± 0.14	3.19 ± 1.06	2.22 ± 0.27
8	1.59 ± 0.03	NA		4.10 ± 1.15α
16	2.37 ± 0.48	**1.74 ± 0.42$^{\delta}$**	**2.40 ± 0.68$^{\delta}$**	**6.32 ± 0.61 $^{\alpha\beta\gamma}$**
28/32	1.48 ± 0.15	1.9 ± 0.24	2.68 ± 1.06	**3.31 ± 0.51$^{\alpha}$**
44	1.92 ± 0.34	1.79 ± 0.21	1.95 ± 0.29	NA
60	2.13 ± 0.28	**2.48 ± 0.69$^{\delta}$**	**1.85 ± 0.25$^{\delta}$**	**9.89 ± 0.49 $^{\alpha\beta\gamma}$**

Significance ($p < 0.05$) of data points are bolded and designated according to what they are compared to: Vs. WT – **α**; Vs. 2X – **β**; Vs. 3X – **γ**; Vs. 5X – **δ**. Data is mean ± standard error.

2.3.1.2.1 2X vs. WT

When comparing 2X mice with WT, cortex CatD expression was only significantly higher in 2X mice at 44 and 60 weeks of age (5.62 ± 0.43 vs 2.96 ± 0.66 and 8.64 ± 0.71 vs 3.58 ± 0.98 %; $p < 0.05$). Two-way ANOVA indicated that both strain [F (1, 19) = 16.68, $p = .0006$, $\eta^2 = 0.186$] and age [F (4, 19) = 8.450, $p = .0004$, $\eta^2 = 0.377$] factors contributed to significant differences. Next, only at 44 (8.15 ± 1.15 vs 3.80 ± 0.81 %; $p < 0.01$) and 60 weeks of age (9.80 ± 1.52 vs 3.66 ± 0.46 %; $p < 0.01$) was the 2X hippocampal CatD staining significantly higher than WT with both strain [F (1, 18) = 23.00, $p = .0001$, $\eta^2 = 0.268$] and age [F (4, 18) = 6.397, $p = .0022$, $\eta^2 = 0.299$] effects contributing. In contrast, no significant differences were noted for the striatum or thalamus.

2.3.1.2.2 3X vs. WT

In 3X mice, only age-dependent difference were observed [F (4, 18) = 1.717, $p < .0033$, $\eta^2 = 0.422$] but no significant differences were measured compared to WT.

2.3.1.2.3 5X vs. WT

The 5X mice presented with a significantly higher amount of staining for CatD throughout the brain. Specifically, a considerable amount of staining was observed in the cortex at 8 (5.26 ± 1.01 vs 2.04 ± 0.31 %), 16 (7.07 ± 1.23 vs 3.39 ± 0.71 %), 28 (10.13 ± 1.34 vs 2.95 ± 0.81 %), and 60 (15.77 ± 1.96 vs 3.58 ± 0.98 %) weeks of age with strain factor [F (1, 18) = 92.39, $p < .0001$, $\eta^2 = 0.548$] and age factor [F (4, 18) = 17.68, $p < .0001$, $\eta^2 = 0.420$] contributing. Similarly, the hippocampus CatD expression values at 28 weeks (12.30 ± 0.56 vs 3.29 ± 0.68; $p < 0.05$) and 60 (3.66 ± 0.46 vs 17.62 ± 1.90; $p < 0.05$) were significantly higher with strain factor [F (1, 17) = 67.16, $p < .0001$, $\eta^2 = 0.443$] and age factor [F (4, 17) = 14.06, $p < .0001$, $\eta^2 = 0.371$] contributing. The striatum had a significantly higher value in the 5X mice at 60 weeks of age (15.63 ± 1.26 vs. 1.54 ± 1.10) with strain [F (1, 15) = 83.12, $p < .0001$, $\eta^2 = 0.279$] and age [F (4, 15) = 47.01, $p < .0001$, $\eta^2 = 0.632$] factors contributing to the differences between the groups. Lastly, the 5X thalamus was found stain significantly higher (6.40 ± 1.06 vs. 2.37 ± 0.83; $p <$

0.05) at as early as 16 weeks, 28 weeks (3.31 ± 0.51vs 1.48 ± 0.15) and 60 weeks (9.89 ± 0.49 vs 2.13 ± 0.28) with strain [F (1, 17) = 74.16, $p < .0001$, $\eta^2 = 0.545$] and age factors [F (4, 17) = 12.68, $p < .0001$, $\eta^2 = 0.372$] contributing significantly.

2.3.1.2.4 Tg vs. Tg

There were no significant differences between the CatD staining for any of the Tg mice at 5 weeks, but at 16 weeks the 5X cortex, striatum and thalamus had significantly more CatD staining than the 3X and the 2X, whereas only the 5X hippocampus region presented with more CatD staining than the 3X hippocampus. At 28 weeks, the 5X cortex, hippocampus and striatum DAB stain area was larger than those measured for 2X and 3X. At 60 weeks, the 5X cortex, hippocampus, striatum and thalamus stained areas were all larger compared to 2X and 3X. At this age, the 2X also presented significantly larger staining area in the cortex and hippocampus compared with the 3X.

2.3.1.2.5 CatD levels at different ages

The levels of DAB staining are shown in Fig. 2-3 over time. In Fig. 2-4, pseudo colour maps are used to show the lease-square linear fitting associated slopes indicating the "rate of change" in positive DAB staining in different brain regions over the age of the mouse (% DAB stain/ week of aging). In 2X mice, only the cortex and hippocampus presented significantly higher slopes than WT. In 3X, only the hippocampal CatD expression was significantly higher than that of WT mice. But both the hippocampal and cortex presented with significantly lower slopes than those calculated for 2X. Finally, all of 5X brain regions tested presented with significantly higher slopes than those of the corresponding 2X, 3X and WT brain regions. An interesting observation is that the 2X hippocampal and cortex slopes for CatD expression were higher than that for the $A\beta_{42}$ stain in the same brain region. Similarly, the 5X hippocampal slope for CatD expression was higher than the corresponding brain region $A\beta_{42}$ stain slope.

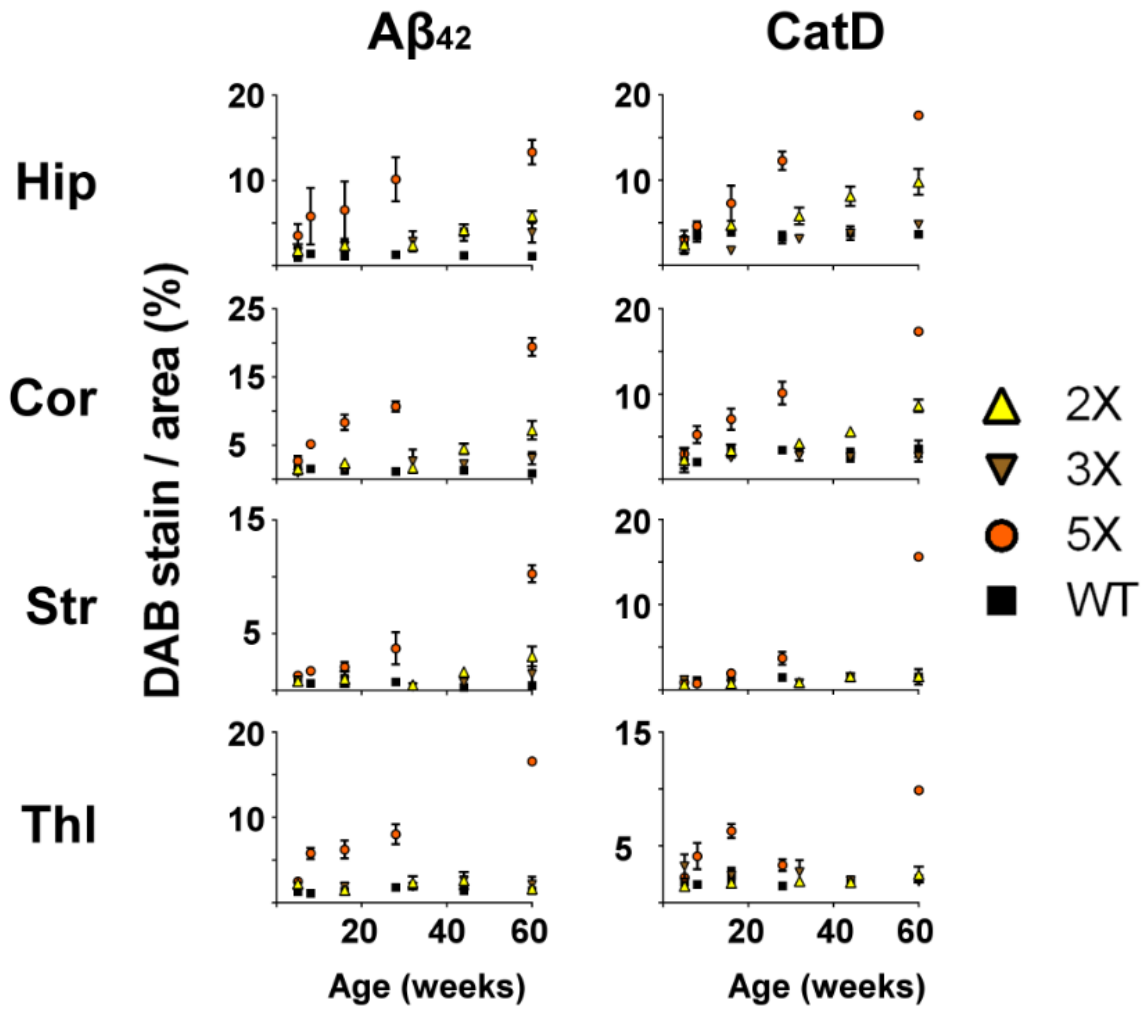

Figure 2-3 CatD and $A\beta_{42}$ positive Immunohistochemistry assessment in aging Tg and control WT mice levels at different ages (5-60 weeks). The average ± standard error of the mean is shown for N=3 mice for the indicated brain regions on the left, with the associated positive DAB staining for the respective antibody on top. Mice strains are indicated on the right (2X, yellow upright tringle; 3X brown upside-down triangle1 5X, red circle, and WT in black box).

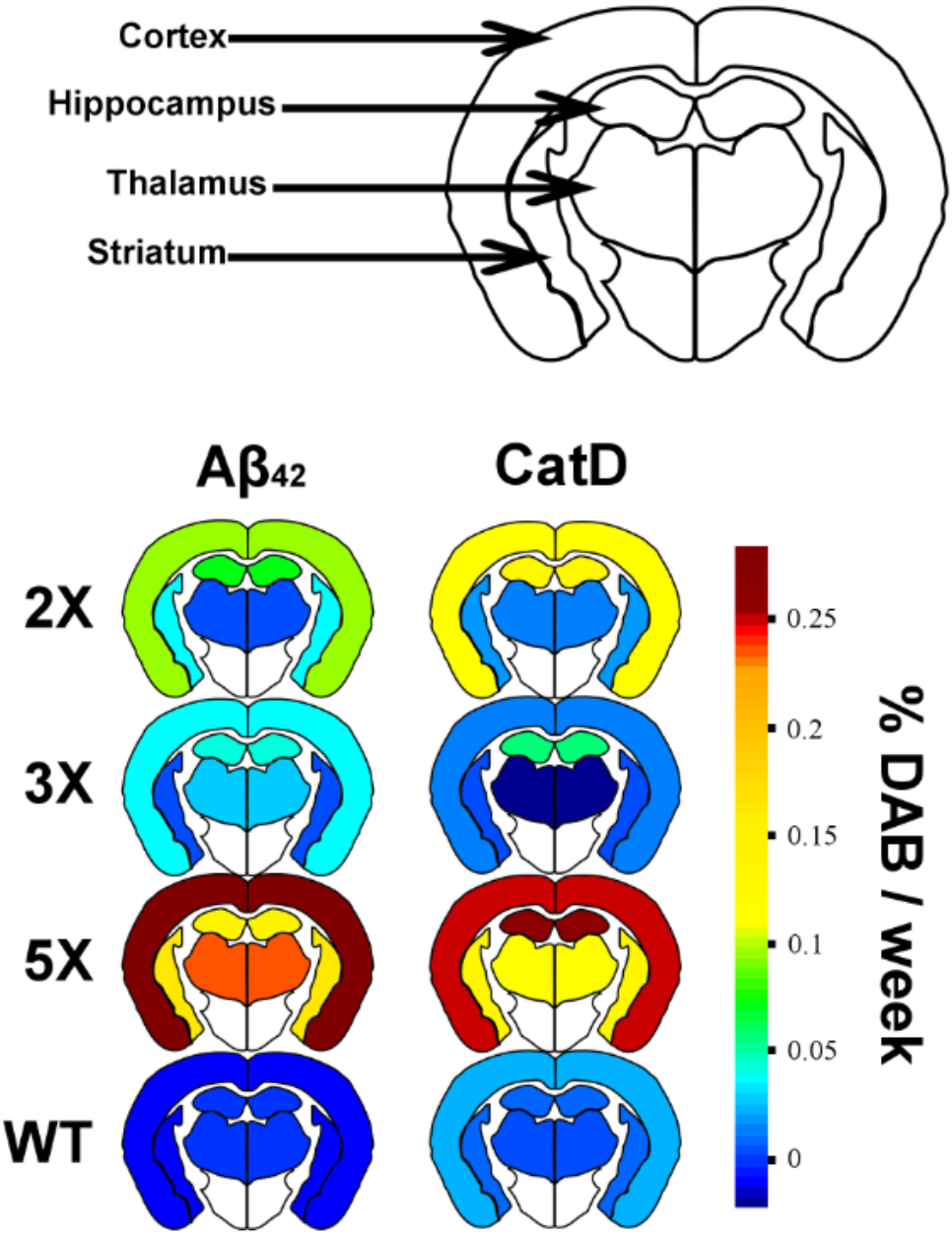

Figure 2-4 Estimated rate of change of DAB staining levels for all mice strains. Colour bar represents the slope of a least squares linear fit to the data in Fig. 2-3. Brain regions have been grossly countored and represent a broad generalization of the change in $A\beta_{42}$ and CatD expression within the associated brain regions. Brain regions are depicted in the top image, with indicated mouse strains on the left and antibody of interest at the top.

2.3.1.2.6 Cathepsin D Correlates With $A\beta_{42}$

When testing the correlation between the CatD staining and $A\beta_{42}$, we found the 2X cortex (p = 0.011; Pearson r = 0.957) as well as the hippocampus (p= 0.015; Pearson r = 0.947) were highly correlated. Only the hippocampus of the 3X mice presented a similar correlation (p = 0.019; Pearson r = 0.936). However, the 5X mice presented high correlation between CatD and $A\beta_{42}$ staining in the cortex (p < 0.001; Pearson r = 0.997), hippocampus (p = 0.001; Pearson r = 0.992), striatum (p < 0.001; Pearson r =0.997) and thalamus (p = 0.044; Pearson r =0.888).

2.3.2 Western Blots

Representative WB images are shown in Fig. 2-5 together with the associated plots showing longitudinal data for the three strains and three brain regions. Similar to the IHC analysis, the 5X mice consistently exhibited the highest level of expression of CatD compared to the other two Tg strains as well as the control WT mice at all time points.

Examining values for the 2X mice compared to age matched WT, no significant differences were noted in the cortex. In contrast, striatum 2X CatD expression was significantly higher and dependent on AD mutations [F (1, 20) = 21.38, p = .0002, η^2 = 0.315] as well as age [F (4, 20) = 3.274, p = .0322, η^2 = 0.193]. Lastly, hippocampal CatD expression was only significantly higher in 2X mice due to strain factor differences [F (1, 20) = 6.395, p = .02, η^2 = 0.191] since no age-based differences were observed. For specific ages, hippocampal CatD expression was not found to be significantly different between the 2X and the WT controls.

Examining the 3X mice, there were no significant differences with the WT mice at any specific time points when comparing cortex, striatum or hippocampus CatD expression. Overall though, the 3X striatum had significantly higher expression [F (1, 20) = 5.534, p = .029, η^2 = 0.099] with older mice having more CatD than younger ones [F (4, 20) = 3.327, p = .030, η^2 = 0.238]. Hippocampal CatD expression was also significantly higher in 3X mice [F (1, 20) = 7.472, p = .0128, η^2 = 0.154], with age

contributing significantly to the variability in CatD expression [F (4, 20) = 3.873, p = .0173, η^2 = 0.319].

Finally, 5X mice presented a consistent increase in CatD expression across all brain regions with age. Cortex CatD expression was significantly higher ($p < 0.05$) as measured in 5X mice compared to age-matched WT at 8 weeks (2.68 ± 0.88 vs 1.10 ± 0.13 AU) and 28 weeks (5.29 ± 1.74 vs 1.76 ± 0.53 AU). Two-way ANOVA indicated that strain factor was significant [F (1, 48) = 49.83, $p < .0001$, η^2 = 0.255] with 5X having overall higher CatD levels compared to WT age-matched controls. Age factor was also significant with older mice having higher CatD expressions [F (3, 48) = 19.91, $p < .0001$, η^2 = 0.306] compared to younger mice. The interaction of age and AD mutations was also significant [F (3, 48) = 12.58, $p < .0001$, η^2 = 0.193]. Similarly, CatD expression in the striatum was significantly higher with 5X older age; however only at 28 weeks did the 5X mice present with significantly higher CatD expression in the striatum (9.35 ± 5.83 vs 0.85 ± 0.46 AU; $p < .05$). Using two-way ANOVA, the 5X striatum is considered to have significantly higher CatD expression [F (1, 16) = 137.3, $p < .0001$, η^2 = 0.240] compared with WT age-matched controls. In addition, older mice presented significantly higher CatD expressions [F (3, 16) = 55.85, $p < .0001$, η^2 = 0.293] compared to younger mice. The interaction of age and AD mutations was also significant [F (3, 16) = 83.66, $p < .0001$, η^2 = 0.439]. Lastly, hippocampal CatD expression was significantly ($p <0.01$) higher at 16 (8.47 ± 1.67 vs 4.10 ± 1.17 AU) and 28 (8.44 ± 1.42 vs 3.88 ± 0.95 AU) weeks of age compared to age-matched WT controls with strain factor, not age, being the only significant contributor to the significant differences [F (1, 24) = 33.63, $p < .0001$, η^2 = 0.532].

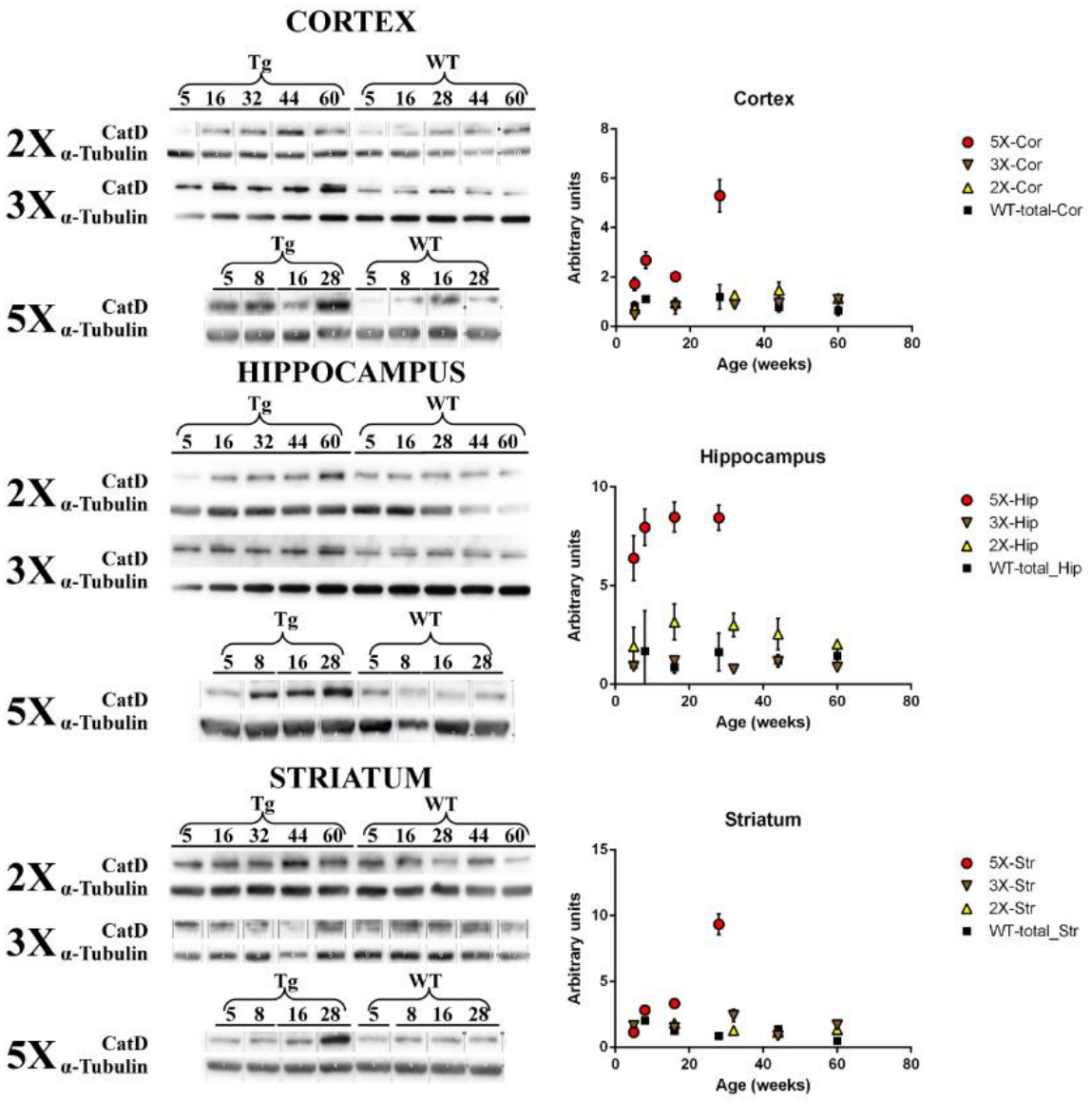

Figure 2-5 Western Blots analysis. Analysis of the amount of CatD protein expression in the three main associated regions of the Cortex, Hippocampus and Striatum is shown for the 2X, 3X, 5X and WT controls. Representative blots of N=3 are shown where both Tg and WT lanes are on the same blot with the CatD showing on top, and the loading control on the bottom. The 2X and 3X shared all common age time points but only 2 with the 5XFAD as shown. The associated change in protein quantification is plotted on the right handside with respective graphs for the three brain regions. Data is mean±standard error of the mean (N=3).

2.4 Discussion

In this study, we compare the levels of amyloid pathology across three different Tg strains of AD mice and WT mice, and compared these with the level of CatD. AD models as well as WT control were investigated at ages ranging from just over a month to one year after birth. The 2X, 3X and 5X Tg mouse models that were selected for this study have been investigated extensively to study the various aspects of early onset AD [18, 20, 21]. However, the pattern of progressive CatD expression over the age of mice has not been previously described across different strains. Here, we report for the first time, the quantitative analysis of CatD expression both by IHC and WB alongside the evaluation of $A\beta_{42}$ plaque burden in three main brain regions.

The three AD mice strains were selected because they show a range of pathology, with the 5XAD mice expected to show amyloid deposition more rapidly and more aggressively than the 2X mice, while the 3X mice were added to examine if Tau expression altered CatD expression. Unlike both the 2xTg and 3xTg, the 5XFAD mice do exhibit neuronal cell death by 9 months [18] and CatD over expression at a month younger age. The choice of C57Bl/6 as the control mouse strain was a compromise for the lack of better control (non-transgenic littermates) since all three Tg mice were established at least partially using this commonly used parental background mouse strain. These control mice are not known to develop AD pathology naturally; although they have been reported to develop age dependent hippocampal granular deposits similar to Tau pathology which were immunoreactive to Tau protein and alpha synuclein, but not to Aβ [23]. In addition, Lipofuscin can often be found in the hippocampus of these aging mice [24] but we did not suspect this to be a problem for our study.

Through the work presented herein, we showed that the levels of CatD expressed in several brain regions of Tg mice were significantly enhanced with age above the levels measured in younger mice, as well as above the levels of the age-matched wildtype controls (C57Bl/6). Furthermore, the 5X mouse model presented the highest levels of CatD expression, followed by the 2X, then the 3X and finally the lowest in WT controls. Three regions were examined for protein quantification using Western blots analysis

including the cerebral cortex, striatum, and hippocampus. The same three regions as well as the thalamus were also quantified by measuring the percent DAB staining by means of IHC. In addition to investigating the lysosomal enzymatic expression, measurements of the hallmark pathology of AD, namely $A\beta_{42}$, were also performed by IHC analysis. The dual-assay approach allowed us to uncover data undetected by the WB analysis as well as provide spatial understanding of the AD-like pathology developed in the Tg mice studied. The time course of plaque deposition and Cathepsin D staining in the mice is required to allow an optimized selection of the appropriate animal model for the purposes of testing CatD targeting contrast agents that may help with early diagnosis of AD.

Although there have been a number of observations of lysosomal upregulation in human AD brains [2-5, 25], it was not clear if lysosomal upregulation would be a uniform feature in mouse models. A few, previous studies have made the observation of lysosomal enzymes upregulation in the 5X mouse model [22, 26] which were in agreement with the human AD brains pathology. Enhancement of CatD expression has been argued to be the result of an enhanced neuronal expression, activated glial cells, or neuritic plaques [22]. But it remains unclear whether these changes in CatD expression are the cause of, or simply correlated to AD pathology as well as other neuropathological conditions where upregulation of lysosomal system activity (e.g. CatD expression) has been observed [5]. The lysosomal system (including CatD) has been shown to be involved in the production and degradation of $A\beta_{42}$ peptides [27-29]. But the enhancement of intracellular CatD in AD brains could be indicative of not only neurons involved in the production of the pathogenic $A\beta_{42}$ peptides [2, 5, 30] but also certain activated microglia that are involved in the deposition and/ or removal of the pathogenic peptides by phagocytic pathways [31-33]. These activated microglia as well as reactive astrocytes involved in modulation of toxicity and Aβ degradation, have been shown to be located around neuritic plaques [35, 36]. In addition, some microglia surrounding the neuritic plaques have shown to be positive for CatD expression [22]. The observation of elevated lysosomal enzymes in skin fibroblast from AD patients [34] suggests that lysosomal defects might be systemic in AD. Alternatively, a recent study suggests the accumulation of CatD in neurons first, followed by microglia and astrocytes, is associated both spatially and temporally with intracellular cholesterol accumulation and

neurodegeneration as was shown in a non-AD mouse model [37]. As for extracellular lysosomal enzymes, the origin of these in plaques remains unsettled. No loss of neurons has been reported in either 3X or 2X Tg mice lines used and so the measured CatD activity above base-line levels may likely be extracellular deposition of the lysosomal enzymes due to their release from intact cells or from vulnerable neurons attempting to regulate their environment [4]. In contrast, the 5X Tg mice used in this study have been shown to present neurodegeneration and neuronal loss [18] and therefore may have supplemental CatD staining originating from lysed neurons burdened with excessive intracellular $A\beta_{42}$ pathology, releasing their cytoplasmic contents into the extracellular space to form neuritic plaques [38].

On analyzing the $A\beta_{42}$ staining, there was a clear propensity for the 5X to stain positive compared with all other Tg mice as was seen by the early and progressive accumulation of plaques and intracellular accumulation of $A\beta_{42}$ in the hippocampus, cortex and thalamus over time. While the 3X mice presented with very limited extracellular $A\beta_{42}$ and plaque formation until the very last two time points (aged 44 and 60 weeks) this was in agreement with another longitudinal study of this strain showing progressive accumulation of extracellular $A\beta_{42}$ in plaques only at and after 12 months of age [39]. Our observation that CatD expression correlates with severity of AD pathology in the 5X mice (i.e. heavy lysosomal system involvement with heavy $A\beta_{42}$ positive plaques) is supported considering the 5X mice present a very aggressive pathology as well as CatD overexpression compared with 2X and 3X Tg mice. This coincides with previous observation that lysosomal receptors/ enzymes levels were enhanced profoundly in Tg mice, which exhibit high $A\beta_{42}$ levels and deposition [22]. Interestingly, and potentially important for future trials of CatD investigation as an AD biomarker, was the faster increase of CatD expression in the hippocampus of both 2X and 5X models as well as the cortex of 2X compared to the increase in $A\beta_{42}$ synthesis measured over the age of the mice.

A potential weakness of the study was the difference between antigen retrieval in IHC and protein processing in WB. Specifically, no formic acid was used in the tissue preparation for WB, and therefore it is likely that some CatD not solubilized and trapped

in insoluble plaque formations within the homogenized tissue lysates. This means the WB analysis could have a bias for under-estimating the amount of CatD available. Alternatively, while the pretreatment of AD tissues using formic acid for IHC enhances the immunological detection of extracellular plaques, it might have an opposing effect on intracellular Aβ peptides [40]. In addition, the different Tg mice express different mutations, and therefore could have produced different formation of oligomers and consequentially differently formed plaques that as consequence could require separate optimization for staining using the same $A\beta_{42}$ antibody. Finally, considering the report of 3X mice developing plaques as early as 6 months, the location of our IHC investigation was concentrated on a more posterior region that allowed the visualization of the striatum (caudoputamen), the thalamus, the cortex (isocortex) and the hippocampal formation. It is therefore possible that the earlier pathology reported by others [16, 21, 41] was missed.

In summary, we report a significantly progressive accumulation of CatD in both intracellular compartments as well as extracellular plaques in the 5X mouse model correlated to an aggressive $A\beta_{42}$ pathology. This was mirrored but to a lesser extent in our findings from the 2X mouse model. The 3X mouse model presented a smaller distribution of plaques within the examined areas and reduced CatD expression compared with the age-matched 5X and 2X counterparts. Overall, CatD expression depended on both AD mutations load and age. These studies demonstrate that CatD lysosomal enzyme expression correlates with AD pathology, showing that CatD may be a suitable biomarker for following AD progression.

2.5 Acknowledgments

The authors gratefully acknowledge student stipend support donated by William Shipman and from the Alzheimer Society of London and Middlesex, the Queen Elizabeth II Graduate Scholarships in Science and Technology and the Ontario Graduate Scholarships. In addition, the authors thank Zengxaun Nong and Caroline O'Neil for their superb technical support with histology and staining expertise. Lastly, funding for this study was provided by the Canadian Institutes of Health Research (MOP-106535).

2.6 References

[1] 2014 Alzheimer's disease facts and figures, *Alzheimers Dement*, **10** (2014), e47-92.

[2] A.M. Cataldo, J.L. Barnett, S.A. Berman, J. Li, S. Quarless, S. Bursztajn, C. Lippa and R.A. Nixon, Gene expression and cellular content of cathepsin D in Alzheimer's disease brain: evidence for early up-regulation of the endosomal-lysosomal system, *Neuron*, **14** (1995), 671-680.

[3] A.L. Schwagerl, P.S. Mohan, A.M. Cataldo, J.P. Vonsattel, N.W. Kowall and R.A. Nixon, Elevated levels of the endosomal-lysosomal proteinase cathepsin D in cerebrospinal fluid in Alzheimer disease, *J Neurochem*, **64** (1995), 443-446.

[4] A.M. Cataldo, P.A. Paskevich, E. Kominami and R.A. Nixon, Lysosomal hydrolases of different classes are abnormally distributed in brains of patients with Alzheimer disease, *Proc Natl Acad Sci U S A*, **88** (1991), 10998-11002.

[5] R.A. Nixon, A.M. Cataldo and P.M. Mathews, The endosomal-lysosomal system of neurons in Alzheimer's disease pathogenesis: a review, *Neurochem Res*, **25** (2000), 1161-1172.

[6] E.M. Strome and D.J. Doudet, Animal models of neurodegenerative disease: insights from in vivo imaging studies, *Mol Imaging Biol*, **9** (2007), 186-195.

[7] J. Chin, Selecting a mouse model of Alzheimer's disease, *Methods Mol Biol*, **670** (2011), 169-189.

[8] D. Games, D. Adams, R. Alessandrini, R. Barbour, P. Berthelette, C. Blackwell, T. Carr, J. Clemens, T. Donaldson, F. Gillespie and et al., Alzheimer-type neuropathology in transgenic mice overexpressing V717F beta-amyloid precursor protein, *Nature*, **373** (1995), 523-527.

[9] K. Duff, C. Eckman, C. Zehr, X. Yu, C.M. Prada, J. Perez-tur, M. Hutton, L. Buee, Y. Harigaya, D. Yager, D. Morgan, M.N. Gordon, L. Holcomb, L. Refolo, B. Zenk, J. Hardy and S. Younkin, Increased amyloid-beta42(43) in brains of mice expressing mutant presenilin 1, *Nature*, **383** (1996), 710-713.

[10] L. Holcomb, M.N. Gordon, E. McGowan, X. Yu, S. Benkovic, P. Jantzen, K. Wright, I. Saad, R. Mueller, D. Morgan, S. Sanders, C. Zehr, K. O'Campo, J. Hardy, C.M. Prada, C. Eckman, S. Younkin, K. Hsiao and K. Duff, Accelerated Alzheimer-type phenotype in transgenic mice carrying both mutant amyloid precursor protein and presenilin 1 transgenes, *Nat Med*, **4** (1998), 97-100.

[11] T. Hryciw, J.I. MacDonald, R. Phillips, C. Seah, S. Pasternak and S.O. Meakin, The fibroblast growth factor receptor substrate 3 adapter is a developmentally regulated microtubule-associated protein expressed in migrating and differentiated neurons, *J Neurochem*, **112** (2010), 924-939.

[12] B.H. Jackson Laboratories, ME, USA, Alzheimer's Disease Mouse Model Strains, Vol. 2015.

[13] J.L. Jankowsky, D.J. Fadale, J. Anderson, G.M. Xu, V. Gonzales, N.A. Jenkins, N.G. Copeland, M.K. Lee, L.H. Younkin, S.L. Wagner, S.G. Younkin and D.R. Borchelt, Mutant presenilins specifically elevate the levels of the 42 residue beta-amyloid peptide in vivo: evidence for augmentation of a 42-specific gamma secretase, *Hum Mol Genet*, **13** (2004), 159-170.

[14] A. Volianskis, R. Kostner, M. Molgaard, S. Hass and M.S. Jensen, Episodic memory deficits are not related to altered glutamatergic synaptic transmission and plasticity in the CA1 hippocampus of the APPswe/PS1deltaE9-deleted transgenic mice model of ss-amyloidosis, *Neurobiol Aging*, **31** (2010), 1173-1187.

[15] W. Zhang, J. Hao, R. Liu, Z. Zhang, G. Lei, C. Su, J. Miao and Z. Li, Soluble Abeta levels correlate with cognitive deficits in the 12-month-old APPswe/PS1dE9 mouse model of Alzheimer's disease, *Behav Brain Res*, **222** (2011), 342-350.

[16] S. Oddo, A. Caccamo, M. Kitazawa, B.P. Tseng and F.M. LaFerla, Amyloid deposition precedes tangle formation in a triple transgenic model of Alzheimer's disease, *Neurobiol Aging*, **24** (2003), 1063-1070.

[17] S. Oddo, A. Caccamo, L. Tran, M.P. Lambert, C.G. Glabe, W.L. Klein and F.M. LaFerla, Temporal profile of amyloid-beta (Abeta) oligomerization in an in vivo model of Alzheimer disease. A link between Abeta and tau pathology, *J Biol Chem*, **281** (2006), 1599-1604.

[18] H. Oakley, S.L. Cole, S. Logan, E. Maus, P. Shao, J. Craft, A. Guillozet-Bongaarts, M. Ohno, J. Disterhoft, L. Van Eldik, R. Berry and R. Vassar, Intraneuronal beta-amyloid aggregates, neurodegeneration, and neuron loss in transgenic mice with five familial Alzheimer's disease mutations: potential factors in amyloid plaque formation, *J Neurosci*, **26** (2006), 10129-10140.

[19] P. Benes, V. Vetvicka and M. Fusek, Cathepsin D--many functions of one aspartic protease, *Crit Rev Oncol Hematol*, **68** (2008), 12-28.

[20] M. Garcia-Alloza, E.M. Robbins, S.X. Zhang-Nunes, S.M. Purcell, R.A. Betensky, S. Raju, C. Prada, S.M. Greenberg, B.J. Bacskai and M.P. Frosch, Characterization of amyloid deposition in the APPswe/PS1dE9 mouse model of Alzheimer disease, *Neurobiol Dis*, **24** (2006), 516-524.

[21] S. Oddo, A. Caccamo, J.D. Shepherd, M.P. Murphy, T.E. Golde, R. Kayed, R. Metherate, M.P. Mattson, Y. Akbari and F.M. LaFerla, Triple-transgenic model of Alzheimer's disease with plaques and tangles: intracellular Abeta and synaptic dysfunction, *Neuron*, **39** (2003), 409-421.

[22] A. Amritraj, C. Hawkes, A.L. Phinney, H.T. Mount, C.D. Scott, D. Westaway and S. Kar, Altered levels and distribution of IGF-II/M6P receptor and lysosomal enzymes in mutant APP and APP + PS1 transgenic mouse brains, *Neurobiol Aging*, **30** (2009), 54-70.

[23] K.L. Krass, V. Colinayo, A. Ghazalpour, H.V. Vinters, A.J. Lusis and T.A. Drake, Genetic loci contributing to age-related hippocampal lesions in mice, *Neurobiol Dis*, **13** (2003), 102-108.

[24] C.H. Lamar, G.A. McKinley and E.J. Hinsman, The fine structure of lipofuscin in the mouse hippocampus, *Anat Anz*, **147** (1980), 215-219.

[25] L.M. Callahan, W.A. Vaules and P.D. Coleman, Quantitative decrease in synaptophysin message expression and increase in cathepsin D message expression in Alzheimer disease neurons containing neurofibrillary tangles, *J Neuropathol Exp Neurol*, **58** (1999), 275-287.

[26] K.L. Youmans, L.M. Tai, T. Kanekiyo, W.B. Stine, Jr., S.C. Michon, E. Nwabuisi-Heath, A.M. Manelli, Y. Fu, S. Riordan, W.A. Eimer, L. Binder, G. Bu, C. Yu, D.M. Hartley and M.J. LaDu, Intraneuronal Abeta detection in 5xFAD mice by a new Abeta-specific antibody, *Mol Neurodegener*, **7** (2012), 8.

[27] E.A. Mackay, A. Ehrhard, M. Moniatte, C. Guenet, C. Tardif, C. Tarnus, O. Sorokine, B. Heintzelmann, C. Nay, J.M. Remy, J. Higaki, A. Van Dorsselaer, J. Wagner, C. Danzin and P. Mamont, A possible role for cathepsins D, E, and B in the processing of beta-amyloid precursor protein in Alzheimer's disease, *Eur J Biochem*, **244** (1997), 414-425.

[28] S.A. Frautschy, D.L. Horn, J.J. Sigel, M.E. Harris-White, J.J. Mendoza, F. Yang, T.C. Saido and G.M. Cole, Protease inhibitor coinfusion with amyloid beta-protein results in enhanced deposition and toxicity in rat brain, *J Neurosci*, **18** (1998), 8311-8321.

[29] J.R. McDermott and A.M. Gibson, Degradation of Alzheimer's beta-amyloid protein by human cathepsin D, *Neuroreport*, **7** (1996), 2163-2166.

[30] R.A. Nixon, P.M. Mathews and A.M. Cataldo, The neuronal endosomal-lysosomal system in Alzheimer's disease, *J Alzheimers Dis*, **3** (2001), 97-107.

[31] D. Morgan, Modulation of microglial activation state following passive immunization in amyloid depositing transgenic mice, *Neurochem Int*, **49** (2006), 190-194.

[32] D.M. Paresce, H. Chung and F.R. Maxfield, Slow degradation of aggregates of the Alzheimer's disease amyloid beta-protein by microglial cells, *J Biol Chem*, **272** (1997), 29390-29397.

[33] J. Wegiel, K.C. Wang, H. Imaki, R. Rubenstein, A. Wronska, M. Osuchowski, W.J. Lipinski, L.C. Walker and H. LeVine, The role of microglial cells and astrocytes in

fibrillar plaque evolution in transgenic APP(SW) mice, *Neurobiol Aging*, **22** (2001), 49-61.

[34] L. Urbanelli, C. Emiliani, C. Massini, E. Persichetti, A. Orlacchio, G. Pelicci, S. Sorbi, A. Hasilik and G. Bernardi, Cathepsin D expression is decreased in Alzheimer's disease fibroblasts, *Neurobiol Aging*, **29** (2008), 12-22.

[35] M.R. Domenici, S. Paradisi, B. Sacchetti, S. Gaudi, M. Balduzzi, A. Bernardo, M.A. Ajmone-Cat, L. Minghetti and F. Malchiodi-Albedi, The presence of astrocytes enhances beta amyloid-induced neurotoxicity in hippocampal cell cultures, *J Physiol Paris*, **96** (2002), 313-316.

[36] T. Wyss-Coray, J.D. Loike, T.C. Brionne, E. Lu, R. Anankov, F. Yan, S.C. Silverstein and J. Husemann, Adult mouse astrocytes degrade amyloid-beta in vitro and in situ, *Nat Med*, **9** (2003), 453-457.

[37] G. Liao, Y. Yao, J. Liu, Z. Yu, S. Cheung, A. Xie, X. Liang and X. Bi, Cholesterol accumulation is associated with lysosomal dysfunction and autophagic stress in Npc1 -/- mouse brain, *Am J Pathol*, **171** (2007), 962-975.

[38] M.R. D'Andrea, R.G. Nagele, H.Y. Wang, P.A. Peterson and D.H. Lee, Evidence that neurones accumulating amyloid can undergo lysis to form amyloid plaques in Alzheimer's disease, *Histopathology*, **38** (2001), 120-134.

[39] S.L. Montgomery, M.A. Mastrangelo, D. Habib, W.C. Narrow, S.A. Knowlden, T.W. Wright and W.J. Bowers, Ablation of TNF-RI/RII expression in Alzheimer's disease mice leads to an unexpected enhancement of pathology: implications for chronic pan-TNF-alpha suppressive therapeutic strategies in the brain, *Am J Pathol*, **179** (2011), 2053-2070.

[40] T.A. Bayer and O. Wirths, Intracellular accumulation of amyloid-Beta - a predictor for synaptic dysfunction and neuron loss in Alzheimer's disease, *Front Aging Neurosci*, **2** (2010), 8.

[41] L.M. Billings, S. Oddo, K.N. Green, J.L. McGaugh and F.M. LaFerla, Intraneuronal Abeta causes the onset of early Alzheimer's disease-related cognitive deficits in transgenic mice, *Neuron*, **45** (2005), 675-688.

Chapter 3

3 Prolonged in-vivo retention of a Cathepsin D targeted optical contrast agent in a mouse model of Alzheimer's disease

Jonatan A. Snir[a,b], Mojmir Suchy[b,c], Keith St. Lawrence[a,d], Robert H.E. Hudson[c], Stephen H. Pasternak[e,f] and Robert Bartha[a,b]

[a]Department of Medical Biophysics, University of Western Ontario, London, Ontario, Canada,

[b]Centre for Functional and Metabolic Mapping, Robarts Research Institute, University of Western Ontario, London, Ontario, Canada

[c]Department of Chemistry, University of Western Ontario, London, Ontario, Canada,

[d]Medical Imaging, Lawson Health Research Institute, London, Ontario, Canada

[e]J. Allyn Taylor Centre for Cell Biology, Molecular Brain Research Group, Robarts Research Institute, University of Western Ontario, London, Ontario, Canada,

[f]Department of Clinical Neurological Sciences, Schulich School of Medicine, University of Western Ontario, London, Ontario, Canada

3.1 Introduction

An estimated 115 million people will have dementia by 2050 worldwide with Alzheimer's disease (AD) being the most common cause [1]. The first description of AD over a century ago highlighted neurofibrillary tangle (NFT) and amyloid plaque accumulation [2] as two pathological changes associated with the disease. These have remained central to the post mortem confirmation and definitive diagnosis of AD to this day; however, the development of AD involves many subcellular and morphological features associated with loss of synapses [3], mitochondrial dysfunction and oxidative stress [4] and neuro-vasculature disruption [5, 6]. Currently, diagnosis of AD is based upon clinical assessment and although biomarkers have been proposed, these are not uniformly recommended for clinical use. This problem has taken on urgency, as several promising clinical trials may have failed, because treatment was initiated too late in the disease, when irreversible synaptic and neuronal loss had already occurred [7-11].

The development of imaging biomarkers provides a means to non-invasively detect brain changes associated with AD to monitor disease progression and the effects of treatment. Imaging biomarkers include brain structural changes [12], blood flow [13, 14], function [15], and glucose utilization [16, 17]. Recently, positron emission tomography (PET) imaging with the ^{11}C-labelled Pittsburgh compound B, or PIB [18] has provided insight into the accumulation of amyloid pathology in the brain. PIB binding correlates with cerebral atrophy [19], it inversely correlates with cerebral glucose metabolism [20], and it strongly relates to the degree of memory impairment [21]. However, some studies have also shown PIB uptake in a significant proportion of non-demented elderly controls [22]. Moreover, many anti-amyloid treatments have failed in clinical trials and therefore interest in NFT pathology has intensified [23]. Imaging this biomarker, an aggregate of hyperphosphorylated Tau protein, could provide important information about the course of the disease [24]. Novel ligands targeting NFT have shown promise in murine models of AD [25, 26] and more recently in humans [27, 28]. Currently, however, the aforementioned biomarkers are hampered by variability and are frequently positive in normal older patients [7, 23, 29] sometimes more than 15 years before clinical symptoms [30].

One possible novel biomarker for AD is Cathepsin D (CatD). CatD is a lysosomal aspartic endopeptidase (EC 3.4.23.5) involved in normal protein turnover associated with tissue homeostasis including tissue renewal, remodeling, and regulation of aging and programmed cell death [31]. However, CatD is elevated within brain parenchyma and the cerebrospinal fluid of AD patients and active CatD is present at high levels in amyloid plaques [32-34]. In addition, increased expression of CatD has been proposed to be the earliest histopathological feature of AD [33]. Therefore, there is increasing interest in developing molecular imaging techniques targeting CatD for the early diagnosis of AD [35].

Animal models provide a consistent platform for testing early diagnostic techniques and can provide insight into the etiology and pathophysiology of human neurodegenerative diseases [36]. Transgenic (Tg) mice are the most common model of AD, while very few rat [37], and even fewer non-human primate models exist [37-39]. Although many different Tg mouse strains are available, the 5XFAD model [40] has several key features requisite for AD modeling. These mice rapidly accumulate cerebral pathogenic amyloid protein (Aβ) that begins at two months and reaches a very large burden by nine months. They are also characterized by hippocampal synaptic dysfunction as early as six months [41], and impaired memory as well as neuronal loss and synaptic degeneration by nine months that worsens by 12 months [40]. Furthermore, previous work using this strain showed co-localization of the CatD enzyme with intra-lysosomal Aβ aggregates at one month of age [42] and increased CatD expression compared to non-transgenic controls at 3.5 months [43]. The latter suggests that this strain is an appropriate platform for investigating contrast agents (CA) targeting CatD.

The passage of molecules from the circulation across the blood brain barrier (BBB) into the brain is highly selective, making drug delivery difficult [44-47]. Most CAs do not normally cross the BBB unless it is damaged. One strategy to deliver contrast agents into the brain is to use cell penetrating peptides (CPP) [48]. One CPP is derived from Tat peptide (YGRKKRRQRRR) of the HIV-1 virus, which allows transport both into and out of the brain [48]. This CPP has been explored for drug delivery [49] as well as cellular delivery of CAs [50]. It is believed that hydrophilic arginine-rich CPPs

such as HIV-1 Tat may be transported across membranes by direct penetration at high concentrations [51], and by endocytosis at lower concentrations [52], although there is no consensus on the mechanism of uptake and maintenance of functionality of cargos after delivery [53].

We have previously described a dual modality (MRI and fluorescence) CatD targeted CA consisting of an imaging moiety conjugated to a peptide composed of a CatD cleavage site and a CPP [54, 55]. The CPP allows transport across membranes bidirectionally. In regions with increased CatD activity, cleavage at the CatD site removes the CPP, causing prolonged retention of the imaging moiety. Because each CatD enzyme molecule can cleave many substrate CA molecules, this strategy potentially offers amplification compared to contrast agents that depend on target binding. We have shown that this CA is taken up preferentially by cultured cells overexpressing CatD [54]. In addition, it exhibited a distinct difference in uptake and retention over a two-hour period post administration in an APPswe, PSEN1dE9 Tg mouse model compared to wild-type mice in *ex-vivo* studies [55]. In the current study, we have conjugated this agent with IRDye800, a near infra-red (NIR) fluorescent dye that can be detected though several centimeters of tissue [56] and exhibits a much higher fluorescence than the commonly used NIR dye indocyanine green [57]. This fluorophore has increased stability in blood [58] and is non-toxic at doses up to ~428 nmol [59]. As little as 5 pmol [58, 60] of this dye is required for detection in rodents. This new agent is suited for *in-vivo*, non-invasive optical imaging to examine CA washout kinetics following intravenous (IV.) administration in small animals as a proof of concept, but will naturally fall short in its applicability in the clinic due to the significantly thicker human skull.

The objective of this study was to evaluate the uptake and washout kinetics of the newly modified CA in vivo in 5XFAD transgenic AD and wild-type (WT) control mice using NIR optical imaging. We hypothesized that the agent would be preferentially retained in the brain of 5XFAD Tg mice compared to WT mice. To better understand the mechanism of uptake of this agent we compared washout kinetics for three similar CAs in 12 month old 5XFAD and WT mice: 1) a diagnostic CatD Targeted agent having an imaging moiety, a CatD cleavage site and a CPP, 2) a control Non-Penetrating agent

having an imaging moiety, an incomplete CatD cleavage site lacking the CPP, and 3) a control Non-Targeted agent having only an imaging moiety and a CPP but no CatD cleavage site. Here we show that the cell penetrating CatD Targeted CA is taken up and retained more efficiently in the brain than the Non-Penetrating and Non-Targeted agents, and that this agent can distinguish AD mice from wild type mice at 5 months and 12 months of age.

3.2 Materials and Methods

3.2.1 CA synthesis and characterization

The IRDye800 from LI-COR Biosciences (Lincoln, NE, USA) was chosen for NIR detection (part of the detection probe along with the chelated Gd^{3+} lanthanide metal). Peptide sequences were assembled on a Wang resin using a standard solid phase peptide synthesis protocol (59). Conjugation of DOTA-derived terminal monomer and subsequent HPLC purification of peptides **1a-c** was performed as previously described [54, 55] (Fig. 3-1). In separate reaction vessels (Falcon tubes) peptides **1a** (4.2 mg, 1.2×10^{-6} mol), **1b** (0.7 mg, 3.0×10^{-7} mol) and **1c** (2.7 mg, 1.5×10^{-6} mol) were treated with the solution of IRDye 800CW maleimide (**2**; 1.4 mg, 1.2×10^{-6} mol, peptide **1a**; 0.4 mg, 3.0×10^{-7} mol, peptide **1b**; 1.8 mg, 1.5×10^{-6} mol, peptide **1c**) in acetonitrile (200 μL, peptide **1a**; 100 μL, peptide **1b**; 400 μL, peptide **1c**) and water (1 mL, peptide **1a**; 400 μL, peptide **1b**; 1.6 mL, peptide **1c**). The tubes were set aside for 48 h at room temperature in the dark (wrapped in the Al foil). The solvents were removed by lyophilization, the residues were dissolved in acetonitrile (200 μL, peptide **1a**; 50 μL, peptide **1b**; 300 μL, peptide **1c**) and water (1 mL, peptide **1a**; 100 μL, peptide **1b**; 300 μL, peptide **1c**) and 0.1 M solution of $GdCl_3 \cdot 6H_2O$ (38 μL, 3.8×10^{-6} mol, peptide **1a**; 10 μL, 1.0×10^{-6} mol, peptide **1b**; 30 μL, 3.0×10^{-6} mol, peptide **1c**) was added. The tubes were set aside for another 48 h at room temperature in the dark (wrapped in Al foil). The solvents were removed by lyophilization, the residues were dissolved in water and were purified by dialysis (for 5 days) using a membrane with a molecular weight cut-off of 500 Da. The solutions were lyophilized to produce the desired peptides **3a-c** as

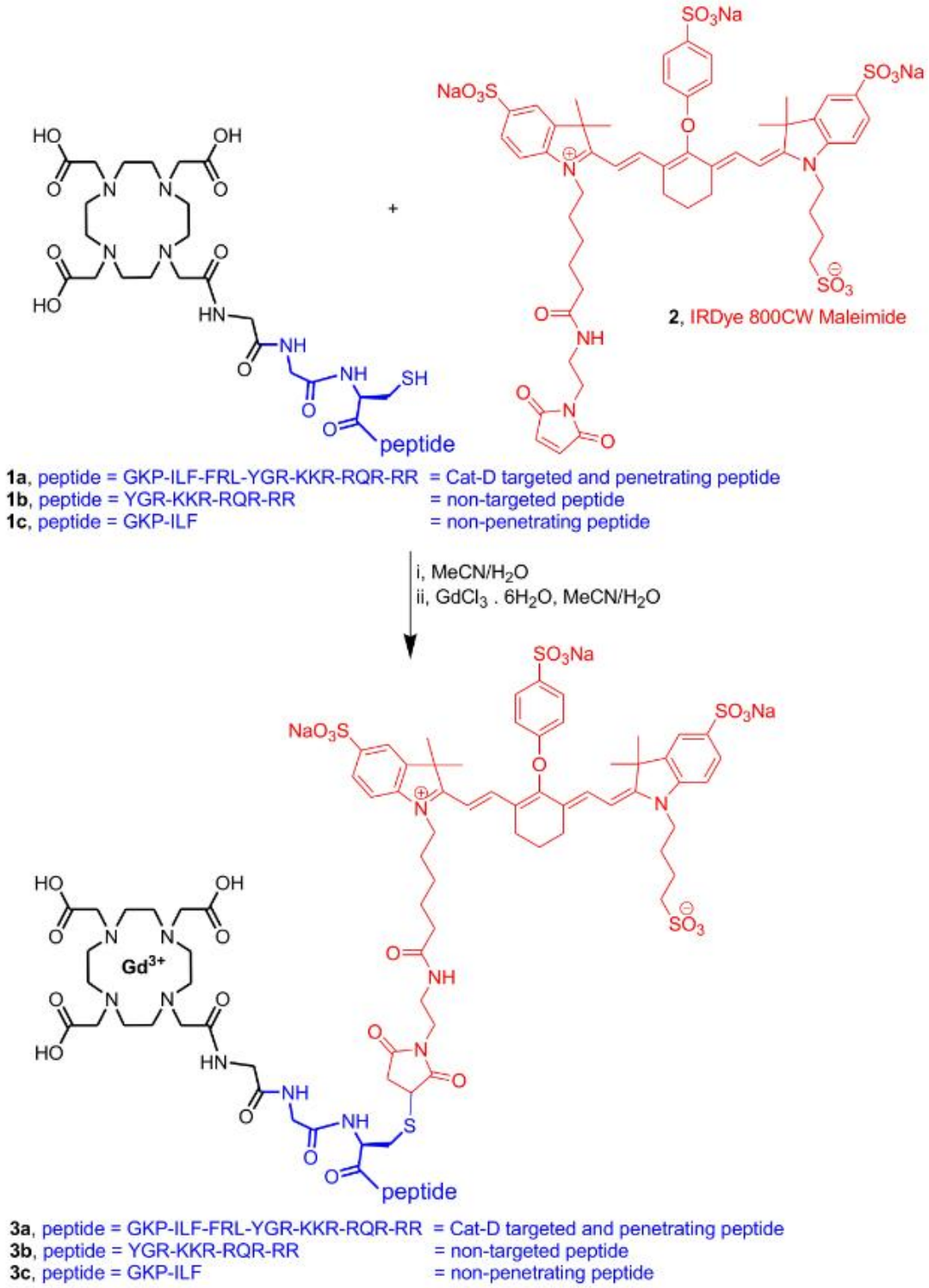

Figure 3-1. Synthesis of the different CAs. CatD Targeted (3a), Non-Targeted (3b) and Non-Penetrating (3c) conjugates used in this study

green solids. The conjugates were characterized by high resolution electrospray ionisation mass spectrometry (HR-ESI-MS) as follows:

Conjugate **3a** (1.9 mg, 35%), HRMS (ESI) *m/z*: found 4512.0560 $[M-2H]^+$ (4512.0456 calculated for $C_{194}H_{299}N_{56}O_{49}S_5Gd$).

Conjugate **3b** (0.9 mg, 90%), HRMS (ESI) *m/z*: found 3387.3570 $[M-2H]^+$ (3387.3615 calculated for $C_{137}H_{210}N_{42}O_{39}S_5Gd$).

Conjugate **3c** (4.2 mg, 78%), HRMS (ESI) *m/z*: found 2584.8555 (formic acid adduct) $[M-2H]^+$ (2584.8543 calculated for $C_{110}H_{152}N_{18}O_{34}S_5Gd$).

The three conjugates were named according to their functional characteristics: Conjugate **3a** (Fig. 3-1) was dubbed the CatD Targeted or diagnostic CA (having a CatD cleavage site and a CPP), conjugate **3b** (Fig. 3-1) was dubbed the Non-Targeted CA (having only a CPP), and conjugate **3c** (Fig. 3-1) was dubbed the Non-Penetrating CA (having only a partial CatD cleavage site, similar to what remains following cleavage by an active CatD enzyme).

3.2.2 CA optical properties

Optical properties were characterized using a SpectraMax M5 spectorphotometer plate reader (Molecular Dynamics Devices, Sunnyvale, CA USA). The optimal excitation wavelength of our CA was determined for emission at 845 nm using excitation between 600 to 820 nm (no cut-off filter, high precision reading, and 2 nm step size). The optimal emission wavelength was made at wavelengths ranging from 790 to 850 nm following excitation at 780 nm. To control for backscatter and lamp light contamination, the purified milli-Q water fluorescence values were subtracted from all other measurements. Furthermore, to measure CA fluorescence following cleavage with the targeted enzyme (C3138-10UN; Sigma-Aldrich Canada Co. Oakville, Ontario), 25 µM solutions of either CatD targeted, non-penetrating, or non-targeted CA were maintained at 37°C and a low pH (~4.5) to replicate in-vivo lysosomal conditions. Six wells were used to test each CatD targeted CA but three wells also included the CatD enzyme (0.7 µM) incubated

with the CA for ~30 minutes. Additionally, the fluorescent signal from each sample was measured as a function of time using the eXplore Optix system (GE Healthcare, Milwaukee, Wisconsin). The fluorescence signal was examined in both the eXplore Optix system and the SpectraMax M5 Molecular Devices plate reader by measuring the signal from 1.35, 2.75, 5.5 and 11µM concentrations of the CA corresponding to 0.27, 0.55, 1.1 and 2.2 nmol respectively. These solutions were placed in a black solid Costar 96-well plate (Corning Life Science, Tewksbury MA USA).

3.2.3 Animals

All animal studies were conducted in accordance with the guidelines of the Subcommittee on Animal Care at Western University, conformed to the Canadian Council on Animal Care guide for the care and use of laboratory animals as well as the ARRIVE guidelines. B6SJL-Tg (APPSwFlLon, PSEN1*M146L*L286V) 6799 Vas/Mmjax transgenic mice, commonly known as the 5XFAD line Tg6799 of a C57Bl/6 and B6SJL hybrid background and age-matched wild type C57Bl/6 (both from Jackson Laboratories, Bar Harbor, ME, USA) were used for this study. The 5XFAD mice overexpress human APP(695) with the Swedish (K670N, M671L), Florida (I716V), and London (V717I) Familial Alzheimer's Disease (FAD) mutations and the human PS1 gene harboring two FAD mutations, namely, M146L and L286V [43].

There was no significant difference in average mouse weight (5XFAD: 23.1 ± 1.6g; WT: 23.5 ± 2.5g) between the groups at five months, however at 12 months, the body weight of the 5XFAD mice (23 ± 1.5g) was significantly lower ($p<0.05$) than the WT mice (31 ± 1.9g).

3.2.4 Experimental Design

To examine whether the CatD Targeted diagnostic CA could be used to differentiate between old 5XFAD mice having progressive disease pathology and old yet healthy control mice, six (N=6) 5XFAD and six (N=6) age-matched WT (C57Bl/6) control mice were studied at 12 months of age. To determine whether observed differences could be attributed to the targeting and BBB penetrating moieties attached to

the CA, the uptake and washout of the three different CA versions were compared. The ability of the CatD Targeted CA to differentiate between the 5XFAD and WT control mice at an earlier disease stage was also studied at five months of age.

3.2.5 Optical Imaging

Animals were kept warm (~37°C) using a latex glove containing warm water placed over the lower back and extremities. The warm water was replaced every 10 minutes. Two animals were scanned simultaneously using a Y-shape nose cone for isofluorane anesthesia with a scavenger system connected to a charcoal filter. Hair was removed from the scalp using an electric razor, and depilatory agent (e.g Nair; Brookvale Australia) prior to optical imaging. All mice received an intravenous injection of 5 nmol CA suspended in 200 µL PBS through a tail catheter. One (N=1) 5 month old 5XFAD mouse received a subcutaneous (sc) injection in the flank to examine the time delay for peak fluorescent signal.

Optical imaging was performed using the eXplore Optix system (GE Healthcare, Milwaukee, Wisconsin); a reflectance-based, raster scanning, time domain optical imaging system with a 3 mm source–detector distance. An 80 MHz, 780 nm pulsed diode laser (picoQuant, Berlin, Germany) was employed with a 10 nm FWHM bandpass excitation filter centered at 780 nm (Thorlabs, Newton, New Jersey). Light was collected with a 55 nm FWHM bandpass excitation filter centered at 845 nm (Chroma Technology Corp., Bellows Falls, Vermont). The maximum power output of the laser at the surface of the sample or animal did not exceed 10 µW, and signal was collected with an integration time of 100 ms resulting in an image acquisition time of ~2 minutes. Images were acquired for a maximum duration of 4.5 hours (270 minutes), with a variable temporal step size depending on the magnitude of the observed signal changes. The horizontal level of heads of both animals was manually adjusted to be of equal distance to the detector. Optimization was performed prior to execution of the experiment as well as considerations to utilize the time-domain imaging capacity of the scanner as is shown in Appendix 2. However, only the intensity of the light (amplitude) was considered for purposes of this preliminary work.

3.2.6 Optical Signal Analysis

All optical signal data were recorded as photon counts per second for each pixel. Optical signal maps were analyzed using ImageJ 1.46r (National Institutes of Health U.S.A). Statistical analysis was performed using Prism 5 (GraphPad Software, Inc. CA USA). The average fluorescence signal (average pixel intensity ± standard deviation) time course from within a selected region of interest (ROI) was used for analysis. Unless otherwise stated, the ROI was drawn around only the head region visualized under plain white light (WL). The baseline signal amplitude was centered at zero by subtracting the background signal measured prior to the injection of agent. To equalize the step sizes, a piecewise cubic Hermite interpolation was applied to the data and binned into 1 minute intervals using MATLAB (The MathWorks, Inc., Natick, Massachusetts, United States.). For all parameters excluding the absolute peak enhancement values, the CA signal was normalized to the maximum intensity. The CA washout following maximum peak enhancement was modeled and fitted using a least squares minimization method in Prism. The model function incorporated a constant maximum enhancement period followed by a one phase exponential decay [Eq 1] to determine the washout coefficient (λ_{Total}) and asymptote ($Plateau_{Total}$).

$$\text{Eq 1.} \quad Y(t) = \begin{cases} Y_0 & , \ t < T_0 \\ Plateau_{Total} + (Y_0 - Plateau_{Total})e^{-\lambda_{Total}(t-T_0)} & , \ t \geq T_0 \end{cases}$$

The initial values of Y_0 (Y-intercept) were set to 1 because the data were normalized. T_0, the time delay from CA administration to washout was fitted by Prism to account for variability in the start time of observed CA washout, and the asymptote $Plateau_{Total}$ was restricted to values greater than zero. The latter constraint is reasonable because the CA will not clear from the body completely within the scan time allotted for the current study, however, we observed the signal return to baseline levels (N=2) within 24 hours; data not shown. For statistical purposes, the extra sum-of-squares F-test was used to compare the parameters λ_{Total} and $Plateau_{Total}$ between groups with a p-value < 0.05 required to achieve significance.

The time delay following maximum enhancement to signal washout ($T_{0,}$), the absolute maximum peak signal intensity value (SI_{max}), the linear slope (SI_{2hrs}–$SI_{1\text{hrs}}$) between the signal at one hour post injection (SI_1) and the signal at two hours (SI_2) post injection, and the attenuation coefficient for data collected during the first hour post peak enhancement (λ_{1hr}) assuming a plateau of zero were measured in each animal. Both SI_{2hrs}–$SI_{1\text{hrs}}$ and λ_{1hr} were calculated to provide a straight-forward metric that could be easily applied in patients. A Student's t-test was used to compare parameters between the different groups with a p-value < 0.05 required to achieve significance. Receiver Operating Characteristic (ROC) curve analysis was performed using the Prism 5 built-in analysis tool with 95% confidence level to determine whether CA washout parameters (T_0, $\lambda_{1hr,}$ and SI_{max}) could differentiate between the AD model to WT control mice.

3.2.7 Cathepsin D Expression in Brain Tissue

WT and 5XFAD mice (4 and 12 months old) were perfused with saline followed by 10% neutral buffered formalin (NBF). Brains were dissected and immersed in 10% NBF for 24 hours, embedded in paraffin, and 5 µm sections were cut. Antigen retrieval was performed using formic acid (70%, 2 minutes) and sections were immunolabeled with antibody against CatD (1:200; C-20 sc-6486 from Santa Cruz Biotechnology; Santa Cruz, CA, USA). This antibody was detected using an anti-goat secondary antibody conjugated to horseradish peroxidase, prior to colorimetric detection using nickel 3,3'-diaminobenzidine (DAB; 0.15 mg/ml in 0.03% H_2O_2; Sigma-Aldrich, Oakville,ON, Canada) with the Vectastain ABC kit (Dako, Burlington, ON, Canada) and counterstaining with Hematoxylin and Eosin (H&E; Leica Microsystems Inc. Concord, Ontario, Canada). Sections were imaged and digitized using a TISSUEscope CF slide scanner (Huron Technologies, Waterloo, ON) at a 0.5 µm resolution using bright field imaging (at 40X). Staining area was measured in three regions (each covering >200,000 µm2) of primary somatosensory cortex in each of three sections per mouse, in each of three mice per group using ImageJ (v. 1.46r, http://rsbweb.nih.gov/ij/) with staining identified using the color deconvolution plugin written by Dr. Gabriel Landini (available via the aforementioned website) and quantified using the ImageJ built-in threshold tool.

3.3 Results

3.3.1 CA Optical Properties

Measuring the fluorescence at 845 nm, each CA had an excitation peak at 780 nm (similarly to non-conjugated IRDye800). We then measured the emission intensity spectrum for all three CA variants using an excitation laser at 780 nm. The CatD Targeted (Fig. 3-2 A, blue triangles) and Non-Targeted (data not shown) agents had a similar peak emission centered at ~805 nm. The Non-Penetrating CA (Fig. 3-2 A, green circles), lacking the CPP, produced higher peak at a slightly lower wavelength, which could not be fully measured because it overlapped with the excitation light source. The CatD Targeted CA incubated with the CatD enzyme (Fig. 3-2 A, red triangles) produced an intermediate curve with significantly higher fluorescence than the intact, CatD Targeted CA at wavelengths below 800 nm. Furthermore, the Optix eXplore pre-clinical scanner measurements of the CatD Targeted CA after CatD enzyme addition showed a gradual increase in fluorescence over time, to about 1.5 times the original signal (Fig. 3-2 B). The optical fluorescent signal changes detected using the M5 plate reader (Fig. 3-2 C) were linear with CA concentration (em/ex 780/845 nm; R^2=.986) and correlated strongly (Pearson correlation R^2=.97; p =0.01) with the optical signal measured using the Optix eXplore pre-clinical scanner measurements (Fig. 3-2 D) which were similarly linear with CA concentration (R^2=0.997).

3.3.2 Optical Signal Dynamics

An example of the NIR imaging data acquired on the GE eXplore Optix scanner is shown in Figure 3-3. Following injection of the contrast agent, signal was acquired from the head (Fig. 3-3A; white rectangular ROI) to produce images. Signal changes from ROIs over the brain (Fig. 3-3A; red elliptical ROI) and from the skin and soft tissue over the neck (Fig. 3-3A; green ROI) were examined. Generally, optical signal increased rapidly following injection, reached a peak value, and then declined over time; a typical curve is shown in Figure 3-3B. The signal from the skin/neck was more than 10 fold lower than the signal from the brain region.

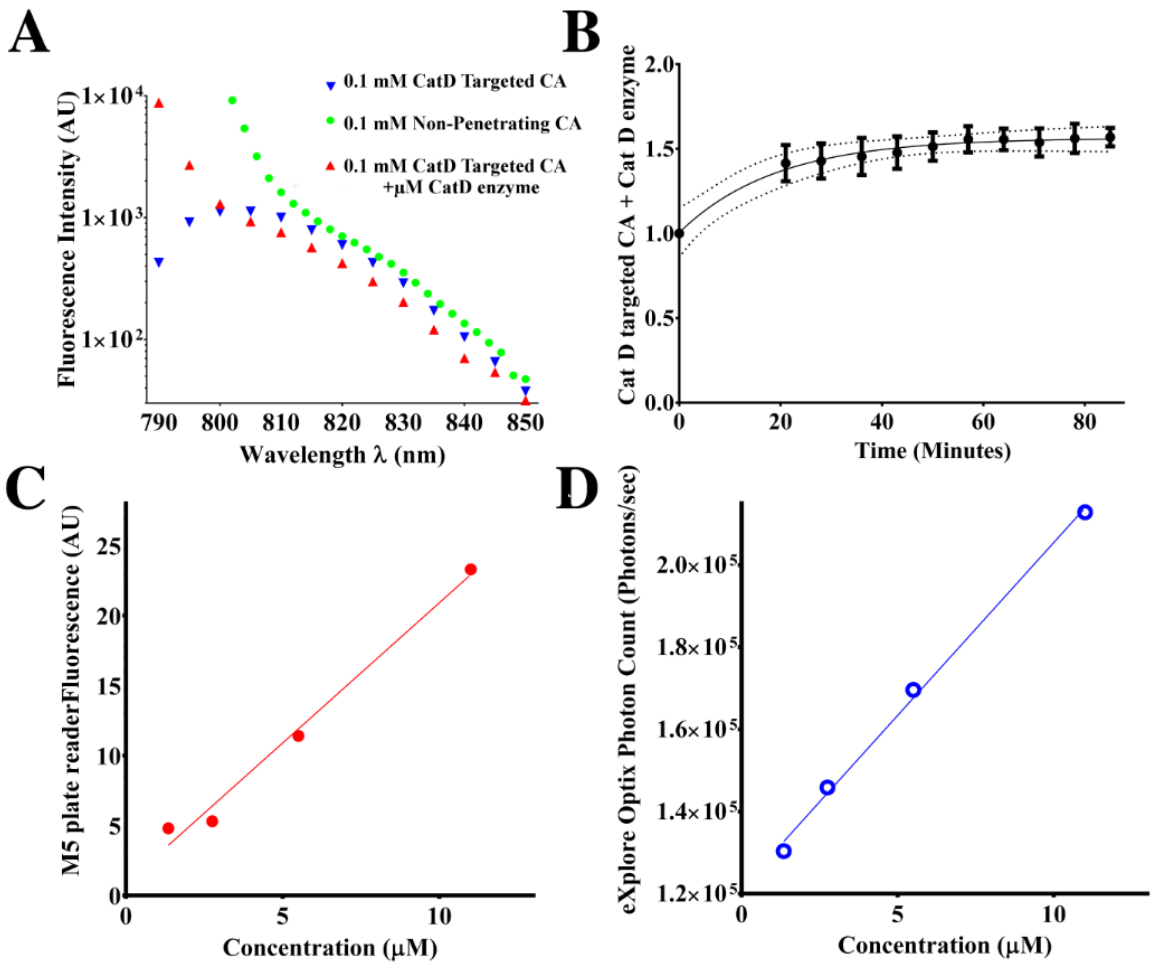

Figure 3-2. Fluorescence characteristics of the CAs. A. Emission spectrum observed using the M5 plate reader at different wavelengths following excitation at 780 nm for the CatD Targeted CA (blue), the Non-Penetrating CA (green) and the CatD Targeted CA incubated with CatD (red). The CatD Targeted agent has a peak width of about 15 nm (FWHM) centered at ~805 nm, whereas the Non-Penetrating agent has a peak emission centered below 790 nm (Not shown). B. Relative fluorescence intensity of the CatD Targeted CA when interacting with a CatD enzyme measured using the GE Optix eXplore optical scanner. The fluorescent signal intensity, normalized to the signal intensity prior to enzyme addition (0.7 µM), increases to ~1.5 times the baseline level one hour after incubation with the enzyme at 37°C. The fluorescence measurements by both C. M5 plate reader (red) and D. eXplore optix (blue) for the same concentrations of CatD targeted CA in PBS are shown where regression lines for each set are plotted.

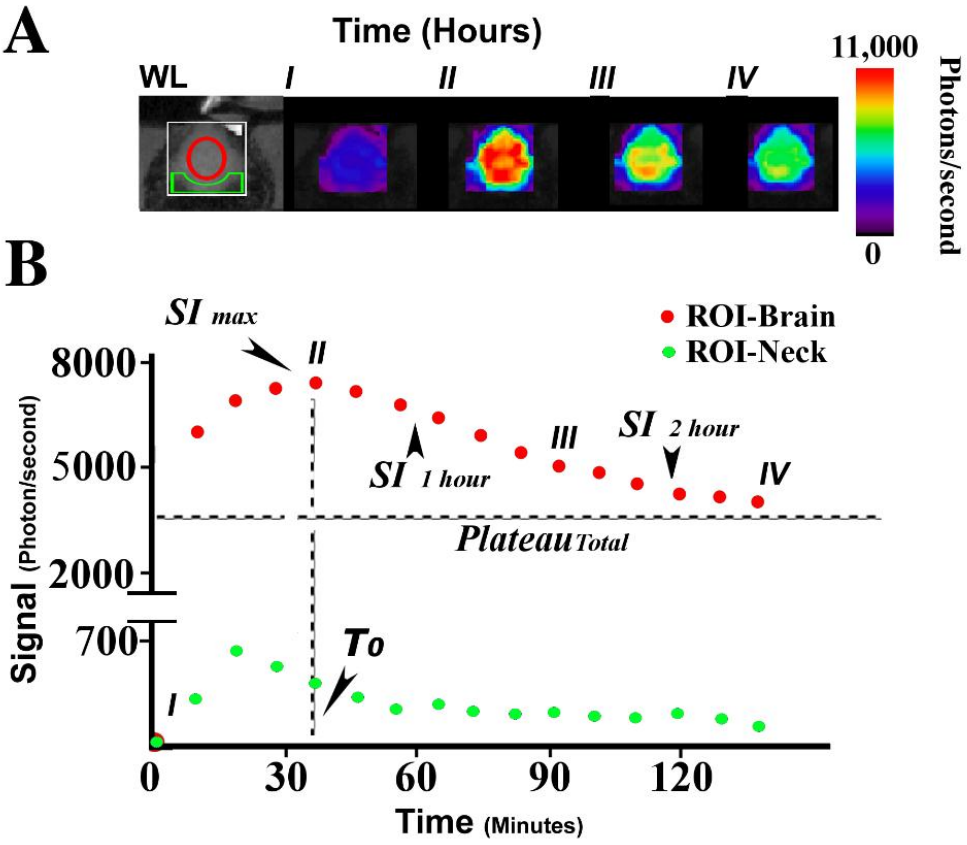

Figure 3-3. Uptake and washout of the CatD targeted CA in a 5XFAD mouse. The NIR signal is collected over time from an ROI (white outline in A) with associated pseudo color bar indicating photons/second (A). The brain signal is then analyzed from an elliptical ROI (red outline in A; red data in B) drawn over the brain region and a control region closer to the neck (green outline in A; green data in B). Representative images of signal intensity are shown (left to right; I to IV) that correspond to epochs designated by the assigned letters on the NIR intensity curve (B). Analyzed variables include (some are indicated in B): the time delay from CA administration to washout (T_0), the peak signal intensity (SI_{max}), the exponential signal decay coefficient for the duration of each scan (λ_{Total}), the signal value at asymptote ($plateau_{Total}$), the exponential signal decay coefficient for 1 hour washout ($\lambda_{1\mathrm{hr}}$), the signal intensity at 1 hour and 2 hours after injection ($SI_1$and SI_2 respectively) and their associated signal decay rate ($SI_{2hrs}-SI_{1hrs}$).

More importantly, there were no significant differences observed in the uptake/washout kinetics of the CatD targeted CA between 5XFAD and WT mice in the skin/neck region (data not shown), therefore all subsequent analyses focus on the signal measured from the brain region only. The key features of the uptake and washout curve include the time delay to signal washout (T_0), the peak signal intensity (SI_{max}), the exponential signal

decay coefficient for the entire scan period (λ_{Total}) or 1 hour washout (λ_{1hr}) starting at peak value, the asymptotic signal ($Plateau_{Total}$), and lastly, the linear slope ($SI_{2hrs}-SI_{1hrs}$) between the signal measured at 1 and 2 hours post injection. The measured characteristics of these curves are summarized in Table 3-1 for the 12 month old mice and in Table 3-2 for the 5 month old mice.

3.3.3 Cathepsin D Targeted Contrast agent pharmacokinetics in 12 month old mice

The pharmacokinetics of the different contrast agents were compared in 12 month old WT mice (Fig. 3-4; Table 3-1). As expected, the signal from the Non-Penetrating CA (green curve, Fig. 3-4) peaked very quickly following injection (T_0 = 14.1 ± 2.3 minutes;λ_{1hr} = -1.42 ± 0.14 × 10^{-2} $minutes^{-1}$). The Non-Targeted CA (orange curve, Fig. 3-4) had a slightly longer T_0 (18.9 ± 3.5 minutes) with a 10% increase in signal at peak compared to initial measurements, and washed out more slowly (λ_{1hr} = -1.25 ± 0.2 × 10^{-2} $minutes^{-1}$). Finally the CatD Targeted CA (blue curve, Fig. 3-4) exhibited the longest time delay to peak (T_0 = 46.5 ± 8.2 minutes), and was cleared much more slowly (λ_{1hr} = -0.52 ± 0.03 × 10^{-2} $minutes^{-1}$) than the control CAs demonstrating the prolonged retention of the Targeted agent requires both the CPP and the CatD cleavage site.

The uptake and washout curves for each contrast agent were compared between 12 month old WT and 5XFAD mice in Fig. 3-5, and the analyses of five different features is summarized for all groups in Table 3-1. Following injection of the Targeted CA, the uptake and washout curves of the 5XFAD and WT animals are clearly separated throughout the experiment (Fig. 3-5 A). Although the CatD Targeted agent shows a trend to take longer to reach maximum signal intensity in 5XFAD mice (72.2 ± 43.8 minutes) compared to controls (46.5 ± 8.2 minutes) this difference was not statistically significant.

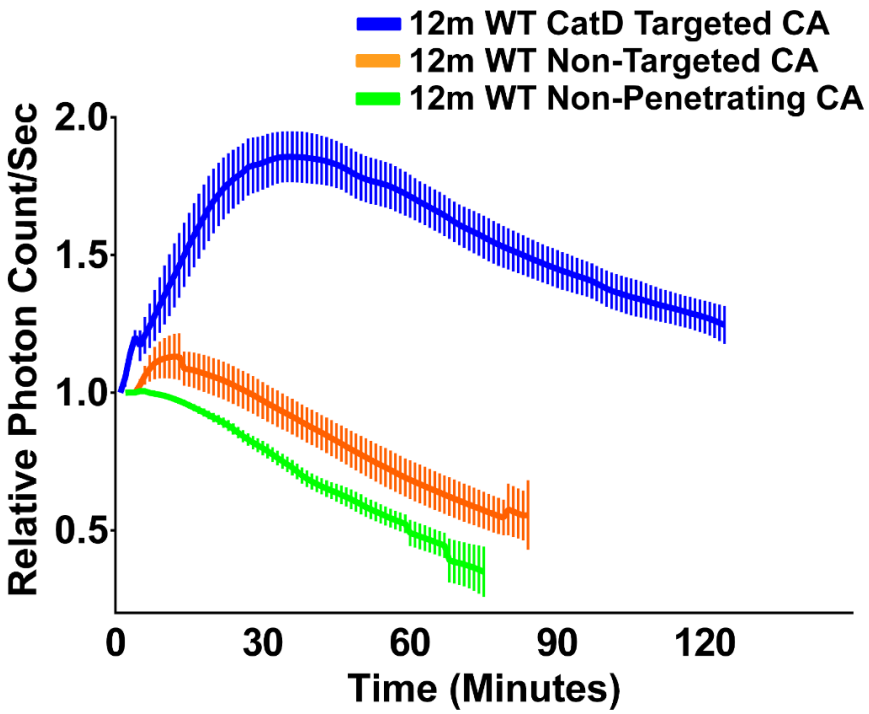

Figure 3-4. CA mechanistic uptake and washout. Average optical imaging signal measurements for twelve-month-old WT mice injected with either the Non-Penetrating CA, Non-Targeted CA or CatD Targeted CA. Data were normalized to the first post CA administration measurement (mean ± SEM).

The CatD Targeted agent reached a higher SI_{max} in the 5XFAD mice (7.1 ± 0.8 × 10^3 photons/s, Fig. 3-5 A) compared to the WT mice (4.6 ± 0.5 × 10^3 photons/s; p = 0.019). The CatD Targeted agent washout coefficient fitted at one hour (λ_{1hr}) for 5XFAD mice (-0.28 ± 0.08 × 10^{-2} $Minutes^{-1}$) was significantly different than for the WT controls (-0.52 ± 0.03 × 10^{-2} $Minutes^{-1}$; $p < 0.05$, Fig. 3-5 B, Table 3-1) as was the washout parameter λ_{Total} (-3.68 ± 0.2 vs -0.68 ± .03 for 5XFAD and control respectively; $p < 0.01$, Fig. 3-5 B, Table 3-1). In addition, the asymptote ($Plateau_{Total}$) was almost four times higher in the 5XFAD mice (82 ± 1%) compared to the control mice (23 ± 2 %, $p < 0.01$). Finally, there was a significant difference between SI_{2hrs}–SI_{1hrs} (-0.43 ± 0.02 vs -0.15 ± 0.08 for 5XFAD and control respectively (Table 3-1, $p < 0.01$) in 5XFAD mice and WT controls. Taken together these results indicate that the contrast agent reached a significantly higher plateau in the 5XFAD mice compared to the WT mice and reached it faster.

To test whether the CatD targeted CA could differentiate between 5XFAD and WT mice, a receiver operating characteristic (ROC) analysis was performed incorporating three different parameters (T_0, $\lambda_{1hr,}$ and SI_{max}) (Null hypothesis: true area = 0.5). For the 12 month old 5XFAD compared to WT mice, the area under the curve (AUC) was 0.78 (p = 0.11), 0.81 (p = 0.07) and 0.86 (p = 0.04), for T_0 , $\lambda_{1\text{hour}}$ and SI_{max} respectively.

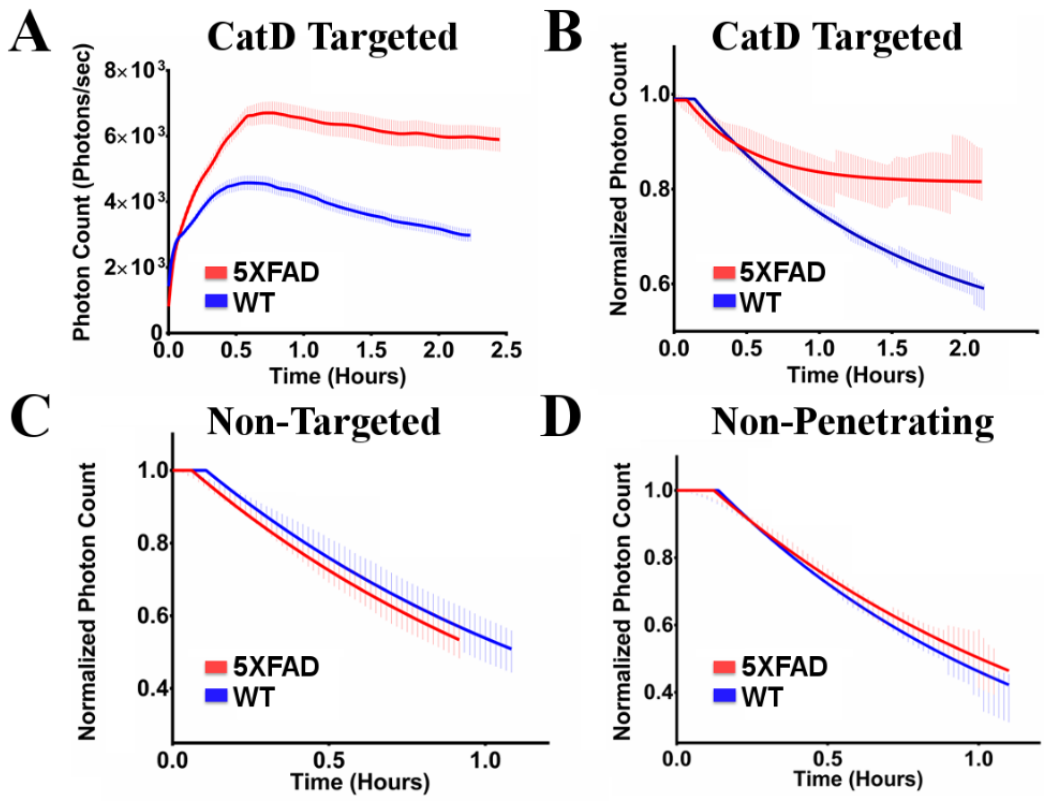

Figure 3-5. Uptake and washout in 12 months old WT and 5XFAD mice following CA administration. Non-normalized data for twelve month old mice injected with CatD targeted CA (A; 5XFAD in red, WT in blue), normalized shifted data for twelve month old mice injected with CatD Targeted CA (B; 5XFAD in red, WT in blue), mice injected with non-targeted CA (C; 5XFAD in red, WT in blue), and mice injected with Non-Penetrating CA (D; 5XFAD in red, WT in blue) are shown. Data are the mean ± standard error of fluorescent signal as a function of time (N=6).

Table 3-1. Fluorescent Signal Intensity Curve Characteristics (12 months old mice).

Data is average ± standard error (N=6) in 12 months old 5XFAD and WT mice following different CA injections.

	WT			5XFAD		
Curve Characteristic	**Non-Penetrating**	**Non-Targeted**	**CatD Targeted**	**Non-Penetrating**	**Non-Targeted**	**CatD Targeted**
T_θ (min)	14.1 ± 2.3ΨΨ	18.9 ± 3.5§§	46.5 ± 8.2 §§ ΨΨ	11.4 ± 2.8[α]	9.8 ± 4.1 *	72.2 ± 43.8 §§ ΨΨ
λ_{1hr} (× 10^{-2} min^{-1})	-1.42 ± 0.15	-1.25 ± 0.18	-0.52 ± 0.03§§ΨΨ	-1.42 ± 0.13	-1.28 ± 0.20	-0.28 ± 0.08 * §§ ΨΨ
λ_{Total} (× 10^{-2} min^{-1})	-1.48 ± 0.03Ψ	-1.15 ± 0.07§	-0.68 ± .03 §§ΨΨ	-1.33 ± 0.27	-1.23 ± 0.45	-3.68 ± 0.20 **§§ΨΨ
$Plateau_{Total}$ (%)	0 ± 2	0 ± 3	23 ± 2 §§ΨΨ	1 ± 1	0	82 ± 1 ** §§ ΨΨ
SI_{2hrs}–SI_{1hrs} (× 10^{-2} min^{-1})			-0.43 ± 0.02			-0.15 ± 0.08 **

*Significantly different from WT group (same CA) $p \leq 0.05$; **$p \leq 0.01$

§Significantly different from *non-penetrating* CA (same strain) $p \leq 0.05$; §§$p \leq 0.01$

ΨSignificantly different from *non-targeted* CA (same strain) $p \leq 0.05$; ΨΨ$p \leq 0.01$

[α]n=2

3.3.4 Non-Targeted and Non-Penetrating Contrast Agents in 12 month old mice

When WT mice were injected with the Non-Targeted CA, it took significantly longer for the signal to reach peak enhancement (T_0) compared to the 5XFAD mice (Table 3-1, $p<0.01$). However, there was no difference between groups in the time to peak for the Non-Penetrating agent. Most importantly, there were no significant differences between the parameters λ_{Total}, $plateau_{Total}$, and λ_{1hr} when comparing the 5XFAD and WT mice after administration of either the Non-Targeted (Fig. 3-5 C) or Non-Penetrating (Fig. 3-5 D) CAs (Table 3-1).

3.3.5 Cathepsin D Targeted Contrast agent pharmacokinetics in 5 month old mice

The uptake and washout of the CatD Targeted CA is shown in both five-month old 5XFAD and WT mice in Fig. 3-6 and the average fitted curve parameter values are provided in Table 3-2. Although there was a trend for the T_0 to be prolonged in the 5XFAD mice vs control mice (64.1 ± 25.8 vs 39.2 ± 28.8 min), this difference was not significant. As with 12 month old mice, the clearance of the CatD Targeted agent at 1 hour (λ_{1hr}) was significantly slower in 5XFAD mice compared to WT mice (-0.62 ± 0.08 $\times 10^{-2}$ Minutes $^{-1}$ vs. -0.92 ±0.08 $\times 10^{-2}$ Minutes $^{-1}$; $p<0.05$) as was the overall clearance rate (λ_{Total}) (-1.02 ± 0.06 vs. -1.25 ± 0.03 $\times 10^{-2}$ Minutes; $p<0.05$). However, the $Plateau_{Total}$, *and* SI_{2hrs}–SI_{1hrs} were not different between groups. The AUC for the ROC was evaluated for λ_{1hr} (null hypothesis: true area = 0.5). For the 5 months old 5XFAD compared to WT mice, the AUC was significantly higher than the null hypothesis (0.89; p = 0.02) for λ_{1hr}, demonstrating that this agent can successfully differentiate between WT and 5XFAD mice at 5 months of age.

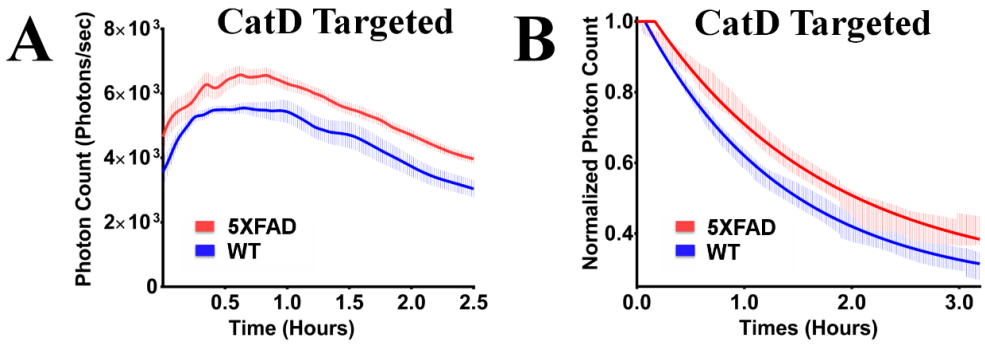

Figure 3-6. CA washout in 5 months old WT and 5XFAD mice following CatD targeted CA administration. Non-normalized data for five month old mice injected with CatD targeted CA (A; 5XFAD in red, WT in blue, N=5), Normalized shifted data for twelve month old mice injected with CatD targeted CA (B; 5XFAD in red, WT in blue, N=6), Data shown is mean ± standard error of fluorescent signal as a function of time.

Table 3-2. Fluorescent signal intensity curve characteristics (5 months old mice).

Data are average ± standard error (N=6) in 5 months old 5XFAD and WT mice following injections of the CatD Targeted CA

	WT	5XFAD
Curve Characteristic	**CatD Targeted**	**CatD Targeted**
T_0 (Minutes)	39.2 ± 28.8	64.1 ± 25.8
λ_{1hr} ($\times 10^{-2}$ Minutes^{-1})	-0.92 ±0.08	-0.62 ± 0.08 *
λ_{Total} ($\times 10^{-2}$ Minutes^{-1})	-1.25 ± 0.03	-1.02 ± 0.06 **
$Plateau_{Total}$ (%)	24 ± 1	27 ± 2
$SI_{2hrs}-SI_{1hrs}$ ($\times 10^{-2}$ Minutes^{-1})	-0.48 ± 0.08	-0.35 ± 0.08

* **Significantly different from WT group (using CatD Targeted CA) $p \leq 0.05$; where ** is $p \leq 0.01$**

3.3.6 CatD expression

CatD expression was examined in primary somatosensory cortex of WT and 5XFAD mice at 4 and 12 months of age using histology. Representative tissue sections are shown in Figure 3-7. In these sections, CatD staining was visible intracellularly in WT mice at four months of age, and staining increased at twelve months of age. The 5XFAD mice also showed intracellular CatD staining at both time points (Fig. 3-7; arrow heads) but also demonstrated CatD staining in large extracellular deposits resembling amyloid plaques at both ages (Fig. 3-7; arrows) In these sections, there appeared to be increase CatD staining in 5XFAD mice compared to wild type controls at both ages.

The expression of CatD in these sections was quantified by measuring the area covered by CatD immunostaining using ImageJ (Figure 3-8). At 4 months of age, CatD staining covered 3.2 ± 0.3 % of the cortex in WT mice, and this increased to 16.2 ± 1.2 % in the 5XFAD mice ($p<0.01$). Similarly, at 12 months of age, CatD staining covered 5.8 ± 1.1 % of the cortex in WT mice, which increased to 29.5 ± 1.2 % in the 5XFAD mice ($p<0.01$). Staining was increased with age in the 5XFAD mice ($p<0.01$) but not in WT controls. These results demonstrate that CatD expression is increased in 5XFAD mice, and that this difference increases with age.

3.4 Discussion

Here, we characterize the behavior of a novel contrast agent targeting CatD for the diagnosis of Alzheimer's disease in the 5XFAD Tg Alzheimer mouse model. The CA was composed of an MR/optical detection probe that incorporated a chelated lanthanide metal (Gd) and a NIR dye. The chelating DOTA structure allows clinically translatable tomographic imaging modalities to be pursued at a later time point (e.g. PET or MRI) without the need for any chemical structural changes. [55]. The NIR dye was conjugated to a known and validated [54] enzymatic hydrolysis site for CatD and a cell penetrating Tat peptide. The Tat peptide allows the agent to permeate the BBB and enter the brain in a bidirectional fashion [48]. The Tat peptide has previously been shown to enter into the hippocampus and portions of the cortex (known sites of heightened AD

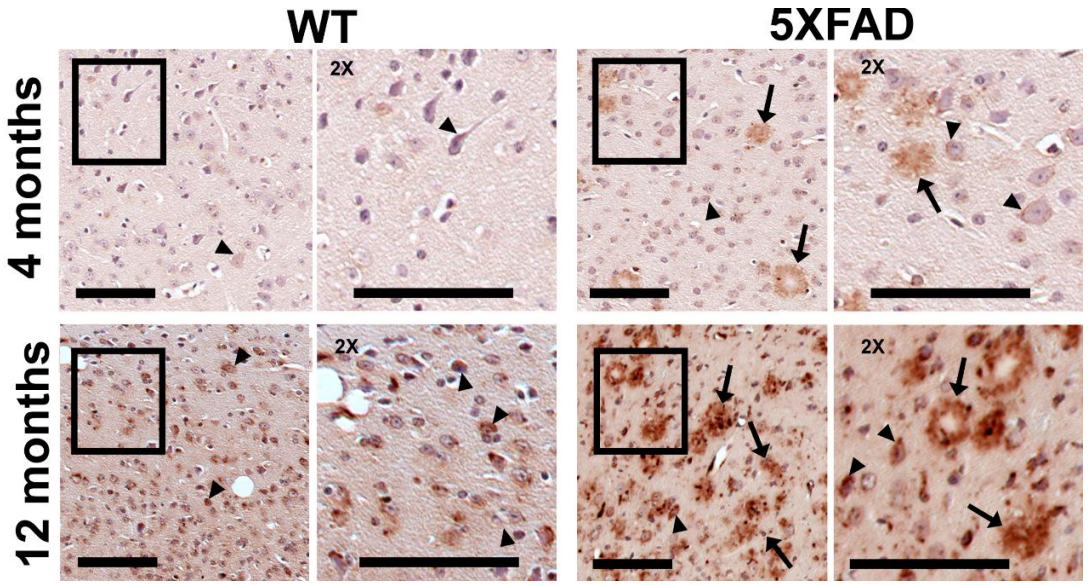

Figure 3-7. Immunohistochemistry of CatD in WT and 5XFAD mice at 4 and 12 months of age. Photomicrographs of the cortex in mice showing CatD staining (brown) with Hematoxylin counter staining of the nuclei (blue). Enlarged views (×2) show the vicinity near the black framed rectangles. CatD staining is present intracellularly (e.g arrow heads) and in amyloid plaques (e.g. arrows). Scale bar 100µm.

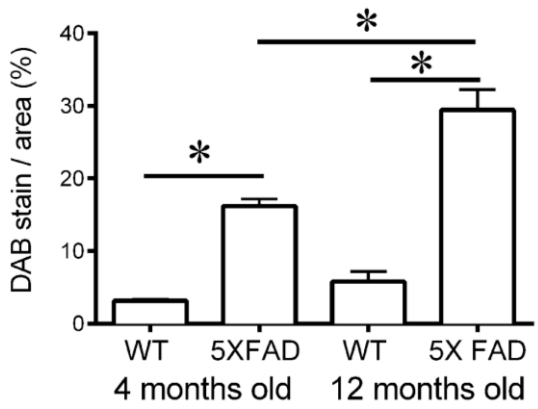

Figure 3-8 Quantification of CatD-specific DAB staining. The area covered by CatD staining shown in Fig.3-7 was quantitated using ImageJ software (mean ± standard error of the mean; N=3). Significant differences are noted with an asterisk for $p \leq 0.01$.

pathology) with at least 0.2% of the intravenous dose taken up per gram of brain [48]. Once inside the brain the cleavage at the CatD site removes the Tat peptide. This enables the diffusion of the Tat peptide out of the cell [54] while temporarily trapping the CA in the CNS compartment.

Comparing the uptake and washout between the 12-month 5XFAD mice and WT controls, the CatD Targeted agent demonstrated clearly different uptake and washout kinetics, with a higher SI_{max}, a slower washout (λ_{1hr}, λ_{Total}, and $SI_{1hr}-SI_{2h}$) and a higher plateau. In the five-month old the cell penetrating CatD Targeted CA exhibited a significantly lower rate of clearance (λ_{1hr}, $SI_{1hr}-SI_{2hr}$) from the brain compared to age matched WT control mice resulting in higher CA retention.

These results are consistent with our previous ex-vivo examination [55] of the uptake and washout of a similar CatD Targeted CA in 12 month old APP/PS1-dE9 (APP/PS1) mice. The previous study also demonstrated greater retention of the cell penetrating CatD Targeted agent in APP/PS1 mice compared to WT mice [55]. In the current study we were able to provide a more complete in-vivo evaluation of the CA washout kinetics with the inclusion of Non-Targeted and Non-Penetrating control agents. In the current study no differences in CA washout between 5XFAD and WT animals were observed when using the control CAs, suggesting that both the Tat peptide and the CatD cleavage site were required for the uptake and specificity of the agent. Additional control experiments with use of inhibitors targeting CatD activity would have helped proving the specificity of the cell penetrating CatD targeted CA. But we are unaware of inhibitors that have the required kinetics and ability to cross through the BBB.

The 5XFAD mice also exhibited a significantly ($p < 0.05$) higher SI_{max} compared to the WT control mice following administration of the Non-Penetrating CA (~35% higher signal in 5XFAD), Non-Targeted CA (~64% higher signal in 5XFAD) and CatD-Targeted CA (~55% higher signal in 5XFAD). The significantly higher SI_{max} of the 5XFAD compared to the WT mice coincided with a significant 26% lower body weight ($p < 0.05$). Since the CA dose remained at 5 nmol/ injection regardless of weight, the SI_{max} was likely higher in the 5XFAD mice as a result of an average 35% higher CA plasma concentration. The fact that the Targeted and Non-Targeted agents had SI_{max} that averaged 64% and 55% higher respectively implies increased uptake of the agents, and not merely increased plasma concentration.

Another possible source of increased signal in the 5XFAD mice is the change in structure of the contrast agent itself after interaction with Cathepsin D. For example, the Non-Penetrating CA produced a higher emission intensity at a shorter wavelength compared to the CatD Targeted CA, while cleavage of the CatD Targeted CA by CatD produced an emission spectrum that was intermediate (Fig. 3-2A; red) as expected. The increased fluorescence of the cleaved agent compared to the intact CatD Targeted CA is likely due to quenching of the fluorophore by the longer amino acid peptide backbone in the CatD Targeted CA. As a result, enzymatic cleavage of the CA could have contributed to the significant increase in fluorescence intensity in the 5XFAD mice compared to WT controls.

There are several limitations that must be considered in the current study. The first is that we did not asses the stability of the CA. However, the the serum-based half-lives of the CPP and IRDye800CW are ~8.8 hours [61] and ~8 days [62] respectively, so, it is unlikely that these components would degrade significantly in the 4 hour post-injection window studied here. We must also consider the mouse models studied. Although 5XFAD mice only recapitulate some aspects of the pathology observed in humans, this study used the 5XFAD because this model is known to have higher levels of Cathepsin D compared to controls [42, 43] as is the case in humans [32, 34]. Whether increased levels of CatD precedes amyloid pathology in 5XFAD mice similar to humans AD pathology [33] has yet to be shown; however, it is not a necessity for the preliminary investigation of our CA. In addition, we used WT C57Bl/6 mice as the control group. Non-transgenic littermates would be preferred as they are a better genetic match to the experimental group, and further studies comparing Tg to non-Tg littermates are on-going. Moreover, although cerebral perfusion and vascular permeability were not measured in these animals, the lack of a significant difference in the washout kinetics of the Non-Targeted and Non-Penetrating CAs between WT and 5XFAD mice suggests that these factors were not significantly different between these groups. Finally, due to the nature of the non-tomographic optical imaging used, the exact contribution of the CA accumulated within the brain, skull, vasculature, and skin to the detected signal is unknown. However, there were no significant differences in the skin signal kinetics between the 5XFAD and wild type animals when using the CatD targeted CA, no significant differences between

the 5XFAD and wild type animals when using the control CAs, and increased levels CatD in the brain of 5XFAD mice was validated. Therefore, we believe that the significant differences in observed signal kinetics between the 5XFAD and wild type animals are dominantly the result of preferential brain uptake in the 5XFAD mice. Future utilization of tomographic imaging techniques will provide further insight to the brain-specific accumulation of the CA compared to other tissues.

The major strengths of this study are the use of the engineered control CAs and the use of a NIR dye. The use of agents lacking a CPP or CatD cleavage site demonstrates that the uptake and retention of the CA are not non-specific, and depend on the CPP and the CatD cleavage. Although complicated light scattering of the NIR signal reduces resolution compared to Oregon Green fluorescence in our previous work, the NIR signal provides much higher signal-to-background contrast, and reduced auto-fluorescence. Furthermore, because NIR light can penetrate tissues for up to several centimeters, it allows imaging of the agents in live animals.

In conclusion, we have developed a contrast agent that targets Cathepsin D and shows promise as a tool for the diagnosis of AD. Specifically, the measured λ_{1hr} as well as λ_{Total} with its associated $Plateau_{Total}$ following administration of the cell-penetrating CatD Targeted CA may be used to differentiate between AD model mice and WT controls at 5 months and 12 months of age. At 12 months of age, $SI_{1hr}-SI_{2hr}$ and $Plateau_{Total}$ may also be used to differentiate between AD and WT mouse models. This study is the first to provide proof of principle for in-vivo detection of AD in an animal model with CatD overexpression, a unique yet validated human pathology associated with AD. Future studies will examine CatD expression over the lifespan of several animal models and correlate these findings with the development of AD pathology.

3.5 Acknowledgments

The authors gratefully acknowledge student stipend support donated by William Shipman and from the Alzheimer Society of London and Middlesex, the Queen Elizabeth II Graduate Scholarships in Science and Technology and the Ontario Graduate

Scholarships. Additionally, the authors express much gratitude to the Lawson Health Research Institute optical imaging lab, Jennifer Hadway and Lise Desjardins (both RVT, RLAT-R) for their experimental and animal handling support, Dr. Mamadou Diop for hardware technical support and finally Zengxaun Nong and Caroline O'Neil for histology and staining expertise. Additionally, funding for this study was provided by the Canadian Institutes of Health Research (MOP-106535).

3.6 References

[1] K. Samsi and J. Manthorpe, Care pathways for dementia: current perspectives, *Clin Interv Aging*, **9** (2014), 2055-2063.

[2] D.P. Perl, Neuropathology of Alzheimer's disease, *Mt Sinai J Med*, **77** (2010), 32-42.

[3] R.D. Terry, E. Masliah, D.P. Salmon, N. Butters, R. DeTeresa, R. Hill, L.A. Hansen and R. Katzman, Physical basis of cognitive alterations in Alzheimer's disease: synapse loss is the major correlate of cognitive impairment, *Ann Neurol*, **30** (1991), 572-580.

[4] A. Maruszak and C. Zekanowski, Mitochondrial dysfunction and Alzheimer's disease, *Prog Neuropsychopharmacol Biol Psychiatry*, **35** (2011), 320-330.

[5] B.V. Zlokovic, Neurovascular pathways to neurodegeneration in Alzheimer's disease and other disorders, *Nat Rev Neurosci*, **12** (2011), 723-738.

[6] E. Storkebaum, A. Quaegebeur, M. Vikkula and P. Carmeliet, Cerebrovascular disorders: molecular insights and therapeutic opportunities, *Nat Neurosci*, **14** (2011), 1390-1397.

[7] J. Cummings and K. Zhong, Biomarker-driven therapeutic management of Alzheimer's disease: establishing the foundations, *Clin Pharmacol Ther*, **95** (2014), 67-77.

[8] N. Coley, S. Andrieu, J. Delrieu, T. Voisin and B. Vellas, Biomarkers in Alzheimer's disease: not yet surrogate endpoints, *Ann N Y Acad Sci*, **1180** (2009), 119-124.

[9] L.S. Schneider, F. Mangialasche, N. Andreasen, H. Feldman, E. Giacobini, R. Jones, V. Mantua, P. Mecocci, L. Pani, B. Winblad and M. Kivipelto, Clinical trials and late-stage drug development for Alzheimer's disease: an appraisal from 1984 to 2014, *J Intern Med*, **275** (2014), 251-283.

[10] J.L. Cummings, T. Morstorf and K. Zhong, Alzheimer's disease drug-development pipeline: few candidates, frequent failures, *Alzheimers Res Ther*, **6** (2014), 37.

[11] C. Berk and M.N. Sabbagh, Successes and failures for drugs in late-stage development for Alzheimer's disease, *Drugs Aging*, **30** (2013), 783-792.

[12] N.E. Carlson, M.M. Moore, A. Dame, D. Howieson, L.C. Silbert, J.F. Quinn and J.A. Kaye, Trajectories of brain loss in aging and the development of cognitive impairment, *Neurology*, **70** (2008), 828-833.

[13] N.A. Johnson, G.H. Jahng, M.W. Weiner, B.L. Miller, H.C. Chui, W.J. Jagust, M.L. Gorno-Tempini and N. Schuff, Pattern of cerebral hypoperfusion in Alzheimer disease and mild cognitive impairment measured with arterial spin-labeling MR imaging: initial experience, *Radiology*, **234** (2005), 851-859.

[14] B. Borroni, D. Anchisi, B. Paghera, B. Vicini, N. Kerrouche, V. Garibotto, A. Terzi, L.A. Vignolo, M. Di Luca, R. Giubbini, A. Padovani and D. Perani, Combined 99mTc-ECD SPECT and neuropsychological studies in MCI for the assessment of conversion to AD, *Neurobiol Aging*, **27** (2006), 24-31.

[15] B.C. Dickerson and R.A. Sperling, Functional abnormalities of the medial temporal lobe memory system in mild cognitive impairment and Alzheimer's disease: insights from functional MRI studies, *Neuropsychologia*, **46** (2008), 1624-1635.

[16] G. Chetelat, B. Landeau, F. Eustache, F. Mezenge, F. Viader, V. de la Sayette, B. Desgranges and J.C. Baron, Using voxel-based morphometry to map the structural changes associated with rapid conversion in MCI: a longitudinal MRI study, *Neuroimage*, **27** (2005), 934-946.

[17] C.J. Moulin, M. Laine, J.O. Rinne, V. Kaasinen, H. Sipila, J. Hiltunen and A. Kangasmaki, Brain function during multi-trial learning in mild cognitive impairment: a PET activation study, *Brain Res*, **1136** (2007), 132-141.

[18] C.A. Mathis, Y. Wang, D.P. Holt, G.F. Huang, M.L. Debnath and W.E. Klunk, Synthesis and evaluation of 11C-labeled 6-substituted 2-arylbenzothiazoles as amyloid imaging agents, *J Med Chem*, **46** (2003), 2740-2754.

[19] H.A. Archer, P. Edison, D.J. Brooks, J. Barnes, C. Frost, T. Yeatman, N.C. Fox and M.N. Rossor, Amyloid load and cerebral atrophy in Alzheimer's disease: an 11C-PIB positron emission tomography study, *Ann Neurol*, **60** (2006), 145-147.

[20] W.E. Klunk, H. Engler, A. Nordberg, Y. Wang, G. Blomqvist, D.P. Holt, M. Bergstrom, I. Savitcheva, G.F. Huang, S. Estrada, B. Ausen, M.L. Debnath, J. Barletta, J.C. Price, J. Sandell, B.J. Lopresti, A. Wall, P. Koivisto, G. Antoni, C.A. Mathis and B. Langstrom, Imaging brain amyloid in Alzheimer's disease with Pittsburgh Compound-B, *Ann Neurol*, **55** (2004), 306-319.

[21] A. Forsberg, H. Engler, O. Almkvist, G. Blomquist, G. Hagman, A. Wall, A. Ringheim, B. Langstrom and A. Nordberg, PET imaging of amyloid deposition in patients with mild cognitive impairment, *Neurobiol Aging*, **29** (2008), 1456-1465.

[22] C.R. Jack, Jr., V.J. Lowe, M.L. Senjem, S.D. Weigand, B.J. Kemp, M.M. Shiung, D.S. Knopman, B.F. Boeve, W.E. Klunk, C.A. Mathis and R.C. Petersen, 11C PiB and structural MRI provide complementary information in imaging of Alzheimer's disease and amnestic mild cognitive impairment, *Brain*, **131** (2008), 665-680.

[23] N. Okamura, R. Harada, S. Furumoto, H. Arai, K. Yanai and Y. Kudo, Tau PET imaging in Alzheimer's disease, *Curr Neurol Neurosci Rep*, **14** (2014), 500.

[24] E.R. Zimmer, A. Leuzy, V. Bhat, S. Gauthier and P. Rosa-Neto, In vivo tracking of tau pathology using positron emission tomography (PET) molecular imaging in small animals, *Transl Neurodegener*, **3** (2014), 6.

[25] M.V. Fawaz, A.F. Brooks, M.E. Rodnick, G.M. Carpenter, X. Shao, T.J. Desmond, P. Sherman, C.A. Quesada, B.G. Hockley, M.R. Kilbourn, R.L. Albin, K.A. Frey and P.J. Scott, High affinity radiopharmaceuticals based upon lansoprazole for PET imaging of aggregated tau in Alzheimer's disease and progressive supranuclear palsy: synthesis, preclinical evaluation, and lead selection, *ACS Chem Neurosci*, **5** (2014), 718-730.

[26] T. Tago, S. Furumoto, N. Okamura, R. Harada, Y. Ishikawa, H. Arai, K. Yanai, R. Iwata and Y. Kudo, Synthesis and preliminary evaluation of 2-arylhydroxyquinoline derivatives for tau imaging, *J Labelled Comp Radiopharm*, **57** (2014), 18-24.

[27] R. Ossenkoppele, D.R. Schonhaut, S.L. Baker, J.P. O'Neil, M. Janabi, P.M. Ghosh, M. Santos, Z.A. Miller, B.M. Bettcher, M.L. Gorno-Tempini, B.L. Miller, W.J. Jagust and G.D. Rabinovici, Tau, amyloid, and hypometabolism in a patient with posterior cortical atrophy, *Ann Neurol*, **77** (2015), 338-342.

[28] D.T. Chien, A.K. Szardenings, S. Bahri, J.C. Walsh, F. Mu, C. Xia, W.R. Shankle, A.J. Lerner, M.Y. Su, A. Elizarov and H.C. Kolb, Early clinical PET imaging results with the novel PHF-tau radioligand [F18]-T808, *J Alzheimers Dis*, **38** (2014), 171-184.

[29] H.J. Aizenstein, R.D. Nebes, J.A. Saxton, J.C. Price, C.A. Mathis, N.D. Tsopelas, S.K. Ziolko, J.A. James, B.E. Snitz, P.R. Houck, W. Bi, A.D. Cohen, B.J. Lopresti, S.T. DeKosky, E.M. Halligan and W.E. Klunk, Frequent amyloid deposition without significant cognitive impairment among the elderly, *Arch Neurol*, **65** (2008), 1509-1517.

[30] R.J. Bateman, C. Xiong, T.L. Benzinger, A.M. Fagan, A. Goate, N.C. Fox, D.S. Marcus, N.J. Cairns, X. Xie, T.M. Blazey, D.M. Holtzman, A. Santacruz, V. Buckles, A. Oliver, K. Moulder, P.S. Aisen, B. Ghetti, W.E. Klunk, E. McDade, R.N. Martins, C.L. Masters, R. Mayeux, J.M. Ringman, M.N. Rossor, P.R. Schofield, R.A. Sperling, S. Salloway and J.C. Morris, Clinical and biomarker changes in dominantly inherited Alzheimer's disease, *N Engl J Med*, **367** (2012), 795-804.

[31] P. Benes, V. Vetvicka and M. Fusek, Cathepsin D--many functions of one aspartic protease, *Crit Rev Oncol Hematol*, **68** (2008), 12-28.

[32] A.M. Cataldo, P.A. Paskevich, E. Kominami and R.A. Nixon, Lysosomal hydrolases of different classes are abnormally distributed in brains of patients with Alzheimer disease, *Proc Natl Acad Sci U S A*, **88** (1991), 10998-11002.

[33] A.M. Cataldo, J.L. Barnett, S.A. Berman, J. Li, S. Quarless, S. Bursztajn, C. Lippa and R.A. Nixon, Gene expression and cellular content of cathepsin D in Alzheimer's disease brain: evidence for early up-regulation of the endosomal-lysosomal system, *Neuron*, **14** (1995), 671-680.

[34] A.L. Schwagerl, P.S. Mohan, A.M. Cataldo, J.P. Vonsattel, N.W. Kowall and R.A. Nixon, Elevated levels of the endosomal-lysosomal proteinase cathepsin D in cerebrospinal fluid in Alzheimer disease, *J Neurochem*, **64** (1995), 443-446.

[35] V.J. De-Paula, M. Radanovic, B.S. Diniz and O.V. Forlenza, Alzheimer's disease, *Subcell Biochem*, **65** (2012), 329-352.

[36] E.M. Strome and D.J. Doudet, Animal models of neurodegenerative disease: insights from in vivo imaging studies, *Mol Imaging Biol*, **9** (2007), 186-195.

[37] K. Meguro, X. Blaizot, Y. Kondoh, C. Le Mestric, J.C. Baron and C. Chavoix, Neocortical and hippocampal glucose hypometabolism following neurotoxic lesions of the entorhinal and perirhinal cortices in the non-human primate as shown by PET. Implications for Alzheimer's disease, *Brain*, **122 (Pt 8)** (1999), 1519-1531.

[38] I. Millien, X. Blaizot, C. Giffard, F. Mezenge, R. Insausti, J.C. Baron and C. Chavoix, Brain glucose hypometabolism after perirhinal lesions in baboons: implications for Alzheimer disease and aging, *J Cereb Blood Flow Metab*, **22** (2002), 1248-1261.

[39] Y.A. Bhagat, A. Obenaus, J.S. Richardson and E.J. Kendall, Evolution of beta-amyloid induced neuropathology: magnetic resonance imaging and anatomical comparisons in the rodent hippocampus, *MAGMA*, **14** (2002), 223-232.

[40] H. Oakley, S.L. Cole, S. Logan, E. Maus, P. Shao, J. Craft, A. Guillozet-Bongaarts, M. Ohno, J. Disterhoft, L. Van Eldik, R. Berry and R. Vassar, Intraneuronal beta-amyloid aggregates, neurodegeneration, and neuron loss in transgenic mice with five familial Alzheimer's disease mutations: potential factors in amyloid plaque formation, *J Neurosci*, **26** (2006), 10129-10140.

[41] R. Kimura and M. Ohno, Impairments in remote memory stabilization precede hippocampal synaptic and cognitive failures in 5XFAD Alzheimer mouse model, *Neurobiol Dis*, **33** (2009), 229-235.

[42] K.L. Youmans, L.M. Tai, T. Kanekiyo, W.B. Stine, Jr., S.C. Michon, E. Nwabuisi-Heath, A.M. Manelli, Y. Fu, S. Riordan, W.A. Eimer, L. Binder, G. Bu, C. Yu,

D.M. Hartley and M.J. LaDu, Intraneuronal Abeta detection in 5xFAD mice by a new Abeta-specific antibody, *Mol Neurodegener*, **7** (2012), 8.

[43] A. Amritraj, C. Hawkes, A.L. Phinney, H.T. Mount, C.D. Scott, D. Westaway and S. Kar, Altered levels and distribution of IGF-II/M6P receptor and lysosomal enzymes in mutant APP and APP + PS1 transgenic mouse brains, *Neurobiol Aging*, **30** (2009), 54-70.

[44] W.H. Oldendorf, Brain uptake of radiolabeled amino acids, amines, and hexoses after arterial injection, *Am J Physiol*, **221** (1971), 1629-1639.

[45] W.H. Oldendorf, Lipid solubility and drug penetration of the blood brain barrier, *Proc Soc Exp Biol Med*, **147** (1974), 813-815.

[46] M.L. Penichet, Y.S. Kang, W.M. Pardridge, S.L. Morrison and S.U. Shin, An antibody-avidin fusion protein specific for the transferrin receptor serves as a delivery vehicle for effective brain targeting: initial applications in anti-HIV antisense drug delivery to the brain, *J Immunol*, **163** (1999), 4421-4426.

[47] W.A. Banks, Characteristics of compounds that cross the blood-brain barrier, *BMC Neurol*, **9 Suppl 1** (2009), S3.

[48] W.A. Banks, S.M. Robinson and A. Nath, Permeability of the blood-brain barrier to HIV-1 Tat, *Exp Neurol*, **193** (2005), 218-227.

[49] J. Temsamani and P. Vidal, The use of cell-penetrating peptides for drug delivery, *Drug Discov Today*, **9** (2004), 1012-1019.

[50] D. Maxwell, Q. Chang, X. Zhang, E.M. Barnett and D. Piwnica-Worms, An improved cell-penetrating, caspase-activatable, near-infrared fluorescent peptide for apoptosis imaging, *Bioconjug Chem*, **20** (2009), 702-709.

[51] F. Madani, S. Lindberg, U. Langel, S. Futaki and A. Graslund, Mechanisms of cellular uptake of cell-penetrating peptides, *J Biophys*, **2011** (2011), 414729.

[52] J.P. Richard, K. Melikov, E. Vives, C. Ramos, B. Verbeure, M.J. Gait, L.V. Chernomordik and B. Lebleu, Cell-penetrating peptides. A reevaluation of the mechanism of cellular uptake, *J Biol Chem*, **278** (2003), 585-590.

[53] R. Mishra, W. Su, R. Pohmann, J. Pfeuffer, M.G. Sauer, K. Ugurbil and J. Engelmann, Cell-penetrating peptides and peptide nucleic acid-coupled MRI contrast agents: evaluation of cellular delivery and target binding, *Bioconjug Chem*, **20** (2009), 1860-1868.

[54] M. Suchy, R. Ta, A.X. Li, F. Wojciechowski, S.H. Pasternak, R. Bartha and R.H. Hudson, A paramagnetic chemical exchange-based MRI probe metabolized by cathepsin D: design, synthesis and cellular uptake studies, *Org Biomol Chem*, **8** (2010), 2560-2566.

[55] R. Ta, M. Suchy, J.H. Tam, A.X. Li, F.S. Martinez-Santiesteban, T.J. Scholl, R.H. Hudson, R. Bartha and S.H. Pasternak, A dual magnetic resonance imaging/fluorescent contrast agent for Cathepsin-D detection, *Contrast Media Mol Imaging*, **8** (2013), 127-139.

[56] J.L. Kovar, M.A. Simpson, A. Schutz-Geschwender and D.M. Olive, A systematic approach to the development of fluorescent contrast agents for optical imaging of mouse cancer models, *Anal Biochem*, **367** (2007), 1-12.

[57] H.A. Robinson, S. Kwon, M.A. Hall, J.C. Rasmussen, M.B. Aldrich and E.M. Sevick-Muraca, Non-invasive optical imaging of the lymphatic vasculature of a mouse, *J Vis Exp* (2013), e4326.

[58] L. Sampath, W. Wang and E.M. Sevick-Muraca, Near infrared fluorescent optical imaging for nodal staging, *J Biomed Opt*, **13** (2008), 041312.

[59] M.V. Marshall, D. Draney, E.M. Sevick-Muraca and D.M. Olive, Single-dose intravenous toxicity study of IRDye 800CW in Sprague-Dawley rats, *Mol Imaging Biol*, **12** (2010), 583-594.

[60] J.L. Kovar, X. Xu, D. Draney, A. Cupp, M.A. Simpson and D.M. Olive, Near-infrared-labeled tetracycline derivative is an effective marker of bone deposition in mice, *Anal Biochem*, **416** (2011), 167-173.

[61] D. Sarko, B. Beijer, R. Garcia Boy, E.M. Nothelfer, K. Leotta, M. Eisenhut, A. Altmann, U. Haberkorn and W. Mier, The pharmacokinetics of cell-penetrating peptides, *Mol Pharm*, **7** (2010), 2224-2231.

[62] L. Sampath, S. Kwon, S. Ke, W. Wang, R. Schiff, M.E. Mawad and E.M. Sevick-Muraca, Dual-labeled trastuzumab-based imaging agent for the detection of human epidermal growth factor receptor 2 overexpression in breast cancer, *J Nucl Med*, **48** (2007), 1501-1510.

Chapter 4

4 A Novel Positron Emission Tomography Contrast Agent Targeting Cathepsin-D: In-vivo retention in an Alzheimer's disease mouse model Introduction

Jonatan A. Snir[1,2], Mojmir Suchy[2,3], Geron A. Bindseil[4], Blaine A. Chronik[2,4], Robert H.E. Hudson[3], Stephen H. Pasternak[5,6] and Robert Bartha [1,2]

[1]Department of Medical Biophysics, University of Western Ontario, London, Ontario, Canada,

[2]Centre for Functional and Metabolic Mapping, Robarts Research Institute, University of Western Ontario, London, Ontario, Canada,

[3]Department of Chemistry, University of Western Ontario, London, Ontario, Canada,

[4]Department of Physics and Astronomy, University of Western Ontario, London, Canada

[5]J. Allyn Taylor Centre for Cell Biology, Molecular Brain Research Group, Robarts Research Institute, University of Western Ontario, London, Ontario, Canada,

[6]Department of Clinical Neurological Sciences, Schulich School of Medicine, University of Western Ontario, London, Ontario, Canada

4.1 Introduction

Alzheimer's disease (AD) was first described over 100 years ago and today it is the most common type of dementia affecting over 750,000 Canadians, a number that will triple by 2050 [1]. There are two hallmark pathologies required for a conclusive post-mortem diagnosis of the disease: the progressive accumulation of the protein fragment β-amyloid (plaques) outside neurons in the brain and twisted strands of the protein Tau (tangles) inside neurons [1]. These pathological targets have been the subject of intense pre-clinical investigation to understand disease etiology, ongoing clinical trials [2-4] to delay disease progression, and FDA approved diagnostic agents (e.g. Florbetapir [5]) to detect the disease early. However, our inability to define the causative features of AD requires new non-invasive research tools. Currently, there are many techniques undergoing testing to detect features of AD in the clinic. These include the examination of the metabolic function of the brain [6], amyloid plaque (Aβ, [7]) and Tau burden [8], and neurotransmitter systems [9]. However, when targeting Aβ with imaging contrast agents (CA) the number of false positives remains high [10]; and when targeting Tau, one requires an accurate understanding of age-dependent normal accumulation of Tau [2, 8, 11] and its involvement in the different forms of dementia such as frontotemporal dementia or other tauopathies [12]. Therefore to improve the differential diagnosis of AD early in the disease course, other biomarkers should be investigated to supplement existing tools. With no cure currently available and the most recent treatment options having a limited capacity for long-term symptomatic relief, it is believed an earlier and more specific diagnosis of AD could increase the effectiveness of new drugs or perhaps even drugs that have previously failed [13, 14].

It has been suggested that brain changes caused by AD may begin as early as 20 or more years before clinical signs [7]. In order to provide an early and specific diagnosis of AD it has been suggested that the lysosomal aspartyl protease, Cathepsin D (CatD), could serve as a potential biomarker [15-17]. Previously, we introduced a novel Contrast Agent (CA) that consisted of a cell penetrating peptide (CPP) derived from the Tat peptide of HIV-1, conjugated to a CatD cleavage sequence and an imaging moiety containing a fluorescent dye and a DOTA conjugate chelating gadolinium [18, 19]. The

cell penetrating peptide allowed the agent to bi-directionally cross the blood brain barrier. Once exposed to CatD, the recognition sequence was cleaved, resulting in separation of the CPP from the imaging probe, trapping the agent in the brain. We have demonstrated it to be preferentially taken up by CatD over-expressing cells, and able to transverse across the BBB (*ex-vivo*) [19]. We have also found significantly increased brain retention at five month and one year in a transgenic (Tg) mouse model of AD compared to age matched wild type (C57BL/6) controls using a near-infrared-labeled version of the CA [20]. In the same experiment we found no differences between mice in the uptake and washout of control CAs (lacking the CatD targeting moiety, or the CPP portion).

In the current study, our primary objective was to produce and test a third generation CA labeled with the ^{68}Ga isotope for imaging by PET. This modification resulted in a probe that allowed us to acquire tomographic images and gain pharmacokinetic information about the CA accumulation in the brain as well as study uptake and retention in different organs longitudinally. There are many different AD mouse models; with many that aim to reproduce amyloid pathology, Tau pathology, or both [21]. One particular strain, the 5XFAD, presents many AD-like characteristics such as amyloid pathology, cognitive decline, neuronal cell death, and synaptic disruption [22]. Interestingly, these mice have also shown increased levels of CatD [20, 23, 24], and therefore were used in the current study. The purpose of this work was to determine whether a CatD targeted contrast agent would show differential uptake and retention in 5XFAD mice compared to controls using a ^{68}Ga PET tracer. Based on previous studies, we hypothesized that increased retention would be evident in the 5XFAD mice. Additionally, considering the important role that ^{18}F Fluorodeoxyglucose (FDG) plays in clinical evaluation of AD [9], the relative metabolic function of the forebrain compared to hindbrain was evaluated in Tg and non-Tg control mice at 10 months. Here we demonstrate that our novel CatD targeting agent is preferentially retained in the brains of an AD mouse model.

4.2 Materials and Methods

4.2.1 [^{68}Ga] Cathepsin D targeted CA

4.2.1.1 General Peptide synthesis and labeling protocol

Reagents were commercially available and all solvents were HPLC or peptide synthesis grade except for water (18.2 MΩ cm^{-1} millipore water), aqueous solutions were lyophilized. Peptides used in this study were assembled on a peptide synthesizer (CEM Liberty Blue) using a standard solid phase peptide synthesis (SPPS) protocol. Rink Amide MBHA resin (100-200 mesh) was used, corresponding amino acid monomers were protected as follows: (R-Pbf, Q-Trt, K-Boc, Y-*t*Bu, C-Trt, '*N*' terminal-Fmoc). Ultra performance liquid chromatography (UPLC) was performed using a chromatograph (Waters Acquity) equipped with an autoinjector, HR-ESI-MS detector and a UV detector on a BEH C18 column (particle size 1.7μm; 1.0 id × 100 mm). Mobile phase: Method A: 100% H_2O to 100% MeCN (both solvents containing 0.1% HCOOH) over 5 min, then 100% MeCN over 2 min, linear gradient, flow rate 0.1 mL/min. HPLC purification (Method B) was performed on a chromatograph (Waters Delta 600) equipped with an in-line filter, an autoinjector, a fraction collector and a UV detector using a Delta-Pak C_{18} 300 Å column (particle size 15 μm; 8 × 100 mm Radial-Pak cartridge). Mobile phase for Method B was 0 min, 99% H_2O – 1% MeCN (both solvents containing 0.1% TFA) to 10 min, 32% H_2O – 68% MeCN, 3 mL/min. Verification of radiolabeled conjugate purity was carried out on a chromatograph equipped with a radiodetector and a UV detector, on an analytical Sunfire C_{18} 300 Å column (particle size 15 μm; 8 × 100 mm). Mobile phase: Method C: 0 min, 70% H_2O – 30% MeCN (both solvents containing 0.1% TFA) to 10 min, 100% MeCN, 1 mL/min. Mass spectra (MS) were obtained on a mass spectrometer (Micromass LCT Premier XE) using electrospray ionisation (ESI). Radiolabeling was performed on a fully automated ^{68}Ge/^{68}Ga generator (type). 4-(2-Hydroxyethyl)-1-piperazineethanesulfonic acid (HEPES) buffer (1 M) used for radiolabeling was prepared by dissolving HEPES (23.8 g, 100 mmol) in water (100 mL), followed by adjusting the pH to 3.50.

4.2.1.2 Preparation of DOTA-peptide conjugate for radiolabeling

Conjugation (Fig. 4-1A) of the DOTA terminal monomer with a peptide on the resin and subsequent labeling with Oregon Green (Fig. 4-1A; **2**) was performed as described previously [18]. Crude conjugate **1** **(**Fig. 4-1A) was purified by semi-preparative HPLC as described in General experimental protocols. Pure conjugate **1** was obtained as 14 × CF_3COO^- salt (4.1 mg, 5%, based on 0.05 mmol scale used for the SPPS), yellow solid, HPLC (Method B): t_R 8.0 min; HRMS (ESI) *m/z*: found 3697.8918 $[M+H]^+$ (3697.9003 calcd for $C_{166}H_{252}F_2N_{53}O_{40}S$).

4.2.1.3 Metallation of DOTA-peptide conjugate 1 with "cold" GaCl3

Conjugate **1** (1.8 mg, 3×10^{-7} mol) was dissolved in an acetate buffer (250 μL, pH 3.5), followed by the addition of $GaCl_3$ solution in water (0.002 M, 300 μL). The mixture was incubated for 20 min at 80 ºC; the completion of the reaction was verified by mass spectrometry as described in General experimental protocols. The mixture was transferred to a centrifuge tube, was frozen and was lyophilized. The residue was used as a "cold" standard for radiotracer **3** (Fig. 4-1A) without further purification, HPLC (Method C): t_R 2.52 min; HRMS (ESI) *m/z*: found 3764.7918 $[M-2H]^+$ (3764.7937 calcd for $C_{166}H_{248}F_2N_{53}O_{40}S^{71}Ga$).

4.2.1.4 Radiolabeling of conjugate 1

A solution of conjugate **1** (0.1 mg, 1.9×10^{-8} mol) in water (190 μL) was added to 1 M HEPES buffer (700 μL) in a sterile vial. A solution of $^{68}GaCl_3$ in 0.1 M HCl was eluted into the vial to reach an average (± standard deviation of the mean) activity of 303.9 ± 102.0 MBq as described in General experimental protocols. The vial was incubated for 10 min at 100 ºC, followed by solid phase extraction on Waters light tC18 Sep-pak cartridge, consecutively eluting with water (2 mL) and EtOH (2.5 mL). Radiolabeled peptide **3** was obtained as a solution in EtOH (in a sterile vial), the activity of the peptide solution was 53.5 ± 14.5 MBq, at a radiochemical yield of 60.3 ± 3.5 with a specific activity of 2.0 ± 0.5 GBq/μmol. EtOH was removed by a stream of N_2 at 80 ºC; the residue was subsequently used for the animal studies as described below.

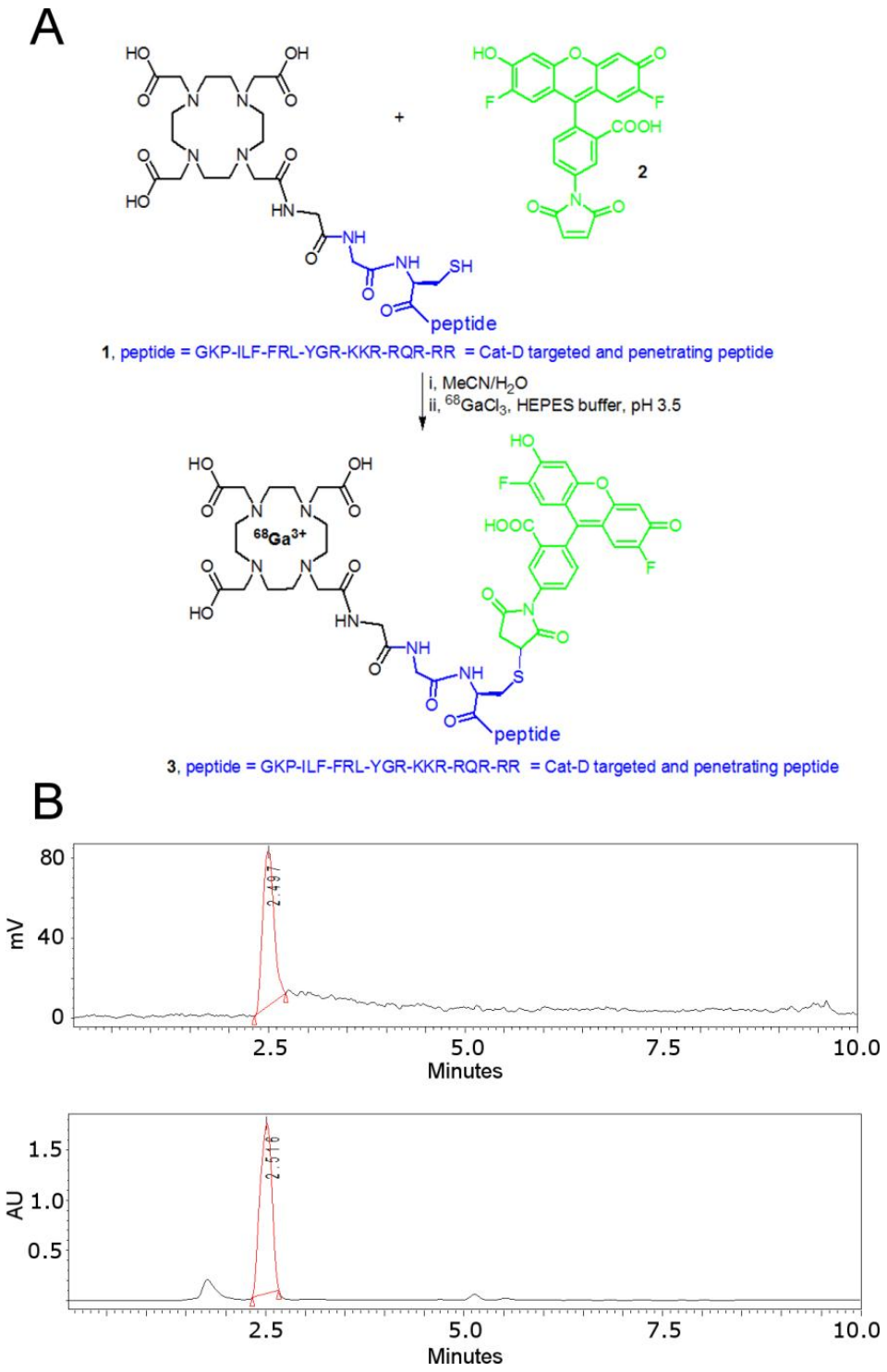

Figure 4-1. Contrast Agent Synthesis. A. Reaction of conjugate 1 with the Oregon Green (2) and subsequent radiolabeling with $^{68}GaCl_3$ to produce peptide 3. **B**. HPLC chromatograms (Method C) of radiotracer 3 (top) and corresponding "cold" standard (bottom).

The purity of radiotracer **3** was verified by HPLC (General experimental protocols, Method C, t_R 2.50 min), by comparison with the chromatograms corresponding to the "cold" standard described above (Fig. 4-1B).

4.2.2 Fluorodeoxyglucose (18F) Radiotracer

Fluorodeoxyglucose (^{18}F-FDG; or simply FDG) was synthesized (Nordal Cyclotron & PET Radiochemistry Facility) in accordance to standard procedures. An average activity of ~500MBq was available as residual from earlier clinical use and was transferred for research purposes.

4.2.3 Animals

All animal studies were conducted in accordance with the ARRIVE guidelines as well as the Subcommittee on Animal Care at The University of Western Ontario, and conformed to the Canadian Council on Animal Care guide for the care and use of laboratory animals. B6SJL-Tg (APPSwFlLon, PSEN1*M146L*L286V) 6799 Vas/Mmjax transgenic female only mice (Jackson Laboratories, Bar Harbor, ME, USA), commonly known as the 5XFAD line Tg6799 of a C57Bl/6 and B6SJL hybrid background and age-matched non-transgenic littermates were used for this study. The 5XFAD mice overexpress human APP(695) with the Swedish (K670N, M671L), Florida (I716V), and London (V717I) Familial Alzheimer's Disease (FAD) mutations and the human PS1 gene harboring two FAD mutations, namely, M146L and L286V [24] known to develop significant Aβ plaques. Animals had access to food (2018 Teklad Global 18% Protein Rodent Diet, Harlan Laboratories) and water ad libitum and were kept in a 12 hour light/dark cycle, housed in rooms with temperature and humidity controls, within standard mouse shoebox-type cages (maximum four, minimum two mice per cage) supplied with nestlets (Ancare) and Bed-o'Cobs® Combo bedding (The Andersons Lab Bedding). Using the resource equation [25], having two groups consisting of 5-7 mice each has an adequate probability of finding a significant result while minimizing the number of animals used. Specific details of the number of mice examined for each experiment, age and weight are recorded in Table 4-1.

Table 4-1: Experimental information of microPET study.

		N	Strain	Age (months)	Weight (g)
CatD targeted CA					
	1st TP	6	Tg	2	20 ± 1
		5	Non-Tg	2	20 ± 2
	2nd TP	7	Tg	6	23 ± 2
		6	Non-Tg	6	23 ± 2
	3rd TP	6	Tg	9	22 ± 1*
		5	Non-Tg	9	26 ± 1
FDG					
		3	Tg	10	21 ± 2*
		3	Non-Tg	10	28 ± 2

*denotes Tg value is significantly different from the non-Tg ($P < 0.05$); TP – time point.

4.2.4 Aβ42 pathology in brain tissue

5XFAD mice (~12 months old) were perfused with saline followed by 10% neutral buffered formalin (NBF). Brains were dissected and immersed in 10% NBF for 24 h, embedded in paraffin, and 5 µm sections were cut. Antigen retrieval was performed using formic acid (70%, 2 min) and sections were immunolabeled with antibody against $A\beta_{42}$ (1:200; made in-house). This antibody was detected using an anti-rabbit secondary antibody conjugated to horseradish peroxidase, prior to colorimetric detection using nickel 3,3'-diaminobenzidine (DAB; 0.15 mg/ml in 0.03% H_2O_2; Sigma-Aldrich, Oakville, ON, Canada) with the Vectastain ABC kit (Dako, Burlington, ON, Canada) and counterstaining with Hematoxylin and Eosin (H&E; Leica Microsystems Inc. Concord, Ontario, Canada). Sections were imaged and digitized using a TISSUEscope CF slide scanner (Huron Technologies, Waterloo, ON, Canada) at a 0.5 µm resolution using bright field imaging (at 40X).

4.2.5 microPET Imaging

Imaging was performed using the Inveon preclinical PET system (Siemens Medical Solutions, Knoxville TN, USA) on transgenic and non-transgenic age-matched littermate mice using list mode scanning. Acquisition, histograms, and reconstructions were all performed using the Siemens Inveon acquisition and reconstruction software

supplied with the scanner. An energy bandwidth of 350 to 650 keV was used for acquisition with a timing window of 3.432 nanoseconds. Decay correction and detector normalization were applied, excluding attenuation and scatter corrections due to the small size of the mouse body. Histograms were set using separate delay handling, global deadtime correction, and 79 ring difference for maximum sensitivity [26]. Reconstruction was accomplished using the Ordered-Subsets Expectation Maximization (OSEM3D) with ordinary Poisson Maximum *a posteriori* OP-MAP (2 OSEM3D iterations, 18 MAP iterations) algorithm to produce a 3D data set with a resolution of 128×128×159 and a voxel size of 0.78×0.78×0.80 millimeter in the *x*-, *y*- and *z*-directions. Animals were kept warm (~37°C) using a heat lamp before, during and immediately after the imaging session with body temperature monitored by rectal probe. Anesthesia was achieved using a nose cone to supply isofluorane (<1.5%) with a scavenger system connected to a charcoal filter. The mice head and body were "fixed" in position using medical tape and using heparinized saline for catheterization, a catheter (31G) was placed into either lateral tail veins for CA administration under anesthesia before scanning was initiated.

4.2.6 CatD targeting CA

Mice were studied at 2, 6 and 9 months of age. All mice received a slow intravenous injection of 11.2 ± 1.0 MBq ^{68}Ga chelated CA suspended in ~200 µL heparinized saline (0.9% NaCl) through a tail vein catheter. To reduce discomfort, the solution was adjusted to a nearly neutral pH ≈ 7 by titration with 1M NaOH prior to administration at 6 and 9 months of age. Imaging was initiated up to 1 minute before injection of contrast agent, and lasted for up to 4 hours (median 3 hours). Histograms were set to 5×30s, 5×60s, 5×300s and remaining time-steps set at 600s intervals.

4.2.7 FDG study

Mice were examined at ~10 months of age. All mice were examined using a static 30 minutes long scan which was initiated 1 hour after injection of the FDG (12.4 ± 1.5 MBq in a volume of 100-200 µL of physiological 0.9% NaCl) into the tail vein; after

which the mice were left safely without anesthesia. Static scan image reconstruction was achieved in the manner described above. Analysis is described below.

4.2.8 Quantitative Analysis of PET Images

The μPET image voxel intensities correspond to units of Bq/cc. Analysis was performed using AsiPro software (Concorde Microsystems, Knoxville, Tenn, USA) to view and analyze the microPET images as well as Carimas^{TM} developed at the Turku PET Centre (Turku, Finland) for 3D rendering [27]. Measurements were made from 3D volumes of interest (VOI) that were drawn over the brain. Specifically, approximate segmentations of the hindbrain and forebrain were made using a magnetic resonance imaging data set to guide VOI selection. The head of the animal was fixed and the brain clearly delineated making identification straightforward. The brain-periphery measurement was also uncomplicated and achieved by placing a VOI on the lateral and superior regions of the head excluding the brain cavity. In contrast, the delineation of the VOI for the other organs within a live, breathing animal was less accurate (in particular the liver and lungs) without the use of gating and image registration. For this preliminary study, organ VOI segmentation was guided solely by an anatomical reference image and activity (signal visualized in the PET image). This approach adds some uncertainty to the absolute activity measurements in the aforementioned organs but was considered insignificant for this preliminary investigation of the CA pharmacokinetics. The signal accumulation/washout of the radioisotope was observed in the axial, coronal and sagittal planes. The average ± standard deviation of the signal intensity was used for analysis.

Due to the low signal within the brain, a moving average filter was used for analysis of CA dynamics as it is optimal for reducing random noise while retaining a sharp step response making it the premier filter for time domain encoded signals [28].

The standardized uptake values (*SUV*) were calculated using Equation 4-1:

$$\boldsymbol{SUV(t) = \frac{C(t)}{ID(t)/W}} \qquad \textbf{(4-1)}$$

using the image derived radioactivity (in Bq/cc) concentrations *C* at time *t* measured pixel-wise or from a volume of interest (VOI) normalized to the injected dose (*ID)* measured prior to the scan (Bq) corrected for radioactive decay at time *t* normalized to the weight of the animal *W* (g). *SUV* could then be considered unit-less with the reasonable assumption that 1 cc = 1 g. The hindbrain was used for the calculation of the relative *SUV* ($SUVR = SUV_{forebrain}/SUV_{hindbrain}$) because it is mainly occupied by the cerebellum, which has been shown to be devoid of important AD pathology (Aβ plaques) in humans, and has only limited pathology in 5XFAD mice [22]. In addition, the cerebellum has been shown to have a significantly reduced pathologic burden in other AD model mice [29, 30]. The reduced pathology in the cerebellum was corroborated by histological examination in our lab (Figure 4-2). The time constants associated with the change of *SUVR* with time were obtained from least square line fitting (Prism; GraphPad Software, Inc. CA USA) of the *SUVR* data. The rate of relative contrast agent uptake (change of *SUVR* with time) was calculated starting at ~7 minutes post injection (p.i) to avoid signal from the first pass of the contrast agent through the brain. Finally, considering the previous NIR CA data [20], differences between diseased and normal mice become more pronounced with time p.i, and therefore a weighted average of the dynamic *SUVR* was created for the last full hour of the scan to approximate a single 60 minute static scan beginning at 120 minutes post injection. In this study, the primary experimental outcome assessed was the rate of change (linear slope) in activity measured over time in the forebrain relative to the hindbrain (*SUVR*). Secondary to the latter, the absolute *SUVR* measurements for the delayed static scan were compared between Tg and nonTg mice at different ages. No randomization procedures were taken when assessing results; however the VOI segmentations were defined purely based on anatomical reference.

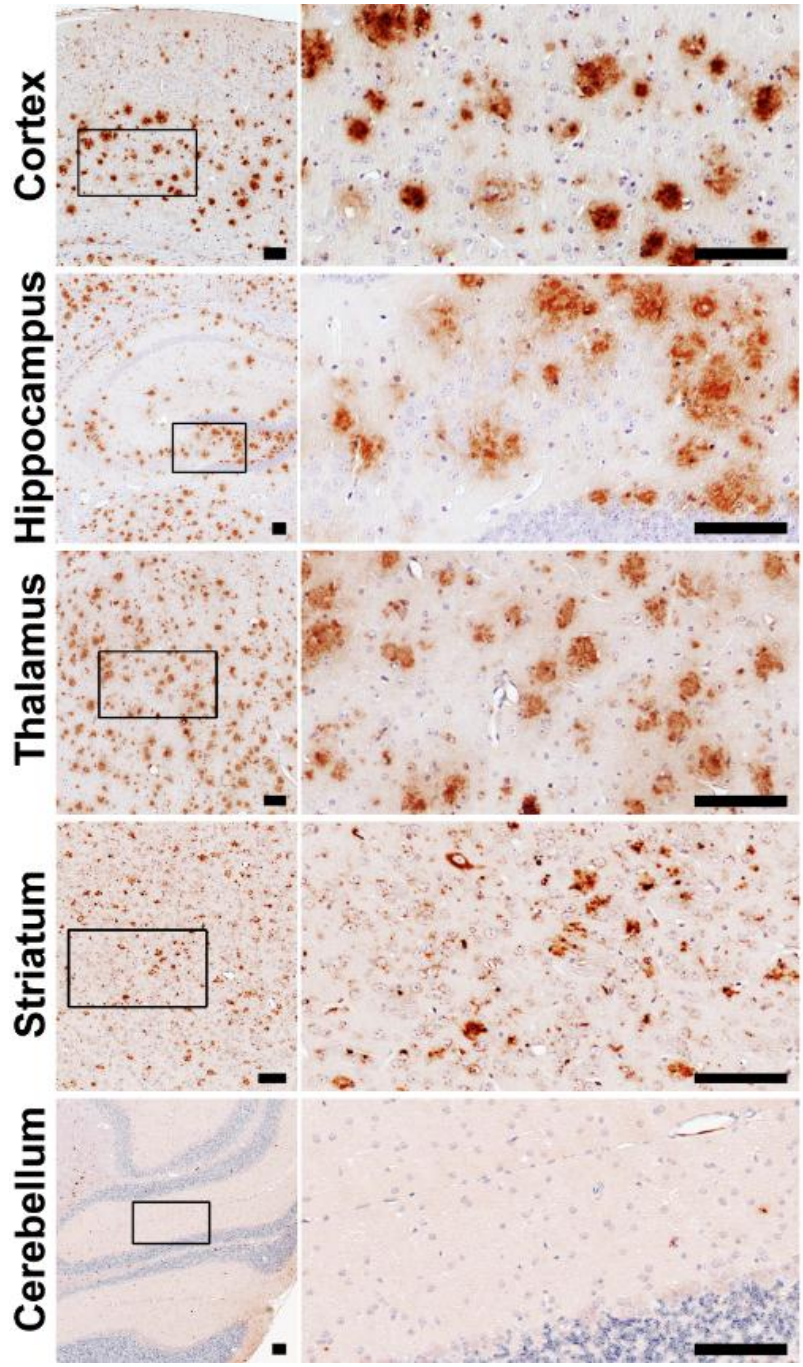

Figure 4-2. Mouse brain $A\beta_{42}$ DAB staining. Aβ plaques formations occupy large portions of the 5XFAD mouse brain at 12 month of age. Regions found in the cortex, hippocampus, thalamus and striatum displayed large plaque burden. In contrast, there were less $A\beta_{42}$ positive staining plaques in areas of the cerebellum corresponding to the region selected as part of the hindbrain VOI. The sub-micrographs on the right correspond to an enlarged region as indicated on the left in black rectangles. All scale-bar are 100 μm.

4.2.9 Statistical Evaluation

To test for statistical significance in the differences between Tg and non-Tg littermates the Student's T-test (two-tailed, unequal variance) or extra sum-of-squares F-test were performed using Prism 5 (GraphPad Software, Inc. CA USA) with an alpha-level of $P \leq 0.05$. To evaluate the effect of age and genotype, a two-way analysis of variance (ANOVA) was used to test the change in *SUVR* values (slopes) in mice that were either positive (Tg) or negative (non-Tg) for AD mutations, in the three different age groups.

4.3 Results

4.3.1 CatD Targeting Ca In Vivo Imaging

PET data were successfully acquired in all animals. The dynamic-signal *SUV* and *SUVR* in the brain of one animal are presented in Figure 4-3. The 3D render of the mouse on the scanning bed (Fig. 4-3A), with a reference CT image showing the VOI for the forebrain (Fig. 4-3B; pink curve) and the hindbrain (Fig. 4-3B; green curve) used for measurements are shown. Due to the blurring caused by positron motion (root mean squared effective range of ~1.2 mm [31]) VOIs were drawn conservatively, avoiding signal from brain periphery. The dynamic signal from within the head is displayed over time in Fig 4-3C during sequential epochs marked with roman numerals (I-VIII) within the head. The associated forebrain and hindbrain dynamic *SUV* (correcting for subject weight and injected dose) as well as *SUVR* are shown in Fig 4-3D. The images and respective time activity curves (activity measured over time) displayed in Fig 4-3 present the fast perfusion

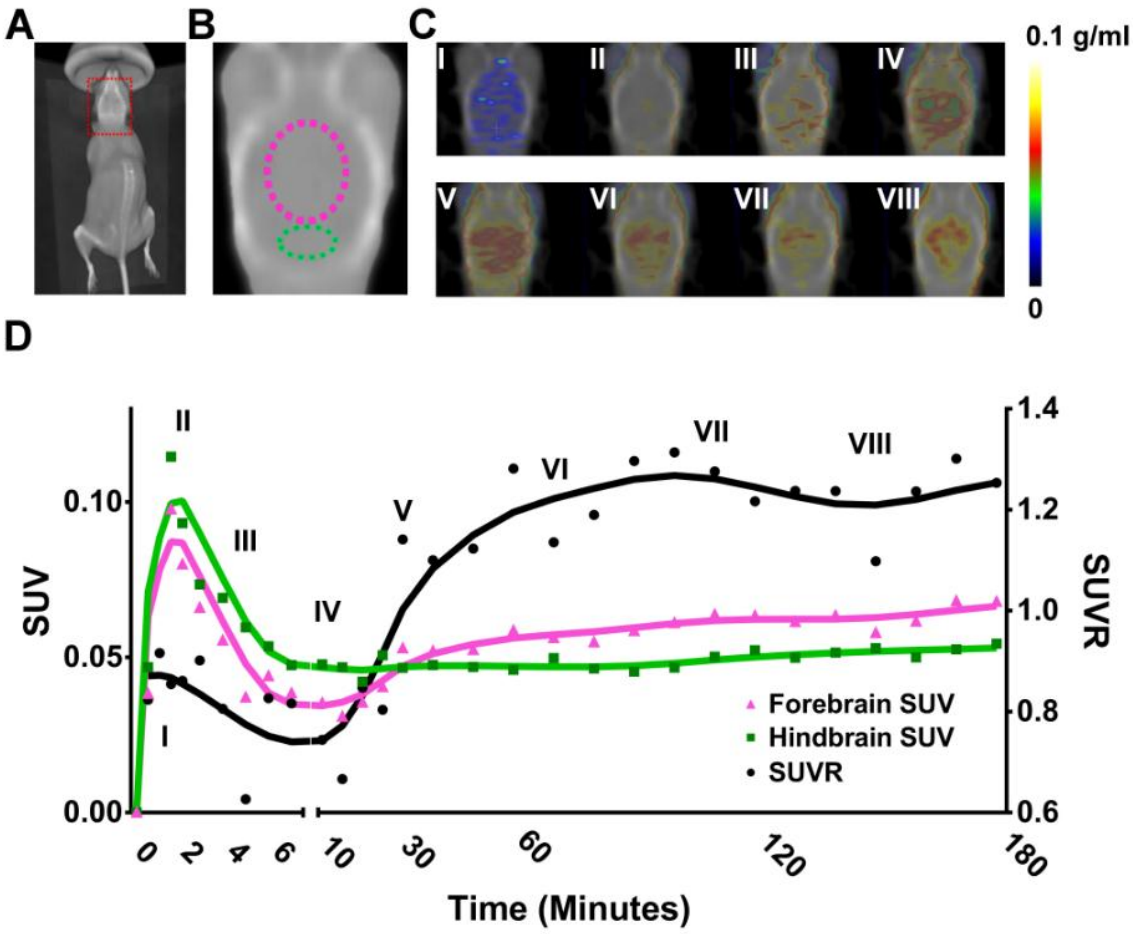

Figure 4-3. Brain signal dynamics - *SUVR* calculation. A 3D CT image showing the mouse on the scanning bed (**A**) with corresponding orienting red box around the head. The head is shown in more detail using a 2D cross sectional axial CT image with outlines of the hindbrain (green) and the forebrain (pink) contours (**B**). The sample CT image from **B** is fused with the dynamic PET images that are shown chronologically with roman numerals indicating order as displayed in **C**. The sample data is that of a single 12 month old Tg mouse following administration of our CatD CA. The corresponding data (TAC) for both the forebrain (pink) and hindbrain (green) regions SUV (**D**; left y-axis) are shown together with the calculated *SUVR* ratio of the two (**D**; right y-axis, black circles). The x- axis is shown with two segments to properly display the early signal kinetics. 2nd order smoothing (4 neighbors) was used to produce the TAC and *SUVR* curves for demonstration purposes only (pink, green and black curves respectively).

of the CA following administration (under 3 minutes) and gradual changes in accumulation within the hindbrain (green) and the forebrain (pink) over the course of the

rest of the scan. The resultant ratio (forebrain over hindbrain; black) was observed to increase in value over time in this mouse.

The average *SUVR* time courses in the brain of both animal groups are provided in Figure 4-4 at 2, 6, and 9 months of age. At 2 months of age there was a decrease in forebrain *SUVR* values over time for both Tg and non-Tg age matched controls (Figure 4-4A). However, the non-Tg mice had a significantly greater negative slope (k = -0.070 ± 0.011) compared to the Tg mice (k = -0.037 ± 0.011; P = 0.035; $F_{(1, 197)}$ = 4.507). In contrast, the forebrain *SUVR* in 6 and 9 month old mice (Figures 4-4B and 4-4C respectively) showed a slow increase in Tg mice but a decreasing trend in the non-Tg mice. This result is likely due to differences in CA kinetics (illustrated in Figure 4-3) in the forebrain and hindbrain between Tg and non-Tg mice. At six months of age (Fig. 4-4B), the rate of change of Tg mice forebrain *SUVR* (slope) was k = 0.014 ± 0.010 and was different from the non-Tg mice k = -0.023 ± 0.008 (P = 0.0015; $F_{(1, 40)}$ = 11.579). Similarly, at 9 months of age, Tg mice (Fig. 4-4C) had a rate of change in forebrain *SUVR* k = 0.027± 0.014, which was significantly higher compared to the non-Tg mice k = -0.033 ± 0.010 ($p < 0.0001$; $F_{(1, 40)}$ = 28.082). The forebrain *SUVR* slopes at 6 and 9 months were significantly higher than at 2 months for both Tg and non-Tg mice. However, the slopes at 9 months were not significantly different from those at 6 months for both Tg and non-Tg mice. Using two-way ANOVA for all time points and mice groups, Tg mice, showed a significantly higher forebrain *SUVR* slope [$F_{(1, 29)}$ = 139.6, P < .0001, η^2 = 0.403] compared to non-transgenic age-matched controls. Older mice presented significantly higher forebrain SUVR slopes [$F_{(2, 29)}$ = 83.80, P < .0001, η^2 = 0.483] compared to younger mice. The interaction of age and AD mutations was also significant [$F_{(2, 29)}$ = 5.3, P = 0.011, η^2 = 0.031]. Finally, it was found that the *SUVR* values calculated for the approximated delayed static scan (60 min long) for the Tg compared to the non-Tg mice were significantly different at 6 and 9 months for scans at ~2 hours p.i.

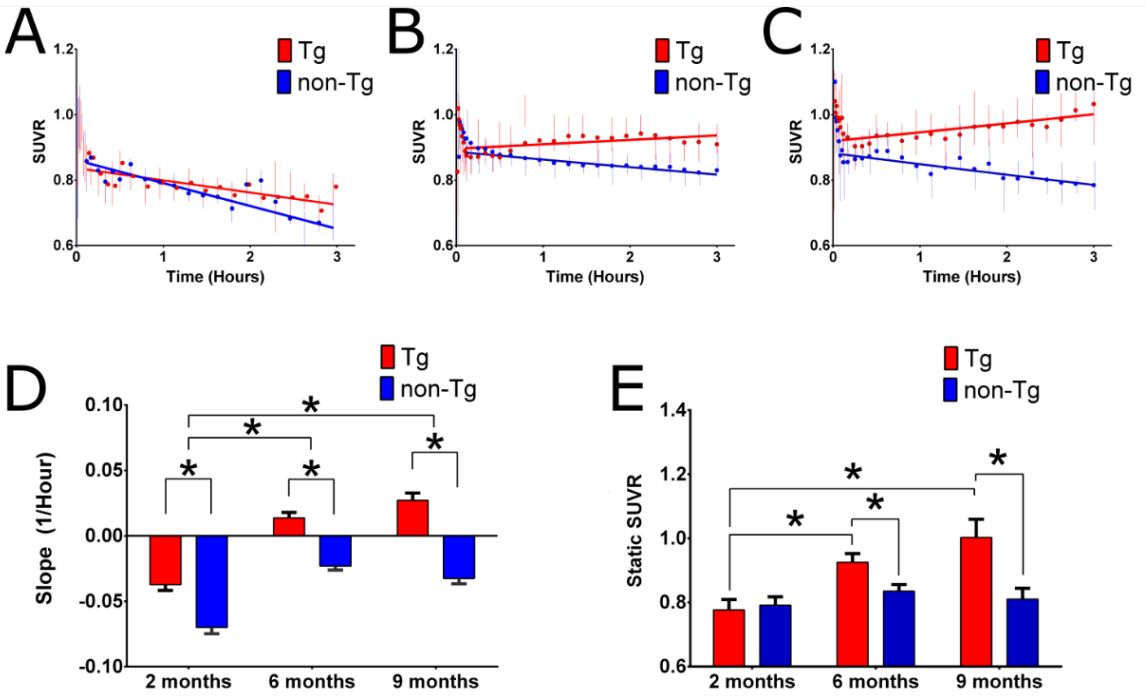

Figure 4-4. *SUVR* in transgenic and non-transgenic mice at 2, 6 and 9 months of age. Calculated *SUVR* from the TAC of forebrain and hindbrain is shown for both Tg (red) and non-Tg (blue) at 2 (**A**), 6 (**B**) and 9 (**C**) months with corresponding fitted slope coefficient displayed in **D** respectively. Vertical lines in **A**, **B** and **C** represent original *SUVR* data points and standard error (N=5-6) used for fitting, with symbols (circles) representing the corresponding smoothed average data (moving average). The linear least square fitting for data after ~6-7 minutes p.i is shown by thick horizontally oriented lines (Tg – Red, non-Tg – blue). Slopes were significantly different (P <0.01) for 2, 6 and 9 month old mice (**A B** and **C** respectively) when comparing the Tg (red) with the non-Tg controls (blue). A summary of the slopes is shown in **D**. The static SUVR calculated at different ages is also shown in **E**. Statistical significance ($P \leq 0.05$) is denoted with an asterisk (*). All data is mean ± standard error of the mean (N=5-7).

Specifically, the average forebrain *SUVR* was significantly higher in the Tg mice at 6 months (0.926 ± 0.033 versus 0.835 ± 0.021; P = 0.024) as well as 9 months (1.003 ± 0.057 versus 0.811 ± 0.034; P = 0.022) for an hour long scan starting at 2 hours p.i.

A sample 3D render of a single 6 months old Tg mouse data are shown in Figure 4-5 with activity displayed using different colours for signal observed during distinct epochs showing the head, heart, liver, lungs and bladder. The activity emanating from areas including but not limited to the skull and adjacent muscle, skin and other tissues were higher than in the brain. There were no significant differences in the signal kinetics

(fitting) as well as absolute *SUV* values from tissues outside the brain as a function of age or strain ($P >> 0.05$). Overall there were no significant differences between the Tg and Non-Tg age matched littermates in the liver, spleen and bladder. While the liver and spleen had a rapid uptake at first, the absolute signal remained stable over time. Finally, the signal in the lungs decayed progressively after the first 30 minutes. The lungs exhibited a trichotomous behavior: at two months of age there was no significant difference between Tg and non-Tg lung SUVs, at six months of age the Tg mice presented a significantly higher lung *SUV* and at nine months of age they presented a significantly lower lung *SUV* ($p < 0.01$) compared to their age-matched non-Tg counterparts. However, the fitted decay coefficients were found to be the same at 2, 6 and 9 months old mice.

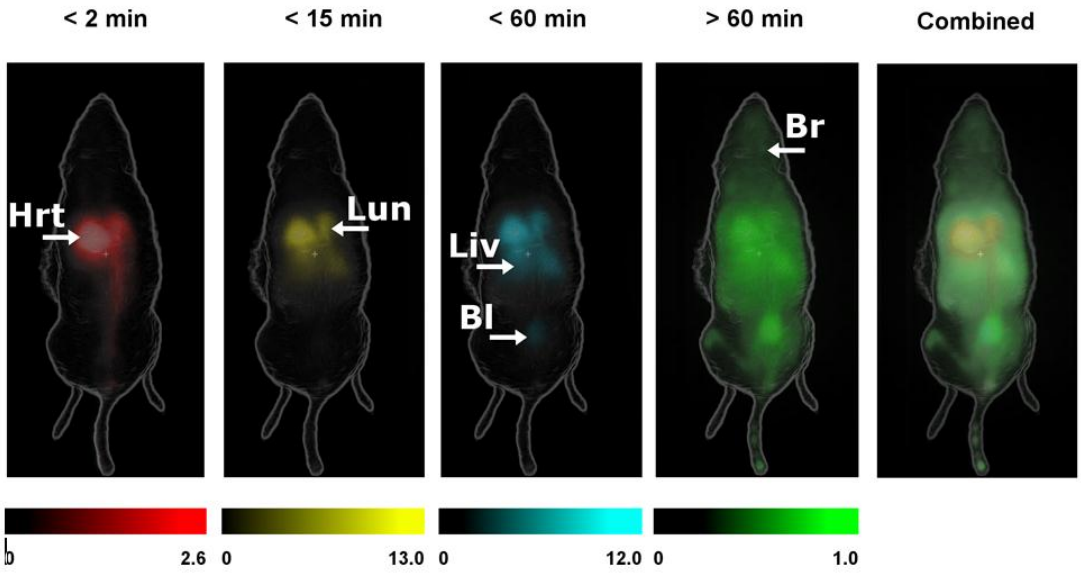

Figure 4-5. Mouse whole body PET. A sample 3D render of PET data for a single 6 months old Tg mouse injected with the CatD targeted CA is shown by overlaying semi-transparent 3D images of the mouse body (outlined in white) with the activity displayed using different colours depending on the time frame: All activity detected, per voxel, under 2 minutes is shown in red; under 15 minutes in yellow, under 60 minutes in teal and over 60 minutes in green. The brain (Br), heart (Hrt), liver (Liv), lungs (Lun) and bladder (Bl) are noted. Pseudo-colour bars correspond to the range of SUV values displayed in each time point of the scan.

4.3.2 FDG

When administered FDG, mice (N=3 per group) presented heterogeneous metabolic function across the brain in both Tg and non-Tg mice. Examining individual

brain regions (forebrain versus hindbrain) and measuring the *SUV*, significantly reduced FDG signal (hypometabolism) was observed in the Tg mice compared to the non-Tg controls. Specifically, hypometabolism was noted in both the forebrain (1.560 ± 0.066 (Tg) versus 1.851 ± 0.085 (non-Tg), $P = 0.009$) and the hindbrain (1.667 ± 0.100 (Tg) versus 1.905 ± 0.078 (non-Tg), $P = 0.031$). As a result, no significant differences were observed in the forebrain *SUVR* between the Tg and the non-Tg mice. A sample image of both Tg and non-Tg mice is shown in Fig. 4-6 with the measured SUV. The image is showing the distribution of PET FDG signal overlaid a sample unrelated MRI of a mouse brain for anatomical reference purposes only. Gross VOI of the forebrain as well as the hind brain (including the cerebellum) were used for calculation of the SUVR values, which were not different between the different strains. It is important to note though that the absolute SUV values calculated in the Tg mice were significantly lower in several particular brain regions compared to the non-Tg age-matched controls.

4.3.3 Biodistribution

Methods, results and partial discussion for a limited (N=3) biodistribution study are available in Appendix 3. These data are not discussed further in the scope of this chapter.

4.4 Discussion

In this study, in agreement with our hypothesis, Tg 5XFAD mice could be differentiated from age matched non-Tg littermates at 2, 6 and 9 months of age by PET using a novel CatD targeted contrast agent. Supporting our primary objective, significant differences in the relative forebrain *SUVR* kinetics of the CatD targeted CA were measured in all age groups. In contrast to our CatD targeted CA *SUVR* analysis, FDG forebrain *SUVR* was not significantly different when comparing the 10 months old Tg mice to their age matched non-Tg littermates. However it is important to note that the

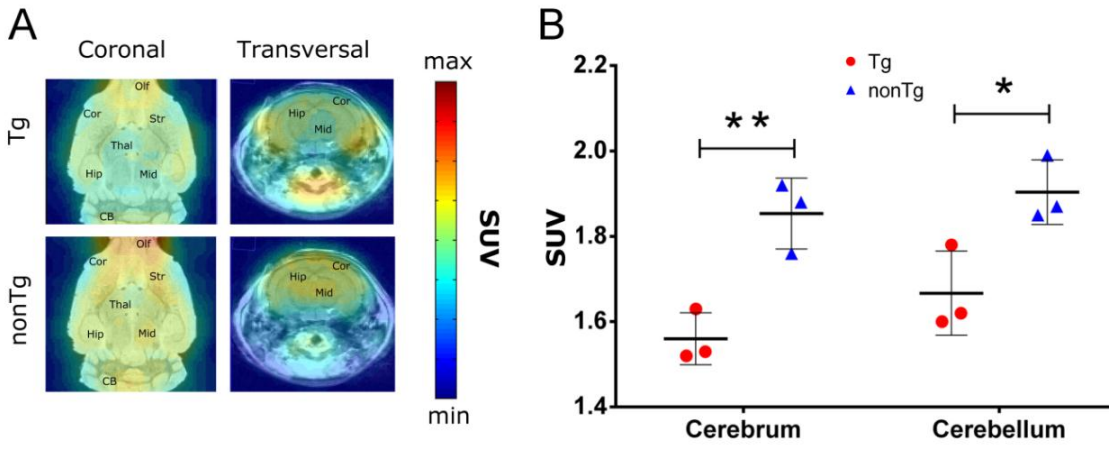

Figure 4-6. FDG analysis. Representative coronal and transverse images corrected for injected dose and mouse weight (*SUV*) are shown of microPET data (**A**). Signal was obtained from a 30 min long static scan following intravenous administration of [^{18}F]-FDG and an hour-long uptake period. Characteristic qualitative differences between the strains could be distinguished especially in the midbrain, thalamus and hippocampus. Areas of interest are noted: Hip – Hippocampus, Str – Striatum, Cor – Cortex, Mid – Midbrain, Thal – Thalmus, Olf – Olfactory, CB – Cerebellum. **B**. *SUV* measurements were performed for the whole cerebrum and cerebellum (easier to correctly contour with smaller segmentation errors without individual registration to pre-PET scan MRI or CT acquisition catered to provide accurate anatomical reference). Both the cerebrum and cerebellum presented lower *SUV* in the Tg mice (red) compared to the nonTg counterparts (blue). The cerebrum and cerebellum were significantly different between the strains. * denotes a significant difference *p* value of $P \leq 0.05$; similarly so ** denotes $P \leq 0.01$. Data are mean ± standard error (N=3).

activity measured was reduced across the brain compared to the controls, implying lowered metabolic demand in several brain regions in the Tg mouse brain. The SUVR is an important relative measurement that can eliminate some experimental differences unrelated to pathology that could contribute to differences between groups.

The current study builds on a previous *in vivo* animal AD model examination of a CatD targeting CA using optical near-infrared imaging [20]. While the structure of the CA is slightly different in this study (different chelated metal and a different fluorescent dye) it shares similar characteristics and targeting design (same cleavage site, DOTA cage and cell penetrating peptide). This CA was designed to detect Alzheimer's disease in patients by measuring the upregulation of the lysosomal system [15, 16] and CatD [16, 17]. While our previous optical data were very promising, the drive toward translation to the clinic requires the use of tomographic imaging modalities. To our knowledge this is

the first ever in-vivo PET imaging study using a CatD targeting CA for the detection of AD. Furthermore, unlike the more common targets used in CA development for AD diagnosis (e.g. Aβ and Tau), CatD activity is a unique biomarker that is a direct indicator of biochemical *function* in the brain rather than a marker of peptide/ protein accumulation.

It is important to note that CatD activity as well as increased levels of the enzyme have been measured both intracellularly, as well as extracellularly in senile plaques. This may have implications on the kinetics of the contrast agent, but controlling for this effect would require an extra- or intracellularly sensitive probe to delineate the differential contribution of these compartments on the CA kinetics. Achieving such regional specificity is very challenging. One approach would be to design a CatD inhibitor that penetrates the BBB but not the cellular membrane.

With respect to the CA kinetics observed throughout the body, no significant differences in CA uptake and washout were identified in any organs except the brain using the CatD targeted CA. Substrates (e.g drugs) are commonly cleared from the blood circulation by the liver and kidneys, and so the relative contribution of the liver and kidney to the overall clearance of drugs may be important for pharmacological and toxicological considerations [32]. Therefore, considering their normal physiological function, the liver (hepatic clearance, drug metabolism), spleen (blood filtration) and the kidneys (renal clearance) are not surprisingly the primary organs of CA accumulation in our animals [33] consistent with previous attempts to use CPPs [34, 35]. However, the relatively smaller kidney retention and the remarkable higher lung CA retention are intriguing and deserve further study. Some non-specific CA accumulation in bone, spleen and lungs could be the result of ^{68}Ga dissociation from the CA as well as natural accumulation of the agent in these organs. For example, a loss of the ^{68}Ga radionuclide from the CA while very unlikely, is possible, due to transchelation processes involving transferrin [36].

The observed decrease in FDG SUV values in the Tg mice compared to non-Tg littermates indicates hypometabolism in both the forebrain and hindbrain of the Tg mice.

The cerebellum is commonly used as a reference region, and has been shown to lack Aβ pathology; however, it is possible that the rate of glucose metabolism in this region is reduced regardless. This result is in contrast with one study [37], but in agreement with a more recent study [30] showing unilateral decrease in FDG SUV values in multiple brain regions in 13 month old 5XFAD mice compared to controls (including the cerebellum). Therefore, when using the cerebellum as a reference region, no significant differences between the Tg mice and non-Tg littermates were observed. However, the latter study [30] did remarkably discover significant differences between Tg mice and control as early as 2 months of age when using the ratios (*SUVR*) of basal-forebrain/basal-ganglia, hypothalamus/neocortex and thalamus/neocortex [30]. The lack of significant differences in AD mouse models when using otherwise well accepted CAs utilized in the clinic is not uncommon. In fact in contrast to one study using 5XFAD [37] FDG, ^{11}C PiB and ^{18}F-FDDNP all failed to show significant results in at least two different AD model mice [38, 39]. Our results are in agreement with the above, since we only evaluated the cerebellum-relative *SUVR* values. The reason for the discrepancies emanates likely from the variability of VOI selection between studies, and the specific conditions prior to imaging (temperature and food control).

The current study has several advantages over the previous examination of the related CA [20]. The use of PET is far more clinically translatable than NIR imaging. PET is commonly used in the clinic, and is considered much more sensitive than its nuclear medicine counterpart, SPECT. In addition, in this study we examined the CA uptake and washout at three different ages and observed consistent preferential increased uptake of the CA by the Tg mice at all ages. These results indicate that the agent could be used to discriminate between the AD mice and control mice using a static scan. In fact, the control mice used for this study were non-Tg age matched (unlike our previous work utilizing the parent strain C57Bl/6) providing a better comparison due to the similar genetic make-up and potential non-pathologic phenotypes in the disease and non-disease groups. While the amount of CA administered was not dependent on the subjects' weight the *SUV* analysis corrects for variations in both a subject's weight and administered dose. The ratio of *SUV*s measured from the forebrain and hindbrain, namely *SUVR* was dependent on neither the injection dose nor subjects' weight since those cancel out in the

calculation. Furthermore, *SUVR* analysis could indirectly reduce some phenotypical bias unrelated to AD pathology by using a reference tissue specific to each individual mouse.

Potential weaknesses of our study involve the utilization of a fairly short half-life (~68 minutes) isotope ^{68}Ga which not only decays twice as fast as the more commonly used ^{18}F but also has a higher peak energy and therefore longer root mean squared positron travel range. The former limits the detection timeframe post CA administration to only a few hours, and the latter increases the blurring effect, which reduces the accuracy of pair annihilation localization and resolution. However, the current design of the radioligand allows for the use of other radioisotopes (e. g. ^{64}Cu) with more favorable properties (half-life of 12.7 h) for longer time delays post injection. The low activity measured in the brain was concerning given the possibility of spill-over signal from the extraneous non-brain tissue (e.g. skull, muscle and skin). However, the likelihood of spill-over signal accounting for observed differences within the brain was refuted by the lack of significant differences between the Tg and non-Tg mice data of the extraneous non-brain tissue at all time points. Finally, the use of heparinized saline for catheterization prior to CA administration, while necessary, could have reduced the CA capacity to bind to and enter cells. This is because heparin could competitively inhibit the adsorption of the CPP [40].

Future experiments will involve image registration for more specific brain region analysis as well as graphical analysis tools such as the Patlak parametric graphical analysis technique for irreversible tracer kinetics [41]. The latter will be considered for the calculation of the differences in flow rate constant across the BBB between Tg and non-Tg age matched littermates (following cleavage, the CA should be retained "irreversibly" within the time frame of imaging). Based on the success of this work, translation to further testing in larger animal models of AD (e.g. transgenic rats, dogs) and finally humans is warranted. In conclusion, this study provides further evidence to support the targeting of CatD to differentiate between 5XFAD mice and control mice from 2 to 9 months of age.

4.5 Acknowledgments

The authors gratefully acknowledge student stipend support donated by William Shipman and from the Alzheimer Society of London and Middlesex, the Queen Elizabeth II Graduate Scholarships in Science and Technology, the Ontario Graduate Scholarships, NSERC DG and RTI programs for additional funding. Furthermore, the authors express much gratitude to the Lawson Health Research Institute optical imaging lab, Jennifer Hadway and Lise Desjardins (both RVT, RLAT-R) for their experimental and animal handling support and finally Zengxaun Nong and Caroline O'Neil for histology and staining expertise.

4.6 Funding

Funding for this study was provided by the Canadian Institutes of Health Research (MOP-106535).

4.7 References

[1] 2014 Alzheimer's disease facts and figures, *Alzheimers Dement*, **10** (2014), e47-92.

[2] N. Okamura, R. Harada, S. Furumoto, H. Arai, K. Yanai and Y. Kudo, Tau PET imaging in Alzheimer's disease, *Curr Neurol Neurosci Rep*, **14** (2014), 500.

[3] R. Craig-Schapiro, A.M. Fagan and D.M. Holtzman, Biomarkers of Alzheimer's disease, *Neurobiol Dis*, **35** (2009), 128-140.

[4] W.E. Klunk, H. Engler, A. Nordberg, Y. Wang, G. Blomqvist, D.P. Holt, M. Bergstrom, I. Savitcheva, G.F. Huang, S. Estrada, B. Ausen, M.L. Debnath, J. Barletta, J.C. Price, J. Sandell, B.J. Lopresti, A. Wall, P. Koivisto, G. Antoni, C.A. Mathis and B. Langstrom, Imaging brain amyloid in Alzheimer's disease with Pittsburgh Compound-B, *Ann Neurol*, **55** (2004), 306-319.

[5] N. Okamura and K. Yanai, Florbetapir (18F), a PET imaging agent that binds to amyloid plaques for the potential detection of Alzheimer's disease, *IDrugs*, **13** (2010), 890-899.

[6] L. Mosconi, Brain glucose metabolism in the early and specific diagnosis of Alzheimer's disease. FDG-PET studies in MCI and AD, *Eur J Nucl Med Mol Imaging*, **32** (2005), 486-510.

[7] V.L. Villemagne, S. Burnham, P. Bourgeat, B. Brown, K.A. Ellis, O. Salvado, C. Szoeke, S.L. Macaulay, R. Martins, P. Maruff, D. Ames, C.C. Rowe and C.L. Masters, Amyloid beta deposition, neurodegeneration, and cognitive decline in sporadic Alzheimer's disease: a prospective cohort study, *Lancet Neurol*, **12** (2013), 357-367.

[8] D.T. Chien, A.K. Szardenings, S. Bahri, J.C. Walsh, F. Mu, C. Xia, W.R. Shankle, A.J. Lerner, M.Y. Su, A. Elizarov and H.C. Kolb, Early clinical PET imaging results with the novel PHF-tau radioligand [F18]-T808, *J Alzheimers Dis*, **38** (2014), 171-184.

[9] A. Nordberg, J.O. Rinne, A. Kadir and B. Langstrom, The use of PET in Alzheimer disease, *Nat Rev Neurol*, **6** (2010), 78-87.

[10] H.J. Aizenstein, R.D. Nebes, J.A. Saxton, J.C. Price, C.A. Mathis, N.D. Tsopelas, S.K. Ziolko, J.A. James, B.E. Snitz, P.R. Houck, W. Bi, A.D. Cohen, B.J. Lopresti, S.T. DeKosky, E.M. Halligan and W.E. Klunk, Frequent amyloid deposition without significant cognitive impairment among the elderly, *Arch Neurol*, **65** (2008), 1509-1517.

[11] E.R. Zimmer, A. Leuzy, S. Gauthier and P. Rosa-Neto, Developments in Tau PET Imaging, *Can J Neurol Sci*, **41** (2014), 547-553.

[12] W. Zhang, J. Arteaga, D.K. Cashion, G. Chen, U. Gangadharmath, L.F. Gomez, D. Kasi, C. Lam, Q. Liang, C. Liu, V.P. Mocharla, F. Mu, A. Sinha, A.K. Szardenings, E. Wang, J.C. Walsh, C. Xia, C. Yu, T. Zhao and H.C. Kolb, A highly selective and specific PET tracer for imaging of tau pathologies, *J Alzheimers Dis*, **31** (2012), 601-612.

[13] C. Berk and M.N. Sabbagh, Successes and failures for drugs in late-stage development for Alzheimer's disease, *Drugs Aging*, **30** (2013), 783-792.

[14] J.L. Cummings, T. Morstorf and K. Zhong, Alzheimer's disease drug-development pipeline: few candidates, frequent failures, *Alzheimers Res Ther*, **6** (2014), 37.

[15] A.M. Cataldo, P.A. Paskevich, E. Kominami and R.A. Nixon, Lysosomal hydrolases of different classes are abnormally distributed in brains of patients with Alzheimer disease, *Proc Natl Acad Sci U S A*, **88** (1991), 10998-11002.

[16] A.M. Cataldo, J.L. Barnett, S.A. Berman, J. Li, S. Quarless, S. Bursztajn, C. Lippa and R.A. Nixon, Gene expression and cellular content of cathepsin D in Alzheimer's disease brain: evidence for early up-regulation of the endosomal-lysosomal system, *Neuron*, **14** (1995), 671-680.

[17] A.L. Schwagerl, P.S. Mohan, A.M. Cataldo, J.P. Vonsattel, N.W. Kowall and R.A. Nixon, Elevated levels of the endosomal-lysosomal proteinase cathepsin D in cerebrospinal fluid in Alzheimer disease, *J Neurochem*, **64** (1995), 443-446.

[18] M. Suchy, R. Ta, A.X. Li, F. Wojciechowski, S.H. Pasternak, R. Bartha and R.H. Hudson, A paramagnetic chemical exchange-based MRI probe metabolized by cathepsin D: design, synthesis and cellular uptake studies, *Org Biomol Chem*, **8** (2010), 2560-2566.

[19] R. Ta, M. Suchy, J.H. Tam, A.X. Li, F.S. Martinez-Santiesteban, T.J. Scholl, R.H. Hudson, R. Bartha and S.H. Pasternak, A dual magnetic resonance imaging/fluorescent contrast agent for Cathepsin-D detection, *Contrast Media Mol Imaging*, **8** (2013), 127-139.

[20] J.A. Snir, M. Suchy, K.S. Lawrence, R.H. Hudson, S.H. Pasternak and R. Bartha, Prolonged In Vivo Retention of a Cathepsin D Targeted Optical Contrast Agent in a Mouse Model of Alzheimer's Disease, *J Alzheimers Dis*, **48** (2015), 73-87.

[21] T.L. Spires and B.T. Hyman, Transgenic models of Alzheimer's disease: learning from animals, *NeuroRx*, **2** (2005), 423-437.

[22] H. Oakley, S.L. Cole, S. Logan, E. Maus, P. Shao, J. Craft, A. Guillozet-Bongaarts, M. Ohno, J. Disterhoft, L. Van Eldik, R. Berry and R. Vassar, Intraneuronal beta-amyloid aggregates, neurodegeneration, and neuron loss in transgenic mice with five familial Alzheimer's disease mutations: potential factors in amyloid plaque formation, *J Neurosci*, **26** (2006), 10129-10140.

[23] K.L. Youmans, L.M. Tai, T. Kanekiyo, W.B. Stine, Jr., S.C. Michon, E. Nwabuisi-Heath, A.M. Manelli, Y. Fu, S. Riordan, W.A. Eimer, L. Binder, G. Bu, C. Yu, D.M. Hartley and M.J. LaDu, Intraneuronal Abeta detection in 5xFAD mice by a new Abeta-specific antibody, *Mol Neurodegener*, **7** (2012), 8.

[24] A. Amritraj, C. Hawkes, A.L. Phinney, H.T. Mount, C.D. Scott, D. Westaway and S. Kar, Altered levels and distribution of IGF-II/M6P receptor and lysosomal enzymes in mutant APP and APP + PS1 transgenic mouse brains, *Neurobiol Aging*, **30** (2009), 54-70.

[25] J. Charan and N.D. Kantharia, How to calculate sample size in animal studies?, *J Pharmacol Pharmacother*, **4** (2013), 303-306.

[26] C.C. Constantinescu and J. Mukherjee, Performance evaluation of an Inveon PET preclinical scanner, *Phys Med Biol*, **54** (2009), 2885-2899.

[27] S.V. Nesterov, C. Han, M. Maki, S. Kajander, A.G. Naum, H. Helenius, I. Lisinen, H. Ukkonen, M. Pietila, E. Joutsiniemi and J. Knuuti, Myocardial perfusion quantitation with 15O-labelled water PET: high reproducibility of the new cardiac analysis software (Carimas), *Eur J Nucl Med Mol Imaging*, **36** (2009), 1594-1602.

[28] S.W. Smith, ***The Scientist & Engineer's Guide to Digital Signal Processing***, California Technical Pub, **1998**, 626 pp.

[29] S. Oddo, A. Caccamo, J.D. Shepherd, M.P. Murphy, T.E. Golde, R. Kayed, R. Metherate, M.P. Mattson, Y. Akbari and F.M. LaFerla, Triple-transgenic model of

Alzheimer's disease with plaques and tangles: intracellular Abeta and synaptic dysfunction, *Neuron*, **39** (2003), 409-421.

[30] I.R. Macdonald, D.R. DeBay, G.A. Reid, T.P. O'Leary, C.T. Jollymore, G. Mawko, S. Burrell, E. Martin, C.V. Bowen, R.E. Brown and S. Darvesh, Early detection of cerebral glucose uptake changes in the 5XFAD mouse, *Curr Alzheimer Res*, **11** (2014), 450-460.

[31] S.R. Cherry, J.A. Sorenson and M.E. Phelps, *Physics in nuclear medicine*, Saunders, Philadelphia, Pa., 2003, xiii, 523 p. pp.

[32] T. Watanabe, K. Maeda, T. Kondo, H. Nakayama, S. Horita, H. Kusuhara and Y. Sugiyama, Prediction of the hepatic and renal clearance of transporter substrates in rats using in vitro uptake experiments, *Drug Metab Dispos*, **37** (2009), 1471-1479.

[33] *Contrast Media - Safety Issues and ESUR Guidelines*, Springer-Verlag Berlin Heidelberg, 2014, XVI, 280 pp.

[34] M. Hallbrink, A. Floren, A. Elmquist, M. Pooga, T. Bartfai and U. Langel, Cargo delivery kinetics of cell-penetrating peptides, *Biochim Biophys Acta*, **1515** (2001), 101-109.

[35] B. Cornelissen, K. McLarty, V. Kersemans, D.A. Scollard and R.M. Reilly, Properties of [(111)In]-labeled HIV-1 tat peptide radioimmunoconjugates in tumor-bearing mice following intravenous or intratumoral injection, *Nucl Med Biol*, **35** (2008), 101-110.

[36] V. Sharma, J. Sivapackiam, S.E. Harpstrite, J.L. Prior, H. Gu, N.P. Rath and D. Piwnica-Worms, A Generator-Produced Gallium-68 Radiopharmaceutical for PET Imaging of Myocardial Perfusion, *PLoS One*, **9** (2014).

[37] S. Rojas, J.R. Herance, J.D. Gispert, S. Abad, E. Torrent, X. Jimenez, D. Pareto, U. Perpina, S. Sarroca, E. Rodriguez, A. Ortega-Aznar and C. Sanfeliu, In vivo evaluation of amyloid deposition and brain glucose metabolism of 5XFAD mice using positron emission tomography, *Neurobiol Aging*, **34** (2013), 1790-1798.

[38] C. Kuntner, A.L. Kesner, M. Bauer, R. Kremslehner, T. Wanek, M. Mandler, R. Karch, J. Stanek, T. Wolf, M. Muller and O. Langer, Limitations of small animal PET imaging with [18F]FDDNP and FDG for quantitative studies in a transgenic mouse model of Alzheimer's disease, *Mol Imaging Biol*, **11** (2009), 236-240.

[39] W.E. Klunk, B.J. Lopresti, M.D. Ikonomovic, I.M. Lefterov, R.P. Koldamova, E.E. Abrahamson, M.L. Debnath, D.P. Holt, G.F. Huang, L. Shao, S.T. DeKosky, J.C. Price and C.A. Mathis, Binding of the positron emission tomography tracer Pittsburgh compound-B reflects the amount of amyloid-beta in Alzheimer's disease brain but not in transgenic mouse brain, *J Neurosci*, **25** (2005), 10598-10606.

[40] S. Kameyama, M. Horie, T. Kikuchi, T. Omura, A. Tadokoro, T. Takeuchi, I. Nakase, Y. Sugiura and S. Futaki, Acid wash in determining cellular uptake of Fab/cell-permeating peptide conjugates, *Biopolymers*, **88** (2007), 98-107.

[41] C.S. Patlak, R.G. Blasberg and J.D. Fenstermacher, Graphical evaluation of blood-to-brain transfer constants from multiple-time uptake data, *J Cereb Blood Flow Metab*, **3** (1983), 1-7.

Chapter 5

5 Conclusions and Future Directions

5.1 Conclusions

The work described within this dissertation is relevant to the research community searching for potential biomarkers for the early diagnosis of Alzheimer's disease (AD). The individual studies that have been described encapsulate the realization, planning, execution and outcome of the intelligent design of a functionalized molecular imaging contrast agent with multi-modality capabilities.

Starting from the ground up, a cellular biological niche was discovered in humans with the possibility of being utilized as a biomarker for AD. Specifically, Cataldo et al. presented an observation nearly 25 years ago [1] of the enhancement and involvement of the lysosomal system, especially Cathepsin D (CatD), in human brain regions that have yet to develop local AD pathology. This finding suggests that identification of this protease could provide complementary information for the probable diagnosis of prodromal AD using a CA that targets this particular enzyme.

The CA structure, chemical characterization and optimized synthesis procedure has been previously described [2] and was not elaborated-on further in the thesis. Limited toxicity studies as well as cellular uptake experiments and *ex-vivo* evaluation of CA uptake were also accomplished and published prior to the work [3] presented in this thesis. Briefly, the CatD targeted contrast agent was composed of a cell penetrating peptide (CPP) that allows the bidirectional penetration of the agent across the blood brain barrier (BBB), into and out of the brain delivering cargo such as an imaging probe. The CPP was conjugated to a CatD cleavage site that was in turn conjugated to the imaging probe. The imaging probe was composed of a fluorescence dye (originally Oregon Green, later IRDye800) as well as a DOTA cage that allows the chelation of different metals (e.g. Gallium or Gadolinium).

The many economic, temporal and ethical complications with studying new therapeutic options or diagnostic probes on humans make up the quintessential corner stone behind pre-clinical studies. Therefore, animal models provide a world of options attempting to mirror human disease for the purpose of the ethical investigation of diagnostic and therapeutic options in a timely fashion (within the average lifetime of a graduate student). There are a plethora of AD mouse models, and it was required to seek out the appropriate model to our hypothesis. As is outlined in Fig. 5-1 a work flow was devised in such a way to allow the development, and execution of a study to investigate the CatD targeted CA capacity in differentiating the disease modeled animals from their control counterparts. As is depicted in the figure, before the CA is tested on an animal model, it is important to ensure there is an adequate control, reasonable number of animals, and most importantly that the model is appropriate for the objectives set forth. This was the first major contribution of this work, which was described in detail in Chapter 2. Specifically, we provided the characterization of CatD expression in three different Tg mouse models of AD across a life span of ~5 to 60 weeks after birth in comparison with an age-matched wild-type control mouse model. In this study we demonstrated that the 5XFAD mouse model is the ideal candidate for targeting increased levels of CatD coinciding with AD $A\beta_{42}$ pathology. In fact the rate of increase in CatD positive staining in 5XFAD was higher than $A\beta_{42}$ in the hippocampus. Similarly, but to a lesser extent, the 2X mouse model displayed a significant increase in both CatD and $A\beta_{42}$ pathology compared to WT and the 3X mouse strain. The 2X also presented with a higher rate of change in CatD positive staining compared with that of the $A\beta_{42}$. This work justified moving forward with the aggressive AD model, the 5XFAD mouse model that proved both age and AD mutation to be significant contributors to the significant differences between the 5XFAD CatD expression and the other Tg mouse models as well as the WT controls.

The work presented in Chapter 3 which was accepted for publication in the Journal of Alzheimer Disease in 2014 was the first exciting truly *in-vivo* application of our contrast agent using a NIR modification (2^{nd} generation CA design) on 5XFAD mice and wild type control mice imaged using a unique time domain optical scanner (GE Healthcare, Milwaukee, Wisconsin). Evaluating the signal measured from the mice bare

but intact head shortly after CA administration we investigated the uptake and washout dynamics following the administration of either the CatD targeted or two separate control CA versions; one that lacked the CPP, and another that lacked the CatD targeting moiety. Interestingly the CatD targeted CA had the highest uptake and longest retention within the brain compared to the non-targeted and non-penetrating CA in both 12 months old Tg and age-matched wildtype controls. The main observation made was the significantly different washout coefficient calculated as the exponential decay coefficient of NIR signal measured over time for mice aged 12 and 5 months old. In contrast, there were no significant differences in washout dynamic between the Tg and WT mice when using the control agents, only when using the complete CatD targeted CA. These data demonstrated that the CPP peptide does indeed allow the agent to cross the BBB into the brain where it is retained longer compared to the agent with no Tat peptide. In addition, the relatively short retention time of the agent with the CPP alone, confirms that agent that enters the brain does indeed leave the brain rapidly as predicted. The extended retention of the agent with the CatD cleavage site and CPP, compared to the CPP alone validates our model of how the agent functions; that proteolitically removing the CPP causes retention of the agent in the brain.

The final chapter (4) was made in preparation for a publication describing the synthesis and testing of a radioactive ^{68}Ga chelated CatD targeted CA (3rd generation CA design) using the Inveon microPET scanner (Siemens Medical Solutions, Knoxville TN, USA). We imaged 5XFAD mice at 2, 6 and 9 months of age shortly before the administration of the CA intravenously (dynamic list-mode scan). The reduced pathology observed in the 5XFAD mouse cerebellum (consistent with humans) justified the use of this region to normalize the standard uptake values (SUV; normalized to subject's weight and injection dose) from the cerebrum (forebrain and midbrain) giving the SUVr parametric values that were analyzed over the course of the 3-hour long scans. Though there were no significant differences in the washout coefficient shortly after injection, there was a delayed, but significantly different uptake in the 5XFAD mice compared to the non-transgenic, age matched control mice. This was quantified by least squares linear fitting of the data. Additionally, averaging the signal over the course of the last 30 minutes of the scans provided significantly higher SUVr values in the 5XFAD mice

compared with the age-matched non-transgenic littermates. There were no apparent differences between the mice renal/hepatic clearance according to those organs signal accumulation. Overall, both age as well as AD mutations proved significant contributors to the significant differences between the 5XFAD and controls, mirroring the CatD staining observed using immunohistochemistry.

In conclusion, this work establishes that the 5XFAD mouse model presents increased CatD protein levels as measured by Western blots as well as immunohistochemistry. Furthermore, our novel CatD targeted CA has the capacity to differentiate between the 5XFAD mouse model and age-matched normal controls using both optical NIR techniques and microPET imaging. Taken together, this work validates the idea of CatD expression correlating with Aβ deposition, and the design of a targeted CA to detect increases in CatD *in vivo*. This agent was able to successfully differentiate AD mice from control, demonstrating that it may indeed be useful for diagnosis in humans.

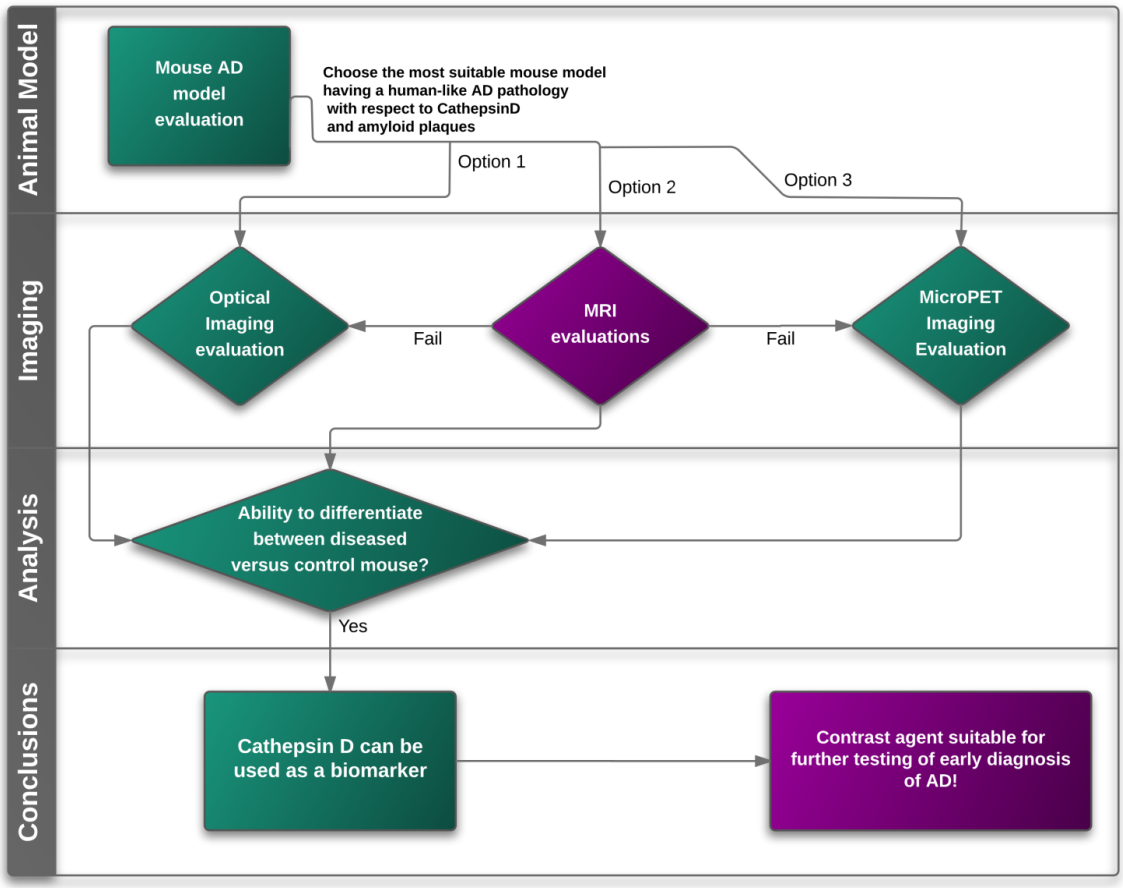

Figure 5-1. Experimental work flow. The work flow is divided into preliminary work investigating the different available animal models, followed by imaging studies to investigate the capacity of the designed CA in differentiating the Tg mouse models from controls. Finally, if indeed differentiation is deemed possible using an imaging modality, which is easily translatable to clinical tools (e.g MRI or PET), then the CA may be considered further in additional toxicity studies and other animal models if found necessary. The original goal to successfully achieve an MRI evaluation of the CA and provide means to differentiate Tg mice with non-Tg controls was not successful. The failure was in part because of the limited sensitivity (e.g relaxivity), and the limited concentration and/or volume of CA allowed to be injected.

5.2 Future Directions

Future directions for this study include: improved understanding of the CA pharmacokinetics, developing MRI detection, improved modeling using a large animal model and finally a move to humans.

5.2.1 Compartment Modeling

The handling of a CA by the body (pharmacokinetics) can be very complex, as several processes (such as absorption, distribution, metabolism, and elimination) work to alter CA concentrations in tissues and fluids. The implications of the CA accumulation at the target site of action or other organs on resulting effects such as toxicity (pharmacodynamics) are crucial for the safety considerations in future clinical use. The Pharmacokinetics as well as the pharmacodynamics of our CA must be evaluated to determine its metabolism and clearance from the body. Excluded from Chapter 4, but may be available for publication as a supplementary figure, was the accumulation of our ^{68}Ga in different clearance organs such as the liver and bladder. This information could be used and is valuable in determining the half-life of the agent within the body. The body processes involved in CA metabolism can be and should be simplified to predict the CA behavior while in circulation throughout the body. One way to make these simplifications is to apply mathematical principles to the various processes. This mathematical model is the compartmental modeling approach that can be extended to our data in order to provide additional information about how our CA works, and how we can improve its utilization. The data presented in Chapter 3 and 4 could be used to model the pharmacokinetic and pharmacodynamics of our contrast agent. While Chapter 4 discussed data that can be used directly for the quantification of CA accumulation in several organs, Chapter 3 presented data that included the use of two control CAs; namely a non-targeted CA and a non-penetrating CA. The modeling can be facilitated by our two different control CAs with different BBB permeabilities, allowing us to separate kinetic coefficients from one compartment (e.g blood pool) to another (e.g. brain).

This is exemplified in the hypothesized compartment modeling showing in Fig. 5-2. Given the compartment modeling shown, a set of ordinary differential equations can be put forth and a solution may be examined using the data acquired with the optical scanner as is shown in Appendix 4. The fact that our CA utilizes a diffusion trap to eliminate (or greatly reduces the egress of the agent from the brain) by having the CPP removed following interaction with the CatD enzyme, would be realized by a significantly lower kinetic rate from the brain compartment back into circulation. A complication in this

approach is the optical "activatable" nature of the contrast agent (while it is not an activatable agent, the fluorescence efficiency is higher following cleavage), leading to the necessity of having a separate compartment for any cleaved CA that experiences higher fluorescence characteristics. Furthermore, this change in fluorescence can skew (if not accommodated for by the set of equations properly) the approximation and/ or solution to the set of equations.

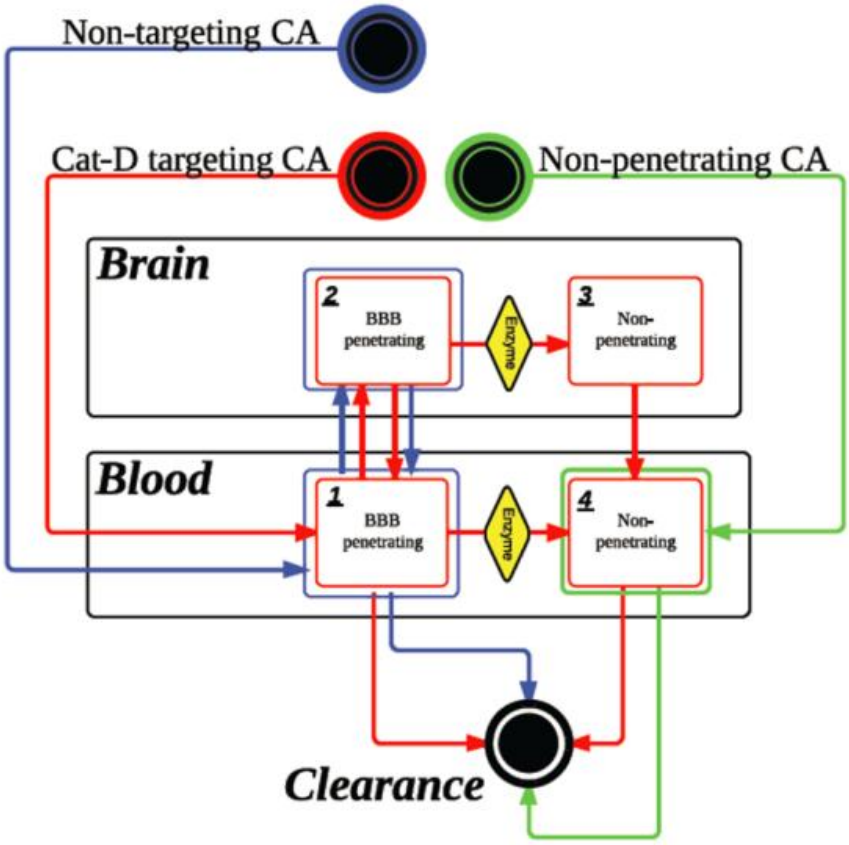

Figure 5-2. Compartment Modeling for the CatD targeted CA and the two separate control CAs. The CatD targeted CA (red) follows a different possible path than that traveled by the non-targeted CA (blue) as well as the non-penetrating CA (green). The CatD targeted CA can become cleaved at which point it may follow kinetic pathway and/or at least experience similar kinetic rates to those experienced by the non-penetrating CA.

5.2.2 MicroPET Parametric Analysis

The analysis of MicroPET data as outlined in Chapter 3, namely the SUVR is a reliable method to generate SUVs that are normalized and therefore compensate for any differences as a result of injected dose (e.g. bioavailability, and concentration dependencies) as well as body weight (e.g. dilution factor). We reported the relative SUV using the "hindbrain" (cerebellum and a portion of the true hindbrain are likely the technical anatomical brain regions) as the reference brain region. While this was justified by reduced pathology in these regions, it may not be ideal. Regardless of the logical benefits of SUVR analysis, it is based on the SUV unit which has been argued to lack easily interpretable biological meaning [4]. Alternatives methods have been developed based on compartmental modeling and pharmacokinetic analysis leading to graphical analysis techniques as such as those proposed by Logan *et. al.* [5] and Patlak *et. al.* [6]. Logan plot analysis could provide the binding potential of a reversible ligand to its target which is related to the amount of targeted receptors or enzymes. Patlak analysis is commonly used for the evaluation of radioactive tracer kinetic flow rate (denoted as *Ki*) of CA relocating into a compartment (e.g. brain) irreversibly within the timeframe of the imaging. The benefit of the graphical analysis methods is their independence from a correctly assumed or otherwise a known compartment model. Future directions will include re-examination of the data taking advantage of graphical parametric analysis such as Logan's binding potential (using the cerebellum as a reference region in lieu of an arterial input function information), or Patlak analysis of K_i [7]. A sample image of a Patlak graphical parametric image for a 6 month old 5XFAD mouse following the administration of our CatD targeted CA is shown. Future examination of the data using this approach will be sought. Furthermore, larger animals could allow the direct sampling of the arterial input function information (blood collection) allowing a more accurate modeling and parametric analysis.

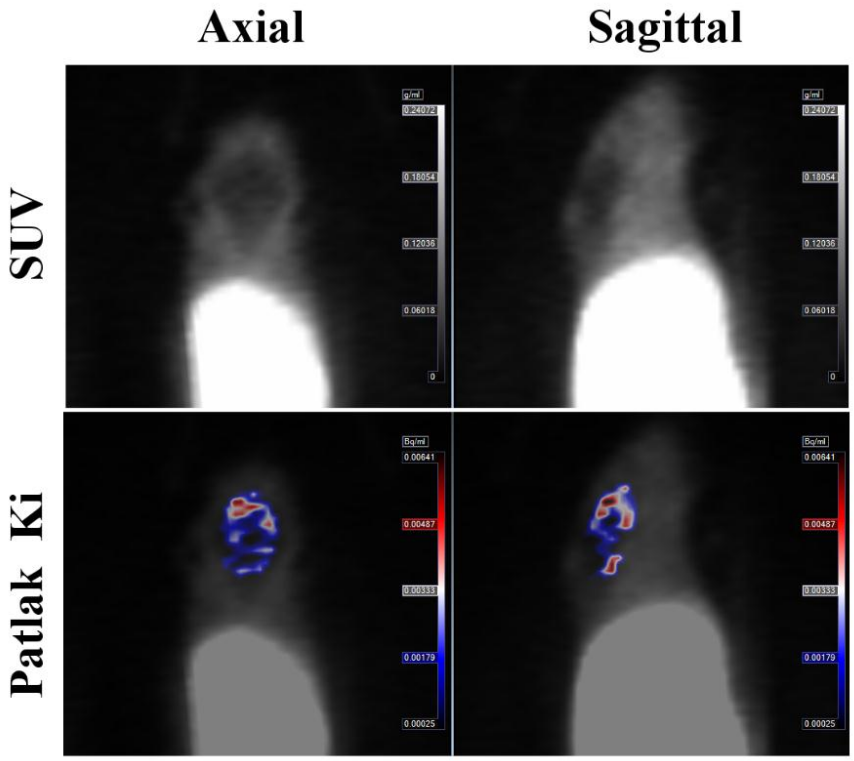

Figure 5-3. SUV values versus graphical analysis (Patlak). Images showing the SUV as well as the Patlak K_i kinetic coefficient values in the brain of a 6 months old Tg 5XFAD mouse following administration of our CatD targeted CA

5.2.3 In-Vivo MRI Contrast Agent Uptake

At the current time, the Gd^{3+}-DOTA-CatD version of contrast agent has not been successfully implemented *in-vivo* due to limited detectability requiring high concentration CA administration, which has proven difficult considering possible diminished solubility in biologically friendly buffer solution (some precipitation occurs in Phosphate buffer solution, as well as saline). The possibility of utilizing Intralipid (fat emulsion) as a solvent has been considered, given its advantage over water-based solvents for other drugs. These have not been adequately attempted as they require further optimization (e.g. of rate of injection and concentration of Intralipid). Additionally, our attempts at detection so far used the 9.4T Agilent animal MRI scanner. However, like all other T_1-weighted CAs, there is likely benefit in going to lower

magnetic strength scanners for the improved relaxivity of the CA and therefore improved contrast. Both the solubility of the CA should be improved allowing safe administration of higher concentrations of the CA, as well as imaging in lower magnetic field (e.g. 1.5T) for improved sensitivity and T_1-weighted contrast. A sample image of a ~13 month old Tg 5XFAD mouse injected with 800 nmol of our CatD targeted CA is shown below (before and ~5 minutes after administration). Unfortunately the mouse used in this experiment expired for unknown reasons, illustrating the safety concerns that still need to be addressed at the concentrations necessary for MRI detectability.

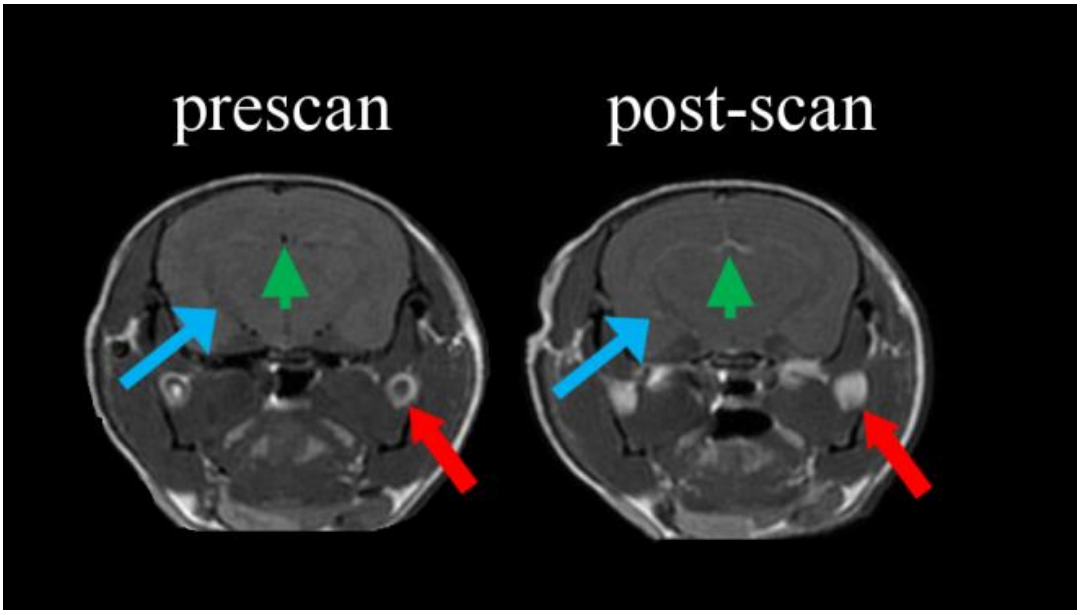

Figure 5-4. MRI experiment. The Spin Echo T_1-weighted images shown above present a coronal slice from a 3T scan before (prescan) and after (post-scan) CA administration showing the body vascular component (red arrows), cerebral vascular component (green arrow) as well as contrast near the lateral ventricle (blue arrows). These images are meant as qualitative observation only and no quantification has been sought at the moment.

5.2.4 3D Fluorescence microscopy CA localization

Because of the dual-modality nature of our CA, we could use *ex-vivo* fluorescence microscopy to study the localization of CA retention at very high resolution across the whole specimen or just the brain. The CryoViz™ (BioInVision Inc. Cleveland, OH, USA) system collects high resolution 2D images sequentially creating a cross sectional 3D volume. We will explore the possibility of using this system to better understand the

exact location of our CA at different time points across the whole brain. In Fig. 5-5 below, one can see the differences between the increased fluorescence observed diffusely in a 13 month old Tg mouse (5XFAD) compared with an age-matched non-Tg control. Both mice received an injection, expired, and frozen for use with the CryoViz™ system. The time delay from injection to being frozen was under 10 minutes for both mice and yet clearly there is some observable difference in fluorescence, likely the result of increased CA retention.

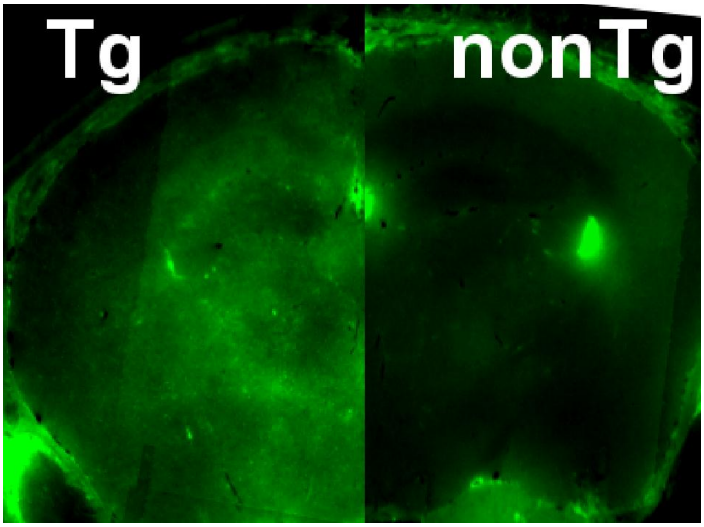

Figure 5-5. CryoViz™ experiment. *Ex-vivo* sample 2D image from the13 month old Tg (5XFAD) mouse is shown on the left and age-matched non-Tg mouse on the right following 800 nmol Gadolinium-Green fluorescence (Oregon Green ™) CA administration.

5.2.5 Toxicology and Safety of Contrast Agents

The potential toxicity of our CatD targeted CA has been examined in a very limited fashion by titration of different concentration incubated with a cancer cell line testing for trypan blue diffusion into the cellular bodies suggestive of cellular death [2]. Before we can use this agent in humans we will need to formally evaluate its toxicity in mice, and then in large animal models. These studies will rely on the PK/PD studies above, which will demonstrate the likely in-vivo concentrations of our agent. They will be critical to move this contrast agent from a pre-clinical to a clinical phase. Further characterization of the safety of the CA at different concentrations would also be of significant importance

especially considering the solubility challenge in order to avoid any possible embolism which may have been the cause of death of at least one mouse injected with a large amount of our CA (>X100 times the concentration used in both Chapter 2 and 3).

5.3 References

[1] A.M. Cataldo, J.L. Barnett, S.A. Berman, J. Li, S. Quarless, S. Bursztajn, C. Lippa and R.A. Nixon, Gene expression and cellular content of cathepsin D in Alzheimer's disease brain: evidence for early up-regulation of the endosomal-lysosomal system, *Neuron*, **14** (1995), 671-680.

[2] M. Suchy, R. Ta, A.X. Li, F. Wojciechowski, S.H. Pasternak, R. Bartha and R.H. Hudson, A paramagnetic chemical exchange-based MRI probe metabolized by cathepsin D: design, synthesis and cellular uptake studies, *Org Biomol Chem*, **8** (2010), 2560-2566.

[3] R. Ta, M. Suchy, J.H. Tam, A.X. Li, F.S. Martinez-Santiesteban, T.J. Scholl, R.H. Hudson, R. Bartha and S.H. Pasternak, A dual magnetic resonance imaging/fluorescent contrast agent for Cathepsin-D detection, *Contrast Media Mol Imaging*, **8** (2013), 127-139.

[4] J.W. Keyes, Jr., SUV: standard uptake or silly useless value?, *J Nucl Med*, **36** (1995), 1836-1839.

[5] J. Logan, J.S. Fowler, N.D. Volkow, G.J. Wang, Y.S. Ding and D.L. Alexoff, Distribution volume ratios without blood sampling from graphical analysis of PET data, *J Cereb Blood Flow Metab*, **16** (1996), 834-840.

[6] C.S. Patlak, R.G. Blasberg and J.D. Fenstermacher, Graphical evaluation of blood-to-brain transfer constants from multiple-time uptake data, *J Cereb Blood Flow Metab*, **3** (1983), 1-7.

[7] M.D. Zwan, R. Ossenkoppele, N. Tolboom, A.J. Beunders, R.W. Kloet, S.M. Adriaanse, R. Boellaard, A.D. Windhorst, P. Raijmakers, H. Adams, A.A. Lammertsma, P. Scheltens, W.M. van der Flier and B.N. van Berckel, Comparison of simplified parametric methods for visual interpretation of 11C-Pittsburgh compound-B PET images, *J Nucl Med*, **55** (2014), 1305-1307.

Appendices

Appendix 1: Preliminary Caspase 3 Targeted Contrast Agent Evaluation using Magnetic Resonance Imaging and Confocal Microscopy

Jonatan A. Snir[1], Mojmir Suchy [2,3], Alex X. Li [2], Robert H.E. Hudson [3], Stephen H. Pasternak [4,5] and Robert Bartha [2]

[1]Department of Medical Biophysics, [2] Centre for Functional and Metabolic Mapping, Robarts Research Institute, [3]Department of Chemistry, [4]J. Allyn Taylor Centre for Cell Biology, Molecular Brain Research Group, Robarts Research Institute, [5] Departments of Clinical Neurological Sciences, Schulich School of Medicine, The University of Western Ontario, London, Ontario, N6A 5K8, Canada

INTRODUCTION

Programmed cell death is an important outcome of a multitude of cellular signals and underlying pathological conditions. Apoptosis is a fundamental type of cell death process involving the activation of proteases, most importantly caspase 8 and 3 which mediate and commit the cell to die. Apoptosis can be triggered using ultraviolet (UVB: 280-320 nm) light causing DNA damage [1] or exposure to lethal thermal shock [2]. The artificial induction of increased apoptosis in tumours is an effective cancer therapy approach, and the reduction of apoptosis may improve prognosis of ischemia and neurological pathologies [3]. Magnetic Resonance Imaging (MRI) and spectroscopy (MRS) are both powerful tools for clinical diagnosis. While MRI is able to detect changes in-vivo in MR image contrast that are thought to reflect the morphological features of apoptosis, these occur late in the process [4]. Paramagnetic Chemical Exchange Saturation Transfer (PARACEST) [5] imaging contrast agents (CA) have been shown to be sensitive to physiologic parameters such as pH and temperature. These CA are indirectly detected by selective saturation of exchangeable agent bound protons [6]. There are three main recognized pathways of cell death and one mode may dominate another depending on the injury and type of cell [7]. DNA damaging agents as well as neurodegenerative disorders are dominated by apoptosis [8]. Apoptosis may be detected using a CA targeted to caspase 3, capable of translocating into cells. It is our belief that cells undergoing apoptosis can be detected using microscopy and MRI, following increased retention of a caspase 3 targeted CA containing a lanthanide metal, and a fluorescent dye, conjugated to a cell penetrating peptide.

MATERIALS AND METHODS

Contrast Agent Synthesis and Characterization

We synthesized a novel CA containing a cleavage site specific to Caspase 3 (a central mediator of the apoptosis pathway) which contains components for both MRI (Tm3+-DOTAM) and fluorescent (Oregon Green ® dye) detection (Fig. A1-1). The CA has also been conjugated to a cell penetrating peptide (CPP) facilitating transport into, and out of a cell. Active Caspase 3 within cells irreversibly removes the CPP segment

from an internalized CA, in effect, reducing the transport kinetics of the cleaved CA out of the respective cells, increasing retention.

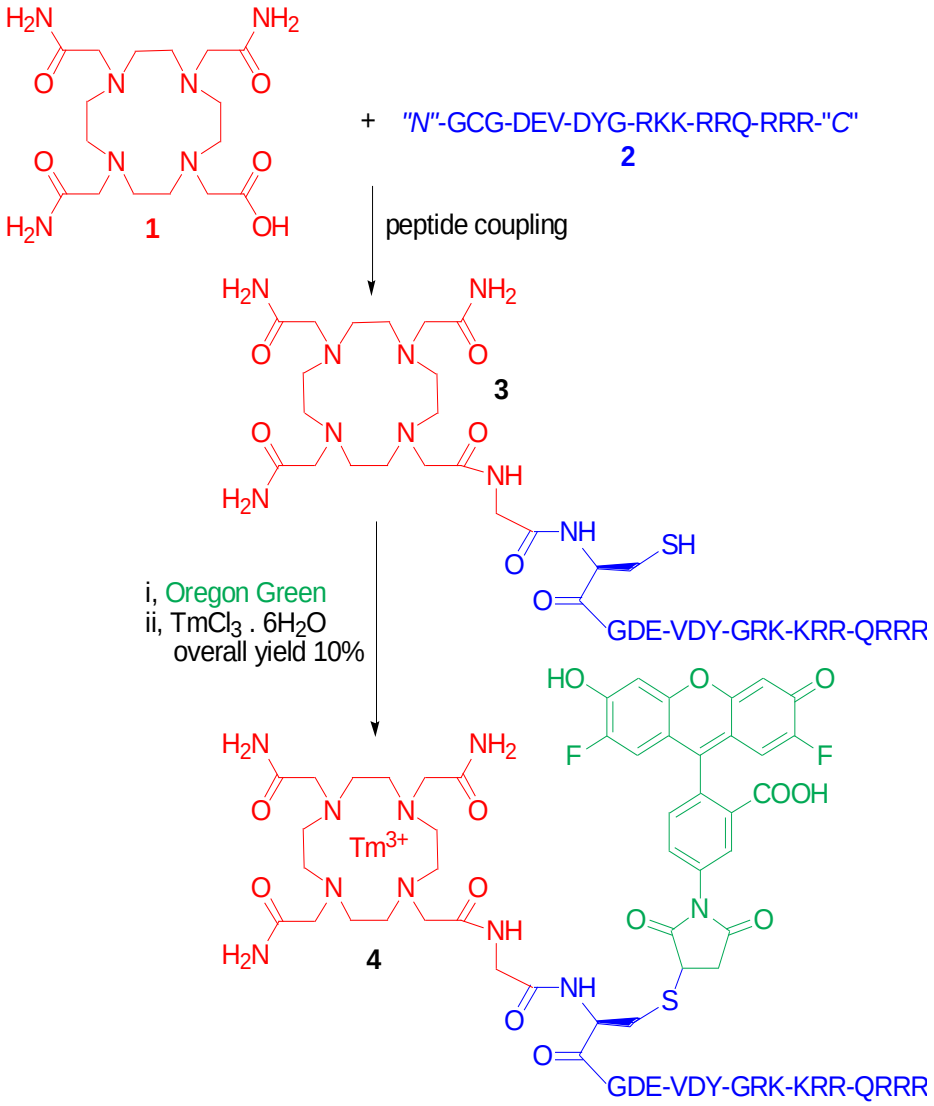

Figure A1-1. Contrast agent synthesis. The first step in the synthesis of the caspase 3 sensitive probe (structure 4) was a peptide coupling (HBTU, DIPEA, DMF) between the DOTAM-derived carboxylic acid 1 and the peptide 2 attached to the resin. Conjugate 3 was purified by semi-preparative HPLC, was characterized by high resolution mass spectrometry and was subjected to conjugation with Oregon Green and metallation with $TmCl_3 \cdot 6H_2O$. Desired probe 4 was obtained in 10% overall yield and was characterized by high resolution mass spectrometry.

Experimental design

As depicted in Fig. A1-2, prostate cancer cells (PC3M) were either irradiated with ultraviolet radiation (UVB; 40 W/m2 312 nm), exposed to thermal shock (45°C for 30 minutes), or maintained without any insult. Immediately after irradiation, cells were incubated overnight (24 hours) with the CA (concentration of 0.68 µM for confocal microscopy and 3.1 µM for PARACEST MRI).

In-vitro experimental design

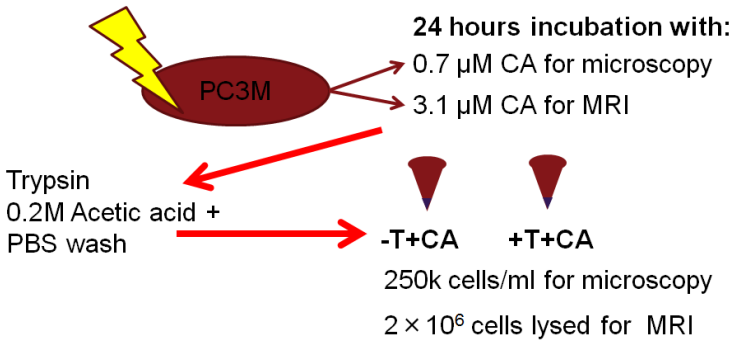

Figure A1-2: Experimental design. Prostate cancer cells were either exposed (T) to injury (UVB 40W/m2 or thermal shock [320]) or not (-T), and incubated with the CA overnight and then collected for microscopy and MRI analysis.

Confocal microscopy

Bright field and fluorescent confocal imaging (LSM510, META-NLO;Carl Zeiss, Inc) of the centrifuged treated (+T) and non-treated (-T) cells prepared as described (Fig. A1-2) allowed visualization of the cells and fluorescent quantification (N=4) of the internalized CA as well as nuclear staining suggesting chromosome condensation associated with cell death.

Magnetic Resonance Imaging – OPARACHEE

MRI detection of cell lysates (2×106 cells per ml for all samples) was achieved using a 9.4 Tesla, 31 cm diameter bore Agilent (Palo Alto, CA) small animal MRI scanner

(N=1). Two images were acquired using a fast low angle shot (FLASH) pulse sequence (TE/TR=2.5/5.3 ms, 25.6 mm x 25.6 mm field of view, 128×128 matrix, 3 mm thick slice, 5 s pre-delay), where the second image was preceded by a WALTZ-16 preparation pulse (480 ms, 6 μT) centered on the bulk water frequency to generate contrast [9] using the on-resonance paramagnetic chemical exchange effect (OPARACHEE).

RESULTS

Apoptosis Induction and Oparachee Contrast

Green fluorescence was expressed diffusely within the cells (Fig. A1-3A and A1-3B). However, fluorescent imaging clearly demonstrated a preferential uptake/retention (75 % vs. 6 %) by the irradiated cells (Fig. A1-3B) compared to the control cells (Fig. A1-3A).

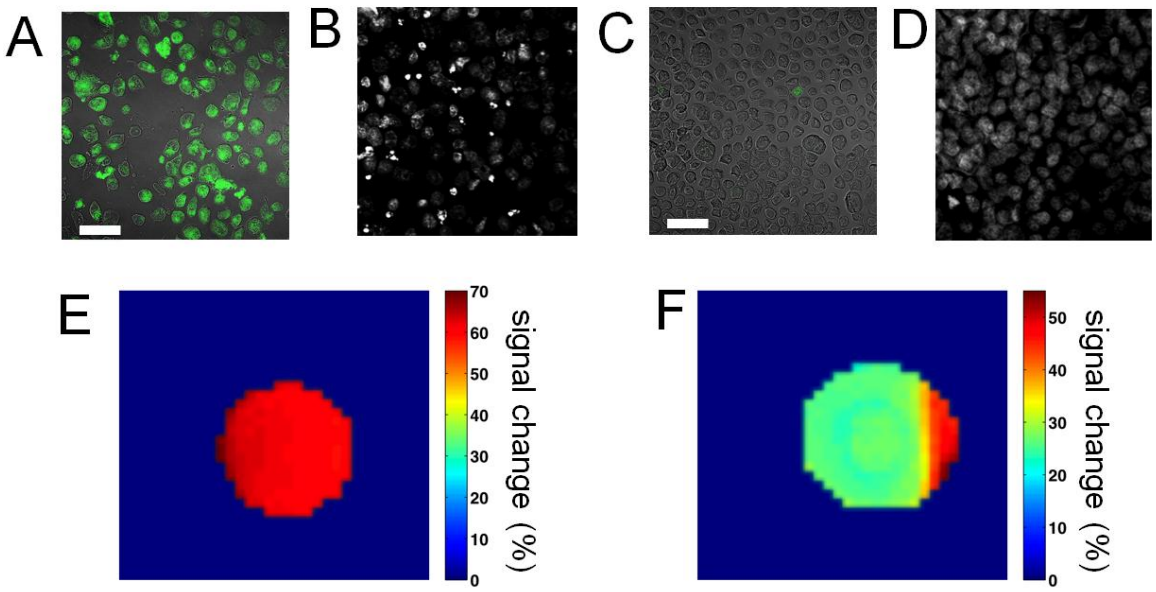

Figure A1-3: UVB Treated cells +T+C (A; green fluorescence from CA) undergoing apoptosis (B; Hoechst stain showing nuclear fragmentation) presented preferential retention of the CA as seen by microscopy compared to control cells -T+CA(C; green fluorescence from CA) which appear "normal" (D; Hoechst staining is not indicative of substantial nuclear fragmentation). Scale bar is 200μm. Lethal Shock treated cell lysates also presented higher contrast (E) compared to control (F). TE/TR=2.5/5.3 ms, 25.6 mm x 25.6 mm field of view, 128×128 matrix, 3 mm thick slice, 5 s pre-delay.

The percent (mean ±standard deviation) of UVB treated cells (Fig. A1-3A,B) having internalized the CA (53.9±16.2 %) was higher ($p>0.05$) than the control cells (Fig. A1-3C,D; 18.0±12.7 %). OPARACHEE contrast of heat-shock treated cells incubated with CA (+T+CA, Fig. A1-3E: 61% across ROI), was higher than the contrast measured for non-treated cells with CA (-T+CA, Fig. A1-3F: 28% across ROI).

DISCUSSION

This study demonstrates preferential uptake of a novel MRI contrast agent targeted to Caspase 3 in cells irradiated with UVB light to induce apoptosis. Detection of the agent by MRI using OPARACHEE suggests in-vivo detection is possible. In the future, the contrast agent will be utilized in an in-vivo murine model of brain cancer to study the spatial and temporal distribution of apoptotic cells prior to and following radiation treatment.

REFERENCES

[1] R. Takasawa, H. Nakamura, T. Mori and S. Tanuma, Differential apoptotic pathways in human keratinocyte HaCaT cells exposed to UVB and UVC, *Apoptosis*, **10** (2005), 1121-1130.

[2] A.E. Caccamo, S. Desenzani, L. Belloni, A.F. Borghetti and S. Bettuzzi, Nuclear clusterin accumulation during heat shock response: implications for cell survival and thermo-tolerance induction in immortalized and prostate cancer cells, *J Cell Physiol*, **207** (2006), 208-219.

[3] F.G. Blankenberg, In vivo detection of apoptosis, *J Nucl Med*, **49 Suppl 2** (2008), 81S-95S.

[4] M. Zhao, D.A. Beauregard, L. Loizou, B. Davletov and K.M. Brindle, Non-invasive detection of apoptosis using magnetic resonance imaging and a targeted contrast agent, *Nat Med*, **7** (2001), 1241-1244.

[5] S. Zhang, M. Merritt, D.E. Woessner, R.E. Lenkinski and A.D. Sherry, PARACEST agents: modulating MRI contrast via water proton exchange, *Acc Chem Res*, **36** (2003), 783-790.

[6] C.K. Jones, A.X. Li, M. Suchy, R.H. Hudson, R.S. Menon and R. Bartha, In vivo detection of PARACEST agents with relaxation correction, *Magn Reson Med*, **63** (2010), 1184-1192.

[7] R.S. Hotchkiss, A. Strasser, J.E. McDunn and P.E. Swanson, Cell death, *N Engl J Med*, **361** (2009), 1570-1583.

[8] L. Annunziato, S. Amoroso, A. Pannaccione, M. Cataldi, G. Pignataro, A. D'Alessio, R. Sirabella, A. Secondo, L. Sibaud and G.F. Di Renzo, Apoptosis induced in neuronal cells by oxidative stress: role played by caspases and intracellular calcium ions, *Toxicol Lett*, **139** (2003), 125-133.

[9] E. Vinogradov, S. Zhang, A. Lubag, J.A. Balschi, A.D. Sherry and R.E. Lenkinski, On-resonance low B1 pulses for imaging of the effects of PARACEST agents, *J Magn Reson*, **176** (2005), 54-63.

Appendix 2: Optical Scanner setup observations and Time-Domain fluorescence lifetime analysis considerations

OPTICAL SCANNER SETUP

When scanning using the Optix eXplore a few careful steps should be taken to maintain the distance between the detector and the top of the sample (or animal) with little variation. Differences will occur as a result of the source - detector distance. If one is imaging with multiple ROIs (e.g. more than one mouse) one must consider the relative height of the different targets. As an example, an examination of the effect of the level (height) of the bed on optical signal was performed. In the figure below, no changes were made between images aside from lowering the bed from its original position such that the horizontal guideline on the surface of the head (A) was moved to be above the head by about 1 cm (B). There is a clear reduction in the fluorescence signal as expected due to the optical divergence of light from the source. This effect was particularly important when using a Y-shaped nose cone to image two mice at the same time, since both require the same level of detector-to-sample distance that could be verified using the scanner setup as seen on the side-view image below.

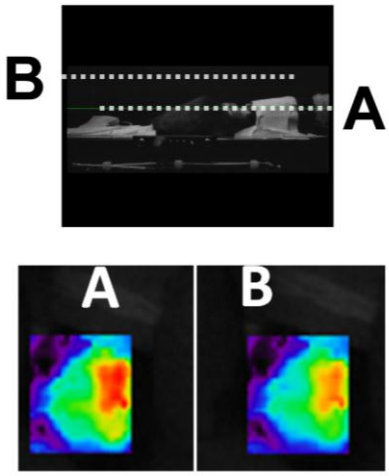

Figure A2-1: Adjustment of scanning bed height.

When it comes to changing the step size (distance between scanning points –> resolution), there were no significant differences in measured signal. Larger step sizes should be considered for smaller temporal resolution as the RASCAL scanning (rapid scanning and correction of multiple sequence alignments)could take up to a few minutes for an ROI drawn over the head of the mouse as below (showing the results of the same mouse with difference spatial step sizes following administration of the CatD targeted CA).

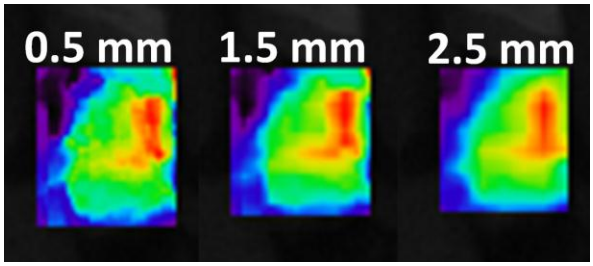

Figure A2-2: Adjustment of scanning resolution

FLUORESCENCE LIFETIME ANALYSIS

An important but rarely used strength of the eXplore Optix optical scanner is the time-domain feature, where unlike continuous light optical scanners, it can capture the lifetime characteristics of the fluorescent signal. This feature has been used previously to evaluate the depth of the dye, the concentration, as well as the environment where the fluorescent dye is residing (e.g. lipids) [1-4]. The fluorescence lifetime is a unique feature specific to each fluorescent dye and its environment. We have briefly examined the fluorescence lifetime of our CAs and notice an interesting finding – a difference in the characteristic lifetime of the complete (CatD targeted CA) versus the non-penetrating (cleaved CatD targeted CA). Therefore it may be possible to examine the enzymatic kinetics using a fast fluorescent lifetime analysis in regions expected to have overexpression of the target enzyme (e.g. AD brain). This effect is shown in the next figure where the fluorescence life time is plotted (intensity over time):

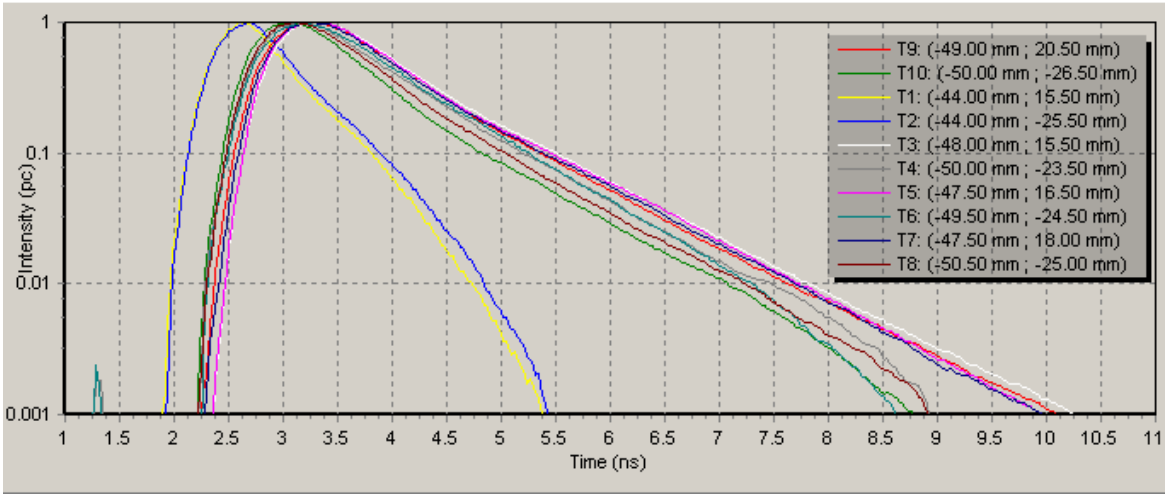

Figure A2-3: Temporal Point Spread Function plots of the NIR signal.

Examining the cleaned Temporal Point Spread Function (TPSF) (using Optiview built in algorithms) several observations can be made: T1and T2 (yellow and blue respectively) are from pre-scan data points over the brain of the mouse prior to injection. T3,T5,T7 and T9 (white, pink, dark blue and red respectively) are from the brains of mice injected with the non-CPP agent. Lastly T4, T6, T8, T10 (grey, teal, brown and green respectively) are from the brains of mice injected with the CPP-containing agent. The peak of the fluorescence lifetime corresponds (assuming all parameters were used correctly) to the depth, or arrival time. The slopes of the lines thereafter are representative of the lifetime of the fluorescence. It is noteworthy, that CatD targeted CA (CPP-containing agent) have a significantly different ($p < 0.01$) x-axis intercept (8.79 ± 0.16) compared to those of the non-CPP (non-penetrating) agent (10.05 ± 0.12). Because the molecular structure of the non-CPP is the same as that of a cleaved CatD targeted CA, future studies could examine the use of this technique to evaluate the enzymatic cleavage of the contrast agent as it circulates in the mouse body.

REFERENCES

[1] A. de la Zerda, S. Bodapati, R. Teed, M.L. Schipper, S. Keren, B.R. Smith, J.S. Ng and S.S. Gambhir, A comparison between time domain and spectral imaging systems for imaging quantum dots in small living animals, *Mol Imaging Biol*, **12** (2010), 500-508.

[2] D. Elson, J. Requejo-Isidro, I. Munro, F. Reavell, J. Siegel, K. Suhling, P. Tadrous, R. Benninger, P. Lanigan, J. McGinty, C. Talbot, B. Treanor, S. Webb, A. Sandison, A. Wallace, D. Davis, J. Lever, M. Neil, D. Phillips, G. Stamp and P. French, Time-domain fluorescence lifetime imaging applied to biological tissue, *Photochem Photobiol Sci*, **3** (2004), 795-801.

[3] S. Keren, O. Gheysens, C.S. Levin and S.S. Gambhir, A comparison between a time domain and continuous wave small animal optical imaging system, *IEEE Trans Med Imaging*, **27** (2008), 58-63.

[4] A. Torricelli, D. Contini, A. Pifferi, M. Caffini, R. Re, L. Zucchelli and L. Spinelli, Time domain functional NIRS imaging for human brain mapping, *Neuroimage*, **85 Pt 1** (2014), 28-50.

Appendix 3: Supplemental information for chapter 4

EXTRANEOUS NON-BRAIN RADIOACTIVITY SPILL-OVER INTO VOLUME OF INTEREST

Time Activity Curves (TAC) for the Tg mouse brain at 6 and 9 months of age were increasing over time. In order to test that this significant difference was not as a result of any peripheral signal washing into adjacent brain tissue voxels, Volumes of Interest (VOI) were drawn over lateral tissue surrounding the brain (skull, skin, muscle) and tested for any significant differences between the Tg and age-matched non-Tg littermates. As can be seen below in Fig. A3-1 no differences were noted, but a consistent increase in signal over time was noted for both groups. This increase overtime may be the result of true CA accumulation in the respective tissues or de-chelated ^{68}Ga accumulation in bone.

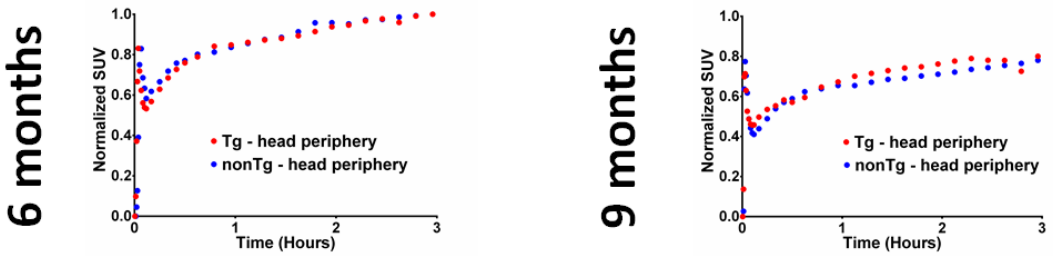

Figure A3-1: periphery *SUV* data. Calculated *SUV* from the TAC from VOI drawn over the peripheral tissue lateral to the brain for both Tg (red) and nonTg (blue) at 6 and 9 months of age.

Furthermore, in order to test whether the signal in the brain can be detected by the microPET scanner even after removal of all (most) the blood content from the brain as well as dissociation from any surrounding tissue, the following procedure was performed prior to an hour long static scan. Following CA administration via tail vein, one six months old 5XFAD Tg mouse was perfused by heparin followed by heparinized saline, dissected carefully to remove the brain and washed x3 in heparinized saline. The brain was then imaged with the resulting sample images in Fig. A3-2 below (unrelated mouse brain SSFP MRI anatomical image is shown for reference only). Because this was an

exploratory experiment not requiring quantification, no repeats of this attempt were pursued.

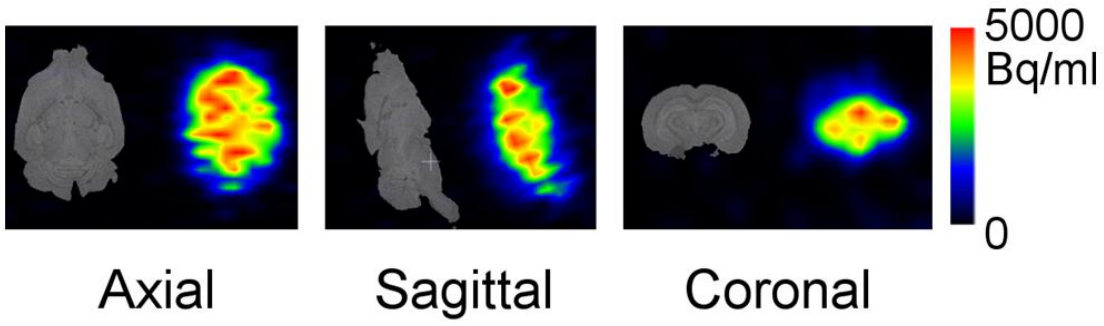

Figure A3-2: Dissected brain signal shortly after injection. Activity (Bq/ml) detected from a dissected perfused heparinized-saline washed brain is displayed over the axial, sagittal and coronal planes using sample non-related anatomical MRI image as reference only.

BIODISTRIBUTION

As a result of the possible requirement of larger sample size, these data were not included in Chapter 4. However, it may provide interesting information with respect to the bioavailability and distribution of our CatD targeted CA in the body.

METHODS AND MATERIALS

Adult female mice (10 months old Tg and age-matched non-Tg littermates) were anesthetized under 2% isoflurane during tail vein catheter insertion, CA injection, cardiac blood extraction and during perfusion with PBS. Three mice per group (N=3) were administered an average of ~3 MBq of ^{68}Ga-GLP-1 peptide. Mice were sacrificed at 1 hour post injection (p.i) by carbon dioxide followed by cardiac puncture for perfusion with cold heparinized saline and PBS, and organs dissection. The brain, muscle (thigh), bone (femur), heart, lungs, liver, spleen, kidneys were excised, washed in cold PBS, weighed, and counted in a high purity Ge gamma counter (Ortec GWL-190-15-S, detection range 51.32-2111.36 keV at 1.4-2.3 keV resolution, linear range of detection 0-4030 Bq). Injected dose (ID) was determined by measuring the activity of a diluted

injected dose CA solution (N=5). Activity of the samples was determined with an energy window of 507.18-515.43 (Energy of pair annihilation product photons is 511keV). To ensure all activity was captured accurately, samples were counted to a dead time of less than or equal to1%. Probe uptake was expressed as percent injected dose per gram tissue (%ID/g) and all activity was decay-corrected to the time of injection.

RESULTS

The biodistribution of the ^{68}Ga-labeled CatD Targeted CA, 1 hour after i.v tail administration of the CatD CA is shown in Table 1 for dissected vital organs as the percentage of the injected dose per gram tissue (%ID/g) for both the 11 month old Tg and age matched non-Tg (N=3). In general, the liver and lungs showed a very high uptake compared to all other organs displayed in Table 2. The spleen and kidney followed second and third respectively. There were no significant differences in the accumulation of the CA in bone, muscle, lungs, heart, spleen, liver and kidneys ($P > 0.1$) between groups. Furthermore, the brain-measured activity (mean ± standard deviation) was 0.03 ± 0.01 and 0.08 ± 0.04 %ID/g for non-Tg and Tg respectively (P = 0.07). The reason for the non-significant differences measured in the brains of the mice could be the result of minor human error (contamination of brain sample with blood) or unequal perfusion state of the mice making variability higher within each group, diminishing the differences between the two groups averages.

Table 1. Biodistribution in Tg and non-Tg mice at 1 hour p.i.

%ID/g

	Non-Tg	Tg	*P*
Brain	0.03 ± 0.01	0.08 ± 0.04	0.07
Bone	0.49 ± 0.34	0.68 ± 0.53	0.31
Muscle	0.68 ± 0.26	0.26 ± 0.24	0.21
Heart	0.51 ± 0.19	0.72 ± 0.23	0.14
Lungs	51.28 ± 77.14	81.51 ± 127.9	0.37
Spleen	32.67 ± 25.07	31.07 ± 15.39	0.46
Liver	62.21 ± 25.73	53.06 ± 25.22	0.34
Kidney	1.95 ± 0.43	2.48 ± 1.47	0.29

N=3

Appendix 4: Compartmental Modeling

To further examine the possible pharmacokinetics expected considering the hypothetical method of action, activation and accumulation of the Cat-D targeted CA as well as the associated controls a four compartment model was designed to qualitatively explore the signal dynamics over time (t). Previous methods have been applied in studies based on dual-tracer compartmental modeling for imaging primary cancer receptor concentrations in detail. The approach described herein was adapted to differentiate between functionalized (CPP) versus un-functionalized CAs, as well as targeted versus untargeted CA uptake over time. The compartment model is seen in Fig. A4-1a. The 1st compartment represents the blood content of the intact CA (non-cleaved) $C_{Bl}(t)$, the 2nd compartment represents the brain content of the intact CA (non-cleaved) $C_{Br}(t)$, the 3rd represents the brain content of the cleaved CA $C_{Br_{Cleaved}}(t)$, and the 4th compartment represents the blood content of the cleaved CA $C_{Bl_{Cleaved}}(t)$. With the exception of k_{el} and $k_{el\_cleaved}$ (which govern the rate of clearance of either the intact CA or the cleaved CA respectively) all other k values indicate the compartment from which the CA originates (first subscript number) to which the CA flows to (second subscript number). k_{12} and k_{21} indicate flow into and out of the brain respectively, k_{23} and k_{14} indicate enzymatic cleavage of the Cat-D targeted CA either in the brain or the blood respectively, and k_{34} indicate the escape of cleaved CA from the brain back into circulation.

The following system of differential equations was developed to govern the rate of change of CA concentration in each compartment:

$$\frac{dC_{Bl}(t)}{dt} = k_{21}C_{Br}(t) - (k_{12} + k_{el} + k_{14})C_{Bl}(t)$$

$$\frac{dC_{Br}(t)}{dt} = k_{12}C_{Bl}(t) - (k_{21} + k_{23})C_{Br}(t)$$

$$\frac{dC_{Br_{Cleaved}}(t)}{dt} = \Omega k_{23}C_{Br}(t) - k_{34}C_{Br_{Cleaved}}(t)$$

$$\frac{dC_{Bl_{Cleaved}}(t)}{dt} = k_{34}C_{Br_{Cleaved}}(t) + k_{14}C_{Bl}(t) - k_{el_{Cleaved}}C_{Bl_{Cleaved}}(t)$$

$$\text{2D Fluorescence Signal} = (\alpha)Signal_{Brain} + (1-\alpha)Signal_{Blood}$$

$$1.\ Signal_{Brain} = \delta\{[C_{Br}(t) + \beta C_{Br_{Cleaved}}(t)]\}$$
$$2.\ Signal_{Blood} = \delta\{[C_{Bl}(t) + \beta C_{Bl_{Cleaved}}(t)]\}$$

where the 2D fluorescence signal represents the weighted sum of the observed fluorescence signal from the brain tissue (See 1. above) and from the blood vessels (See 2. above) surrounding and supplying or draining the brain and head as a function of time, *t*. Furthermore, each fluorescence signal originating from the brain ($Signal_{Brain}$) or from the blood ($Signal_{Blood}$) are proportional (by an arbitrary detection efficiency δ=1 normalized for the purpose of this qualitative model analysis) –to the respective concentration of either a cleaved or un-cleaved CA (the former having a larger fluorescence by a factor of β = 1.6 as was determined experimentally; see Fig 3-2B). The detection efficiency (δ) might be determined from the relationship between concentration of agent and the optical signal – in which case the linear relationship was evaluated (Fig 3-2C&D). The extent to which a Tg (5XFAD) AD mouse model can cleave the Cat-D targeted CA depends on its over-expression (proportional) of the enzyme concentration (increased amount of gene expression or through changes in stability of the protein) respectively. In this case the over-expression factor was estimated to be Ω >2 (Based on having at least twice as much CatD protein by Western blots evaluation (Fig 2-5).

For the non-penetrating CA dynamics the four compartment model collapses onto a one compartment model with $k_{12}, k_{21}, k_{23}, k_{34}, k_{14}, k_{el} = 0$. This can be expressed as follows and visualized in the figure (Fig. A4-1a Compartment model in green):

$$\frac{dC_{Bl_{Cleaved}}(t)}{dt} = -k_{el_{Cleaved}} C_{Bl_{Cleaved}}(t)$$

from which one could extrapolate from the data the value of $k_{el_{Cleaved}}$ accordingly.

For the non-targeted CA dynamics the four compartment model collapses yet again, however, this time onto a two compartment model with $k_{23}, k_{34}, k_{14}, k_{el_{Cleaved}} = 0$. This

can be expressed as follows and visualized in the figure (Fig. A4-1a Compartment model in blue):

$$\frac{dC_{Bl}(t)}{dt} = k_{21}C_{Br}(t) - (k_{12} + k_{el})C_{Bl}(t)$$
$$\frac{dC_{Br}(t)}{dt} = k_{12}C_{Bl}(t) - (k_{21})C_{Br}(t)$$

this in turn provides the grounds to estimate the values of k_{12}, k_{21} and k_{el} accordingly (with k_{el} presumed to be relatively close to $k_{el_{Cleaved}}$) by fitting the available data. It is assumed the 9 amino acid long targeting sequence (attached between the CPP and the NIR dye conjugates and differentiates between the non-targeted versus the complete CA) does not affect the aforementioned coefficients significantly, however may provide insight to estimate the enzymatic cleavage coefficients (k_{23}, k_{14}) and the cleaved CA (non-penetrating) capacity to "escape" retention from the brain (k_{34}). Therefore, it can be seen that for the complete CPP CatD targeting CA, the four compartment model can be explored by observing the estimated fluorescence signal as modeled and qualitatively comparing with the in-vivo results. It may be possible to further understand two key features crucial to the success of the experimental CA for the detection of AD:

1. A drug/CA capacity to enter through the BBB is often very challenging. Comparing the non-penetrating to the non-targeting CAs dynamics we can get an idea of the BBB penetrating capacity of the CPP allowing estimation of the BBB penetration into/out of the brain (i.e of k_{12}, k_{21}).
2. The specificity of a drug/CA and consequentially its capacity to target a specific receptor, enzyme or other targets (binding potential) is very important and has been shown to correlate to the receptor/targeted enzyme concentrations (e.g CatD). By comparing the non-targeting to the complete CAs one can explore the cleavage/binding capacity of an agent to the target molecule (i.e of the enzymatic cleavage coefficients k_{23}, k_{14}).

More considerations and work is required to put this analysis to the test, and provide accurate and meaningful data. However the possibility to gain pharmacokinetic and pharmacodynamics information using this approach is exciting.

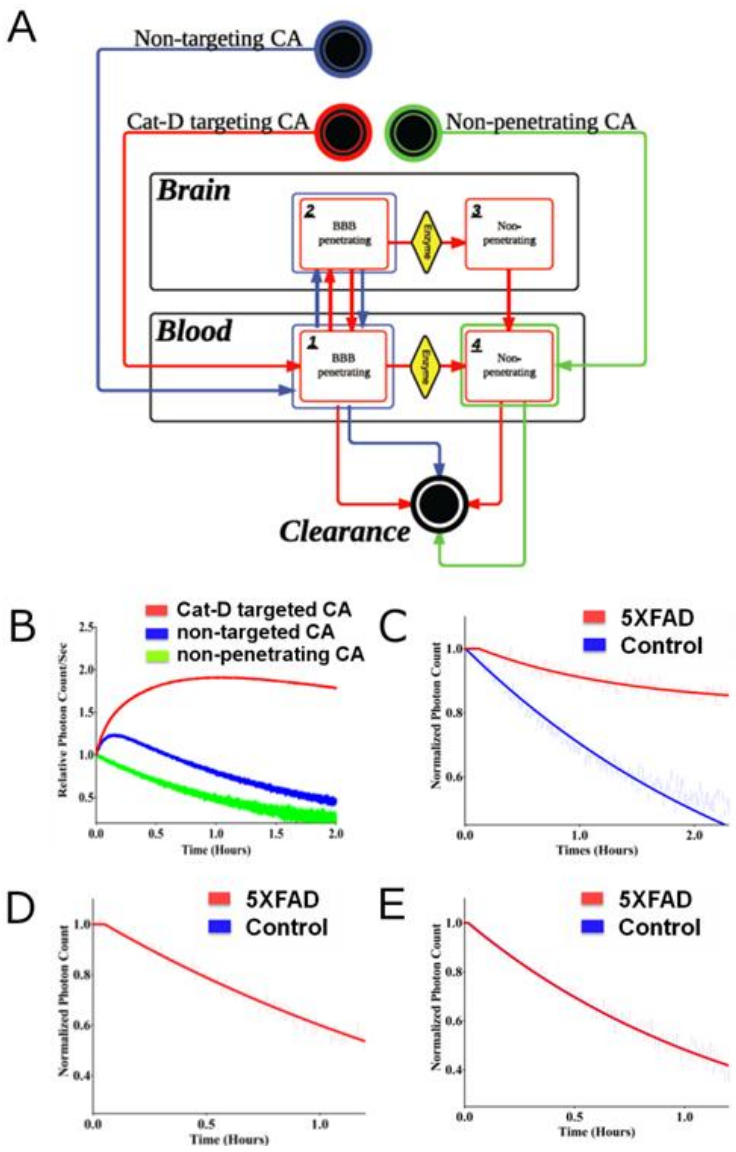

Figure A4-1 Modeling and simulations. (**A**) The CA kinetic compartment model for the Cat-D targeted (Red), non-targeted (Blue), and non-penetrating (Green) CAs. **1** Represents the blood content of the intact CA (non-cleaved), **2** Represents the brain content of the intact CA (non-cleaved), **3** Represents the brain content of the cleaved CA, **4** Represents the blood content of the cleaved CA. Arrows represents possible directions of CA movement from one compartment to another. (**B**) Curves of the estimated average fluorescence as would be measured following administration of either the Cat-D targeted (Red), non-targeted (Blue) and non-penetrating (Green) CAs over time in WT mice only. Comparison between older Tg (5XFAD; in red) and WT (Control; in blue) fluorescence signal as would be measured following the administration of the Cat-D targeted CA (**C**), non-targeted CA (**D**), and non-penetrating CAs (**E**) are shown with Gaussian noise increasing with time (x-axis). An arbitrary value for α was chosen to be 90%.

Appendix 5: Ethics Approval

Western

AUP Number: 2015-005
PI Name: Bartha, Robert
AUP Title: Development Of Novel Targeted Mri Contrast Agents
Approval Date: 04/29/2015

Official Notice of Animal Use Subcommittee (AUS) Approval: Your new Animal Use Protocol (AUP) entitled "Development Of Novel Targeted Mri Contrast Agents" has been APPROVED by the Animal Use Subcommittee of the University Council on Animal Care. This approval, although valid for four years, and is subject to annual Protocol Renewal.2015-005::1

1. This AUP number must be indicated when ordering animals for this project.
2. Animals for other projects may not be ordered under this AUP number.
3. Purchases of animals other than through this system must be cleared through the ACVS office. Health certificates will be required.

The holder of this Animal Use Protocol is responsible to ensure that all associated safety components (biosafety, radiation safety, general laboratory safety) comply with institutional safety standards and have received all necessary approvals. Please consult directly with your institutional safety officers.

Submitted by: Copeman, Laura
on behalf of the Animal Use Subcommittee
University Council on Animal Care

The University *of* Western Ontario
Animal Use Subcommittee / University Council on Animal Care
Health Sciences Centre, • London, Ontario • CANADA – N6A 5C1
PH: 519-661-2111 ext. 86768 • FL 519-661-2028
Email: auspc@uwo.ca • http://www.uwo.ca/animal/website/

Appendix 6: Curriculum Vitae

Jonatan A. Snir PhD, Clin M.Sc

Citizenship: Canadian

EDUCATION

09/2011 – 10/2015	Doctor of Philosophy, Masters of Clinical Medical Biophysics and Molecular Imaging, Schulich School of Graduate Studies and Robarts Imaging Research Laboratories, The University of Western Ontario: *The Development and Validation of a contrast agent targeted to Cathepsin D for the In-vivo detection of Alzheimer Disease.*
09/2006 – 06/2008	Masters of science, Medical Biophysics and Molecular Imaging, Schulich School of Graduate Studies and Robarts Imaging Research Laboratories, The University of Western Ontario: *Tracking Dendritic Cells in the Murine Lymphatic System Using Cellular MRI.*
09/2001 – 04/2006	Bachelor of Science, (Hon), The University of Western Ontario, Physics (Medical Physics concentration and applied mathematics minor): *Implementation of a numerical simulation tool for ultrasound imaging*

AWARDS AND SCHOLARSHIPS

07/2015	$33,000	Endowed Research Fellowship in Care of Older Adults
06/2015	$2000	Travel Fellowship for AAIC (high abstract score).
01/2015	$8,512	*WGRS – Medical Biophysics all terms combined*
10/2014	$650	The 2014 WMIC Excellent Abstract Score Award
01/2014	$9,674	*WGRS – Medical Biophysics all terms combined*
05/2014	$15,000	Queen Elizabeth II Graduate Scholarships in Science and Technology
01/2013	$12,260	*WGRS – Medical Biophysics all terms combined*
05/2013		The 2013 ISMRM Magna Cum Laude Merit Award (top 15% abstract score)
05/2013	$375	Travel Fellowship – complimentary AAIC conference registration.
05/2013	$195	Travel Fellowship – Complimentary AIC conference registration.
05/2013	$15,000	Queen Elizabeth II Graduate Scholarships in Science and Technology
03/2013	$355	ISMRM student stipend award 2013
09/2012	$15,000	Queen Elizabeth II Graduate Scholarships in Science and Technology
01/2012	$5,450	*WGRS – Medical Biophysics all terms combined*
01/2012	$12,500	Alzheimer Society Awards (External)
01/2008	$3590	*WGRS – Medical Biophysics all terms combined*
01/2008	$783	*Schulich Scholarship for Med Research*
09/2007	$784	*Schulich Scholarship for Med Research*
01/2007	$2,732	*WGRS – Medical Biophysics all terms combined*
05/2007	$795	*Schulich Scholarship for Med Research*
11/2005	$600	*UWO Bursaries Science MET*
12/2003	$1,400	*UWO Bursaries Medicine MET*
02/2002	$2,000	*Scholarship of Excellence,* UWO (1 years)
02/2002	$500	*UWO Bursaries Science MET*

RESEARCH EXPERIENCE

09/2011 – 12/2011	Research Assistant (Paid)	*Cellular and molecular MRI studies of LPS- induced cerebral inflammation (mouse model) **Supervisor**: Dr. Paula Foster at Robarts Imaging Research Laboratories, The University of Western Ontario London, ON
01/2011 - 09/2011	Research Assistant (Paid)	*Data collection, input, consolidation and analysis (human) **Supervisor**: Dr. Shahar Levi at the Cardiology dept. University Hospital London, ON
05/2011 - 09/2011	Research Assistant (Paid)	*Cellular and molecular MRI study of EAE (mouse model) **Supervisor**: Dr. Paula Foster at Robarts Imaging Research Laboratories, The University of Western Ontario London, ON
05/2010 – 09/2010	Research Assistant (Paid)	*Evaluation and Optimization of radiation sensitive gels production *Implementation of multiple slot array collimator to minimize stray light in optical cone beam CT *Analysis, recording of results, for future developments in the field of 3D dosimetry (phantom) **Supervisor**: Dr. Kevin Jordan, at the London Regional Cancer Program, London Health Sciences Center. London, ON
06/2009 – 04/2010	Research Assistant (Paid)	*Evaluation of new skin dosimetry devices using Clinac and Helical Tomotherapy machines. (human) *Examine inter-fraction prostate displacement for improving radiotherapy using retrospective studies of kV Cone Beam Computer Tomography (human) **Supervisor**: Dr. Slav Yartsev, at the London Regional Cancer Program, London Health Sciences Center. London, ON
08/2008 – 05/2009	Research Assistant (Paid)	*Heterogeneous gadolinium contrast enhancement in MRI of lymph nodes using Gadofluorine M and Magnevist following intravenous or intradermal injections (mouse model) * LN MRI and cellular tracking using SPIO (mouse model) **Supervisor**: Dr. Paula Foster at Robarts Imaging Research Laboratories, The University of Western Ontario London, ON

PUBLICATIONS

Snir JA, Jonatan A. Snir, Robert Bartha and Stephen H. Pasternak. *Cathepsin D Expression in the Brain across Alzheimer Disease Mice Models*. In preparation for submission to Journal of Alzheimer and Dementia.

Snir JA, Jonatan A. Snir, Mojmir Suchy, Geron A. Bindseil, Blaine A. Chronik, Robert H.E. Hudson, Stephen H. Pasternak and Robert Bartha. *A Cathepsin D targeted PET agent: Application in an Alzheimer Disease mouse model.* Submitted to Journal of Alzheimer and Dementia. In-review Dec 2015.

Snir JA, Suchy M, St. Lawrence K, Hudson RHE, Pasternak SH, Bartha R. *Prolonged in-vivo retention of a Cathepsin D targeted optical contrast agent in an Alzheimer's disease mouse model*. Journal of Alzheimer's Disease. 2015 August 28; 48(1):73-87.

de Chickera, S.N., Willert, C.R., **Snir, J.A**., #Foster, P.J., and #Dekaban, G.A. *Labeling dendritic cells with SPIO has implications for their subsequent in vivo migration as assessed with cellular MRI*. Contrast Media and Molecular Imaging. 2011; 6: 314-327. #Co-senior authors.

Snir JA, Mosalaei H, Jordan K and Yartsev S , Bauman G, Yartsev S. *Surface dose measurement for helical tomotherapy*. Med Phys. 2011 Jun;38(6):3104-7

Snir JA, Battista J, Bauman G, Yartsev S. *Evaluation of inter-fraction prostate motion using kilovoltage cone beam CT during radiotherapy*. Clin Oncol. 2011 Nov; 23(9):625-31.

Jordan K, **Snir JA,** Battista J. *Multiple slot array collimator to minimize stray light in optical cone beam CT*. J Physics: Conference Series 250 (2010) 012062.

Snir JA, Van Dyk J, Yartsev S. *Comment on "Monte Carlo evaluations of the absorbed dose and quality dependence of Al2O3 in radiotherapy photon beams" [Med. Phys. 36, 4421-4424 (2009)]*

Dekaban GA, **Snir JA**, Shrum B, de Chickera S, Willert C, Merrill M, Said EA, Sekaly RP, Foster PJ, O'Connell PJ. *Semiquantitation of mouse dendritic cell migration in vivo using cellular MRI*. J Immunother. 2009 Apr;32(3):240-51.

Foster PJ, Dunn EA, Karl KE, **Snir JA**, Nycz CM, Harvey AJ, Pettis RJ. *Cellular magnetic resonance imaging: in vivo imaging of melanoma cells in lymph nodes of mice.* Neoplasia. 2008 Mar;10(3):207-16.

Joo Ho Tai, Paula Foster, Alma Rosales, Biao Feng, Craig Hasilo, Violetta Martinez, Soha Ramadan, **Snir JA**, Christopher J. Melling, Savita Dhanvantari, Brian Rutt and David J. G. White *Imaging Islets Labeled with Magnetic Nanoparticles at 1.5 Tesla.* Diabetes. 2006 Nov;55(11):2931-8.

Chris Heyn, John A. Ronald, Soha S. Ramadan, **Snir JA**, Andrea M. Barry, Lisa T. MacKenzie, David J. Mikulis, Diane Palmieri, Julie L. Bronder, Patricia S. Steeg, Toshiyuki Yondeda, Ian C. MacDonald, Ann F. Chambers, Brian K. Rutt, Paula J. Foster. *In vivo Tracking of Growth and Dormancy of Solitary Cells in a Mouse Model of Breast Cancer Metastasis to Brain using MRI*. Magn Reson Med. 2006 Nov;56(5):1001-10.

ORAL/ POSTER PRESENTATION

- **Snir JA**, Suchy M, Bindseil GA, Chronik BA, Hudson RHE, Pasternak SH Bartha R. Preclinical Micropet Assessment Of An In-Vivo Imaging Contrast Agent Targeting Cathepsin D In Alzheimer's Disease Mouse Models. Alzheimer Association International Conference (2015) Washington DC. USA. Talk

- **Snir JA**, Suchy M, Bindseil GA, Chronik BA, Hudson RHE, Pasternak SH Bartha R. Preclinical Micropet Assessment Of An In-Vivo Imaging Contrast Agent Targeting Cathepsin D In Alzheimer's Disease Mouse Models. Alzheimer Association International Conference – Alzheimer Imaging Consortium (2015) Washington DC. USA. Poster

- **Snir JA**, Suchy M, St. Lawrence K, Hudson RHE, Pasternak SH and Bartha R. In-Vivo Near-Infrared Imaging of a Cathepsin-D Targeted Contrast Agent for Early Detection of Alzheimer's disease. World Molecular Imaging Congress (WMIC) 2014, Seoul, South Korea. Top abstract score travel stipend. Talk.

- **Snir JA**, Suchy M, St. Lawrence K, Hudson RHE, Pasternak SH and Bartha R. In-Vivo Near-Infrared Imaging of a Cathepsin-D Targeted Contrast Agent for Early Detection of Alzheimer's disease. Robarts Research Retreat 2014, RRR2014, London, Ontario, Canada. Talk and poster.

- **Snir JA**, Suchy M, St. Lawrence K, Hudson RHE, Pasternak SH and Bartha R. A dual Fluorescent/Paramagnetic Chemical Exchange-Based MRI Probe for Cell Death Imaging. In Vivo MRI Cell Tracking symposium, London, Onbtario, Canada. Poster.

- **Snir JA**, Suchy M, St. Lawrence K, Hudson RHE, Pasternak SH and Bartha R. In-Vivo Optical Imaging For Early Detection Of Alzheimer's Disease. 12th Imaging symposium, ImNO 2014, Toronto, Ontario, Canadan. Poster.

- **Snir JA**, Suchy M, St. Lawrence K, Hudson RHE, Pasternak SH and Bartha R. In-Vivo Optical Imaging Of A Macromolecular Near-Infrared Fluorescence Delivery Vehicle For Early Detection Of Alzheimer's Disease Alzheimer's Association International Conference 2013 (AAIC 2013). Boston, Massachusetts, USA. July 13th-18th 2013. Poster.

- **Snir JA**, Suchy M, St. Lawrence K, Hudson RHE, Pasternak SH and Bartha R. A dual Fluorescent/Paramagnetic Chemical Exchange-Based MRI Probe for Cell Death Imaging. Oncology Research & Education Day. London, Ontario, CANADA. June 21st, 2013. Poster.

- **Snir JA**, Suchy M, St. Lawrence K, Hudson RHE, Pasternak SH and Bartha R. Positive Contrast Enhanced Imaging of the Mouse Lymph Nodes: A Comparison between Gd-DTPA and Gadofluorine-M. 21st Joint Annual Meeting ISMRM Salt lake city, Utah, US. 19-26 April 2013. Poster.

- **Snir JA**, Suchy M, St. Lawrence K, Hudson RHE, Pasternak SH and Bartha R. A dual Fluorescent/Paramagnetic Chemical Exchange-Based MRI Probe for Cell Death Imaging. 21st Joint Annual Meeting ISMRM Salt lake city, Utah, US. 19-26 April 2013. Feature 3 minutes teaser talk requested by the cellular and molecular imaging study group chair, 15 min electronic poster talk, and traditional poster

- **Snir JA**, Willert C, Dekaban GA, Foster PJ. Positive Contrast Enhanced Imaging of the Mouse Lymph Nodes: A Comparison between Gd-DTPA and Gadofluorine-M. London Imaging Discovery (LID) June 2012. Poster.

- Kevin Jordan, **Snir JA**, Jerry Battista. Multiple slot array collimator to minimize stray light in optical cone bean CT. IC3DDose: The 6th International Conference on 3D Radiation Dosimetry.

- **Snir JA**, Mosalaei H, Jordan K and Yartsev S , Bauman G, Yartsev S. Surface dose measurement of Helical Tomotherapy. Lawson Research Day March 22 2010. Poster.

- **Snir JA**, Battista J, Bauman G, Yartsev. Evaluation of inter-fraction prostate motion using kilovoltage cone beam CT. Lawson Research Day March 22 2010. Poster

- **Snir JA**, Battista J, Bauman G, Yartsev. Evaluation of inter-fraction prostate motion using kilovoltage cone beam CT. 8th Imaging symposium, ImNO 2010, Toronto, Ontario, Canada. Poster.

- **Snir JA**, Shrum B, de Chickera S, Willert C, Merrill M, Said EA, Sekaly RP, Dekaban GA, Foster PJ, O'Connell PJ. MR Tracking of Dendritic Cells for Investigation of Cancer Vaccines Ontario Consortium for Small Animal Imaging (OCSAI) MRI Workshop. Toronto. 27 May 2008. Talk.

- **Snir JA**, Shrum B, de Chickera S, Willert C, Merrill M, Said EA, Sekaly RP, Dekaban GA, Foster PJ, O'Connell PJ. Measuring Dendritic Cell Migration In Vivo. 16th Joint Annual Meeting ISMRM-ESMRMB Toronto, Canada. 3-9 May 2008. Poster

- **Snir JA.** VGStudioMax 1.2 Training Seminar Series: MR data measurement, representation and visualization. – Going from 2D to 3D.

- **Snir JA**, Shrum B, de Chickera S, Willert C, Merrill M, Said EA, Sekaly RP, Dekaban GA, Foster PJ, O'Connell PJ. In vivo Detection, Tracking and Quantitation of SPIO-Labeled Dendritic Cells in the Mouse Lymphatic System. 15th Joint Annual Meeting ISMRM-ESMRMB Berlin, Germany. 19-25 May 2007. Poster.

- **Snir JA**, Shrum B, de Chickera S, Willert C, Merrill M, Said EA, Sekaly RP, Dekaban GA, Foster PJ, O'Connell PJ. In Vivo Detection, Tracking and Quantitation of SPIO−Labeled Dendritic Cells in the Mouse Lymphatic System. 6th Imaging symposium, INO 2007, Toronto, Ontario, Canadan. Poster.

- **Snir JA**, Shrum B, de Chickera S, Willert C, Merrill M, Said EA, Sekaly RP, Dekaban GA, Foster PJ, O'Connell PJ. *Semiquantitation of mouse dendritic cell migration in vivo using cellular MRI*. Rush Hour Research ™ guest speaker at MaRS centre in Toronto May 9 2007.

- **Snir JA**, Tamie Poepping. B.Sc Honours Thesis: Implementation of a numerical simulation tool for ultrasound imaging. Oral presentation given to the department of Physics at the University of Western Ontario, London Ontario in April 2006

- **Snir JA**, Paula Foster. Canadian Undergraduate Physics Conference 2004 Victoria, BC, Canada. Oral presentation: Future look at 3D imaging applications.

- **Snir JA**, Paula Foster. Canadian Undergraduate Physics Conference 2003 Montreal, Quebec, Canada. Oral presentation:. Spinal Cord Imaging – 3D Visualization Techniques.